Adiabatic Dynamics and Topological Effects in Systems of Classical Spins Coupled to Itinerant Electrons

Dissertation

with the aim of achieving a doctoral degree
at the Faculty of Mathematics, Informatics and Natural Sciences
Department of Physics at the University of Hamburg

submitted by
Simon Peter Michel

Hamburg, November 2023

Gutachter/in der Dissertation:	Prof. Dr. Michael Potthoff
	Prof. Dr. Daniela Pfannkuche
Zusammensetzung der Prüfungskommission:	Prof. Dr. Michael Potthoff
	Prof. Dr. Daniela Pfannkuche
	Prof. Dr. Dorota Koziej
	Prof. Dr. Tim Wehling
	Prof. Dr. Alexander Lichtenstein
Vorsitzende der Prüfungskommission:	Prof. Dr. Dorota Koziej
Datum der Disputation:	March 13, 2024
Vorsitzender Fach-Promotionsausschuss PHYSIK:	Prof. Dr. Markus Drescher
Leiter des Fachbereichs PHYSIK:	Prof. Dr. Wolfgang J. Parak
Dekan der Fakultät MIN:	Prof. Dr.-Ing. Norbert Ritter

Acknowledgement

I would like to thank Michael Potthoff for supporting and supervising my time as a PhD student with dedication and expertise. I am thankful for the inspiring discussions, conceivable explanations and the shared scientific curiosity. Your role as a supervisor, always attentive and supportive throughout this academic endeavor, is deeply appreciated.

I thank Daniela Pfannkuche for co-supervising and evaluating this thesis.

Furthermore, I would like to thank all members and associated members of the group for creating a stimulating scientific environment, but also for the social times off the desk and the shared coffee breaks. I especially thank my long time office colleague Cassian for discussions on numerous spontaneous questions on physics and beyond. My particular gratitude goes to Robin for comprehensible insight to topological issues, for proofreading parts of this thesis and an unforgotten time in Iceland. Thank both of you for being available on request.

I am grateful for all people, family and friends that supported me on my path towards this thesis. Thank you Lukas for proofreading parts of it. Most of all, I am thankful to Paulina for backing me up throughout this at times challenging journey. I am looking forward to the future adventures to come.

Abstract

In this work the dynamic behavior of classical spins coupled via an indirect magnetic exchange and its interplay with topological effects is studied. We investigate the central role of the spin Berry curvature in the adiabatic dynamics of classical impurity spins coupled to a quantum system of itinerant electrons and explore the spin Berry curvature as the pivotal quantity driving a local topological phase transition

Our investigation starts with the study of an effective low-energy theory for slow classical impurity spins embedded in a lattice of fast classical spins. Exploring the adiabatic constraint, we reveal a geometric spin torque arising as a holonomy effect in the close-to-adiabatic regime. This non-Hamiltonian geometric spin torque is found to be the classical analogue of the spin Berry curvature. By comparing our effective theory to numerical solutions, we identify the regime in which the adiabatic approximation is valid, particularly, when there are two well separated slow and fast timescales. We improve the effective theory by relaxation of the adiabatic constraint to encompass a broader range of slow-spin configurations while maintaining a clear separation of timescales.

In the second study, we investigate the adiabatic dynamics of classical impurity spins coupled to an insulating electron system. Deriving the quantum-classical impurity dynamics under the adiabatic constraint, an anomalous non-Hamiltonian geometrical spin torque driven by the spin Berry curvature emerges. To explore the relationship between the spin Berry curvature and the bulk band topology of the electron system, we consider a spinful extension of Haldane's model of a Chern insulator. Our comprehensive theoretical framework and numerical calculations provide insights into the dependence of the spin Berry curvature on model parameters and the spatial impurity structure. We find the effective low-energy theory being sensitive to bulk band topology, which is validated by comparing numerically obtained dynamics for the full system with adiabatic spin dynamics.

Finally, we address the impact of local magnetic impurities, modeled as classical spins $\boldsymbol{S}$, on the electronic structure of the spinful Haldane model. We examine the spectral flow of bound states concerning the coupling strength J, encompassing both the topologically trivial and the Chern-insulating phases of the electron system. Our investigation reveals a local S-space topological phase transition in the J-spectral flow, which is different from the global k-space topology of the Chern insulator. This spatially

local topological phase transition is characterized by the spin Chern number, which is obtained by integrating the spin Berry curvature over the manifold of $\boldsymbol{S}$ configurations. We study implications of the spin Chern transition on the local electronic structure near the impurities, particularly concerning bound in-gap states. The characteristics of bound states induced by local impurities decisively depends on the global topological properties of the host system. We evaluate the local topological phase diagrams for various impurity configurations, providing valuable insights into the interplay between S-space and k-space topology. Eventually, in-gap states induced by local magnetic moments can reveal the bulk band topology of the surrounding electron system.

Kurzzusammenfassung

In dieser Arbeit wird das dynamische Verhalten klassischer Spins, die durch eine indirekte magnetische Wechselwirkung gekoppelt sind, analysiert und dessen Zusammenhang mit topologischen Effekten untersucht. Wir analysieren die zentrale Rolle der Spin-Berry-Krümmung in der adiabatischen Dynamik von klassischen Störstellen-Spins, die mit einem quantenmechanischen System itineranter Elektronen gekoppelt sind. Darüber hinaus wird die Spin-Berry-Krümmung als die definierende Größe eines lokalen topologischen Phasenübergangs erforscht.

Zunächst wird eine effektive Niederenergie-Theorie für langsame klassische Störstellen-Spins hergeleitet, die an ein Gitter aus schnellen klassischen Spins gekoppelt sind. In quasi-adiabatischen Dynamik dieses Systems tritt als Holonomie-Effekt ein geometrisches Spindrehmoment auf. Dieses nicht-Hamiltonsche geometrische Spindrehmoment wird durch das klassische Pendant zur Spin-Berry-Krümmung beschrieben. Durch den Vergleich unserer effektiven adiabatischen Theorie mit numerischen Lösungen der Dynamik des Gesamtsystems identifizieren wir den Parameterbereich, in dem die adiabatische Näherung gültig ist, insbesondere wenn die langsame und die schnelle Zeitskala sich deutlich unterscheiden. Darüber hinaus verfeinern wir die effektive Theorie, indem wir die adiabatische Zwangsbedingung zu einer 'tight-binding'-Zwangsbedingung abschwächen. Hiermit lässt sich ein größeren Bereich der Störstellen-Spin-Konfigurationen effektiv beschreiben, sofern die klare Trennung der Zeitskalen beibehalten wird.

In einer zweiten Studie untersuchen wir die adiabatische Dynamik klassischer Störstellen-Spins, die an ein isolierendes Elektronsystem gekoppelt sind. Die quanten-klassische Dynamik der Störstellen-Spins unter der adiabatischen Näherung beinhaltet ein anomales nicht-Hamiltonsches geometrisches Spindrehmoment, welches durch die Spin-Berry-Krümmung definiert wird. Um die Beziehung zwischen der Spin-Berry-Krümmung und der Bulk-Topologie des Elektronsystems zu untersuchen, betrachten wir als Elektronensystem eine Erweiterung von Haldanes Modell eines Chern-Isolators, welche Spin-Freiheitsgrade einbezieht. Unsere analytischen Betrachtungen sowie numerische Berechnungen liefern Erkenntnisse über die Abhängigkeit der Spin-Berry-Krümmung von Modellparametern und der räumlichen Geometrie der Störstellen-Spins. Wir stellen fest, dass die effektive adiabatischen Spindynamik von der Bulk-Topologie beeinflusst wird. Dies wird validiert durch einen Vergleich der Dynamik des

Gesamtsystems mit der Dynamik, die aus den Bewegungsgleichungen der adabatischen Spindynamik resultiert.
Abschließend widmen wir uns dem Einfluss lokaler magnetischer Störstellen, modelliert als klassische Spins $\boldsymbol{S}$, auf die elektronische Struktur des Spin-beinhaltenden Haldane-Modells. Wir untersuchen den spektralen Verlauf gebundener Zustände in Bezug auf die Störstellen-Kopplungsstärke J, wobei sowohl die topologisch triviale als auch die Chern-isolierende Phase des Elektronsystems betrachtet wird. Im J-abhängigen Spektrum zeigt unsere Untersuchung einen lokalen topologischen Phasenübergang im S-Raum, der sich von der globalen k-Raum-Topologie des Chern-Isolators unterscheidet. Dieser räumlich lokale topologische Phasenübergang wird durch die Spin-Chern-Zahl charakterisiert. Die Spin-Chern-Zahl wiederum ist durch die Integration der Spin-Berry-Krümmung über die Mannigfaltigkeit der $\boldsymbol{S}$-Konfigurationen definiert. Wir analysieren die Einflüsse des Spin-Chern-Übergangs auf die lokale elektronische Struktur in unmittelbarer Nähe der Störstellen, insbesondere in Bezug auf gebundene Zustände, die energetisch innerhalb der Bandlücke liegen. Die Charakteristika der von lokale Störstellen hervorgerufenen gebundenen Zustände sind maßgeblich von den globalen topologischen Eigenschaften des Elektronensystems abhängig. Diese gebundenen Zustände, die energetisch in der Bandlücke liegen, können Aufschluss über die Bulk-Topologie des umgebenden Elektronsystems geben. Wir erstellen lokale topologische Phasendiagramme für verschiedene Störstellenkonfigurationen und betrachten das Zusammenspiel zwischen der S-Raum- und der k-Raum-Topologie.

Table of Contents

1 – Introduction

Condensed matter surrounds us, and our world builds on its properties. Condensed matter physics yields a fascinating variety of features which are, in many cases, related to emergent phenomena. In his highly recognized paper *More is different* from 1972 [1], P.W. Anderson phrased it in apt words: "... we can see how the whole becomes not only more than but very different from the sum of its parts." Many body properties that go beyond the characteristics of their constituent parts are called emergent. Such emergence prevails in numerous facets across various disciplines. Examples are the swarming behavior of animals [2, 3], artificial intelligence, e.g. with large language models like Chat GPT [4–6], and eventually live itself [7]. The essence of emergence in physics arises from an assemblage of constituents 'competing' or 'cooperating' to, e.g., reduce some overall energy functional defining the many body system. Minimizing the energy functional can feature novel phenomena, such as superconductivity [8] or collective magnetism [9, 10].

Emergence-based phenomena can exhibit properties beyond the characteristics of the individual constituents. Examples hereto are emergent excitations like skyrmions [11–14] and effective magnetic monopoles [15–18] or gapless zero modes at the 'edges' of topological insulators [19–21]. In recent years, increasing popularity arose for emergent phenomena in topologically nontrivial states of matter [22]. Topology is a branch of mathematics characterizing properties that remain invariant under continuous transformations. Accordingly, topological quantities refer to global properties of the system. Hence, they are exceptionally robust against local perturbations [23]. This robustness is what makes topologically protected quantities appealing to future applications, e.g. quantum computing is longing for topological quantum-bits due to their predicted stability [23–25]. Hence, investigating topological phases of matter, detecting and eventually controlling emergent topological properties is not only of academic interest but may be crucial for future data storage and processing that surpasses the current limitations. This prompted our investigation on topological properties in condensed matter systems and the observable consequences attributed to these features.

In condensed matter physics, a system is described by a Hamiltonian with a set of parameters which defines the interplay of its constituents. Some change of these parameters can lead to a collective response of the constituents of the ensemble, which

might occur in order to minimize the energy functional according to the new parameter values. Changes of the system's 'structure' caused by such a collective response are known as phase transitions. In the 'conventional' theory of phase transitions, e.g. of the solid-liquid-gas transition of water [26] or the spontaneous magnetization of a paramagnet below the Curie temperature [9], each phase is determined by certain symmetries of the system. Transitions between symmetry-related phases are characterized by Landau's [27] theory of spontaneous symmetry breaking, as the system's symmetry changes right at the phase transition. But beyond the symmetry-defined phase transitions, there is a fundamentally different type of transitions. These are topological phase transitions, where the symmetry of the system remains unchanged among distinct topological phases.

As it yields an alluring field of novel phenomena, the theoretical discovery of topologically distinct phases of matter and transitions between topologically phases was awarded with the Nobel prize in physics 2016 to D.J. Thouless, F.D.M. Haldane and J.M. Kosterlitz [28–30]. An ensuing milestone in the topological understanding of matter was the exhaustive topological classification of gapped non-interacting fermion systems by the means of generic unitary and anti-unitary symmetries [31]. Symmetry classes were linked to topological invariants and defect modes [20, 32]. The 'periodic table' of topological insulators and superconductors is also referred to as the tenfold way, since there are ten classes of generic symmetries.

A quantum system with a Hamiltonian depending on external parameters has been studied in a seminal paper by M. Berry [33]. He pointed out, that the low energy physics of two energy surfaces in parameter space intersecting in a single point is formally always described by a quantum spin-1/2 in an external magnetic field. The spin-1/2 model nicely serves as an illustration of various concepts required for this thesis. The model's ground state $|\psi_0(\boldsymbol{B})\rangle$ is a function of the external parameter $\boldsymbol{B}$. Thus, the question of the quantum system's adaptation to a gradual change of that parameter arises. Berry applied the adiabatic theorem [34–37] when slowly, i.e. adiabatically, 'steering' a gapped quantum system with a unique ground state by an external parameter. The adiabatic theorem states, that a quantum system with gapped spectrum that is in an instantaneous eigenstate remains in this eigenstate when an external perturbation is slow as compared to the inverse gap that separates the eigenergy of this state from the rest of the spectrum. Accordingly, the quantum system remains in its ground state corresponding to the momentary control parameter configuration throughout an adiabatic steering process. The parallel transport of ground states $|\psi_0(\boldsymbol{B})\rangle$ in parameter space can be described by the Berry connection $\boldsymbol{A}$. It is defined by the overlap of ground states to infinitesimally modified external parameters. Integration of the Berry connection along a closed path $\mathcal{C}$ in parameter space yields the Berry phase, also known as the geometric phase, since it results from the parallel transport of $|\psi_0(\boldsymbol{B})\rangle$ on the

manifold of the control parameters [38] and only depends on the path in that manifold. By Stokes' theorem [39], the line integral of the Berry connection $\boldsymbol{A}$ along a closed path $\mathcal{C}$ can be expressed as a surface integral of $d\boldsymbol{A}$ over an 'area' $\mathcal{S}$ enclosed by $\mathcal{C} = \partial\mathcal{S}$. The exterior derivative of the Berry connection defines the Berry curvature $\boldsymbol{\Omega} = d\boldsymbol{A}$, which is invariant under local gauge transformations. The Berry curvature takes a central role for the studies presented in this thesis and it serves a dual purpose. For one, the Berry curvature defines the the quantum system's feedback to adiabatic dynamics of the control parameter. For the other, it is utilized to provide a topological invariant which characterizes the space of the quantum system's ground state 'attached' to a closed orientable manifold. Such manifolds are for example the k-space of translational invariant lattice models or the parameter space of the control parameters $\boldsymbol{B} \in \mathbb{R}^3 \setminus \{0\}$. This twofold character of the Berry curvature sets the theme of this thesis. Berry phase physics is a general concept, that applied to various field of physics. Two popular examples are the adiabatic dynamics of electrons interacting with nuclei in molecules, where the position of nuclei is taken as a classical parameter [40, 41]. Hence, position space is the classical parameter manifold to Born-Oppenheimer surfaces. As it is a system of few localized particles, the energy spectrum is gapped. A different example taken from condensed matter physics is the band structure of an insulator. Though electron states are macroscopically extended, their energy spectrum is gapped. The intrinsic parameter manifold hereto is given by the first Brillouin zone in k-space, which is of purely geometrical origin.

Here, we study yet another setup where Berry curvature effects arise. To probe adiabatic dynamics, we model the local magnetic moments of magnetic atoms as three component 'classical spins' $\boldsymbol{S}_i$ of unit length and take these as the slowly varying external control parameter that steer the quantum system. The classical approximation of magnetic moments of the adsorbed atoms (adatoms) is appropriate in limit of large $|\langle\hat{\boldsymbol{S}}\rangle|$ [42]. In a setup of local magnetic moments coupled to a quantum system, the classical parameter manifold is $\mathcal{S} = \mathcal{S}^2 \times \mathcal{S}^2 \times ...$, i.e. a two sphere $\mathcal{S}^2$ for each magnetic impurity. Contrary to the torus $\mathcal{T}^d$ that characterizes the first Brillouin zone of a d-dimensional topological insulator, $\mathcal{S}$ is extrinsic to the quantum system. Since impurities $\boldsymbol{S}_i$ locally couple to the electronic degrees of freedom, unlike the k-space Berry curvature, the spin Berry curvature is not related to the lattice geometry of the quantum system.

Importantly, the Berry curvature is known to feed back to the dynamics of the external parameters that adiabatically steer the quantum system [43–47]. Our approach provides an adiabatic equation of motion for the external parameter $\boldsymbol{S}_i$, that determines their dynamics when coupled to a gapped quantum system with a unique ground state [48]. The adiabatic equation of motion features a geometric torque beyond the Hamiltonian dynamics. That non-Hamiltonian contribution is generated by the spin

Berry curvature $\mathbf{\Omega}$. The electron system must, however, break time-reversal invariance inherently to exhibit a non-zero spin Berry curvature in the limit of weak exchange coupling between impurities and the electron system. Hence, Haldane's two dimensional model of a topological quantum Hall insulator [28] is a suitable quantum host. It serves the dual purpose of breaking time reversal symmetry as well as featuring topologically nontrivial insulating phases. Furthermore, the Haldane model marked an inception for the ensuing advances in topological band theory [20, 49, 50], as it was the first model of a topological Chern insulator without external fields.

To start off, we study the geometric spin torque in a purely classical system. Next, we transfer the gained insight to a quantum-classical setup, where only magnetic adatoms are modeled by classical spins. The quantum host of the semiclassical setup is a spinful Haldane model, which is trivially composed of one copy of the Haldane model for each spin-projection $\sigma \in \{\uparrow, \downarrow\}$. The two copies are interconnected by the local interaction with the classical impurities. We investigate the feedback of the topology of a spinful Haldane model to the dynamics of the impurities $\boldsymbol{S}_i$. Particular interest is in the spin Berry curvature which gives rise to a geometric spin torque beyond Hamiltonian dynamics. We study the spin Berry curvature in various geometries and its dependence on parameters of the quantum-classical hybrid model.

Moreover, the spin Berry curvature is the curvature of a fiber bundle, which intrigued us to study the spin Chern number as it is a topological invariant of this bundle. It was S.S. Chern that linked (global) topology to intrinsic geometry, which was achieved by means of the (local) curvature in the context of fiber bundles [51]. We utilize Chern numbers, which are topological invariants resulting from Chern's findings [20, 39, 52], to identify topologically distinct phases. A change of a Chern number requires a topological transition in its defining space. In our case, that space is a fiber bundle, compounded by the quantum system's ground state 'attached' to each point of a base manifold. Here, that base manifold is either the k-space torus $\mathcal{T}^2$ of the Haldane model or the configuration space $\Pi_i \mathcal{S}_i^2$ of the classical control parameters $\boldsymbol{S}_i$. We emphasize that the spin Chern topology has to be distinguished from the band topology of the Haldane model, as it is subject to a different topological space. The spin Chern number results from a suitable integration of the spin Berry curvature over $\Pi_i \mathcal{S}_i^2$, while the Chern number that defines the band topology of the Haldane model results from an integral of the Berry curvature over the k-space torus $\mathcal{T}^2$. We address the uncharted question of the interplay of quantum-host band topology and the spin Chern topology induced by magnetic impurities. As a function of the host-impurity exchange coupling J, we find a transition of the spin Chern number and study the J-dependent electronic structure. Notably, in-gap states are found to be indicators of the k-space topology of the host.

2 – Setting the Stage

In these preparatory considerations, we introduce fundamental concepts that are utilized throughout the course of this thesis. Initially, the adiabatic theorem is introduced and subsequently applied to a quantum system steered by external parameters. Adiabatic dynamics of the external control parameters features effects emerging from the Berry curvature, for example the Berry phase. The Berry curvature in the context of differential geometry and topology is the curvature of a fiber bundle. Thus, the Berry curvature can be utilized to compute a topological invariant, the Chern number. We guide to the Chern number as topological invariant and briefly integrate this invariant in a topological context. As the Chern number is frequently utilized in (condensed matter) physics, our approach draws a rather pedagogical picture without the endeavor of a rigorous mathematical derivation. For the proceedings of sections 2.1 and 2.2 we follow [33, 53]. Moreover, section 2.3 is based on [39, 54].

2.1 – Adiabatic Theorem

We introduce the adiabatic theorem by discussing a Hamiltonian $H(\boldsymbol{R})$, that smoothly depends on a set of parameters $\boldsymbol{R} = (R_1, ..., R_N)$. The configuration space of these parameters is a smooth N-dimensional manifold $\mathcal{M}^N$. Throughout the scope of this thesis we assume non-degenerate ground states. A distinct ground state $|\psi_0(\boldsymbol{R})\rangle$ implies a finite gap $\Delta(\boldsymbol{R})$ to the first excited state $|\psi_1(\boldsymbol{R})\rangle$. To each set of parameters $\boldsymbol{R} \in \mathcal{M}^N$, the Hilbert space local to that point of the manifold is given by the orthonormal eigenbasis of $H(\boldsymbol{R})$, thus $H(\boldsymbol{R})|\psi_j(\boldsymbol{R})\rangle = E_j(\boldsymbol{R})|\psi_j(\boldsymbol{R})\rangle$. Next, we slowly vary the external parameters in time, so $\boldsymbol{R}(t)$ is a trajectory in $\mathcal{M}$. Consequently, the Hamiltonian becomes explicitly time dependent, $H(t) = H(\boldsymbol{R}(t))$. Time evolution of a state $|\Psi(0)\rangle$ is described by the Schrödinger equation. We set $\hbar = 1$, as we do throughout the thesis, and denote time ordering by $\mathcal{T}$, which leads to

$$|\Psi(t)\rangle = \mathcal{T} \exp\left(-i \int_0^t dt' H(t') \right) |\Psi(0)\rangle. \tag{2.1}$$

If the system is in its ground state to the initial $H(\boldsymbol{R}(0))$, so $|\Psi(0)\rangle = |\psi_0(\boldsymbol{R}(0))\rangle$, the adiabatic theorem [34–37] states that the system remains in its ground state when the

evolution of parameters $\boldsymbol{R}(t)$ is sufficiently slow. Assuming that this is the case, the system at time t is in the instantaneous ground state to $H(\boldsymbol{R}(t))$, so $|\Psi(t)\rangle \propto |\psi_0(\boldsymbol{R}(t))\rangle$. The sole degree of freedom that remains to be determined for the adiabatically time-evolved state $|\Psi(t)\rangle$ is its phase, hence we note

$$|\Psi(t)\rangle = e^{-i\gamma(t)}|\psi_0(\boldsymbol{R}(t))\rangle. \tag{2.2}$$

We refer to this constraint resulting from the adiabatic theorem as the adiabatic constraint. It is not easy to rigorously define when the dynamics of $\boldsymbol{R}$ is sufficiently slow for this statement to hold true. As a general rule, the adiabatic constraint is deemed valid when the parameter dynamics is slow as compared to the inverse gap. Say Δ is the gap between the ground and the first excited state and τ is the typical time scale of the parameter dynamics, then $\tau >> 1/\Delta$ is necessary to validate equation 2.2.

2.2 – Berry Phase, Connection and Curvature

In order to derive adiabatic dynamics, the holonomic adiabatic constraint (eq. 2.2) has to be applied to a description of the system that is suited to derive constraint dynamics. The Lagrange formalism provides such a framework. In 1984 Michael Berry [33] showed, that deriving equations of motion from the constraint Lagrangian yield insight of the phase $\gamma(t)$.
From the stationary action principle $\delta S = \delta \int dt L = 0$ of Lagrangian

$$L(\langle\Psi|, |\Psi\rangle, \partial_t\langle\Psi|, \partial_t|\Psi\rangle, t) = \langle\Psi|\big(i\partial_t - H(\boldsymbol{R}(t))\big)|\Psi\rangle \tag{2.3}$$

the Schrödinger equation is obtained. In fact, $0 = \partial L/\partial\langle\Psi| - \partial_t\big(\partial L/\partial(\partial_t\langle\Psi|)\big) = \big(i\partial_t - H(\boldsymbol{R}(t))\big)|\Psi\rangle$ is obtained when utilizing the second Euler-Lagrange equation with respect to $\langle\Psi|$. The effective Lagrangian subject to the adiabatic constraint is

$$\begin{aligned} L_{eff} =& e^{i\bar{\gamma}(t)}\langle\psi_0(\boldsymbol{R}(t))|\big(i\partial_t - H(\boldsymbol{R}(t))\big)|\psi_0(\boldsymbol{R}(t))\rangle e^{-i\gamma(t)} && (2.4)\\ =& e^{i\bar{\gamma}(t)}e^{-i\gamma(t)}\big[\boldsymbol{A}_0(\boldsymbol{R}(t))\partial_t\boldsymbol{R}(t) + \partial_t\gamma(t) - E_0(\boldsymbol{R}(t))\big] && (2.5)\end{aligned}$$

with

$$\boldsymbol{A}_0(\boldsymbol{R}) = i\langle\psi_0(\boldsymbol{R})|\nabla_{\boldsymbol{R}}|\psi_0(\boldsymbol{R})\rangle, \tag{2.6}$$

where $\nabla_{\boldsymbol{R}} = (\frac{\partial}{\partial R_1}, ..., \frac{\partial}{\partial R_N})$ is the gradient with respect to $\boldsymbol{R}$. Here, we exploited that $|\psi_0(\boldsymbol{R})\rangle$ is the eigenstate to eigenvalue $E_0(\boldsymbol{R})$ of $H(\boldsymbol{R})$ and $\boldsymbol{A}_0(\boldsymbol{R})\partial_t\boldsymbol{R} = \sum_{\alpha=1}^{N} A_{0,\alpha}(\boldsymbol{R})\dot{R}_\alpha$ with $\dot{R}_\alpha = \partial_t R_\alpha$, where we omit the time argument. $\boldsymbol{A}_0(\boldsymbol{R})$ is the Berry connection, which mediates between the ground state at $\boldsymbol{R}$ and the one at $\boldsymbol{R} + d\boldsymbol{R}$. It connects

'adjacent' ground states that are $d\boldsymbol{R}$ 'apart' on $\mathcal{M}$. For more details on the connection we refer to section 2.3 and to literature for further insight on the connection in the context of differential geometry, e.g. [39]. Since $i\nabla_{\boldsymbol{R}}$ is a hermitian operator and $|\psi_0(\boldsymbol{R})\rangle$ can be normalized, $\boldsymbol{A}_0(\boldsymbol{R})$ is a real quantity. The effective Lagranginan is a function $L_{eff} = L_{eff}(\gamma, \bar{\gamma}, \partial_t\gamma, \partial_t\bar{\gamma}, t)$. Initially, γ and $\bar{\gamma}$ have to be treated independently just like $\langle\Psi|$ and $|\Psi\rangle$ in order to apply the Euler-Lagrange equation correctly. Doing so for $\gamma(t)$ results in

$$\dot{\gamma}(t) = E_0(\boldsymbol{R}(t)) - \boldsymbol{A}_0(\boldsymbol{R}(t))\dot{\boldsymbol{R}}(t). \tag{2.7}$$

Straight forward integration yields $\gamma(t) = \gamma(0) + \int_0^t E_0(\boldsymbol{R}(t'))dt' - \int_0^t \boldsymbol{A}_0(\boldsymbol{R}(t'))\frac{\partial \boldsymbol{R}(t')}{\partial t'}dt'$. We rewrite the last term to $\int_{\mathcal{C},\boldsymbol{R}(0)}^{\boldsymbol{R}(t)} \boldsymbol{A}_0(\boldsymbol{R})d\boldsymbol{R}$, where $\mathcal{C}$ is the trajectory $\boldsymbol{R}$ traces in $\mathcal{M}$ parameterized by time t'. Trajectory $\mathcal{C}$ ranges from $\boldsymbol{R}(0)$ to $\boldsymbol{R}(t)$. Without loss of generality we set $\gamma(0) = 0$ and substitute the result to eq. 2.2, which leads to

$$|\Psi(t)\rangle = \exp\left(-\int_0^t E_0(\boldsymbol{R}(t'))dt'\right)\exp\left(i\int_{\mathcal{C},\boldsymbol{R}(0)}^{\boldsymbol{R}(t)} \boldsymbol{A}_0(\boldsymbol{R})d\boldsymbol{R}\right)|\psi_0(\boldsymbol{R}(t))\rangle. \tag{2.8}$$

The first phase factor is referred to as the 'dynamic' phase, while the second one is the 'geometric' phase. The latter is solely determined by trajectory $\mathcal{C}$ in the parameter manifold and is therefore labeled as geometric. Unlike the dynamical phase, the geometric phase is independent of the rate at which $\mathcal{C}$ is traversed.

Next, we discuss the physical relevance of the obtained geometrical phase. To this end, we consider gauge transformations as observable quantities are linked to gauge invariance. Choosing an orthonormal eigenbasis $\{\psi_i(\boldsymbol{R})\}$ implies the choice of phases $\phi_i(\boldsymbol{R})$. Unlike the initial ambiguity of the phase, a phase change may induce nontrivial effects. We perform a local gauge transformation to the ground state

$$|\psi_0(\boldsymbol{R})\rangle \mapsto e^{i\phi(\boldsymbol{R})}|\psi_0(\boldsymbol{R})\rangle, \tag{2.9}$$

which is local as $\phi(\boldsymbol{R})$ is a function on $\mathcal{M}$. A global transformation would, however, affect $|\psi_0(\boldsymbol{R})\rangle$ equally on all of $\mathcal{M}$, i.e., $|\psi_0(\boldsymbol{R})\rangle \mapsto e^{i\phi}|\psi_0(\boldsymbol{R})\rangle$.

The Berry connection (eq. 2.6) is gauge dependent and transforms as

$$\boldsymbol{A}_0(\boldsymbol{R}) \mapsto \boldsymbol{A}_0'(\boldsymbol{R}) = \boldsymbol{A}_0(\boldsymbol{R}) - \frac{\partial\phi(\boldsymbol{R})}{\partial\boldsymbol{R}} \tag{2.10}$$

under the local gauge transformation defined in equation 2.9. Since the initial choice of the local phase of the ground state is ambiguous, this gauge dependence is of no measurable consequence. Along an open path in $\mathcal{M}$, one can find a local gauge transformation, such that the product of the dynamical phase factor $\exp\left(-\int_0^t E_0(\boldsymbol{R}(t'))dt'\right)$

and the geometric phase factor $\exp\left(i\int_{\mathcal{C},\boldsymbol{R}(0)}^{\boldsymbol{R}(t)}\boldsymbol{A}_0(\boldsymbol{R})d\boldsymbol{R}\right)$ becomes trivial. Contrarily, along a closed path $\mathcal{C}$ in $\mathcal{M}$, the geometric phase factor is gauge invariant. The integral of the Berry connection over a closed path $\mathcal{C}$ is the Berry phase $\gamma_\mathcal{C}$ [33], which transforms as

$$\gamma_\mathcal{C} = \oint_\mathcal{C} \boldsymbol{A}_0(\boldsymbol{R})d\boldsymbol{R} \mapsto \gamma_\mathcal{C} - \oint_\mathcal{C} \frac{\partial\phi(\boldsymbol{R})}{\partial\boldsymbol{R}}d\boldsymbol{R} = \gamma_\mathcal{C} + 2\pi k \tag{2.11}$$

with $k \in \mathbb{Z}$. Consequently, the Berry phase factor $e^{i\gamma_\mathcal{C}}$ is gauge invariant and of physical relevance. Gauge invariance of the Berry phase itself is satisfied as a consequence of rather general conditions specific to the Poicaré lemma. In particular, continuity of $\frac{\partial\phi(\boldsymbol{R})}{\partial\boldsymbol{R}}$ is required to argue $\gamma_\mathcal{C} \mapsto \gamma_\mathcal{C} - \oint_\mathcal{C} \frac{\partial\phi(\boldsymbol{R})}{\partial\boldsymbol{R}}d\boldsymbol{R} = \gamma_\mathcal{C}$.

As $\mathcal{C}$ is a closed path in $\mathcal{M}$, it encloses an area $\mathcal{S}$, thus $\mathcal{C} = \partial\mathcal{S}$. Accordingly, the Berry phase is also obtained by

$$\gamma_\mathcal{C} = \oint_\mathcal{C} \boldsymbol{A}_0(\boldsymbol{R})d\boldsymbol{R} = \int_\mathcal{S} \boldsymbol{\Omega}_0(\boldsymbol{R})d\boldsymbol{S}, \tag{2.12}$$

where $d\boldsymbol{S}$ is an area element on $\mathcal{M}$ and $\boldsymbol{\Omega}_0(\boldsymbol{R})$ is the Berry curvature. In three dimensions ($\dim(\mathcal{M}) = 3$) the Berry curvature is the curl of the Berry connection, $\boldsymbol{\Omega}_0(\boldsymbol{R}) = \nabla_{\boldsymbol{R}} \times \boldsymbol{A}_0(\boldsymbol{R})$, and eq. 2.12 exploits Stokes' theorem to transform the line integral into a surface integral. Theory of differential forms generalizes the relation of the Berry connection, the Berry curvature and the Berry phase to arbitrary dimensions (see e.g. [55] or [39]). In that language, the Berry connection is extended to a differential 1-form (Berry connection one form A) and the Berry curvature to a differential 2-form (Berry curvature two form ω). Stokes' theorem states, that integrating Berry connection over $\mathcal{C}$ equals an integral of the Berry curvature over a compact orientable submanifold of $\mathcal{M}$. Generalization requires replacement of $\nabla_{\boldsymbol{R}}$ by the exterior derivative d. Subsequently, wedge products yield the total antisymmetic nature of the Berry curvature. Further details are discussed in section 5.1.

Next, we seek to express the components $\Omega_{0,\alpha\beta}(\boldsymbol{R})$ of the Berry curvature matrix $\boldsymbol{\Omega}_0(\boldsymbol{R})$ in a way that does not require any state derivatives. Exploiting orthogonality of the eigenbasis (see appendix A.2.2.1), $\Omega_0, \alpha\beta(\boldsymbol{R})$ is expressed in terms of derivatives of the Hamiltonian instead. We use the compact notion $\partial_\alpha = \frac{\partial}{\partial R_\alpha}$ for partial derivatives with $\alpha \in \{1, ..., N\}$ and exploit the anti-symmetry of the wedge product $dR_\alpha \wedge dR_\beta = -dR_\beta \wedge dR_\alpha$ to define the Berry curvature tensor $\boldsymbol{\Omega}_0$ with elements $\Omega_{0,\alpha\beta}$.The Berry connection one-form reads

$$A_0(\boldsymbol{R}) = \sum_\alpha A_{0\alpha}(\boldsymbol{R}) = \sum_\alpha i\langle\psi_0(\boldsymbol{R})|\partial_\alpha|\psi_0(\boldsymbol{R})\rangle dR_\alpha, \tag{2.13}$$

and the Berry curvature two-form

$$\begin{aligned}\omega_0(\boldsymbol{R}) =& dA_0(\boldsymbol{R}) = \sum_{\alpha,\beta} \partial_\alpha A_{0\beta}(\boldsymbol{R}) dR_\alpha \wedge dR_\beta \\ =& \sum_{\alpha<\beta} \left(\partial_\alpha A_{0\beta}(\boldsymbol{R}) - \partial_\beta A_{0\alpha}(\boldsymbol{R})\right) dR_\alpha \wedge dR_\beta \\ =& \sum_{\alpha<\beta} \Omega_0, \alpha\beta(\boldsymbol{R}) dR_\alpha \wedge dR_\beta, \end{aligned} \tag{2.14}$$

with

$$\begin{aligned}\Omega_0, \alpha\beta(\boldsymbol{R}) =& \partial_\alpha A_{0\beta}(\boldsymbol{R}) - \partial_\beta A_{0\alpha}(\boldsymbol{R}) = -2\mathrm{Im} \sum_{j\neq 0} \langle \partial_\alpha \psi_0(\boldsymbol{R}) | \psi_j(\boldsymbol{R}) \rangle \langle \psi_j(\boldsymbol{R}) | \partial_\beta \psi_0(\boldsymbol{R}) \rangle \\ =& -2\mathrm{Im} \sum_{j\neq 0} \frac{\langle \psi_0(\boldsymbol{R}) | \frac{\partial H(\boldsymbol{R})}{\partial R_\alpha} | \psi_j(\boldsymbol{R}) \rangle \langle \psi_j(\boldsymbol{R}) | \frac{\partial H(\boldsymbol{R})}{\partial R_\beta} | \psi_0(\boldsymbol{R}) \rangle}{\left(E_0(\boldsymbol{R}) - E_j(\boldsymbol{R})\right)^2} \end{aligned} \tag{2.15}$$

as elements of the Berry curvature tensor. Anti-symmetry of the wedge product yields $\Omega_0, \alpha\beta = -\Omega_0, \beta\alpha$, thus, the Berry curvature matrix is antisymmetric. Intermediate steps in the derivation of the Berry curvature tensor are analogue to the detailed discussion of the spin Berry curvature (eq. 4.16) in section 4.1.2. Commonly, index '0' is omitted as a unique ground state is considered. In the language of fiber bundles subsequently introduces in section 2.3, that is a one dimensional fiber, but the generic framework is not restricted to this assumption.

Qualitatively, the Berry phase γ_C can be understood as a measure of the non-preservation of geometrical information during parallel transport. On flat manifolds $\mathcal{M}$, parallel transport along a closed path is trivial in the sense that orientations, e.g. of vectors, are preserved. But on manifolds of nontrivial curvature, e.g. the surface of a sphere, parallel transport along a closed loop can affect geometric information. Depending on the path and the manifold, a vector's orientation may differ from its initial orientation after traversing a closed path γ_C.

Furthermore, an analogy to electrostatics can be made. In this picture, γ_C is the flux of a 'magnetic field' $\boldsymbol{\Omega}$ through the surface $\mathcal{S}$ bounded by path $\mathcal{C}$. The Berry connection $\boldsymbol{A}$ takes the role of a vector potential when the Berry curvature is interpreted as a magnetic field. A prime example hereto is the situation of a quantum spin 1/2 in an external magnetic field. The magnetic field is treated as the external parameters $\boldsymbol{R} \in \mathcal{M} = \mathbb{R}^3 \setminus \{0\}$. The two level Hamiltonian

$$H = -\frac{1}{2} \boldsymbol{R}\boldsymbol{\sigma}, \tag{2.16}$$

with $\boldsymbol{\sigma} = (\boldsymbol{\sigma}_1, \boldsymbol{\sigma}_2, \boldsymbol{\sigma}_3)^T$ as the vector of Pauli matrices, describes this situation. Straight

forward proceedings (see [19] or [53] for a detailed analysis) yield

$$\boldsymbol{\Omega}_0(\boldsymbol{R}) = -\frac{1}{2}\frac{\boldsymbol{R}}{R^3} \tag{2.17}$$

for the Berry connection and

$$\boldsymbol{A}_0(\boldsymbol{R}) = -\frac{1}{2R^2}\frac{\boldsymbol{e}\times\boldsymbol{R}}{1+\boldsymbol{e}\boldsymbol{R}/R} \tag{2.18}$$

for the Berry curvature, where $\boldsymbol{e}$ is an arbitrary unit vector. The curl of vector potential $\boldsymbol{A}_0(\boldsymbol{R})$ (eq. 2.18) leads to the field strength $\boldsymbol{\Omega}(\boldsymbol{R})$ of a 'magnetic monopole' as pointed out by P. Dirac 1931 [15]. That monopole is a 'magnetic point charge' of $q = -1/2$ and located at the origin $\boldsymbol{R} = 0$. At $\boldsymbol{R} = -R\boldsymbol{e}$ the vector potential is singular and choosing a different gauge results in a different $\boldsymbol{e}$. Thus, another gauge only moves this singularity around, but we cannot get rid off it by a gauge transformation. The ray defined by unit vector $\boldsymbol{e}$ is commonly called a Dirac string. The existence of the Dirac string implies $\boldsymbol{\Omega}_0(\boldsymbol{R}) = \nabla_R \times \boldsymbol{A}_0(\boldsymbol{R})$ can only be true locally. It tells us, that there exists no global gauge, such that $\boldsymbol{\Omega}_0(\boldsymbol{R}) = \nabla_R \times \boldsymbol{A}_0(\boldsymbol{R})$ holds everywhere, e.g. on all of $\mathbb{R}^3 \setminus \{0\}$ or $\mathcal{S}^2$. Therefore, the Poincaré lemma cannot be applied and $\boldsymbol{\Omega}_0(\boldsymbol{R})$ is not divergence-free.

The Berry phase to any great circle $\mathcal{C} = \partial\mathcal{S}$, respectively any half-sphere $\mathcal{S}$ is nontrivial, as $\gamma_\mathcal{C} = \int_\mathcal{S}(\boldsymbol{R}/R^3)d\boldsymbol{S} = \pm\pi$. This path corresponds to a rotating of the spin-1/2 by 2π caused by (manually) rotating the magnetic field $\boldsymbol{R}$. The external field adiabatically traverses a great circle $\mathcal{C}$ in time t so $\boldsymbol{R}(t) = \boldsymbol{R}(0)$. Such a rotation results in the well known minus sign $|\psi_0(\boldsymbol{R}(0)\rangle \to e^{\pm i\pi}|\psi_0(\boldsymbol{R}(t)\rangle = -|\psi_0(\boldsymbol{R}(0)\rangle$. Accordingly, the spin-1/2 state remains invariant under rotations of multiples of $4\pi = 720°$. The sign of $\gamma_\mathcal{C}$ depends on the arbitrary choice of the gauge, but as the Berry phase is defined up to multiples of 2π only, thus the Berry phase factor is unaffected by the gauge. Characteristic to a nontrivial Berry phases is the fact, that one cannot find a global gauge satisfying $\boldsymbol{\Omega}_0(\boldsymbol{R}) = \nabla_{\boldsymbol{R}} \times \boldsymbol{A}_0(\boldsymbol{R})$ on the entire manifold $\mathcal{M}$. One can, however, always find a local gauge that satisfies $\Omega_{\alpha\beta}(\boldsymbol{R}) = \partial_\alpha A_\beta(\boldsymbol{R}) - \partial_\beta A_\alpha(\boldsymbol{R})$ locally, which corresponds to $\boldsymbol{\Omega} = \nabla \times \boldsymbol{A}$ in three dimensions. Consequently, the Berry curvature is invariant under local gauge transformations (eq. 2.9) and effects due to finite Berry curvature $\boldsymbol{\Omega}$ are measurable.

2.3 – Chern Number as a Topological Invariant

It is a natural and insightful question to ask, whether two topological spaces are the same, i.e. homeomorphic to one another. Unfortunately, the complete homeomorphism classification of topological spaces is so vast a problem, that it has not been

accomplished yet. In order to discern whether two topological spaces are the same or not, we therefore resort to comparing properties that we call topological invariants of such spaces. A topological invariant is any property of (or any object associated to) a topological space, that is invariant under homeomorphisms. A homeomorphism is a bijective continuous transformation and can roughly be thought of as continuous (smooth) deformation of a geometrical object. Two topological spaces that differ in at least one topological invariant cannot be homeomorphic. One topological invariant of bundle spaces is obtained when the Berry curvature is integrated over the entire parameter manifold $\mathcal{M}$. That invariant is the Chern number, but a general formulation demands some further mathematical machinery. Here, we cover a brief introduction only, as details are beyond the scope of this thesis. For extensive proceedings we refer to the literature, e.g. [39, 56–58]. Within this section, the Chern number is motivated as a topological invariant without being mathematically rigorous in the subsequent proceedings. We rather draw a comprehensible picture from the physical perspective to provide (intuitive) understanding of the widely utilized Chern number. A selection of primary literature with fundamental contributions that lead to the development of the presented proceedings can be found in [51, 59–65].

At first, the space of the parameter manifold $\mathcal{M}$ and the ground states $e^{i\phi(\boldsymbol{R})}|\psi_0(\boldsymbol{R})\rangle$ with $\boldsymbol{R} \in \mathcal{M}$ is generalized. Mathematically, this space is a fiber bundle, that is locally a product space, but globally can have a nontrivial topological structure. For our considerations it is sufficient to imagine a fiber bundle as a possibly twisted product of a base manifold $\mathcal{M}$ and the fiber $e^{i\phi(\boldsymbol{R})}|\psi_0(\boldsymbol{R})\rangle$. To each point of the base manifold there is a ground state $|\psi_0(\boldsymbol{R})\rangle$ with a phase $\phi(\boldsymbol{R})$. The space of phase factors is $U(1) \simeq \{z \in \mathbb{C} || z| = 1\}$, which defines the typical fiber. Topological properties of the system are governed by the map $\boldsymbol{R} \mapsto e^{i\phi(\boldsymbol{R})}$ with $\boldsymbol{R} \in \mathcal{M}$ as the following example illustrates.

Imagine a circle as a base manifold ($\mathcal{M} = \mathcal{S}^1$) and a typical fiber $\mathcal{F} = \{z \in \mathbb{R} | -1 < z < 1\}$. Locally we 'glue' a copy of the typical fiber to each point in $\mathcal{M}$, but globally there are topologically distinct ways to construct this fiber bundle. For illustration, we imagine the product of the two one-dimensional manifolds $\mathcal{M}$ and $\mathcal{F}$ embedded in three dimensional space. One option is to glue all fibers 'pointing' in the same direction, so the resulting object is cylindrical. A second possibility is to 'glue' the fibers with some twist, so adjacent fibers are not collinear in the embedded three dimensional space. A well known result of a total twist of π among fibers along the full base manifold results in a Möbious strip. Locally, the cylinder and the Möbius strip appear to be the same, but globally they are clearly different. In fact, they are of different curvature and yield a distinct connection among fibers. Ultimately, they are associated with different values of a topological invariant. A topological invariant attributed to both object is the orientability, which is clearly of different nature among these two object.

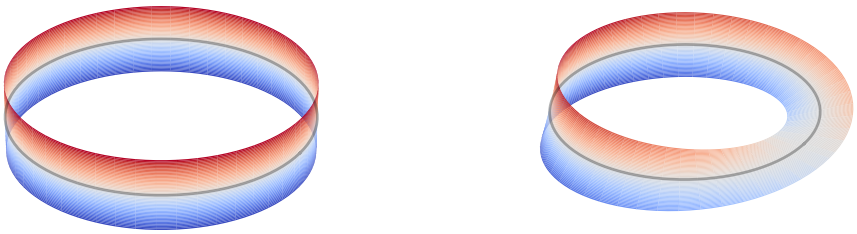

Figure 2.1: Fiber bundles of $\mathcal{M} = \mathcal{S}^1$ and a typical fiber $\mathcal{F} = \{z \in \mathbb{R} | -1 < z < 1\}$ embedded in $\mathbb{R}^3$. The base manifold is indicated by the gray line. A trivial structure group results in a cylinder like geometry (left) and $G = \mathbb{Z}_2$ as a structure group in a Möbius-strip-like geometry (right).

While the cylinder has a clear orientation, i.e., pictorially one can identify an inside and an outside, the Möbius strip is not orientable. Consequently, these two bundles are topologically distinct and they cannot be continuously deformed into one another. As it is natural to ask about 'higher windings', we briefly comment on odd and even 'twists', but leave a detailed elaboration to literature. In three dimension, a twist by 2π appears different from a cylinder (take a paper strip and glue the ends together with a twist of 2π) and cannot be unwound. The cylinder and the doubly twisted Möbisus strip are not isotopic in $\mathbb{R}^3$, i.e., cannot be deformed into each other without tearing. They are, however, a geometric instantation of the same trivial cylinder bundle and there is an isotopy in $\mathbb{R}^4$ that continuously transforms them one into the other. In fact, one finds that any two bundles with an even (odd) number of π-twists can be deformed into each other in $\mathbb{R}^4$ such that there are only two distinct bundles that can be constructed from $\mathcal{S}^1$ and $\mathcal{F}$: the cylinder and the Möbius strip. This pictorial example emphasizes the importance of structure group to a fiber bundle. Even though, a fiber bundle is locally the direct product of the base manifold and a (typical) fiber, the structure group determines how to 'glue' the fibers to the base manifold globally. A rigorous definition of a fiber bundle is relinquished to literature, e.g. chapter 9.2 of [39]. The preceding discussion on topologically distinguishing between a cylinder and a Möbius strip emphasizes our objective to quantify a topological invariant that classifies fiber bundles.

Topological invariants in general are quantities, that are invariant under continuous transformations. One way to approach a topological classification is to quantify 'holes' in topological spaces, which is a rather universal concept. Homotopy is a first approach

that classifies 'different ways to catch a hole' in a topological space $\mathcal{M}$ with an n-sphere $\mathcal{S}^n$. The $\mathcal{S}^n$ can be pictured as an n-dimensional lasso. In fact, the equivalence classes of homotopy-equivalent loops ($F : \mathcal{S}^n \to \mathcal{M}$) in $\mathcal{M}$ form a group $\Pi_n(\mathcal{M})$, that we call the n-th homotopy group of $\mathcal{M}$. For instance the winding of an $\mathcal{S}^2$ lasso around an $\mathcal{M} = \mathcal{S}^2$ topological space intuitively leads to $\Pi_2(\mathcal{S}^2) = \mathbb{Z}$. One can wrap a two-sphere any number of times around another $\mathcal{S}^2$ and orientation determines the sign. There is no such thing as 'half a wrapping', so intuitively $\Pi_2(\mathcal{S}^2)$ is integer. But it turns out, that the holes detected by homotopy are not consistent with our 'natural' notion of holes. For example, $\Pi_6(\mathcal{S}^2) = \mathbb{Z}_{12}$ or $\Pi_{14}(\mathcal{S}^2) = \mathbb{Z}_{84} \times \mathbb{Z}_2^2$. Wrapping a six-dimensional sphere around a two-sphere is hard to imagine and why there are exactly 12 different ways to accomplish this wrapping is not conceived by our intuition.

We therefore proceed to another approach that does not include the counterintuitive scenario of 'strange-dimensional' holes in $\mathcal{M}$ caught with lassos of higher dimension than $N = \dim \mathcal{M}$. To this end we proceed to Homology. The guiding idea is to find closed n-dimensional submanifolds, i.e. submanifolds without boundary, of a manifold $\mathcal{M}$ that are not boundaries to $n+1$-dimensional submanifolds themselves. The equivalence classes of such closed regions that are not boundaries themselves again form a group, which is referred to as the n-th Homology group. Roughly, n-th Homology group is

$$H_n(\mathcal{M}) = \frac{n\text{-dimensional things without boundary}}{\text{boundaries of } n+1\text{-dimensional things}}.$$

Numerator and denominator of this quotient are free Abelian groups on the respective objects. One benefit of $H_n(\mathcal{M})$ over $\Pi_n(\mathcal{M})$ is that nontrivial $H_n(\mathcal{M})$ terminate at $n = N = \dim \mathcal{M}$. H_n with $n > N$ are trivial ($H_{n>N}(\mathcal{M}) = 0$) by definition, which matches our intuitive understanding of holes. Two illustrative examples are

$$H_0(\mathcal{S}^2) = \frac{\text{points of } \mathcal{S}^2}{\text{points that are end-points (boundaries) of lines}} = \mathbb{Z}$$

and

$$H_1(\mathcal{T}^2) = \frac{\text{closed lines, i.e., 1-cycles in } \mathcal{T}^2}{\text{closed lines that are boundaries of areas, i.e., 2-chains}} = \mathbb{Z}^2.$$

The latter is the group of equivalence classes of closed $1D$-paths on a 2-torus ($\mathcal{M} = \mathcal{T}^2$) that are not boundaries of $2D$-areas. Representatives of the two group elements of $H_1(\mathcal{T}^2)$ are the two black lines a and b in figure 2.2. They are toplogically distinct, as the two path cannot be deformed into each other continuously. Lines a and a', however, are representatives of the same group element, as a' can be generated by a continuous 'shift' of a, as indicated by the shaded area. In fact, a and b are orientable

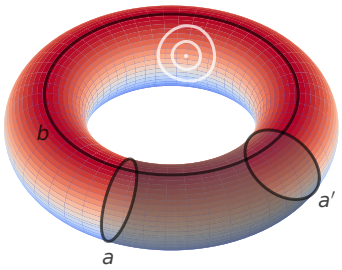

Figure 2.2: $\mathcal{T}^2$ torus with examplary representants a and b of $H_1(\mathcal{T}^2)$. a and a' are representants of the same group element, as a' can be generated by a continuous transformation of a. White lines are point-contractable, hence elements of $H_0(\mathcal{T}^2)$.

closed one-dimensional paths, each circumventing a 'hole' of the torus and referred to as nontrivial cycles. Any cycle that is homologous to a point (white paths in fig. 2.2) is accounted for by the intersection point of two nontrivial cycles.
Next, we proceed to de Rham cohomology, as it can be used to conveniently access topological information since it involves rich algebraic and geometric structure. It is, for instance, utilized to deduce topological information of fiber bundles over smooth orientable manifolds, i.a. due to their appearance in index theorems. Stokes' theorem $\int_C d\omega = \int_{\partial c} \omega$ [39] formulates a duality of a boundary of a manifold ∂C and a closed differential form $d\omega$. This outlines the way in which de Rham cohomology is a dual theory of homology. The n-th de Rham cohomology group $H^n(\mathcal{M})$ of a smooth orientable manifold $\mathcal{M}$ is loosely speaking the class of closed differential forms modulo exact differential forms [39],

$$H^n(\mathcal{M}) = \frac{\text{closed forms}}{\text{exact forms}}.$$

Characteristic classes are a particular kind of cohomology classes, which measure the 'twisting' of a fiber bundle [39]. Furthermore, characteristic classes are a subset of de Rham cohomology classes, which form the Rham cohomology group $H^n(\mathcal{M})$, i.e. characteristic classes are elements of $H^n(\mathcal{M})$. In fact, characteristic classes of a fiber bundle are elements of the cohomology group of the base manifold.
Our objective of a topological classification of fiber bundles can be attained through a representative of $H^{2N}(\mathcal{M})$ with $2N = \dim \mathcal{M}$. We restrict the dimension of the base manifold to be even and refer to the literature for base manifolds of odd dimension, see for example [39]. The base manifold $\mathcal{M}$ of fiber bundles we consider is a closed and orientable manifold. For smooth complex vector bundles, Chern classes are characteristic classes of integer coefficients and all characteristic classes of complex vector bundles are polynomials in Chern classes. The j-th Chern character

$$ch_j(\omega) := \frac{1}{j!}\mathrm{tr}\left(\frac{i\omega}{2\pi}\right)^j \tag{2.19}$$

is a representative of a characteristic class, i.e., an element of the $2j$-th cohomology group $H^{2j}(\mathcal{M})$. The cohomology group $H^{2N}(\mathcal{M})$ is of top degree when $2N = \dim \mathcal{M}$. Pairing a representative of an element of the top degree cohomology group $H^{2N}(\mathcal{M})$, e.g. ch_N, with the entire base manifold (aka with a representative of the fundamental orientation homology-class) leads to an integer [39], since characteristic classes are 'by definition' associated with cohomology groups with integer coefficients.
Characteristic classes are designed to classify bundle spaces and each fiber bundle is naturally assigned with a connection and curvature. The existence of a characteristic connection on a bundle means that de Rham pairing can be used to easily access the topological information contained by the characteristic classes. Adapted to our situation, a topological invariant is determined by an appropriate integral of a representative of a characteristic class over the base manifold $\mathcal{M}$.
Chern characters are of special relevance to us, as they feature prominently in the Atiyah-Singer [52] index theorem. This frequently applied index theorem establishes an equivalence of topological and analytical indices. The analytical index is by definition integer valued, hence, we can 'deduce' the integer nature of the topological index using the Atiyah-Singer index theorem. The topological invariant we are striving for is an instance of such a topological index. The Atiyah Singer index theorem quantifies the number of zero energy modes and relates them to a topological invariant. Thus, it constitutes the essence of the well-known bulk-boundary correspondence in solid-state physics.
The next step is to make the rather general statements more concrete by defining the Chern number. Denoting the exterior derivative by d we can generalize the concept of the Berry connection (eq. 2.6) and Berry curvature (eq. 2.15) to differential forms. Let $\boldsymbol{R}$ be an element of $\mathcal{M}$ with $\boldsymbol{R} = (x_1, ..., x_N)$. Using the sum convention of co- and contra-variant indices, the connection is the differential one-form $A = A_\mu dx^\mu$ and the curvature the differential two form $\omega = \frac{1}{2}\Omega_{\mu\nu} dx^\mu \wedge dx^\nu$. Specifying the fiber to the unique ground state of a quantum system yields

$$A = \langle \psi_0(\boldsymbol{R}) | d | \psi_0(\boldsymbol{R}) \rangle = \langle \psi_0(\boldsymbol{R}) | \frac{\partial}{\partial x^\mu} | \psi_0(\boldsymbol{R}) \rangle dx^\mu \tag{2.20}$$

$$\omega = dA = (d\langle \psi_0(\boldsymbol{R}) |) \wedge (d|\psi_0(\boldsymbol{R})\rangle) = \frac{1}{2} \frac{\partial \langle \psi_0(\boldsymbol{R}) |}{\partial x^\mu} \frac{\partial |\psi_0(\boldsymbol{R})\rangle}{\partial x^\nu} dx^\mu \wedge dx^\nu. \tag{2.21}$$

Connection and curvature are characteristic to each fiber bundle, thus, well suited to generate representatives of the $2N$-th cohomology class, which finally serves a topological classification of the fiber bundle. It was Chern who related the curvature of a fiber bundle to characteristic classes, which eventually linked the curvature to the bundle's topology [51, 56]. The N-th Chern character $ch_N(\omega)$ is a $2N$-form and vanishes for $2N > \dim \mathcal{M}$. Moreover, $ch_N(\omega)$ is a representative of a cohomology class in $H^{2N}(\mathcal{M})$. For $2N = \dim \mathcal{M}$ we can 'pair' the $2N$-form with the $2N$-dimensional base

manifold. This pairing is a natural operation between group and dual group, much like the linear pairing between vector space and covectors space is. Here, we can explicitly carry out the 'pairing' by integrating the form defining a de Rham cohomology class, i.e. $ch_N(\omega)$, over the base manifold, which itself is a representative of the fundamental orientation class. Integrating the N-th Chern character $ch_N(\omega)$ over base manifold $\mathcal{M}$ ($\dim(\mathcal{M}) = 2N$) of a fiber bundle defines the N-th Chern number [20]

$$C_N := \frac{1}{N!}\left(\frac{i}{2\pi}\right)^N \int_{\mathcal{M}} \mathrm{tr}(\omega^N). \tag{2.22}$$

We note, that for one dimensional fibers the trace is trivial. The Chern number is naturally integer, since the Chern character is a representative of a characteristic class that is associated with a cohomology group with integer coefficients.
Topological classification in condensed matter is the classification of Hilbert bundles. They are constituted by a closed orientable base manifold $\mathcal{M}$ and Hilbert spaces $\mathcal{H}(\boldsymbol{R})$ as fibers. Fiber bundles are particular topological spaces, naturally assigned with a connection(form) (eq. 2.20) and a curvature(form) (eq. 2.21). A prominent use case of equation 2.22 is the integer quantum Hall effect, where a quantized Hall conductance is related to the first Chern number [19, 66]. The Chern number also appears in the classification of topological insulators [20]. In this context, the topological band index C_1 is canonically evaluated for the ground state of translational invariant models. The k-space curvature is

$$\Omega_{\mu\nu}(\boldsymbol{k}) = i\frac{\partial\langle\psi_0|}{\partial k_\mu}\frac{\partial|\psi_0\rangle}{\partial k_\nu} - i\frac{\partial\langle\psi_0|}{\partial k_\nu}\frac{\partial|\psi_0\rangle}{\partial k_\mu}, \tag{2.23}$$

where the fiber is isomorphic to $U(1)$ for non-degenerate ground states. The k-space curvature is integrated over a two-torus $\mathcal{T}^2$ for translational invariant models in two dimensions to obtain C_1. An exemplary model, where distinct phases of the bulk band topology are characterized by C_1, is the Haldane model discussed in section 4.2. In fact, $2d$-models that are time reversal invariant (even or odd under time reversal) inevitably lead to $C_1 = 0$. Consequently, these models do not feature an (integer) quantum Hall effect [19, 66]. Time reversal invariant systems can, however, still exhibit topological phenomena. A prominent example is the quantum spin Hall effect [66,67] that features a topological $\mathbb{Z}_2$-invariant, e.g. in the Kane-Mele model [68]. Generalization of 2.20 and 2.21 to degenerate ground-states leads to a non-Abelian curvature $\boldsymbol{\Omega}$ which is beyond the scope of this thesis and we refer to [39,69] for further insight. Physically interpreted, the Chern number is sensitive to the 'obstruction' of smoothly defining a set of Bloch wave functions over the entire base manifold [20]. A prime example prompting this issue is the study of a spin-1/2 in an external magnetic field, thoroughly studied in literature [19, 53] and briefly referred to in section 5.2.1.2.

3 – Classical Adiabatic Spin Dynamics

The interaction between two local magnetic moments can manifest as a direct coupling, such as the short-range quantum Heisenberg exchange interaction and the long-range classical dipole interaction, or as an indirect coupling [70–72]. Indirect coupling mechanisms, such as the Ruerman-Kittel-Kasuya-Yoside (RKKY) interaction [73–75], the Anderson super exchange [76] or the double exchange [77] share a commonality in that they are derived through the use of perturbation theory. All of these approaches provide an effective interaction between local magnetic moments or spins, which takes the generic form $J_{eff}\boldsymbol{S}_1\boldsymbol{S}_2$. Typically, the effective interaction strength J_{eff} is significantly weaker than the intrinsic energy scales of the host that mediates the indirect coupling between the local magnetic moments. Such effective low energy exchange coupling results from a clear separation of timescales and can be utilized to predict real time spin dynamics [78].

When considering the RKKY-exchange, magnetic impurities are imbedded in an electronic host system, typically a metallic host system. To evade intertwining of RKKY coupling and the Kondo effect [79–83], we model the local magnetic moments by classical Heisenberg spins. At sufficiently weak host-impurity exchange K, the inherent timescales of the host and the dynamics due to an indirect coupling of the impurities are of well separated timescales. In this limit of weak K, time-dependent first-order-in-K perturbation theory, i.e., linear-response theory, is applicable [84–86]. Linear-response theory predicts, that the effective coupling among impurities is a ground state property of the host, which is given in terms of the ground-state magnetic susceptibility in case of the effective RKKY coupling. Closely related to linear response theory is the idea that the host system remains in its ground state to the momentary impurity configuration $(\boldsymbol{S}_1(t), \boldsymbol{S}_2(t))$ at any instant of time t, which is referred to as the adiabatic constraint.

Dynamics under the adiabatic constraint results from the separation of timescales given weak K. When the host system's electronic structure is gapped, the adiabatic theorem [34–37] enforces the adiabatic constraint throughout slow dynamics of the impurities. Adiabatic dynamics is a suitable approximation when the relaxation time of inherent host dynamics is significantly shorter than the typical timescale of impurity dynamics. For physical reasons, the host system is expected to be close to the momentary ground

state under these circumstances.
Here, we reassess this paradigm in a simplified setup where both the host system and the local impurities are modeled by classical spins. The interaction among classical Heisenberg spins of the fast host-spin system is defined by J. Our primary focus is on the adiabatic dynamics of the slow spins that emerges from a time-scale separation caused by $1/|J| \ll 1/|K|$. Concepts and results presented within this chapter are published in [87, 88].

3.1 – Theory of Classical Adiabatic Spin Dynamics

In the subsequent section we derive equations of motion for the classical spins. Devoid of constraints, both the slow and fast degrees of freedom display individual equations of motion. Our aim is an effective equation of motion for the slow degrees of freedom when a constraint is applied to the fast degrees of freedom. Such an effective description of the impurity dynamics drastically reduces the dynamical degrees of freedom. Furthermore, the effective equations of motion provide valuable insights to the underlying mechanisms that determine the dynamics when the constraint applies.

3.1.1 – Derivation of the Adiabatic Equation of Motion

Within this section the adiabatic equations of motion for classical Heisenberg spins under the 'adiabatic constraint' are derived. To this end, we introduce two types of classical spins, slow spins $\boldsymbol{S}$ and fast spins $\boldsymbol{F}$. The full system is considered to be in an adiabatic state if the fast spins arrange themselves in the state of lowest energy, i.e., the ground state, to a given configuration of the slow spins. This setting is noted as $\boldsymbol{F} = \boldsymbol{F}^0(\boldsymbol{S})$.
When the fast spins evolve on a significantly faster typical timescale than the slow spins, the dynamics of the entire system can be approximated by assuming that the system is in an adiabatic state at all times. Accordingly, as the slow spins configuration evolves over time, the fast spins instantaneously adapt their ground state to the momentary slow spin configuration. This constraint is known as the adiabatic approximation, which results in adiabatic spin dynamics when enforced at all times.
A system of the aforementioned form is described by the Hamiltonian

$$H(\boldsymbol{S}, \boldsymbol{F}) = -\frac{1}{2}\sum_{i,j} J_{ij}\boldsymbol{F}_i\boldsymbol{F}_j - \sum_{q,i} K_{qi}\boldsymbol{S}_q\boldsymbol{F}_i \tag{3.1}$$

where the typical timescale of the fast spins is of order $\frac{1}{|J|}$ while the typical timescale of the slow spins is proportional to $\frac{1}{|K|}$. Thus, the desired timescale separation which justifies the adiabatic approximation is satisfied when $|J| \gg |K|$.

As is known, e.g., from analytical mechanics [89], holonomic constraints are properly applied to the Lagrangian, resulting in an effective Lagrangian. Applying the stationary-action principle [90] to the effective Lagrangian leads to the constraint equations of motion. Applying constraints directly to the Hamiltonian, and deriving the constraint equations of motion solely form an effective Hamiltonian obtained in this manner, is conceptually incorrect. Such dynamics obtained via $\dot{\boldsymbol{S}}_q^N = \frac{\partial H(\boldsymbol{S};\boldsymbol{F}^0(\boldsymbol{S}))}{\partial \boldsymbol{S}_q} \times \boldsymbol{S}_q$ is referred to as the naive approach to adiabatic spin dynamics. In the context of these classical spin systems, the Lagrangian is not directly obtained through Legendre transformation of the Hamiltonian [87]. Instead, it reads

$$L(\boldsymbol{S}, \boldsymbol{F}, \dot{\boldsymbol{S}}, \dot{\boldsymbol{F}}) = \sum_q \boldsymbol{A}(\boldsymbol{m}_q) S_q \frac{d}{dt} \boldsymbol{S}_q + \sum_i \boldsymbol{A}(\boldsymbol{n}_i) F_i \frac{d}{dt} \boldsymbol{F}_i - H(\boldsymbol{S}, \boldsymbol{F}) - \sum_q \lambda_q (\boldsymbol{m}_q^2 - 1). \tag{3.2}$$

In the first two terms, spins are expressed in terms of there magnitudes (S_q and F_i) as well as their direction unit vectors ($\boldsymbol{m}_q$ and $\boldsymbol{n}_i$), i.e. $\boldsymbol{S}_q = \boldsymbol{m}_q S_q$ and $\boldsymbol{F}_i = \boldsymbol{n}_i F_i$. This notion proofs to be convenient since the magnitude of each classical spin is preserved throughout the dynamics. The latter is explicitly ensured by the last term containing Lagrange multipliers λ_q. Hence, only directionality is a dynamical variable and the adiabatic constraint can be reformulated as $\boldsymbol{n}_i = \boldsymbol{n}_i^0\big(\boldsymbol{m}(t)\big)$.

As the stationary-action principle is applied to the unconstrained Lagrangian, the well known Landau-Lifschitz-like [91, 92] equations of motion

$$\dot{\boldsymbol{S}}_q = \frac{\partial H\big(\boldsymbol{S}, \boldsymbol{F}\big)}{\partial \boldsymbol{S}_q} \times \boldsymbol{S}_q = \sum_{\alpha\beta\gamma} \frac{\partial H\big(\boldsymbol{S}, \boldsymbol{F}\big)}{\partial S_{q\alpha}} S_{q\beta}\, \boldsymbol{e}_\gamma\, \epsilon_{\alpha\beta\gamma} \tag{3.3}$$

$$\dot{\boldsymbol{F}}_i = \frac{\partial H\big(\boldsymbol{S}, \boldsymbol{F}\big)}{\partial \boldsymbol{F}_i} \times \boldsymbol{F}_i \tag{3.4}$$

are obtained. $\boldsymbol{e}_\alpha$ is the unit vector in α-direction ($\alpha \in \{x, y, z\}$) and $\epsilon_{\alpha\beta\gamma}$ the total antisymmetric Levi-Civita tensor in three dimensions. These equations of motion are equally derived through a Hamiltonian framework [87] or by the spin Poisson bracket [93], which justifies the Lagrangian (eq. 3.2).

In the Lagrangian (e.q. 3.2), $\boldsymbol{A}(\boldsymbol{m}_q)$ takes the form of the vector potential of a magnetic monopole at the origin [15, 16, 47], satisfying

$$\boldsymbol{\nabla}_{m_q} \times \boldsymbol{A}(\boldsymbol{m}_q) = -\frac{\boldsymbol{m}_q}{|\boldsymbol{m}_q|^3}. \tag{3.5}$$

The vector potential can be defined as $\boldsymbol{A}(\boldsymbol{m}_q) = -\frac{1}{m_q} \frac{\boldsymbol{e}_z \times \boldsymbol{m}_q}{m_q + \boldsymbol{e}_z \boldsymbol{m}_q}$ in standard gauge [15].

Subsequently, applying the stationary-action principle to the effective Lagrangian, we derive the adiabatic equations of motion, with a detailed derivation presented in ap-

pendix A.1.1. The effective Lagrangian under the adiabatic constraint reads:

$$L^{\text{eff}}\big(\boldsymbol{m},\dot{\boldsymbol{m}};\boldsymbol{n}^0(\boldsymbol{m})\big) = \sum_{q\alpha} S_q A_\alpha(\boldsymbol{m}_q)\dot{m}_{q\alpha} + \sum_{i\beta} F_i A_\beta\big(\boldsymbol{n}_i^0(\boldsymbol{m})\big) \sum_{q\alpha} \frac{\partial n^0_{i\beta}}{\partial m_{q\alpha}}\dot{m}_{q\alpha} - H^{\text{eff}}(\boldsymbol{m};\boldsymbol{n}^0(\boldsymbol{m})) - \sum_q \lambda_q(\boldsymbol{m}_q^2 - 1). \tag{3.6}$$

As a consequence of the stationary-action principle $\delta \int dt L(\boldsymbol{m},\boldsymbol{n},\dot{\boldsymbol{m}},\dot{\boldsymbol{n}}) = 0$, the Euler-Lagrange equation $\frac{\partial L}{\partial m_{q\alpha}} - \frac{d}{dt}\frac{\partial L}{\partial \dot{m}_{q\alpha}} = 0$ [90] are obtained. Explicitly utilizing the previously mentioned property of the curl of the vector potential (e.q. 3.5) and the Euler-Lagrange equation result in

$$0 = S_r \sum_{\alpha\nu} m_{r\nu}\dot{m}_{r\alpha}\varepsilon_{\alpha\mu\nu} + \sum_{\substack{i,q\\ \alpha\beta\gamma\nu}} F_i n^0_{i\nu} \frac{\partial n^0_{i\gamma}}{\partial m_{r\mu}} \frac{\partial n^0_{i\beta}}{\partial m_{q\alpha}} \dot{m}_{q\alpha}\varepsilon_{\beta\gamma\nu} - \frac{\partial H^{\text{eff}}}{\partial m_{r\mu}} - 2\lambda_r m_{r\mu}\,. \tag{3.7}$$

By taking the vector product of this result (eq. 3.7) and $\boldsymbol{m}_r$, the implicit equations of motion are obtained. Consequently, a classical pendant to the spin Berry curvature defined as

$$\Omega_{r\mu,q\alpha} := \sum_{\substack{i\\ \beta\gamma\nu}} F_i \frac{\partial n^0_{i\beta}}{\partial m_{q\alpha}} \frac{\partial n^0_{i\gamma}}{\partial m_{r\mu}} n^0_{i\nu}\varepsilon_{\beta\gamma\nu} \tag{3.8}$$

emerges is in the adiabatic equations of motion. $\boldsymbol{\Omega}$ is a quantity of major interest to our studies, as it gives rise to an anomalous non-Hamiltonian dynamics of the slow spins.

The Lagrange multipliers are determined by the condition

$$\lambda_r = \sum_\mu \frac{m_{r\mu}}{2}\left(\sum_{q\alpha}\Omega_{r\mu,q\alpha}\dot{m}_{q\alpha} - \sum_\mu \frac{\partial H^{\text{eff}}}{\partial m_{r\mu}}\right). \tag{3.9}$$

Hence, the implicit form of the adiabatic equations of motion reads

$$\dot{S}_{r\kappa} = \sum_{\mu\lambda} \frac{\partial H^{\text{eff}}}{\partial m_{r\mu}} m_{r\lambda}\varepsilon_{\mu\lambda\kappa} - \sum_{\substack{q\\ \alpha\mu\lambda}} \Omega_{r\mu,q\alpha} m_{r\lambda}\dot{m}_{q\alpha}\varepsilon_{\mu\lambda\kappa}\,. \tag{3.10}$$

Since implicit differential equations can be difficult to work with, the aim is an explicit formulation of the adiabatic equations of motion. This is achieve through the definition of a tensor $T_{r\kappa,q\alpha} := \frac{1}{S_q}\sum_{\mu\lambda}\Omega_{r\mu,q\alpha}m_{r\lambda}\epsilon_{\mu\lambda\kappa}$. At the expense of performing a matrix

inversion, the explicit adiabatic equation of motion for classical spins is

$$\dot{\boldsymbol{S}} = \left(\mathbf{1} + \boldsymbol{T}\right)^{-1} \cdot \left(\frac{\partial H^{\text{eff}}}{\partial \boldsymbol{S}} \times \boldsymbol{S}\right). \tag{3.11}$$

With N_S counting the number of slow spins, $\mathbf{1}$ and $\boldsymbol{T}$ are $3N_S \times 3N_S$ matrices and $\boldsymbol{S}$ is a $3N_S$-component vector.
The adiabatic equation of motion (eq. 3.10 in an implicit and eq. 3.11 in an explicit form) meets the aim of an effective description of the $\boldsymbol{S}$-spin dynamics. It relies solely on the slow system's degrees of freedom $\boldsymbol{S}$ and the geometric property $\boldsymbol{\Omega}$ (eq. 3.8) of the fast subsystem. Notably, $\boldsymbol{\Omega}$ remains constant throughout the dynamics.

3.1.2 – Analytical Analysis of the $\boldsymbol{F}$-spin Ground State

In a setup with slow $\boldsymbol{S}$ and fast $\boldsymbol{F}$ classical spins as discussed in the section 3.1.1, the timescale disparity required for adiabatic dynamics can be realized by a significant difference in the modulus of coupling parameters ($|J| \gg |K|$). While the intra-class coupling (J) of the fast subsystem is of large magnitude to ensure fast dynamics, the inter-class coupling (K) between slow and fast spins is of much smaller magnitude. Within our proceedings we omit direct coupling between the slow degrees of freedom $\boldsymbol{S}$, which are indirectly interconnected solely via the fast subsystem $\boldsymbol{F}$. Incorporation of direct coupling between $\boldsymbol{S}$-spins is, however, straight forward.
An intuitive understanding of $|J| \gg |K|$ can be obtained by examining the Hamiltonian, which corresponds to the energy of the system. First, imagine the entire system to be in its overall ground state where classical spins are of fixed magnitude. Any excitation requires a deviation of one or multiple spins from their ground state configuration, which results in a relative change of some spins' directionality. Mismatches between host spins $\boldsymbol{F}_i$ from their energetically most favorable configuration are scaled by a large $|J|$, while mismatches between host and impurity spin are scaled by the small $|K|$. In the limit of $\frac{|K|}{|J|} \to 0$ with $|K| \neq 0$, an energetically weak excitation therefore favors impurity-host deviations from the overall ground state configuration, while the host itself rather remains in its free ground state configuration. The free ground state configuration of the host is the lowest energy configuration of the host with $K = 0$. This assumption of weak interaction between impurities and host is a significant simplification when compared to the much more complex scenario of arbitrary host spin configurations.
Two remarks concerning this idea should be made. To begin with, any $\frac{|K|}{|J|}$ will be finite in numerical calculations, thus, only approximate the limit $\frac{|K|}{|J|} \to 0$. Furthermore, the presented idea includes an upper bound in the excitation energy where adiabatic dynamics is feasible. For a system with a fixed set of parameters the miss-alignment of the host relative to a given impurity configuration can only account for some finite

excitation energy. Any excitation energy exceeding this upper limit causes excitation of the host, which renders the concept of adiabatic dynamics infeasible.

Scenarios considered here do not take external fields into account and the host-impurity coupling is deemed to be isotropic. The host spins $\boldsymbol{F}_i = F\boldsymbol{n}_i$ are considered to be classical (three component) Heisenberg spins of fixed magnitude F, thus, the host spin ground state configuration is $SO(3)$ degenerate. However, any weak coupling to the impurities $\boldsymbol{S}_q = S\boldsymbol{m}_q$ typically breaks this degeneracy. Thus, the host-spin ground state orientation $\boldsymbol{F}^0 = F\boldsymbol{n}^0 = \boldsymbol{F}^0(\boldsymbol{S})$ is obtained by minimizing the energy, or to be precise, the host-impurity interaction $-\sum_{q,i} K_{qi}\boldsymbol{S}_q\boldsymbol{F}_i$ of the Hamiltonian [88]. Host spins are in their free ground state $\boldsymbol{n}_{0,i}$ and small but finite K lead to $\boldsymbol{n}_i^0 = \boldsymbol{R}\boldsymbol{n}_{0,i}$ with some fixed $\boldsymbol{R} \in SO(3)$. $\boldsymbol{R} = \boldsymbol{R}(\boldsymbol{S})$ depends on the impurity configuration. We assume, that the host system's ground-state orientation that minimizes the overall impurity-host interaction is realized at all times. In contrast to the degenerate free ground state configuration $\boldsymbol{n}_{0,i}$ notion $\boldsymbol{n}_i^0$ indicates the typically unique ground state configuration of the host spins with respect to the impurity configuration.

Our goal is to find the $\boldsymbol{R}(\boldsymbol{S})$ that minimizes

$$-SF\sum_{q,i} K_{qi}\boldsymbol{m}_q\big(\boldsymbol{R}\boldsymbol{n}_{0,i}\big) \stackrel{!}{=} \min. \tag{3.12}$$

for some given impurity configuration $\boldsymbol{S} = S\boldsymbol{m}$. To this end it proofs to be beneficial to express $\boldsymbol{R} \in SO(3)$ in terms of the real, antisymmetric generators $\boldsymbol{\mathcal{R}}_\alpha \in so(3)$ of $SO(3)$ [94], where $\boldsymbol{\mathcal{R}}_\alpha$ are the components of $\boldsymbol{\mathcal{R}}$ (see eq. A.15 for an explicit form of $\boldsymbol{\mathcal{R}}_\alpha$ with $\alpha \in \{x, y, z\}$). When unit vector $\boldsymbol{a}$ defines the axis of a rotation and φ the rotation angle one can write $\boldsymbol{R} = \boldsymbol{R}(\boldsymbol{a}, \varphi) = \exp(\varphi\boldsymbol{\mathcal{R}}\boldsymbol{a})$.

In the case where $\boldsymbol{n}_i = \boldsymbol{n}_i^0 \; \forall\, i$ the energy is minimized for a given $\boldsymbol{m}$-configuration, which implies condition 3.12 to be satisfied for $\varphi = 0$ and for any axis $\boldsymbol{a}$. Therefore, the derivative of equation 3.12 with respect to φ has to vanish at $\varphi = 0$. Using the general relation [88, 94] $\frac{\partial}{\partial\varphi}\exp(\varphi\boldsymbol{L}\boldsymbol{a})\big|_{\varphi=0}(\cdot) = \boldsymbol{a} \times (\cdot)$ the necessary condition

$$\sum_{q,i} K_{qi}\boldsymbol{m}_q\big(\boldsymbol{a} \times \boldsymbol{n}_i^0\big) = 0 \tag{3.13}$$

for the impurity-host interaction to be minimal is derived. This condition holds for any $\boldsymbol{a}$ as well as any K_{qi} and reduces to

$$\sum_{q,i} K_{qi}\boldsymbol{n}_i^0 \times \boldsymbol{m}_q = \boldsymbol{0} \tag{3.14}$$

due to the triple product being invariant under cyclic permutations. From a physical standpoint, the assumptions above result in an equilibrium condition where the total

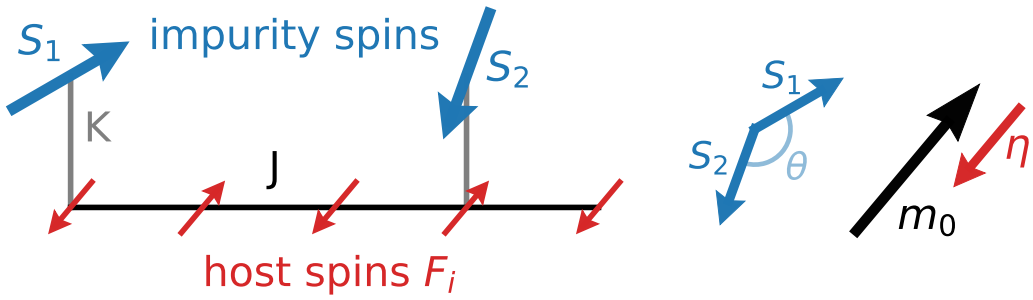

Figure 3.1: Typical setup of slow spins $\boldsymbol{S}_1$ and $\boldsymbol{S}_2$ locally coupled via K to fast host spins $\boldsymbol{F}_{i_1}$ and $\boldsymbol{F}_{i_2}$. $\boldsymbol{F}_i$ are coupled via J to their nearest neighbor host spins. Impurities $\boldsymbol{S}_1$ and $\boldsymbol{S}_2$ enclose relative angle $\theta \measuredangle(\boldsymbol{S}_1, \boldsymbol{S}_2)$ and define $\boldsymbol{m}_0$, which eventually defines orientation $\boldsymbol{\eta}$ of the overall host orientation (eq. 3.20).

torque between the impurities and host system becomes zero.

In general, any configuration $\boldsymbol{n}_i$ can be expressed via some axis $\boldsymbol{\eta}_i$ ($|\boldsymbol{\eta}_i| = 1$) as well as an azimutal angle θ_i and a polar angle ϕ_i for each individual spin relative to $\boldsymbol{\eta}_i$. The ground state configuration $\boldsymbol{n}_i^0$ of any classical host-system can therefore be expressed as $\boldsymbol{n}_i^0 = \boldsymbol{n}_i(\phi_i^0, \theta_i^0, \boldsymbol{\eta}_i)$. Given some overall orientation of that host spin configuration, respectively fixing a global frame of coordinates, $\boldsymbol{\eta}_i = \boldsymbol{\eta}$ is generic for all impurities. Hence, one can define some rotation matrix $\boldsymbol{R}_i^0 := \boldsymbol{R}(\phi_i^0, \theta_i^0)$ and denote $\boldsymbol{n}_i^0 = \boldsymbol{R}_i^0 \boldsymbol{\eta}$.

This general representation of $\boldsymbol{n}^0$ can be used to compute $\boldsymbol{\Omega}$, since our setup of constraint dynamics enforces all $\boldsymbol{R}_i^0$ to remain constant. Hence, $\boldsymbol{\eta} = \boldsymbol{\eta}(\boldsymbol{m}(t))$ in the adiabtic limit, which results in

$$\frac{\partial \boldsymbol{n}_i^0}{\partial m_{q\alpha}} = \boldsymbol{R}_i^0 \frac{\partial \boldsymbol{\eta}(\boldsymbol{m}(t))}{\partial m_{q\alpha}}. \tag{3.15}$$

A general requirement of the classical adiabatic spin dynamics is obtained by substituting $\boldsymbol{n}_i^0 = \boldsymbol{R}_i^0 \boldsymbol{\eta}$ into condition 3.14, resulting in

$$\begin{aligned} 0 &= \sum_{q,i} \sum_{\mu\alpha\beta} K_{qi} R^0_{i\alpha\mu} \eta_\mu m_\beta \, \varepsilon_{\alpha\beta\gamma} \quad \forall\gamma \\ \rightarrow \; \boldsymbol{\Lambda}\boldsymbol{\eta} &= \boldsymbol{0}, \text{ with } \Lambda_{\gamma\mu} := \sum_{q,i} \sum_{\alpha\beta} K_{qi} R^0_{i\alpha\mu} m_\beta \, \varepsilon_{\alpha\beta\gamma}. \end{aligned} \tag{3.16}$$

Accordingly, $\boldsymbol{\eta}$ has to be in the kernel of $\boldsymbol{\Lambda}$, which obligates $\det(\boldsymbol{\Lambda}) = 0$ to be able to calculate any nontrivial $\boldsymbol{\eta}$ from eq. 3.14. Note, that $\det(\boldsymbol{\Lambda}) \neq 0$ is found to be an obstruction to adiabatic dynamics.

Aforementioned ideas apply to generic systems, but next, the focus is on bipartite lattices with nearest-neighbor interaction and collinear host spin ground states. In those cases $\boldsymbol{n}_i^0 = z_i \boldsymbol{\eta}$ with $\boldsymbol{\eta}$ being a unit vector determined by equation 3.14 and $z_i \in \{-1, +1\}$. Hence, the ansatz of a collinear host configuration is applied to the

equilibrium condition to fix $\boldsymbol{\eta}$. Choosing the sign of e.g. one particular z_i lifts the remaining redundancy, as the host spin ground state would be invariant under a simultaneous transformation of $\boldsymbol{\eta} \to -\boldsymbol{\eta}$ and $z_i \to -z_i$. Exploiting the ansatz of a collinear host yields

$$\sum_{q,i} K_{qi} z_i \boldsymbol{\eta} \times \boldsymbol{m}_q = \boldsymbol{\eta} \times \sum_{q,i} K_{qi} z_i \boldsymbol{m}_q = \mathbf{0}. \tag{3.17}$$

As one can see, $\boldsymbol{\eta}$ has to be parallel or antiparallel to

$$\boldsymbol{m}_0 := \sum_{q,i} K_{qi} z_i \boldsymbol{m}_q = \sum_q Z_q \boldsymbol{m}_q \tag{3.18}$$

$$Z_q := \sum_i K_{qi} z_i \tag{3.19}$$

to fulfill condition 3.14. A brief check of the energy related to $\boldsymbol{\eta} \sim \pm \boldsymbol{m}_0$ clarifies, that the negative sign is related to the maximal host-impurity interaction and the positive sign to minimal one. Since the latter one is our case of interest, we define $\boldsymbol{\eta} := \frac{\boldsymbol{m}_0}{m_0}$ with $m_0 = |\boldsymbol{m}_0|$. Thus,

$$\boldsymbol{n}_i^0\big(\boldsymbol{m}\big) = z_i \boldsymbol{\eta} = z_i \boldsymbol{m}_0 / |\boldsymbol{m}_0| = z_i \frac{\sum_{q,j} K_{qj} z_j \boldsymbol{m}_q}{|\sum_{q,j} K_{qj} z_j \boldsymbol{m}_q|} \tag{3.20}$$

defines the host-spin ground state $\boldsymbol{n}^0$ as a function of the impurity spin configuration $\boldsymbol{m}$ to fixed system parameters K_{qi}.

One final remark has to be made on cases where $\boldsymbol{m}_0 = \sum_{q,i} K_{qi} z_i \boldsymbol{m}_q = 0$. The submanifold at which $m_0 = 0$ is of zero measure in the full space of $\boldsymbol{m}$ configurations, nonetheless, such initial conditions have to be excluded. Furthermore, trajectories $\boldsymbol{m}(t)$ are not allowed to cross this submanifold in the given setup of adiabatic spin dynamics, because $m_0 = 0$ leaves an ambiguity in the orientation of the host, i.e., $\boldsymbol{\eta}$. Such scenarios can lead to dynamics incompatible with the initially made assumption of impurities evolving slowly as compared to the host spins. Already known from other applications of the adiabatic approximation [87], $m_0 = 0$ implies an inherent breakdown of the theory for singular points of the parameter space.

3.1.2.1 The Effective Hamiltonian and Naive Adiabatic Theory for Host Systems with a Collinear Ground State

Preceding considerations clarified the determination of the host system's ground state to a given impurity spin configuration. The resulting constraint $\boldsymbol{n}^0(\boldsymbol{m})$ (eq. 3.20) is now applied to the Hamiltonian $H(\boldsymbol{m}, \boldsymbol{n})$ which leads to an effective Hamiltonian $H^{eff}(\boldsymbol{m}) = H\big(\boldsymbol{m}, \boldsymbol{n}^0(\boldsymbol{m})\big)$. The effective Hamiltonian H^{eff} contains only impurity

degrees of freedom as dynamical variables.

Within the adiabatic approximation the functional relation $\boldsymbol{n}^0(\boldsymbol{m})$ holds at all times, thus, it eliminates all independent dynamical host degrees of freedom. Dynamics that is solely derived from such constraint Hamiltonians is referred to as the naive approach to adiabatic spin dynamics. The constraint Hamiltonian for the case considered here is

$$H^{eff}(\boldsymbol{m}) = -\frac{1}{2}\sum_{i,j} J_{ij}F_iF_jz_iz_j - \sum_{q,i} K_{qi}S_qF_iz_i\boldsymbol{m}_q\boldsymbol{\eta}(\boldsymbol{m}) - \sum_q S_q\boldsymbol{m}_q\boldsymbol{B}_q. \tag{3.21}$$

The first part $H^0_{host} = -\frac{1}{2}\sum_{i,j} J_{ij}F_iF_jz_iz_j$ is the constant, free ground state energy of the host which does not depend on $\boldsymbol{m}$ and the last term describes some local magnetic fields $\boldsymbol{B}_q$ interacting with the impurities. All impurity spins are assumed to be of magnitude S, and all host spins are assumed to have the magnitude F. In the interaction term one can identify $\boldsymbol{m}_0 = \sum_{q,i} K_{qi}z_i\boldsymbol{m}_q$ to simplify the constraint Hamiltonian even further. With $\boldsymbol{\eta} = \boldsymbol{m}_0/|\boldsymbol{m}_0|$ the effective Hamiltonian reads

$$H^{eff}(\boldsymbol{m}) = H^0_{host} - SFm_0 - \sum_q S\boldsymbol{m}_q\boldsymbol{B}_q. \tag{3.22}$$

The Hamiltonian time evolution of classical spins is determined by equation 3.3. With $\frac{\partial m_0}{\partial \boldsymbol{m}_r} = Z_r\frac{\boldsymbol{m}_0}{m_0}$ where $Z_r = \sum_i K_{ri}z_i$, the naive approach to adiabatic dynamics results in

$$\begin{aligned}\dot{\boldsymbol{m}}^N_r =& \frac{1}{S}\frac{\partial H^{eff}(\boldsymbol{m})}{\partial \boldsymbol{m}_r} \times \boldsymbol{m}_r \\ =& \left(-\frac{FZ_r}{m_0}\boldsymbol{m}_0 - \boldsymbol{B}_r \right) \times \boldsymbol{m}_r \\ =& -\frac{FZ_r}{m_0}\sum_{q,i} K_{qi}z_i\boldsymbol{m}_q \times \boldsymbol{m}_r - \boldsymbol{B}_r \times \boldsymbol{m}_r.\end{aligned} \tag{3.23}$$

The superscript N in $\dot{\boldsymbol{m}}^N_q$ denotes that this equation of motion is obtained when using the constraint in a naive fashion.

Holonomic constraints applied to the equation of motion or the Hamiltonian directly do, however, not lead to a correct description of the constraint dynamics. Rather, such constraints are correctly taken into account in the Lagrangian formalism [89].

Before continuing with the explicit derivation of the conceptually correct adiabatic equation of motion, the naive global host dynamics determined by $\dot{\boldsymbol{m}}_0$ is evaluated in the absence of external magnetic fields $\boldsymbol{B}_q = 0$. We assume the interaction between impurities and host to be isotropic and homogeneous across all impurities. Furthermore host-impurity exchange coupling is taken to be local, which means the q-th impurity spin interacts with the i_q-th host spin only. Under these assumptions, $Z_q = Kz_{i_q}$,

which leads to

$$\begin{aligned}\dot{\boldsymbol{m}}_0 =& \sum_q Z_q \dot{\boldsymbol{m}}_q \\ =& -\frac{F}{m_0}\boldsymbol{m}_0 \times \sum_q (K z_{i_q})^2 \boldsymbol{m}_q \\ =& \frac{FK^2}{m_0}\boldsymbol{m}_T \times \boldsymbol{m}_0. \end{aligned} \tag{3.24}$$

The obtained expression yields that $\boldsymbol{m}_0$ obeys a precessional motion around the total impurity spin ($\boldsymbol{m}_T = \text{const}$) with frequency $\omega_p = FK^2\frac{m_T}{m_0}$. For such dynamics $\boldsymbol{m}_T$, m_0 as well as the total energy H_{eff} are conserved. In this scenario, the relative angle, i.e. the product $\boldsymbol{m}_1\boldsymbol{m}_2$, is also conserved for scenarios with two impurity spins. The impurities then precess in a Larmor-like [91, 95] motion with the same frequency ω_p around the total impurity spin $\boldsymbol{m}_T$ and so does $\boldsymbol{m}_0$.
Assuming $K_{iq} = K\delta_{qi_q}$ and, for the moment, restricting ourselves to two impurities on an antiferromagnetic host system, allows for two fundamentally distinct setups. On the one hand $z_{i_1} = z_{i_2}$ which implies $m_0 = Km_T$, which leads to precession frequency $\omega_p = FK$ and on the other hand $z_{i_1} = -z_{i_2}$, which results in $m_T = \sqrt{2}\sqrt{1+\cos(\theta)}$ and $m_0 = K\sqrt{2}\sqrt{1-\cos(\theta)}$ with θ being the enclosed angle of the impurities. For the latter case, the precession frequency

$$\omega_p = FK\sqrt{\frac{1+\cos(\theta)}{1-\cos(\theta)}} = FK\cot(\theta/2) \tag{3.25}$$

heavily depends on the geometry, respectively the angle between the two impurities. In fact, $\omega_p = FK$ holds for even more than two impurities, when all z_{i_q} are of equal sign and the initial impurity geometry is not collinear. The precession frequency ω_p is independent of the geometry of the impurities in those cases and all impurities precess with that same frequency around $\boldsymbol{m}_T$.
One final remark should be made on a somewhat unconventional consequence of this naive approach. The total impurity spin $\boldsymbol{S}_T = S\boldsymbol{m}_T$ is a constant of motion in the absence of external magnetic fields. The total host spin $\boldsymbol{F}_T = F\sum_i z_i\boldsymbol{\eta}$, however, is proportional to $\dot{\boldsymbol{m}}_0$ (eq. 3.24) when $\Delta := \sum_i z_i \neq 0$. Hence, the overall total spin $\boldsymbol{S}_T + \boldsymbol{F}_T$ is not conserved by this naive approach. This inadequacy is rectified by utilizing the conceptually correct approach to adiabatic spin dynamics.

3.1.2.2 The Explicit Adiabatic Equation of Motion for a Collinear Host-Spin Ground State

Within this section an analytical ansatz (eq. 3.20) for the host-spin ground state is applied to the adiabatic equation of motion (eq. 3.10). To this end, we recall that some classical analogue of the spin Berry curvature $\Omega_{r\mu,q\alpha} = \sum_{i\beta\gamma\nu} F_i \frac{\partial n^0_{i\beta}}{\partial m_{q\alpha}} \frac{\partial n^0_{i\gamma}}{\partial m_{r\mu}} n^0_{i\nu} \varepsilon_{\beta\gamma\nu}$ affects the dynamics beyond the naive approach that has been considered previously (see section 3.1.2.1). To obtain an analytical expression for $\mathbf{\Omega}$, derivatives $\frac{\partial n^0_{i\beta}}{\partial m_{q\alpha}}$ are evaluated using equation 3.20

$$\frac{\partial n^0_{i\beta}}{\partial m_{q\alpha}} = z_i \frac{\partial}{\partial m_{q\alpha}} \frac{m_{0\beta}}{m_0} = \frac{Z_q \delta_{\alpha\beta}}{m_0} - \frac{Z_q m_{0\alpha} m_{0\beta}}{m_0^3}. \tag{3.26}$$

Detailed calculations are presented in A.1.2. With this expression at hand it is straight forward to obtain an analytical expression for the spin Berry curvature analogue, which reads

$$\begin{aligned}
\Omega_{r\mu,q\alpha} &= \sum_{i\beta\gamma\nu} F_i \frac{\partial n^0_{i\beta}}{\partial m_{q\alpha}} \frac{\partial n^0_{i\gamma}}{\partial m_{r\mu}} n^0_{i\nu} \varepsilon_{\beta\gamma\nu} \\
&= \sum_{i\beta\gamma\nu} F_i \left(\frac{Z_q \delta_{\alpha\beta}}{m_0} - \frac{Z_q m_{0\alpha} m_{0\beta}}{m_0^3} \right) \left(\frac{Z_r \delta_{\mu\gamma}}{m_0} - \frac{Z_r m_{0\mu} m_{0\gamma}}{m_0^3} \right) \frac{z_i m_{0\nu}}{m_0} \varepsilon_{\beta\gamma\nu} \\
&= \sum_{i\nu} F_i \frac{z_i Z_q Z_r}{m_0^3} m_{0\nu} \varepsilon_{\alpha\mu\nu}.
\end{aligned} \tag{3.27}$$

If the interaction between impurities and host spins is equal for all impurities and act only locally between impurity q and host spin i_q, Ω takes the form $\Omega_{r\mu,q\alpha} = \sum_{i\nu} K^2 F_i \frac{z_i z_{i_q} z_{i_r}}{m_0^3} m_{0\nu} \varepsilon_{\alpha\mu\nu}$.

Another generic specification is the assumption, that the host is composed of spins of equal magnitude, i.e., $F_i = F \, \forall i$. We define

$$\Delta := \sum_i z_i, \tag{3.28}$$

which is a property of the host system only. This Δ can be seen as a indicator to trace non-Hamiltonian contributions to the dynamics.

With the aforementioned assumptions $\boldsymbol{m}_0 = K \sum_q z_{i_q} \boldsymbol{m}_q$, $\mathbf{\Omega}$ takes the rather simple form

$$\Omega_{r\mu,q\alpha} = F \Delta z_{i_q} z_{i_r} \frac{\sum_{s\nu} z_{i_s} m_{s\nu} \, \varepsilon_{\alpha\mu\nu}}{\left(\sum_\beta \left(\sum_s z_{i_s} m_{s\beta} \right)^2 \right)^{3/2}} = F \Delta K^2 z_{i_q} z_{i_r} \sum_\nu \frac{m_{0\nu}}{m_0^3} \varepsilon_{\alpha\mu\nu}. \tag{3.29}$$

Accordingly, $\Omega_{r\mu,q\alpha}$ is a host and geometry dependent quantity. Noteworthy, however,

is the independence of $\mathbf{\Omega}$ on the host-impurity exchange coupling K. The latter is easily recognized when pointing out $m_0 \sim K$.

Finally, the adiabatic equation of motion (eq. 3.10) is combined with the preceding considerations concerning collinear host systems, which results in

$$\dot{\boldsymbol{m}}_r = \Big(- \frac{FZ_r}{m_0}\boldsymbol{m}_0 - \boldsymbol{B}_r - \frac{F\Delta Z_r}{Sm_0^3}\boldsymbol{m}_0 \times \dot{\boldsymbol{m}}_0 \Big) \times \boldsymbol{m}_r. \tag{3.30}$$

The Hamiltonian part has been calculated in the preceding of section (eq. 3.23) and elements of $\mathbf{\Omega}$ are given by equation 3.29.

Following the steps described in subsection 3.1.1, the dynamics can be expressed as an explicit differential equation (see eq. 3.11) at the cost of a matrix inversion. Elements of the concerning tensor are

$$\begin{aligned} T_{r\kappa,q\alpha} =& \frac{1}{S_q} \sum_{\mu\lambda} \Omega_{r\mu,q\alpha} m_{r\lambda} \epsilon_{\mu\lambda\kappa} \\ =& \frac{F\Delta Z_r Z_q}{Sm_0^3} (\boldsymbol{m}_0 \boldsymbol{m}_r \delta_{\alpha\kappa} - m_{0\kappa} m_{r\alpha}). \end{aligned} \tag{3.31}$$

Next, the dynamics of $\boldsymbol{m}_0$ and $\boldsymbol{m}_T$ are evaluated in the absence of external magnetic fields and again under the assumption of local and homogeneous interaction ($K_{qi} = K\delta_{ii_q}$). For $\dot{\boldsymbol{m}}_0$ we find

$$\begin{aligned} \dot{\boldsymbol{m}}_0 =& K \sum_r z_{i_r} \dot{\boldsymbol{m}}_r \\ =& K^2 \left(- \frac{F}{m_0}\boldsymbol{m}_0 - \frac{F\Delta}{Sm_0^3}\boldsymbol{m}_0 \times \dot{\boldsymbol{m}}_0 \right) \times \boldsymbol{m}_T. \end{aligned} \tag{3.32}$$

In the given from it is straight forward to read of that $\dot{\boldsymbol{m}}_0 \boldsymbol{m}_T = 0$, which is exploited to simplify $\big(\boldsymbol{m}_0 \times \dot{\boldsymbol{m}}_0\big) \times \boldsymbol{m}_T = \dot{\boldsymbol{m}}_0 \big(\boldsymbol{m}_0 \boldsymbol{m}_T\big)$. Using the latter relation, the explicit equation of motion

$$\dot{\boldsymbol{m}}_0 = \frac{1}{\frac{m_0}{FK^2} + \frac{F\Delta}{Sm_0^2}\boldsymbol{m}_0\boldsymbol{m}_T} \boldsymbol{m}_T \times \boldsymbol{m}_0 \tag{3.33}$$

is obtained. Clearly, magnitude $m_0 = |\boldsymbol{m}_0|$ is conserved, since $\dot{\boldsymbol{m}}_0 \boldsymbol{m}_0 = 0$.

Having the previous relations at hand, $\dot{\boldsymbol{m}}_T$ is determined to

$$\begin{aligned} \dot{\boldsymbol{m}}_T =& \sum_r \dot{\boldsymbol{m}}_r = -\frac{F\Delta}{Sm_0} \dot{\boldsymbol{m}}_0 \\ =& \frac{\frac{F\Delta}{Sm_0}}{\frac{m_0}{FK^2} + \frac{F\Delta}{Sm_0^2}\boldsymbol{m}_0\boldsymbol{m}_T} \boldsymbol{m}_0 \times \boldsymbol{m}_T. \end{aligned} \tag{3.34}$$

Analogously to $m_0 = \text{const}$, $\dot{\boldsymbol{m}}_T \boldsymbol{m}_T = 0$ implies $m_T = |\dot{\boldsymbol{m}}_T| = \text{const}$. Furthermore, $\boldsymbol{m}_0 \dot{\boldsymbol{m}}_T = 0$ is deduced. Combining the latter with the previously obtained $\dot{\boldsymbol{m}}_0 \boldsymbol{m}_T = 0$, we find the product of $\boldsymbol{m}_0 \boldsymbol{m}_T$ to be a constant of motion in the adiabatic dynamics.

Moreover, a link to the naive approach can be made when considering $\Delta = \sum_i z_i = 0$. In such scenarios, the non-Hamiltonian geometrical torque in the adiabatic dynamics vanishes. Hence, $\Delta = 0$ referred to as the 'trivial' case. In such trivial cases, $\dot{\boldsymbol{m}}_T = 0$ and $\dot{\boldsymbol{m}}_0$ takes the same form as obtained via the naive approach (eq. 3.24). Consistently, $\boldsymbol{m}_0$ recovers the precessional motion around $\boldsymbol{m}_T$ with frequency $\omega_P = FK^2 \frac{m_T}{m_0}$ for $\Delta = 0$ (see eq. 3.33 and eq. 3.24).

In nontrivial cases ($\Delta \neq 0$), however, the dynamics of the global quantities $\boldsymbol{m_T}$ and $\boldsymbol{m}_0$ is governed by a set of coupled differential equations with an analytical solution that can easily be derived as sketched in Appendix A.1.3. Combining 3.33 and 3.34 to that analytical solution (eq. A.5) results in

$$\omega_p = \sqrt{c_{m_T}^2 m_0^2 + c_{m_0}^2 m_T^2 \pm 2|c_{m_0} c_{m_T}| \boldsymbol{m}_0 \boldsymbol{m}_T}\,. \tag{3.35}$$

with

$$c_{m_0} = \frac{1}{\frac{m_0}{FK^2} + \frac{F\Delta}{Sm_0^2} \boldsymbol{m}_0 \boldsymbol{m}_T} \tag{3.36}$$

$$c_{m_T} = \frac{\frac{F\Delta}{Sm_0}}{\frac{m_0}{FK^2} + \frac{F\Delta}{Sm_0^2} \boldsymbol{m}_0 \boldsymbol{m}_T}. \tag{3.37}$$

This precession takes place around the axis of the total spin $\boldsymbol{F}_T + \boldsymbol{S}_T$, which matches the intuition one may have for physical reasons. Once more, a rather simple expression for ω_p is obtained when specifying to two impurities and $K_{iq} = K\delta_{ii_q}$. Here, $z_{i_1} = -z_{i_2}$ is required to observe nontrivial dynamics with non-Hamiltonian contributions to the equations of motion. Moreover, this choice of the geometry leads to $\boldsymbol{m}_0 \boldsymbol{m}_T = 0$ and results in a precession frequency

$$\omega_p = \frac{FK^2}{m_0} \sqrt{\frac{\Delta^2 F^2}{S^2} + m_T^2}. \tag{3.38}$$

Without loss of generality one can choose $z_{i_1} = 1$ resulting in $m_0 = K|\boldsymbol{m}_1 - \boldsymbol{m}_2|$ for two impurities. With θ as the conserved enclosed angle of $\boldsymbol{m}_1$ and $\boldsymbol{m}_2$, an analytical expression for ω_p is given by

$$\omega_p = FK \sqrt{\frac{\Delta^2 F^2}{2S^2(1 - \cos(\theta))} + \cot^2\left(\frac{\theta}{2}\right)}\,. \tag{3.39}$$

The value of ω_p is determined solely by the initial impurity configuration and system

parameters.

Conclusively, some comparing remarks on the conceptually correct adiabatic and the conceptually incorrect naive approach to constraint spin dynamics are made. Assume a setup of two impurities locally coupled to a collinear host with $z_{i_1} = -z_{i_2}$. As the overall system approaches its global ground state ($\theta \to \pi$), the adiabatic theory predicts $\omega_p^A \to \frac{KF^2|\Delta|}{2S}$. In contrast thereto, the naive approach predicts fundamentally different dynamics with $\omega_p^N \to 0$ in that case. The initial configuration of highest energy on the other hand ($\theta \to 0$) results in diverging precession frequencies $\omega_p(\theta \to 0) \sim \frac{1}{\theta}$ in both cases. The proportionality constant, however, differs as $\omega_p^N \to \frac{2FK}{\theta}$ while $\omega_p^A \to \frac{FK}{S\theta}\sqrt{\frac{\Delta F^2+4S^2}{2}}$. This divergence originates from an intrinsic singularity of the constraint, since $\theta \to 0$ causes $m_0 \to 0$. But $m_0 = 0$ is associated with a singular, ill-defined point in the configuration space. An impurity configuration of this kind leaves ambiguity to the host configuration, which is not compatible with the employed constraint as mentioned in the discussion preceding eq. 3.20.

3.1.3 – Beyond the Adiabatic Constraint: Tight Binding Spin Dynamics

The tight-binding spin dynamics exploits the same picture of an overall system build up by fast $\boldsymbol{F}$ and a slow $\boldsymbol{S}$ subsystem. Compared to adiabatic spin dynamics, however, the constraint imposed on the dynamics of the fast subsystem is somewhat relaxed. The adiabatic approximation implies, that the fast subsystem is in its ground state to a given slow subsystem configuration $\boldsymbol{F} = \boldsymbol{F}^0(\boldsymbol{S})$ at all times. Hence, all dynamical host degrees of freedom are eliminated. While the tight-binding constraint also requires the host system to remain in its ground state, i.e. fast spins are tightly bound among each other, it is now assumed that this ground state is a function of an independent dynamical axis $\boldsymbol{\eta}(t)$ ($|\boldsymbol{\eta}| = \eta = 1$). Accordingly, the tight-binding constraint reads $\boldsymbol{F} = \boldsymbol{F}^0(\boldsymbol{\eta})$. Contrary to the adiabatic constraint, $\boldsymbol{F}^0(\boldsymbol{\eta})$ includes dynamic host degrees of freedom.

We apply this holonomic constraint to the spin Lagrangian (eq. 3.2) and add a Lagrange multiplier to ensure that the norm of $\boldsymbol{\eta}$ is fixed to unity. Thus, the effective tight-binding Lagrangian is

$$\begin{aligned} L^{\text{eff}}\big(\boldsymbol{m}, \dot{\boldsymbol{m}}, \boldsymbol{\eta}, \dot{\boldsymbol{\eta}}; \boldsymbol{n}^0(\boldsymbol{\eta})\big) = &\sum_{q\alpha} S_q A_\alpha(\boldsymbol{m}_q)\dot{m}_{q\alpha} + \sum_{i\beta} F_i A_\beta\big(\boldsymbol{n}_i^0(\boldsymbol{\eta})\big) \sum_\alpha \frac{\partial n_{i\beta}^0}{\partial \eta_\alpha}\dot{\eta}_\alpha \\ &- H^{\text{eff}}(\boldsymbol{m}; \boldsymbol{n}^0(\boldsymbol{\eta})) - \sum_q \lambda_q(\boldsymbol{m}_q^2 - 1) - \lambda(\boldsymbol{\eta}^2 - 1)\,. \end{aligned} \tag{3.40}$$

For the sake of clarity, here, the arguments of L^{eff} and H^{eff} denote dynamical variables in front of the semicolon and the applied constraint hereinafter. The constraint will be omitted in latter proceedings as it is clear from the context.

Analogously to the adiabatic case (section 3.1.1) the equations of motion are derived using the stationary action principle, respectively the Euler-Lagrange equations (eq. A.1). All steps are carried out in a similar fashion as in section 3.1.1 to obtain the dynamics of the impurities. There is, however, an additional equation of motion for $\boldsymbol{\eta}(t)$ in the tight-binding set of coupled differential equations. A detailed derivation is presented in appendix A.1.4. The conditional equations for the Lagrange multipliers are

$$\lambda_r = -\frac{1}{2}\sum_{\mu}\frac{\partial H_{eff}}{\partial m_{r\mu}} m_{r\mu}, \tag{3.41}$$

$$\lambda = \frac{1}{2}\sum_{\alpha\mu}\Omega_{\mu\alpha}\eta_\mu\dot{\eta}_\alpha - \frac{1}{2}\sum_{\mu}\frac{\partial H_{eff}}{\partial \eta_\mu}\eta_\mu. \tag{3.42}$$

Eventually, the tight-binding equations of motion read

$$\dot{\boldsymbol{m}}_r = \frac{1}{S_r}\frac{\partial H_{eff}}{\partial \boldsymbol{m}_r} \times \boldsymbol{m}_r \tag{3.43}$$

$$\dot{\boldsymbol{\eta}} = \tilde{\boldsymbol{T}}^{-1}\left(\frac{\partial H_{eff}}{\partial \boldsymbol{\eta}} \times \boldsymbol{\eta}\right). \tag{3.44}$$

Here, the definitions of $\boldsymbol{\Omega}$ with elements

$$\Omega_{\mu\alpha} := \sum_{i\beta\gamma\nu} F_i \frac{\partial n^0_{i\beta}}{\partial \eta_\alpha}\frac{\partial n^0_{i\gamma}}{\partial \eta_\mu} n^0_{i\nu}\,\varepsilon_{\beta\gamma\nu} \tag{3.45}$$

and $\boldsymbol{T}$ with elements

$$\tilde{T}_{\xi\alpha} := \sum_{\mu\kappa}\Omega_{\mu\alpha}\eta_\kappa\varepsilon_{\mu\kappa\xi} \tag{3.46}$$

are deployed.

Note that the impurity dynamics (eq. 3.43) is nothing but the constraint Hamiltonian equation of motion, despite the derivation being carried out using the conceptually correct approach of applying the constraint to the Lagrangian and utilizing the action principle. The dynamics of $\boldsymbol{\eta}$ (eq. 3.44) is, however, non-Hamiltonian. Matrix $\tilde{\boldsymbol{T}}^{-1}$ might mix and rescale contributions obtained in the tight-binding Hamiltonian dynamics

$$\dot{\boldsymbol{\eta}}^N = \frac{\partial H_{eff}}{\partial \boldsymbol{\eta}} \times \boldsymbol{\eta}. \tag{3.47}$$

3.1.3.1 Tight Binding Spin Dynamics for a Collinear Host

The tight binding equations of motion 3.43 and 3.44 are now formulated for cases of collinear host systems. In such ground states host spins are constraint to

$$\boldsymbol{n}_i^0(\boldsymbol{\eta}) = z_i \boldsymbol{\eta} \tag{3.48}$$

where axis $\boldsymbol{\eta} = \boldsymbol{\eta}(t)$ is a dynamical variable itself. Trivially, $\frac{\partial n_{i\beta}^0}{\partial \eta_\alpha} = z_i \delta_{\alpha\beta}$, so elements of the curvature tensor are

$$\begin{aligned}\Omega_{\mu\alpha} =& \sum_{i\beta\gamma\nu} F_i \frac{\partial n_{i\beta}^0}{\partial \eta_\alpha} \frac{\partial n_{i\gamma}^0}{\partial \eta_\mu} n_{i\nu}^0 \, \varepsilon_{\beta\gamma\nu} \\ =& \sum_{i\nu} F_i z_i \eta_\nu \, \varepsilon_{\alpha\mu\nu} \\ =& F\Delta \sum_\nu \eta_\nu \, \varepsilon_{\alpha\mu\nu}.\end{aligned} \tag{3.49}$$

For the last line $F_i = F \, \forall \, i$ is assumed and we utilize $\Delta = \sum_i z_i$. Exploiting the constraint (eq. 3.48) to evaluate elements of tensor $\tilde{\boldsymbol{T}}$ leads to

$$\tilde{T}_{\xi\alpha} = F\Delta(\delta_{\alpha\xi} - \eta_\xi \eta_\alpha). \tag{3.50}$$

We note, that for $\Delta = 0$ the inverse of that tensor does not exist. Such cases have to be considered cautiously and will be discussed later on. Other than that, only singular points of $\boldsymbol{\eta} \in \mathcal{S}^2$ lead to $\det(\tilde{\boldsymbol{T}}) = 0$ and therewith to an inherent breakdown of the theory. These singular points, however, are of zero measure in the configuration space, similar to the scenario mentioned in section 3.1.2.

We consider a system defined by the Hamiltonian

$$H_{eff}^0(\boldsymbol{m}, \boldsymbol{\eta}) = H_{host}^0 - SF \sum_{q,i} K_{qi} z_i \boldsymbol{m}_q \boldsymbol{\eta} - S \sum_q \boldsymbol{m}_q \boldsymbol{B}_q. \tag{3.51}$$

For the sake of simplicity, $F_i = F \, \forall i$ and $S_q = S \, \forall q$ is assumed to analytically analyzed its dynamics. Again, H_{host}^0 is taken to be $SO(3)$ invariant, respectively, independent of $\boldsymbol{\eta}$. Straight forwardly,

$$\frac{\partial H_{eff}^0}{\partial \boldsymbol{\eta}} = - SF \sum_{q,i} K_{qi} z_i \boldsymbol{m}_q = -SF \boldsymbol{m}_0, \tag{3.52}$$

$$\frac{\partial H_{eff}^0}{\partial \boldsymbol{m}_r} = - SF \sum_i K_{ri} z_i \boldsymbol{\eta} - S \boldsymbol{B}_r \tag{3.53}$$

is obtained. It is convenient to rewrite $\dot{\boldsymbol{\eta}}$ (eq. 3.44) as $\tilde{\boldsymbol{T}} \dot{\boldsymbol{\eta}} = \frac{\partial H_{eff}}{\partial \boldsymbol{\eta}} \times \boldsymbol{\eta}$. Substituting

equation 3.50 herein, exploiting $|\boldsymbol{\eta}| = 1$ and $\boldsymbol{m}_0 = \sum_{q,i} K_{qi} z_i \boldsymbol{m}_q$ results in

$$\Delta\dot{\boldsymbol{\eta}} = -S\boldsymbol{m}_0 \times \boldsymbol{\eta}. \tag{3.54}$$

Dynamics of the impurities, on the other hand, is defined by

$$\dot{\boldsymbol{m}}_r = -F \sum_i K_{ri} z_i \boldsymbol{\eta} \times \boldsymbol{m}_r - \boldsymbol{B}_r \times \boldsymbol{m}_r. \tag{3.55}$$

Here, we substituted the obtained expression for $\frac{\partial H^0_{eff}}{\partial \boldsymbol{m}_r}$ (eq. 3.53) in equation 3.43.

Considering the evolution of the global impurity quantities $\boldsymbol{m}_T$ and $\boldsymbol{m}_0$, local and homogeneous interaction ($K_{qi} = K\delta_{ii_q}$) as well as homogeneous external fields ($\boldsymbol{B}_r = \boldsymbol{B}\,\forall r$) are assumed. For the defining vector of the total impurity magnetization we get

$$\dot{\boldsymbol{m}}_T = \sum_r \dot{\boldsymbol{m}}_r = -F\boldsymbol{\eta} \times \boldsymbol{m}_0 - \boldsymbol{B} \times \boldsymbol{m}_T \tag{3.56}$$

and furthermore

$$\dot{\boldsymbol{m}}_0 = \sum_r K z_{i_r} \dot{\boldsymbol{m}}_r = -FK^2\boldsymbol{\eta} \times \boldsymbol{m}_T - \boldsymbol{B} \times \boldsymbol{m}_0. \tag{3.57}$$

In the absence of external magnetic fields the total spin is conserved, since

$$\frac{d}{dt}(F\boldsymbol{n}_T + S\boldsymbol{m}_T) = F\Delta\dot{\boldsymbol{\eta}} + S\dot{\boldsymbol{m}}_T = 0\,. \tag{3.58}$$

An important remark on the constraint tight-binding dynamics for collinear host spin systems has to be made for cases of $\Delta = 0$. Considering the equation of motion of the global host degrees of freedom $\dot{\boldsymbol{\eta}}$ (eq. 3.54) the left hand site $\Delta\dot{\boldsymbol{\eta}}$ vanishes for $\Delta = 0$. A non-zero right hand side, however, $-S\boldsymbol{m}_0 \times \boldsymbol{\eta} \neq 0$ is compatible with the initial conditions of the tight-binding constraint. This inherent inconsistency arises when the host possesses no net magnetic momentum. It stems from a singular effective Lagrangian, which although subtle, is the source of this inconsistency. Therefore, a brief note on the dynamics of a system of point particles is included to provide further understanding [88].

Consider a point-particle system described by coordinates $\boldsymbol{q} = (q_1, ..., q_N)$ and evaluate the Euler-Lagrange equations for a specific coordinate

$$\begin{aligned} 0 =& \frac{\partial L(\boldsymbol{q}, \dot{\boldsymbol{q}})}{\partial q_i} - \frac{d}{dt}\frac{\partial L(\boldsymbol{q}, \dot{\boldsymbol{q}})}{\partial \dot{q}_i} \\ =& \frac{\partial L}{\partial q_i} - \sum_j \frac{\partial^2 L}{\partial q_j \partial \dot{q}_i}\dot{q}_j - \sum_j \frac{\partial^2 L}{\partial \dot{q}_j \partial \dot{q}_i}\ddot{q}_j. \end{aligned}$$

When the determinant of the Hessian matrix $\boldsymbol{H}$ with elements $H_{ij} = \frac{\partial^2 L}{\partial \dot{q}_i \partial \dot{q}_j}$ equals zero, $\boldsymbol{H}$ cannot be inverted. In such cases, the Lagrangian is said to be singular [96–98]. The Hamiltonian and the Lagrangian of classical spin systems are not related via simple Legendre transformation. In fact, a classical spin system's Lagrangian obtained via Legendre transformation is typically singular (see e.g. supplementary material of [87]). Principally, the Dirac-Bergman formalism [98–100] can be applied to derive a Hamiltonian from a singular Lagrangian. The issue, however, exacerbates if not only the Hessian matrix, but also the coefficient matrix $K_{ij} = \frac{\partial^2 L}{\partial q_i \partial \dot{q}_j}$ becomes singular, e.g. when $L(\boldsymbol{q}, \dot{\boldsymbol{q}}) = L(\boldsymbol{q})$. In such cases, inconsistencies might render the Lagrangian inadmissible. The tight binding constraint that was imposed to the spin Lagrangian can leads to such an unphysical, invalid effective theory.

We illustrate the occurrence of such an inadmissible Lagrangian by imposing the tight-binding constraint for collinear host spin ground states ($\boldsymbol{n}_i^0 = z_i \boldsymbol{\eta}$) to the spin Lagrangian (eq. 3.2). Again, all host and impurity spins are assumed to be of equal magnitude ($F_i = F \, \forall i$ and $S_r = S \, \forall r$), so the effective Lagrangian is

$$\begin{aligned} L^{\text{eff}}\big(\boldsymbol{m}, \dot{\boldsymbol{m}}, \boldsymbol{\eta}, \dot{\boldsymbol{\eta}}; \boldsymbol{n}_i^0 = z_i \boldsymbol{\eta}\big) =& S \sum_{q\alpha} A_\alpha(\boldsymbol{m}_q) \dot{m}_{q\alpha} + F \sum_{i\alpha} A_\alpha(z_i \boldsymbol{\eta}) z_i \dot{\eta}_\alpha \\ & - H^{\text{eff}}(\boldsymbol{m}, \boldsymbol{\eta}; \boldsymbol{n}_i^0 = z_i \boldsymbol{\eta}) - \sum_q \lambda_q (\boldsymbol{m}_q^2 - 1) - \lambda(\boldsymbol{\eta}^2 - 1). \end{aligned} \tag{3.59}$$

Only the curl of the vector potential $\boldsymbol{A}(\boldsymbol{\eta}) \equiv \boldsymbol{A}_{\boldsymbol{e}_z}(\boldsymbol{\eta}) = -\frac{\boldsymbol{e}_z \times \boldsymbol{\eta}}{1 + \boldsymbol{e}_z \boldsymbol{\eta}}$ is of relevance to the equations of motion and $\boldsymbol{\nabla}_{\boldsymbol{\eta}} \times \boldsymbol{A}(\boldsymbol{\eta})$ remains invariant under gauge transformations $\boldsymbol{e}_z \mapsto \boldsymbol{e}$, where $\boldsymbol{e}$ is an arbitrary unit vector. The physical intuition to this is, that measurable effects do not depend on the choice of the coordinate system.

Furthermore, the Euler-Lagrange equations are invariant under local, i-dependent gauge transformations $\boldsymbol{e}_z \mapsto z_i \boldsymbol{e}_z$ with $z_i \in \{-1, 1\}$. Applying this local gauge transformation to the vector potential yields

$$\boldsymbol{A}_{\boldsymbol{e}_z}(z_i \boldsymbol{\eta}) \to \boldsymbol{A}_{z_i \boldsymbol{e}_z}(z_i \boldsymbol{\eta}) = -\frac{(z_i \boldsymbol{e}_z) \times (z_i \boldsymbol{\eta})}{1 + (z_i \boldsymbol{e}_z)(z_i \boldsymbol{\eta})} = -\frac{\boldsymbol{e}_z \times \boldsymbol{\eta}}{1 + \boldsymbol{e}_z \boldsymbol{\eta}} \, . \tag{3.60}$$

The resulting $\boldsymbol{A}_{z_i \boldsymbol{e}_z}(z_i \boldsymbol{\eta}) = \boldsymbol{A}_{\boldsymbol{e}_z}(\boldsymbol{\eta})$ is independent of the site index i.

Now the sum over all host spin sites i can easily be carried out in the second term of the effective Lagrangian (eq. 3.60). The resulting $F \sum_i \boldsymbol{A}_{\boldsymbol{e}_z}(\boldsymbol{\eta}) z_i \dot{\boldsymbol{\eta}} = F \Delta \boldsymbol{A}_{\boldsymbol{e}_z}(\boldsymbol{\eta}) \dot{\boldsymbol{\eta}}$ vanishes for $\Delta = \sum_i z_i = 0$. After the gauge transformation the constraint Lagrangian does not depend on $\dot{\boldsymbol{\eta}}$ when $\Delta = 0$, which causes inconsistencies as it is inadmissible. As discussed earlier, the inconsistency becomes apparent in a contradiction of the left and the right hand side of equation 3.54 for cases when $\Delta = 0$. That contradiction, however, is caused by a conceptual mistake of deriving an equation of motion from an Lagrangian that is not admissible.

3.2 – Numerical Results of the Classical Adiabatic Spin Dynamics

In the following section, we present numerical findings on the purely classical adiabatic spin dynamics, as well as the naive and tight-binding approach to adiabatic dynamics. These results are published in [88]. We assume local and homogeneous interactions throughout the entire section, with all $K, J > 0$, resulting in antiferromagnetic spin alignment in the ground state. The time-scale separation required for the adiabatic limit is attained by ensuring that $K \ll J$.

3.2.1 – Dynamics from $K = J$ to the Adiabatic Limit

We study dynamics of a classical spin setup where impurities are weakly coupled to a host of classical spins, i.e., three component vectors. Our goal is to analyze the parameter regime, where the spin dynamics is adiabatic. Strictly speaking, there is no adiabatic theorem to this purely classical model, in particular, since the spectrum of the host model is not gapped. Nonetheless, we compare predictions of the adiabatic spin dynamics (eq. 3.30 and eq. 3.33) with the numerical solution obtained from the full set of equation of motion (eq. 3.3) and asses the conformity.

For now, we stick to a linear chain of $L = 5$ sites as a host and two impurities locally coupled to that host at sites $i_1 = 1$ and $i_2 = 4$. This exemplary setup is pictured in figure 3.1. Due to $z_{i_1} = -z_{i_2} = 1$ and an uneven number of host spins, this is a prototypical setup of the nontrivial case, where $\Delta = 1$ enables non-zero geometric spin torque, i.e. $\mathbf{\Omega} \neq 0$ (eq. 3.29). Moreover, this setup features dynamics of the total host spin (eq. 3.34) and non-static $\mathbf{\Omega}$, since $\boldsymbol{m}_0 \neq \pm \boldsymbol{m}_T$.

Real-time dynamics of the impurities for $K = J$ to an initial impurity configuration far from the antiferromagnetic ($\theta_0 = \pi$) ground state is displayed in figure 3.2. The host system is initialized in the ground state to the given impurity configuration (eq. 3.20). We observe complex dynamics where trajectories over time cover entire phase space accessible under the restriction of energy and total spin conservation. Such dynamics is characteristic for a non-linear set of classical Hamiltonian equations of motion with numerous degrees of freedom.

Adiabatic spin dynamics, on the other hand, is expected for $K \ll J$. In that limit, the number of effective dynamical degrees of freedom is drastically reduced as compared to a generic setup with K and J being of the same order of magnitude. Figure 3.3a displays exemplary dynamics for $K/J = 10^{-5}$ in the same setup as considered in figure 3.2 obtained via the full set of equations of motion (eq. 3.3 and eq. 3.4). For small ratios of host-impurity interaction K to intra-host-coupling J, the dynamics appears more regular. Impurities generally exhibit precessional motion, with additional nutational

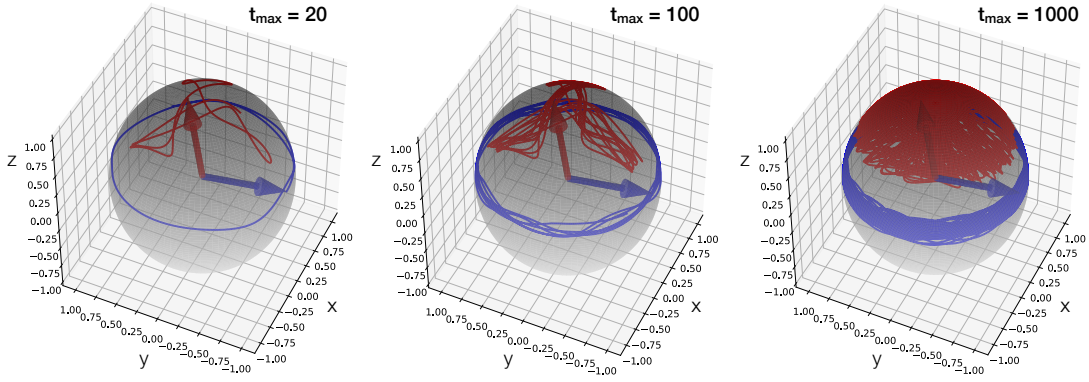

Figure 3.2: Trajectories of the two impurity spins ($\boldsymbol{m}_1$: blue, $\boldsymbol{m}_2$: red) acquired through numerical solutions of the full set of equations of motion (eq. 3.3 and eq. 3.4) plotted on a two-sphere. A setup of equal host-impurity exchange and intra-host coupling ($K = J$) is considered. Initially the total spin is parallel to the z-axis, impurities enclose $\theta = \pi/2$ and the host is in the ground state to the given impurity configuration. Impurity spins at $t = 0$ are indicated by the arrows. The maximum propagation time t_{max} in units of K^{-1} increases from left to right.

dynamics being observed. These nutations are not described by the adiabatic spin dynamics, but accounted for by the tight binding dynamics derived in section 3.1.3. It originates from an unconstraint precession of axis $\boldsymbol{\eta}$ around $\boldsymbol{m}_0$ (eq. 3.18). The feedback of the $\dot{\boldsymbol{\eta}}$ to the impurity dynamics beyond the adiabatic description, where $\boldsymbol{\eta} = \boldsymbol{m}_0$, is less pronounced when the initial configuration is closer to the overall ground state. In the setup under investigation, that corresponds to an angle $\theta_0 = \pi$ enclosed by the impurities.

For $\theta = 0.95\pi = 0.95\theta_0$, the trend towards improved agreement of impurity dynamics obtained from the full set of equations of motion and approximated dynamics in the adiabatic limit is presented in figure 3.3b. It displays the azimuthal angle ϕ of $\boldsymbol{m}_0$ with respect to the conserved total spin $\boldsymbol{S}_T + \boldsymbol{F}_T$ modulo 2π. In the adiabatic limit, this angle grows linearly with time (green trajectory in fig. 3.3b). For $K = J$, the dynamics of the impurities is non-adiabatic and typically intricate as depicted in figure 3.2 for $\theta = \pi/2$. In the $\boldsymbol{m}_0$-dynamics for $K/J = 1$, one observes a smaller rate of increase $d\phi/dt$ than predicted by adiabatic theory. Additionally, there is a superimposed structure beyond the linear increase of $\phi(t)$ predicted by the adiabatic equations of motion.

For smaller K/J values, that additional oscillation superimposed on the precessional motion becomes weaker and is barely notable for $K/J = 10^{-2}$. Also, the incline of ϕ over time seems to approaches adiabatic rate when reducing K/J. The naive approach to adiabatic spin dynamics (orange trajectory in fig. 3.3b), where equations of motion are incorrectly derived solely from the Hamiltonian subjected to the adiabatic constraint, predicts precessional impurity dynamics as well. Incorrectly, however, that precession is predicted to take place around the axis of total impurity spin $\boldsymbol{m}_T$. Figure 3.3b shows, that besides a wrong axis, the angular velocity $d\phi/dt$ of $\boldsymbol{m}_0$ is estimated

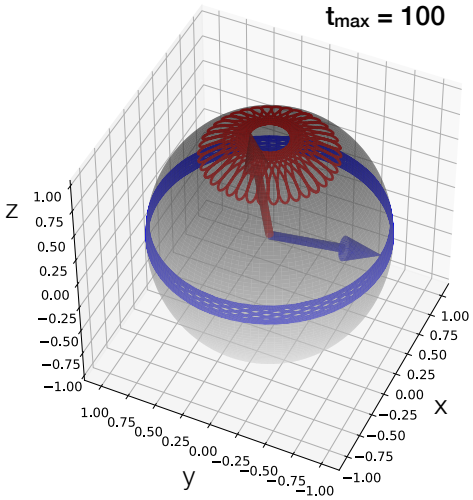

(a) Trajectories of the two impurities, $\boldsymbol{m}_1$ blue and $\boldsymbol{m}_2$ red, for $K/J = 10^{-5}$ obtained by numerical integration of the full set of equations of motion for $t_{max} = 100K^{-1}$ time steps. Initially impurities enclose $\theta = \pi/2$.

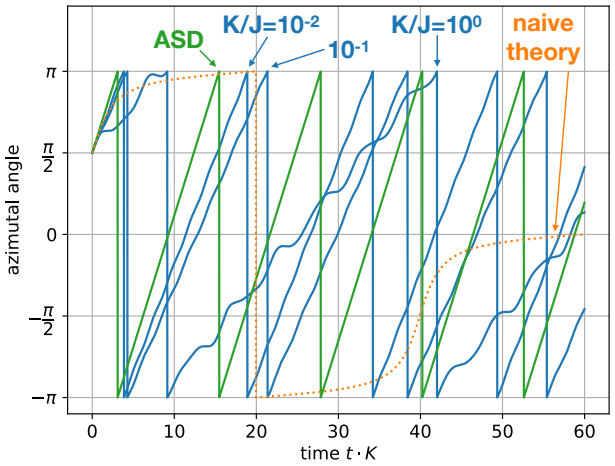

(b) Time evolution of azimuthal angle ϕ (modulo 2π) of $\boldsymbol{m}_0$ around conserved total spin axis for $\theta = 0.95\pi$. Blue indicates Trajectories obtained from the full set of equation of motion for various K/J. Green relates to adiabatic spin dynamics and orange to the naive adiabatic theory.

Figure 3.3: Setup as shown in figure 3.1. Initially, the host is in the ground state to the corresponding impurity spin configuration.

much too small. Even in the limit of $K/J \to 0$ and when θ is close to θ_0 the predicted trajectory of $\boldsymbol{m}_0$ obtained via the naive approach deviates significantly from the trajectory obtained form the full set of equations of motion. Based on these observations, we conclude that the naive approach is an inadequate description of impurity dynamics.

3.2.2 – Analysis of the Precession Frequency

In the preceding section, we qualitatively considered dynamics of the slow impurity spins in the limit of small K/J ratios. Here, we approach a systematic study in parameter space to quantify the characteristics of the naive (eq. 3.23), the adiabatic (eq. 3.30) and the tight-binding (eq. 3.55) approximation. The parameter space to the linear-chain host model with two impurities at sites $i_1 = 1$ and $i_2 = L - 1$, is spanned by K/J and angle θ enclosed by two impurities. We compare impurity dynamics obtained through the aforementioned approximations with the dynamics of the slow spins acquired from the full set of equations of motion (eq. 3.3).

The frequency of dominant weight in the Fourier spectra of impurity trajectories is referred to as ω_p. For the naive approach and the adiabatic theory we derived an analytical expression for ω_p. In the naive theory, ω_p^N (eq. 3.25) depends on θ only. For the adiabatic approach, however, the geometry of the impurity setup affects ω_p^A (eq. 3.39). We consider a setup of nontrivial geometric spin torque ($\Delta = 1$), where the ground state impurity configuration is $\theta_0 = \pi$.

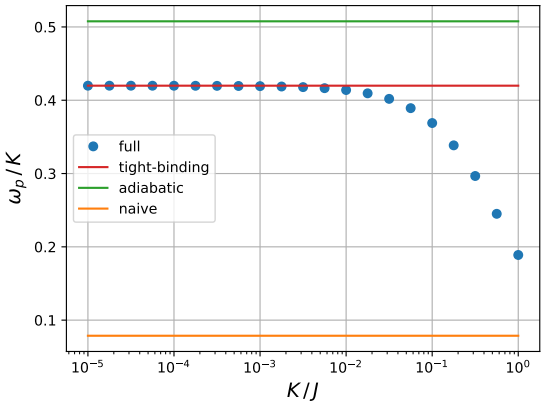

(a) Precessional frequencies as a function of K/J with $\theta = 0.95\pi$.

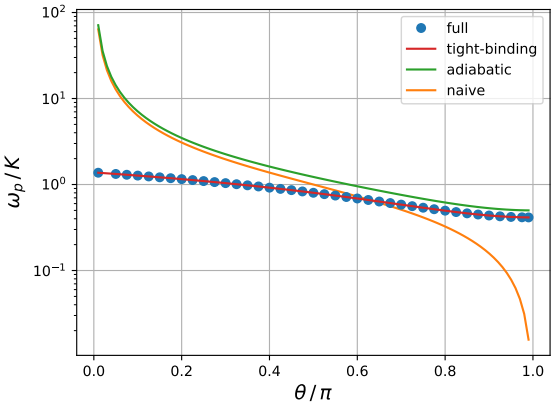

(b) Precessional frequencies as a function of θ with $K/J = 10^{-5}$.

Figure 3.4: Relating dynamics of the impurities obtained within the naive, the adiabatic and the tight-binding approximation to impurity dynamics acquired from the full set of equations of motion. A setup with a collinear host of $L = 5$ sites and impurities at $i_1 = 1$ and $i_2 = 4$ (geometry of fig. 3.1) is considered. Initially, the host is in the ground state to the impurity configuration.

In figure 3.4a, the precession frequencies are studied in the limit $K/J \to 0$. The entire system is initialized close to the ground state with $\theta = 0.95\theta_0$. The normalized precession frequency ω_p^F/K of the full dynamics reaches saturation at $K/J \approx 10^{-3}$. When $K/J < 10^{-3}$, we may construe the system as being in the classical analogue to the adiabatic limit. In this limit, the host system behaves as if it was effectively 'rigid,' maintaining roughly its ground state throughout the entire dynamic process, i.e., $\boldsymbol{F}_i\boldsymbol{F}_{i+1} \approx -F^2$ at all times. Consequently, there is practically no independent inherent dynamics of individual fast spins for $K/J < 10^{-3}$.

The adiabatic prediction ω_p^A is about 15% off, even in the limit of small $K/J \ll 10^{-3}$. A residual miss-prediction of the precession frequency in the adiabatic theory is due to inaccurate anticipation of solely precessional impurity dynamics. The host does not just follow the impurity dynamics, but its orientation-defining axis $\boldsymbol{\eta}$ exhibits inherent dynamics beyond the precessional motion. In fact, $\boldsymbol{S}_q\boldsymbol{F}_{i_q}$ is not constant as foreseen by the adiabatic theory, but only $\sum_q \boldsymbol{S}_q\boldsymbol{F}_{i_q} = \text{const}$ is.

The tight-binding theory allows for independent dynamics of $\boldsymbol{\eta}$. It is for this reason, that the tight-binding approximation is an excellent description of the impurity dynamics in the limit of small K/J. Figure 3.4a shows near perfect agreement of precession frequencies derived from the tight-binding dynamics and dynamics obtained via the full set of equations of motion for $K/J < 10^{-3}$. In the full dynamics, non-constant $\boldsymbol{S}_q\boldsymbol{F}_{i_q}$ feeds back to the impurities, which causes a nutational motion in addition to the presessional dynamics foreseen by the adiabatic theory. This feature is perceptible as a subdominant peak in the Fourier spectra of impurity trajectories (see fig. A.1

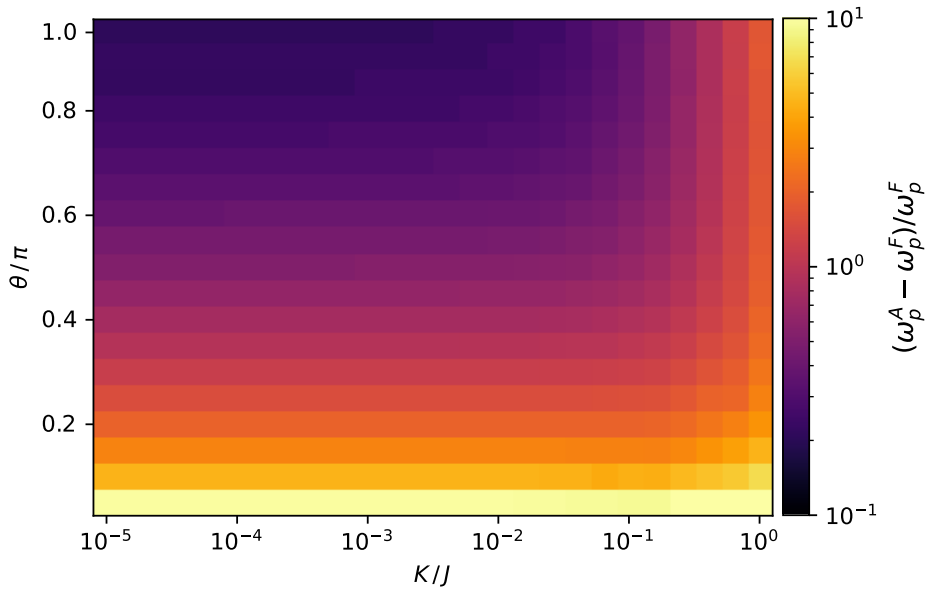

Figure 3.5: Deviation of the precession frequency deduced from the main peak in the Fourier specturm of the real time dynamics of $\boldsymbol{m}_0$ in the θ-K/J parameter space. The color code is the normalized difference of ω_p^A and ω_p^F. ω_p^A is derived from the adiabatic theory (eq. 3.39) and ω_p^F results from numerical time evolution of the full set of equations of motion (eq. 3.3).

in the appendix). Such a second peak is visible in the Fourier spectra of both, the impurity dynamics obtained from the tight-binding approach and from the full set of equations of motion. Such a second peak is, however, absent in the adiabatic and the naive approach.

Aside from an incorrect axis for the impurity precession, the naive approach to adiabatic theory significantly underestimates ω_p as $K/J \to 0$ for the setup studied in figure 3.4a. Again, the naive approach is a insufficient approximation of the impurity dynamics.

Fluctuations of $\boldsymbol{S}_q \boldsymbol{F}_{i_q}$ diminish close to the ground state ($\theta \approx \theta_0$). Figure 3.4b shows, that adiabatic spin dynamics is suited to approximate ω_p in the limit of $\theta \to \theta_0$ when K/J is sufficiently small. Close to the ground state, the adiabatic approach is more accurate in approximating impurity dynamics. We can understand the improvement by noting that in the ground state $m_0 = 0$. The nutational impurity dynamics originates from $\dot{\boldsymbol{\eta}} \sim \boldsymbol{m}_0 \times \eta$, as shown by the tight-binding approach. Hence, nutations diminish for $\theta \to \theta_0$.

Even though timescales of impurity and host dynamics are well separated ($K/J = 10^{-5}$), ω_p^A becomes worse of an approximation for ω_p^F the higher the energy of the initial impurity configuration (see fig. 3.4b). In the adiabatic theory, the frequency of impurity precessions $\omega_p^A \sim 1/\theta$ diverges for the maximally excited impurity configuration ($\theta \to 0$), which is rooted in the ambiguity to determine the host ground state in that case. Moreover, fast impurity dynamics contradicts the assumption of slow, i.e.

adiabatic, dynamics. Consequently, when θ is far from θ_0, i.e. far from the ground state, the adiabatic equations of motion are no longer a reliable approximation of the impurity dynamics.
The naive approach, on the other hand, is a faulty approximation for any θ, although time-scales of host and impurity dynamics are well separated ($K/J = 10^{-5}$). As depicted in figure 3.4b, the naive approach to adiabatic dynamics is non-reliant to approximate the frequency of the impurity precession. It incorrectly predicts that ω_p^N approaches zero as θ approaches the overall ground state, i.e. $\theta \to \theta_0 = \pi$. Moreover, the naive approach suffers the same flaw as the adiabatic approximation for $\theta \to 0$.
A thorough analysis of ω_p^A and ω_p^F over a broad θ-K/J parameter range is presented in figure 3.5. The trend deduced for exemplary parameters in figure 3.4 is confirmed. The agreement of ω_p^A and ω_p^F improves close to ground state and for $K/J \ll 1$. For $\theta \to 0$, i.e. in the limit of maximally excited impurity configurations, the adiabatic theory is an incorrect prediction for ω_p. Even for small K/J the adiabatic theory does not describe impurity dynamics thoroughly, since it lacks to describe the nutational dynamics, which becomes of increasing significance when θ is far from θ_0. The tight binding approach, however, characterizes impurity dynamics in the weak coupling limit very well for all θ (see fig. 3.4b and fig. A.3 in the appendix).
Results of this section similarly apply to larger systems (see fig. A.2). Increasing distance of the impurities demands smaller K/J to ensure an approximately collinear host configuration throughout the dynamics. The approximation, that the host is in its ground state at all times, is justified when inherent canting of host spins is insignificant, i.e. the host can be seen as 'rigid'. Insignificant canting of the host spins, where canting refers to a deviation from the ground state configuration, can always be attained by sufficiently small values of K/J.

3.3 – Summary of the Classical Adiabatic Spin Dynamics

Within this chapter, we consider a purely classical system of localized magnetic moments, where slow degrees of freedom $\boldsymbol{S}$ are weakly coupled to fast degrees of freedom $\boldsymbol{F}$. The goal is to develop an efficient theory for the dynamics of $\boldsymbol{S}$, which minimizes the number of dynamic degrees of freedom. Initially, we apply the adiabatic constraint $\boldsymbol{F} = \boldsymbol{F}_0(\boldsymbol{S})$, where host spins are in the ground state to the momentary impurity configuration at all times. We derived the effective $\boldsymbol{S}$-dynamics through both the naive approach of implementing the adiabatic constraint in the Hamiltonian and the conceptually correct approach of enforcing the constraint in a Lagrangian formulation. When the constraint is imposed to the Lagrangian, we identify a Berry-curvature-like tensor $\boldsymbol{\Omega}$ in the adiabatic equation of motion (eq. 3.10). In the adiabatic approach, the slow degrees of freedom exhibit an additional geometric torque due to $\boldsymbol{\Omega}$ that is absent in the

naive Hamiltonian approach to adiabatic dynamics (eq. 3.23). Moreover, an effective impurity equation of motion is derived in the tight-binding approach (eq. 3.43). Here, the adiabatic constraint is relaxed by allowing for an independent dynamical axis $\boldsymbol{\eta}$ (eq. 3.44) for the host, so the tight-binding constraint reads $\boldsymbol{F} = \boldsymbol{F}_0(\boldsymbol{\eta})$.
Comparing dynamics obtained via each of these effective approaches with dynamics obtained from the full set of equations of motion, the tight binding dynamics is found to cover all relevant features in the limit of well separated timescales. In the discussed linear chain setup (see fig. 3.1), that is achieved by $K/J \ll 1$. Precessional as well as nutational motion of the $\boldsymbol{S}$-spins is observed in the dynamics obtained via the full set of equations of motion (3.3 and 3.4). Both are well approximated within the tight-binding approach to adiabatic impurity dynamics, since it takes an effective impurity coupling, a dynamical axis of the host system as well as the geometric spin torque into account. However, intricate inconsistencies can arise from singular Lagrangian in the thigh-binding approach to adiabatic spin dynamics (see section 3.1.3.1).
The adiabatic approach, on the other hand, does not exhibit such inconsistencies. It is, however, a suitable approximation of the impurity dynamics only close to the overall ground state and when $K/J \ll 1$. Even though it is conceptually correct to derive effective dynamics from a Lagrangian subjected to a constraint, the adiabatic approach is suffers a systematic misconception. In the dynamics, the host remains in its ground state, but not necessarily in the ground state to momentary impurity configuration. The adiabatic approach, however, takes only an effective impurity coupling and the geometric spin torque into account. Nonetheless, adiabatic dynamics is considerably better of an approximation for the precessional impurity dynamics, than the naive approach, which proofs to be insufficient to approach an effective theory for the dynamics of the slow degrees of freedom.
This naive approach of deriving impurity dynamics from an effective-Hamiltonian is incorrect. It predicts a false precession axis and is unreliable for all θ when the host-impurity geometry is nontrivial, i.e., when $\Delta \neq 0$ (eq. 3.28). Accounting solely for an effective impurity coupling is insufficient to generically describe adiabatic dynamics in a setup of slow and fast classical spins.

4 – Quantum-Classical Adiabatic Spin Dynamics

Following the previous study of a purely classical spin model, we now explore a quantum-classical model. This model still utilizes classical spins to model local magnetic impurities, but the role of the host is now taken on by a model of itinerant electrons. Within this chapter we study such a Kondo-impurity-like model in the adiabatic limit.

The model derives its name from the Kondo impurity model introduced by Kondo in 1964 [101] to elucidate the resistance minimum observed in metals such as Au or Cu when slightly doped with magnetic impurities like Fe or Ni. The quantum-classical Kondo impurity model, in which magnetic impurities are modeled by classical spins, departs from the Kondo effect responsible for the resistance minimum. It does, however, capture a variety of captivating phenomena and finds frequent application in various contexts [86, 102–108]. Here, our particularly interest is in the long time dynamics of the quantum-classical model, which is inaccessible in the full quantum description. We review the dynamics of such a quantum classical hybrid model [86, 109] and derive quantum-classical spin dynamics under the adiabatic constraint in section 4.1.

In addition to our focus on adiabatic spin dynamics in the quantum-classical Kondo impurity model, our research is motivated by the burgeoning interest in investigating magnetic impurities in topological insulators [110–121]. Our focus is on the interplay between host topology and the dynamics of the impurities in the adiabatic limit, aiming to answer the question on whether the topological phase of the host is discernible in impurity dynamics. To address this question, we introduce Haldane's model of a Chern insulator [28] in section 4.2. The spinful Haldane model serves as a quantum host in which the bulk band topology can be adjusted via the model's parameters.

In section 4.3 we present numerical results for such a Haldane-impurity setup. Primarily, we address the limit of weak host-impurity coupling where impurities merely disturb the electronic structure of the host. We delve into the influence of the geometric and parametric aspects of the Haldane model on the spin Berry curvature.

Finally, we discuss examples of (adiabatic) spin dynamics and evaluate the quality of the approximations we have made throughout our investigation. This comprehensive exploration provides an example for the interplay between host system's bulk topology

and (adiabatic) impurity dynamics.

4.1 – Theory of Quantum-Classical Adiabatic Spin Dynamics

We begin the analytical considerations with a comprehensive review of the dynamics of quantum-classical hybrid model [86, 109] in section 4.1.1 and obtain a set of coupled differential equations for the equations of motion of the host system and the impurities. Typically, the inherent timescale of the electron system (femtoseconds) is much shorter than the timescale of the comparatively slow classical spins (picoseconds) [48]. Since we consider gapped models, the adiabatic theorem is applicable when the typical slow timescale is large compared to the inverse gap between the ground and the first excited state [122, 123]. Against this backdrop, we derive the adiabatic spin dynamics for the impurities in section 4.1.2 by enforcing the adiabatic constraint to the host model. The resulting adiabatic equation of motion (eq. 4.18) yields a non-Hamiltonian geometric spin torque associated with the spin Berry curvature. We analytically examine the effects of adiabatic spin-torque on the adiabatic dynamics of the model in the context of weak (section 4.1.3) and strong (section 4.1.4) exchange coupling. Eventually, section 4.1.5 addresses the technical realization and computational details.

4.1.1 – Unconstrained Dynamics of the Quantum Host and the Impurities

The host systems considered within this chapter are lattice models of itinerant non-interacting electrons, which can be described by the generic non-interacting quantum Hamiltonian

$$\hat{H}_Q = \sum_{i\sigma,i'\sigma'} T^Q_{i\sigma,i'\sigma'} \hat{c}^\dagger_{i'\sigma'} \hat{c}_{i\sigma}. \tag{4.1}$$

Generically, the elements of the quantum hopping matrix $T^Q_{i\sigma,i'\sigma'}$ are complex numbers that determine the microscopic details of the host system like hopping amplitudes and phase factors. Operator $\hat{c}^\dagger_{i\sigma}$ creates an electron at lattice site i with spin projection $\sigma \in \{\uparrow, \downarrow\}$ and the annihilation operator $\hat{c}_{i\sigma}$ is its adjoint counter part.
We define the reduced one-particle density matrix as

$$\rho_{i\sigma,i'\sigma'} := \langle \hat{c}^\dagger_{i'\sigma'} \hat{c}_{i\sigma} \rangle. \tag{4.2}$$

Its elements are the expectation values of creation-annihilation operator tuples in the system's state at time t [86]. The definition of $\boldsymbol{\rho}$ with elements $\rho_{i\sigma,i'\sigma'}$ is convenient for non-interacting models, as it allows a compact matrix notion of the dynamics. The time evolution of the density matrix is determined by its commutator with the hopping matrix and takes the form of the von Neumann equation $i\frac{d}{dt}\boldsymbol{\rho}(t) = [\boldsymbol{T}^Q, \boldsymbol{\rho}(t)]$ [124].

As the quantum system is coupled to classical impurities, the quantum hopping matrix $\boldsymbol{T}^Q$ can be extended to an effective quantum-classical hopping matrix $\boldsymbol{T}$. To this end we recall the expectation value of a quantum spin-1/2 at site i

$$\langle \hat{\boldsymbol{s}}_i \rangle = \frac{1}{2} \sum_{\sigma\sigma'} \boldsymbol{\sigma}_{\sigma\sigma'} \langle \hat{c}^\dagger_{i\sigma} \hat{c}_{i\sigma'} \rangle = \frac{1}{2} \sum_{\sigma\sigma'} \boldsymbol{\sigma}_{\sigma\sigma'} \rho_{i\sigma',i\sigma}, \tag{4.3}$$

where $\boldsymbol{\sigma} = (\boldsymbol{\sigma}^x, \boldsymbol{\sigma}^y, \boldsymbol{\sigma}^z)^T$ is the vector of Pauli matrices [86]. A standard representation of the Pauli matrices is

$$\boldsymbol{\sigma}^x = \begin{pmatrix} 0 & 1 \\ 1 & 0 \end{pmatrix}, \quad \boldsymbol{\sigma}^y = \begin{pmatrix} 0 & -i \\ i & 0 \end{pmatrix}, \quad \boldsymbol{\sigma}^z = \begin{pmatrix} 1 & 0 \\ 0 & -1 \end{pmatrix}.$$

Accordingly, impurity-host exchange interactions like $\hat{H}_{ex} = \sum_{q\alpha,i\beta} J_{q\alpha,i\beta} S_{q\alpha} \hat{s}_{i\beta}$ add to the effective hopping matrix in form of

$$T_{i\sigma,i'\sigma'}(t) = T^Q_{i\sigma,i'\sigma'} + \sum_{q\alpha} J_{q\alpha,i\beta} S_{q\alpha}(t) \sigma^\beta_{\sigma\sigma'} \delta_{ii'}, \tag{4.4}$$

where $\boldsymbol{\sigma}^\beta$ is the β Pauli matrix ($\alpha, \beta \in \{x, y, z\}$) [86]. Even when the Hamiltonian of the quantum host and thus $\boldsymbol{T}^Q$ is not explicitly time dependent, the effective hopping matrix is a function of time due to the generically time dependent configuration of the impurities. The dynamics of the quantum system in this quantum-classical hybrid model is described through a modification of the von Neumann equation, wherein the quantum hopping matrix is replaced by the effective hopping matrix [86, 125], so

$$i \frac{d}{dt} \boldsymbol{\rho}(t) = [\boldsymbol{T}(t), \boldsymbol{\rho}(t)]. \tag{4.5}$$

Only the combination of the von-Neumann-like equation of motion (eq. 4.5) together with the equations of motion of the classical impurities

$$\dot{\boldsymbol{S}}_q = \frac{\partial \langle \hat{H}_{ex} \rangle}{\partial \boldsymbol{S}_q} \times \boldsymbol{S}_q = J \langle \hat{\boldsymbol{s}}_{i_q} \rangle \times \boldsymbol{S}_q \tag{4.6}$$

form a closed set of differential equations. The second equality in equation 4.6 implies local and homogeneous interaction of the impurities and the host, thus $\hat{H}_{ex} = J \sum_q \hat{\boldsymbol{s}}_{i_q} \boldsymbol{S}_q$. Analytical solutions to this set of coupled differential equations are challenging and often do not exist for generic cases. On that account numerical solutions are prevailing.

4.1.2 – Constraint Quantum-Classical Equation of Motion

Next, we derive equations of motion for the quantum-classical system under the adiabatic constraint. Conceptually the derivation of the quantum-classical adiabatic equations of motion is similar to the classical case discussed in 3.1.1. Let the system be defined by a Lagrangian of the following form

$$L(\langle\psi|, |\psi\rangle, \frac{d}{dt}\langle\psi|, \frac{d}{dt}|\psi\rangle, \boldsymbol{S}, \frac{d}{dt}\boldsymbol{S}) = \langle\psi|i\frac{d}{dt}|\psi\rangle + \sum_q \boldsymbol{A}(\boldsymbol{m}_q)\frac{d}{dt}\boldsymbol{S}_q - \langle\psi|\hat{H}(\boldsymbol{S})|\psi\rangle - \sum_q \lambda_q(\boldsymbol{m}_q^2 - 1). \tag{4.7}$$

The pure multi-particle state of the quantum system is described by $|\psi\rangle = |\psi(t)\rangle$ and the classical spins are given in terms of $\boldsymbol{S} = \{\boldsymbol{S}_q(t)\} = \{S_q\boldsymbol{m}_q(t)\}$, where S_q is the magnitude and $\boldsymbol{m}_q$ a unit vector determining the orientation of the q-th classical impurity spin. Furthermore, $\boldsymbol{A}_q = \boldsymbol{A}(\boldsymbol{m}_q)$ is the vector potential of a unit Dirac monopole located at $\boldsymbol{S}_q = 0$ [15, 16], which satisfies $\boldsymbol{\nabla}_q \times \boldsymbol{A}_r = -\delta_{qr}\frac{\boldsymbol{m}_q}{|\boldsymbol{m}_q|^3}$. The last term of the Lagrangian explicitly ensures conservation of the spin length via Lagrange multipliers λ_q. Moreover, the Hamiltonian $\hat{H}(\boldsymbol{S}) = \hat{H}_Q + \hat{H}_{ex}(\boldsymbol{S}) + H_{cl}(\boldsymbol{S})$ contains contributions defining the quantum system $\hat{H}_Q$ which interacts with the classical spins via $\hat{H}_{ex}$. Direct coupling between the impurities and external fields acting on $\boldsymbol{S}$ are described by the classical Hamiltonian H_{cl}, which contains no quantum degrees of freedom. Our major interest being the indirect exchange between classical spins mediated via the quantum mechanical host we set $H_{cl} = 0$. Including nontrivial H_{cl} to the presented formalism is, however, a straight forward adaptation.

By applying the stationary action principle to this Lagrangian (see A.2.1), a set of coupled differential equations is obtained, that describes the dynamics of all degrees of freedom of the quantum-classical hybrid model. For the classical degrees of freedom this equation of motion is equivalent to the Hamiltonian one [86, 93, 126], where all quantum quantities enter via their expectation values only [125, 127, 128], and for the quantum system that is the Schrödinger equation:

$$\frac{d}{dt}\boldsymbol{S}_r = \dot{\boldsymbol{S}}_r = \{\boldsymbol{S}_r, \langle\hat{H}\rangle\}_r = \frac{\partial\langle\hat{H}\rangle}{\partial\boldsymbol{S}_r} \times \boldsymbol{S}_r \tag{4.8}$$

$$i\frac{d}{dt}|\psi\rangle = \hat{H}|\psi\rangle. \tag{4.9}$$

In equation 4.8, the bracket $\{\boldsymbol{S}_r, \langle\hat{H}\rangle\}_r$ denotes the spin Poisson bracket, which in terms of generic continuously differentiable functions $A(\boldsymbol{S})$, $B(\boldsymbol{S})$ and with respect to

the r-th impurity is defined as [86, 124]

$$\{A(\boldsymbol{S}), B(\boldsymbol{S})\}_r = \sum_{r,\alpha\beta\gamma} \frac{\partial A}{\partial S_{r\alpha}} \frac{\partial B}{\partial S_{r\beta}} S_{r\gamma}\, \varepsilon_{\alpha\beta\gamma}. \tag{4.10}$$

It can be considered as the pendant of the commutator in quantum mechanics. In analogy to equation 4.8, the dynamics of an observable $\hat{O}(t)$ in the Heisenberg picture of quantum mechanics can be determined by the Heisenberg equation of motion [124]

$$i\frac{d}{dt}\hat{O} = [\hat{O}, \hat{H}], \tag{4.11}$$

where $\hat{O}(t)$ is assumed to not be explicitly time dependent ($\partial\hat{O}/\partial t = 0$).

We, however, derive our theory in the Lagrangian formalism using the Schrödinger picture. The Lagrangian formalism is the conceptually correct way to implement constraints to dynamical degrees of freedom, similarly to widespread cases in analytical mechanics [89]. The fundamental adiabatic constraint for the quantum system

$$|\psi(t)\rangle = |\psi_0(\boldsymbol{S}(t))\rangle \tag{4.12}$$

leads to the adiabatic equations of motion for the classical spins. This holonomic constraint enforces the quantum system to be in its ground state to the given impurity configuration $\boldsymbol{S}(t)$ at all times and therefore eliminates any $\boldsymbol{S}$-independent dynamics of the quantum host. We assume the ground state of the quantum system to be non-degenerate for any given impurity configuration. Thus, the subspace of instantaneous ground states $|\psi_0(\boldsymbol{S}(t))\rangle$ of $\hat{H}(\boldsymbol{S}(t))$ contains one pure many-body state for every $\boldsymbol{S}(t)$ only. If, however, there are degenerate ground states to $\hat{H}(\boldsymbol{S}(t))$, an extension to the presented adiabatic theory is required as presented in [69], but that is beyond the scope of this thesis. The smooth map between $\boldsymbol{S}$ and $|\psi_0(\boldsymbol{S})\rangle$ can be characterized topologically by use of its connection, which in our case is the spin Berry connection

$$\boldsymbol{C}_q(\boldsymbol{S}) = i\langle\psi_0(\boldsymbol{S})|\frac{\partial}{\partial \boldsymbol{S}_q}|\psi_0(\boldsymbol{S})\rangle. \tag{4.13}$$

The spin Berry connection is a gauge-dependent quantity, which accumulates the derivative of a smooth function $\chi(\boldsymbol{S})$ under a local gauge transformation. Such a gauge transformation

$$|\psi_0(\boldsymbol{S})\rangle \to |\psi_0'(\boldsymbol{S})\rangle = e^{i\chi(\boldsymbol{S})}|\psi_0(\boldsymbol{S})\rangle \tag{4.14}$$

$$\boldsymbol{C}_m(\boldsymbol{S}) \to \boldsymbol{C}_m'(\boldsymbol{S}) = \boldsymbol{C}_m(\boldsymbol{S}) - \frac{\partial\chi(\boldsymbol{S})}{\partial \boldsymbol{S}_m} \tag{4.15}$$

is local in the sense that the phase $\chi(\boldsymbol{S})$ is a smooth function of the impurity degrees of

freedom. The spin Berry curvature $\boldsymbol{\Omega}$, on the other hand, is gauge invariant. Elements of $\boldsymbol{\Omega}$ are

$$\begin{aligned}\Omega_{q\alpha,r\beta}(\boldsymbol{S}) =& \frac{\partial C_{r\beta}(\boldsymbol{S})}{\partial S_{q\alpha}} - \frac{\partial C_{q\alpha}(\boldsymbol{S})}{\partial S_{r\beta}} \\ =& i\frac{\partial\langle\psi_0|}{\partial S_{q\alpha}}\frac{\partial|\psi_0\rangle}{\partial S_{r\beta}} - i\frac{\partial\langle\psi_0|}{\partial S_{r\beta}}\frac{\partial|\psi_0\rangle}{\partial S_{q\alpha}} \\ =& i\sum_{n\neq 0}\frac{\langle\psi_0|\nabla_{q\alpha}\hat{H}|\psi_n\rangle\langle\psi_n|\nabla_{r\beta}\hat{H}|\psi_0\rangle - \langle\psi_0|\nabla_{r\beta}\hat{H}|\psi_n\rangle\langle\psi_n|\nabla_{q\alpha}\hat{H}|\psi_0\rangle}{(E_n-E_0)^2} \\ =& -2\,\mathrm{Im}\sum_{n\neq 0}\frac{\langle\psi_0|\nabla_{q\alpha}\hat{H}|\psi_n\rangle\langle\psi_n|\nabla_{r\beta}\hat{H}|\psi_0\rangle}{(E_n-E_0)^2},\end{aligned} \tag{4.16}$$

with $\alpha,\beta \in \{x,y,z\}$, impurity labels q,r and $\frac{\partial}{\partial S_{q\alpha}} = \nabla_{q\alpha}$. In his work [33] Michael Berry uses a generalization of the Hellmann-Feynman theorem [129, 130] to rewrite the derivatives of the eigenstates in the Berry-curvature in terms of derivatives of the Hamiltonian. The same idea can straight forwardly be adapted to our derivatives of the ground state using $\langle\psi_m|\nabla\psi_n\rangle = \frac{\langle\psi_m|\nabla\hat{H}|\psi_n\rangle}{E_m-E_n}\ \forall m\neq n$ (see A.2.2.1). $\boldsymbol{\Omega}$ emerges in the adiabatic equations of motion as shown hereinafter, which leads to measurable effects in the dynamics connected to the topology of the smooth map $\boldsymbol{S}\to|\psi_0(\boldsymbol{S})\rangle$.

By enforcing the adiabatic constraint (eq. 4.12) on the Lagrangian (eq. 4.7), all dynamical quantum degrees of freedom are eliminated. That effective adiabatic theory is derived from

$$\begin{aligned}L_{eff}(\boldsymbol{S},\dot{\boldsymbol{S}}) =& \langle\psi_0(\boldsymbol{S})|i\frac{d}{dt}|\psi_0(\boldsymbol{S})\rangle + \sum_q \boldsymbol{A}(\boldsymbol{m}_q)\dot{\boldsymbol{S}}_q \\ & - \langle\psi_0(\boldsymbol{S})|\hat{H}(\boldsymbol{S})|\psi_0(\boldsymbol{S})\rangle - \sum_q \lambda_q(\boldsymbol{m}_q^2-1)\end{aligned} \tag{4.17}$$

in a similar fashion as the purely classical adiabatic spin dynamics in section 3.1.1. Details of the quantum-classical derivation are presented in A.2.2, which lead to the implicit formulation of the quantum classical adiabatic equation of motion given by

$$\dot{\boldsymbol{m}}_r = \frac{\partial\langle\hat{H}\rangle_0}{\partial\boldsymbol{m}_r}\times\boldsymbol{m}_r - \sum_{q\alpha\mu\lambda\kappa}\Omega_{r\mu,q\alpha}m_{r\lambda}\dot{m}_{q\alpha}\varepsilon_{\mu\lambda\kappa}\boldsymbol{e}_\kappa. \tag{4.18}$$

Here, we utilized $\boldsymbol{S}_q = S_q\boldsymbol{m}_q$ and set $S_q = 1$. Defining a tensor $T_{r\kappa,q\alpha} := \sum_{\mu\lambda}\Omega_{r\mu,q\alpha}m_{r\lambda}\varepsilon_{\mu\lambda\kappa}$ analogue to the classical case, the equations of motion can be formulated in an explicit form. The explicit adiabatic equation of motion

$$\dot{\boldsymbol{m}} = (\mathbf{1}+\boldsymbol{T})^{-1}\cdot\left(\langle\psi_0|\frac{\partial\hat{H}}{\partial\boldsymbol{m}}|\psi_0\rangle\times\boldsymbol{m}\right) \tag{4.19}$$

involves the inversion of the matrix $\mathbf{1} + \boldsymbol{T}$, which is generally time-dependent and has dimensions of $3N_S \times 3N_S$, where N_S is the number of impurities. Here, the cross product is to be understood impurity-wise, i.e., $(\langle\psi_0|\frac{\partial\hat{H}}{\partial\boldsymbol{m}}|\psi_0\rangle \times \boldsymbol{m})_q = \langle\psi_0|\frac{\partial\hat{H}}{\partial\boldsymbol{m}_q}|\psi_0\rangle \times \boldsymbol{m}_q$. The naive approach to adiabatic spin dynamics

$$\dot{\boldsymbol{m}}_r^N = \frac{\partial\langle\hat{H}\rangle_0}{\partial\boldsymbol{m}_r} \times \boldsymbol{m}_r \tag{4.20}$$

is obtained by imposing the adiabatic constraint $|\psi(t)\rangle = |\psi_0(\boldsymbol{S}(t))\rangle$ on the Hamiltonian. However, deducing impurity equations of motion solely from that constraint Hamiltonian is conceptually incorrect.

4.1.3 – Weak-J Perturbation Theory of the Constraint Equation of Motion and an Effective Impurity Hamiltonian

By specifying the interaction between the impurities and the local magnetic moments of the host and taking the weak coupling limit, we can conduct a more in-depth analysis of the adiabatic equations of motion (eq. 4.18). For the present analysis, we assume the host-impurity interaction to be local to a single lattice site, equal among all impurities and isotropic, thus

$$\hat{H}_{ex} = \sum_{q\alpha,i\beta} J_{q\alpha,i\beta}\hat{s}_{i\beta}S_{q\alpha} = J\sum_q \hat{\boldsymbol{s}}_{i_q}\boldsymbol{S}_q. \tag{4.21}$$

The Hamiltonian $\hat{H} = \hat{H}_Q + \hat{H}_{ex}$ is expressed in terms of a purely quantum mechanical contribution defining the host $\hat{H}_Q$ and a quantum-classical part. Latter terms determine the exchange interaction between local spin operator $\hat{\boldsymbol{s}}_i$ of the host and the classical impurities $\boldsymbol{S}_q$, whereby the q-th impurity couples with coupling strength J to the local spin operator at the i_q-th site of the host lattice. An interaction of this kind leads to an implicit adiabatic equation of motion that reads

$$\dot{\boldsymbol{m}}_r = J\langle\psi_0|\hat{\boldsymbol{s}}_{i_r}|\psi_0\rangle \times \boldsymbol{m}_r + 2J^2 \sum_{q\alpha\mu\lambda\kappa} \mathrm{Im}\sum_{n\neq 0} \frac{\langle\psi_0|\hat{s}_{i_q\alpha}|\psi_n\rangle\langle\psi_n|\hat{s}_{i_r\mu}|\psi_0\rangle}{(E_n - E_0)^2} m_{r\lambda}\dot{m}_{q\alpha}\varepsilon_{\mu\lambda\kappa}\boldsymbol{e}_\kappa. \tag{4.22}$$

Next, we expand the quantum states $|\psi_n\rangle \equiv |\psi_n(\boldsymbol{S})\rangle = |\psi_n^{(0)}\rangle + |\psi_n^{(1)}(\boldsymbol{S})\rangle + ...$ in orders of J. In this notion, $|\psi_0^{(0)}\rangle$ is the free ($J = 0$) ground state of the host system, which is naturally independent of the impurities. Corrections to that free ground state to the first order in J are $|\psi_0^{(1)}(\boldsymbol{S})\rangle = \sum_{n\neq 0}|\psi_n^{(0)}\rangle \frac{\langle\psi_n^{(0)}|J\sum_q \hat{\boldsymbol{s}}_{i_q}\boldsymbol{S}_q|\psi_0^{(0)}\rangle}{E_0^{(0)} - E_n^{(0)}}$.

The Hamiltonian part of equation 4.18 can therefore be expanded to

$$\begin{aligned}\langle\psi_0|\frac{\partial\hat{H}}{\partial\boldsymbol{S}_r}|\psi_0\rangle =& J\langle\psi_0^{(0)}|\hat{\boldsymbol{s}}_{i_r}|\psi_0^{(0)}\rangle + J^2\sum_{q,n\neq 0}\langle\psi_0^{(0)}|\hat{\boldsymbol{s}}_{i_r}|\psi_n^{(0)}\rangle\frac{\langle\psi_n^{(0)}|\hat{\boldsymbol{s}}_{i_q}|\psi_0^{(0)}\rangle\boldsymbol{S}_q}{E_0^{(0)}-E_n^{(0)}}\\ &+ J^2\sum_{q,n\neq 0}\langle\psi_n^{(0)}|\hat{\boldsymbol{s}}_{i_r}|\psi_0^{(0)}\rangle\frac{\langle\psi_0^{(0)}|\hat{\boldsymbol{s}}_{i_q}|\psi_n^{(0)}\rangle\boldsymbol{S}_q}{E_0^{(0)}-E_n^{(0)}} + \mathcal{O}(J^3)\\ =& J\langle\psi_0^{(0)}|\hat{\boldsymbol{s}}_{i_r}|\psi_0^{(0)}\rangle + 2J^2\mathrm{Re}\sum_{q\alpha,n\neq 0}\frac{\langle\psi_0^{(0)}|\hat{s}_{i_q\alpha}|\psi_n^{(0)}\rangle\langle\psi_n^{(0)}|\hat{\boldsymbol{s}}_{i_r}|\psi_0^{(0)}\rangle}{E_0^{(0)}-E_n^{(0)}}S_{q\alpha} + \mathcal{O}(J^3).\end{aligned} \tag{4.23}$$

Here, we have explicitly specified terms up to the second order in J, with higher orders being comprised in $\mathcal{O}(J^3)$. The non-Hamiltonian part of the adiabatic equation of motion is, however, already of second order in J. Thus, only the 0-th order expansion of quantum states is involved, i.e, solely quantum states of the free host contribute up to the second order in J. The resulting adiabatic equation of motion in weak-J perturbation theory reads

$$\begin{aligned}\dot{\boldsymbol{m}}_r =& J\langle\psi_0^{(0)}|\hat{\boldsymbol{s}}_{i_r}|\psi_0^{(0)}\rangle\times\boldsymbol{m}_r\\ &+ 2J^2\sum_{q\alpha\mu\lambda\kappa}\mathrm{Re}\sum_{n\neq 0}\frac{\langle\psi_0^{(0)}|\hat{s}_{i_q\alpha}|\psi_n^{(0)}\rangle\langle\psi_n^{(0)}|\hat{s}_{i_r\mu}|\psi_0^{(0)}\rangle}{E_0^{(0)}-E_n^{(0)}}m_{r\lambda}m_{q\alpha}\varepsilon_{\mu\lambda\kappa}\boldsymbol{e}_\kappa\\ &+ 2J^2\sum_{q\alpha\mu\lambda\kappa}\mathrm{Im}\sum_{n\neq 0}\frac{\langle\psi_0^{(0)}|s_{i_q\alpha}|\psi_n^{(0)}\rangle\langle\psi_n^{(0)}|s_{i_r\mu}|\psi_0^{(0)}\rangle}{(E_0^{(0)}-E_n^{(0)})^2}m_{r\lambda}\dot{m}_{q\alpha}\varepsilon_{\mu\lambda\kappa}\boldsymbol{e}_\kappa + \mathcal{O}(J^3).\end{aligned} \tag{4.24}$$

In the weak coupling limit, the spin Berry curvature, which leads to the geometric spin torque in the impurity dynamics, becomes independent of the classical impurities and is a host-system only quantity up to $\mathcal{O}(J^2)$.

Moreover one can relate the retarded magnetic spin susceptibility [48, 86] of the free host

$$\chi_{i\alpha,j\beta}(t) = -i\Theta(t)e^{-\eta t}\langle[\hat{s}_{i\alpha}(t),\hat{s}_{j\beta}(0)]\rangle_0^{(0)} \tag{4.25}$$

to equation 4.24. Here, Θ is the Heaviside step function, η a positive infinitesimal and $\langle..\rangle_0^{(0)}$ denotes the expectation value with the free ($J=0$) ground state of the host. Next, we assume the local magnetic moments of the host system to evolve under the free quantum Hamiltonian only, since we aim for a 0-th order in J expression to be related to the adiabatic equation of motion. Accordingly, one obtains $\hat{s}_{i\alpha}(t) = e^{i\hat{H}_Q t}\hat{s}_{i\alpha}(0)e^{-i\hat{H}_Q t}$ with $\hat{H}_Q = \hat{H}\big|_{J=0}$. Noting, that $|\psi_n^{(0)}\rangle$ form an orthogonal basis of eigenstates to $\hat{H}_Q$ with eigenvalues $E_n^{(0)}$, we can express unity as $\sum_n|\psi_n^{(0)}\rangle\langle\psi_n^{(0)}|$. With this, we expand

the commutator in equation 4.24 and insert this representation of unity to obtain

$$\begin{aligned}\chi_{i\alpha,j\beta}(t) =& -i\Theta(t)e^{-\eta t}e^{i(E_0^{(0)}-E_n^{(0)})t}\sum_{n\neq 0}\langle\psi_0^{(0)}|\hat{s}_{i\alpha}(0)|\psi_n^{(0)}\rangle\langle\psi_n^{(0)}|\hat{s}_{j\beta}(0)|\psi_0^{(0)}\rangle \\ &+ i\Theta(t)e^{-\eta t}e^{i(E_n^{(0)}-E_0^{(0)})t}\sum_{n\neq 0}\langle\psi_0^{(0)}|\hat{s}_{j\beta}(0)|\psi_n^{(0)}\rangle\langle\psi_n^{(0)}|\hat{s}_{i\alpha}(0)|\psi_0^{(0)}\rangle. \end{aligned} \tag{4.26}$$

Notably, $n = 0$ terms cancel out. Fourier transformation of the retarded magnetic spin susceptibility now yields

$$\begin{aligned}\chi_{i\alpha,j\beta}(\omega) =& \int_{-\infty}^{\infty} dt e^{i\omega t}\chi_{i\alpha,j\beta}(t) \\ =& \sum_{n\neq 0}\left(\frac{\langle\psi_0^{(0)}|\hat{s}_{i\alpha}|\psi_n^{(0)}\rangle\langle\psi_n^{(0)}|\hat{s}_{j\beta}|\psi_0^{(0)}\rangle}{i\eta+\omega-E_n^{(0)}+E_0^{(0)}} - \frac{\langle\psi_0^{(0)}|\hat{s}_{j\beta}|\psi_n^{(0)}\rangle\langle\psi_n^{(0)}|\hat{s}_{i\alpha}|\psi_0^{(0)}\rangle}{i\eta+\omega+E_n^{(0)}-E_0^{(0)}}\right), \end{aligned} \tag{4.27}$$

where the positive infinitesimal η can be neglected for gapped systems. Next, we evaluate

$$\chi_{i\alpha,j\beta}(0) = -2\mathrm{Re}\sum_{n\neq 0}\frac{\langle\psi_0^{(0)}|\hat{s}_{i\alpha}|\psi_n^{(0)}\rangle\langle\psi_n^{(0)}|\hat{s}_{j\beta}|\psi_0^{(0)}\rangle}{E_n^{(0)}-E_0^{(0)}}, \tag{4.28}$$

$$\left.\frac{\partial\chi_{i\alpha,j\beta}(\omega)}{\partial\omega}\right|_{\omega=0} = -2i\mathrm{Im}\sum_{n\neq 0}\frac{\langle\psi_0^{(0)}|\hat{s}_{i\alpha}|\psi_n^{(0)}\rangle\langle\psi_n^{(0)}|\hat{s}_{j\beta}|\psi_0^{(0)}\rangle}{(E_0^{(0)}-E_n^{(0)})^2}, \tag{4.29}$$

which can be linked to equation 4.24. Comparing the latter expressions (eq. 4.29) with the weak coupling expansion of the spin Berry curvature (see eq. 4.24) we recognize

$$\begin{aligned}\Omega_{q\alpha,r\beta}(\boldsymbol{S}) =& \Omega_{q\alpha,r\beta}^{(0)} + \mathcal{O}(J^3) = -iJ^2\left.\frac{\partial\chi_{i_q\alpha,i_r\beta}(\omega)}{\partial\omega}\right|_{\omega=0} + \mathcal{O}(J^3) \\ =& -2J^2\mathrm{Im}\sum_{n\neq 0}\frac{\langle\psi_0^{(0)}|\hat{s}_{i\alpha}|\psi_n^{(0)}\rangle\langle\psi_n^{(0)}|\hat{s}_{j\beta}|\psi_0^{(0)}\rangle}{(E_0^{(0)}-E_n^{(0)})^2} + \mathcal{O}(J^3). \end{aligned} \tag{4.30}$$

Thus, the adiabatic equation of motion in the weak coupling limit can be formulated as:

$$\begin{aligned}\dot{\boldsymbol{m}}_r =& J\langle\psi_0^{(0)}|\hat{\boldsymbol{s}}_{i_r}|\psi_0^{(0)}\rangle\times\boldsymbol{m}_r \\ &+ J^2\sum_{q\alpha\mu\lambda\kappa}\chi_{i_q\alpha,i_r\mu}(0)m_{r\lambda}m_{q\alpha}\varepsilon_{\mu\lambda\kappa}\boldsymbol{e}_\kappa \\ &- iJ^2\sum_{q\alpha\mu\lambda\kappa}\left.\frac{\partial\chi_{i_q\alpha,i_r\beta}(\omega)}{\partial\omega}\right|_{\omega=0} m_{r\lambda}\dot{m}_{q\alpha}\varepsilon_{\mu\lambda\kappa}\boldsymbol{e}_\kappa + \mathcal{O}(J^3). \end{aligned} \tag{4.31}$$

Accordingly, the spin Berry curvature can be seen as the linear magnetic response of the quantum host system due to a slow time-dependent perturbation [48]. Here,

the perturbation is caused by the classical impurities, which have to be slow in the sense that the quantum system adiabatically follows the time evolution of these classical degrees of freedom. The spin Berry curvature is interpreted as the first nontrivial correction to the unperturbed ($J\langle\psi_0^{(0)}|\hat{\boldsymbol{s}}_{i_r}|\psi_0^{(0)}\rangle \times \boldsymbol{m}_r$) and static perturbation ($J^2\sum_{q\alpha\mu\lambda\kappa}\chi_{i_q\alpha,i_r\beta}(0)m_{r\lambda}m_{q\alpha}\varepsilon_{\mu\lambda\kappa}\boldsymbol{e}_\kappa$) of the dynamics where J sets the timescale. Notably this dynamic correction comes with the same order in J as the static perturbation.

Commonly, the second term of eq. 4.31 is written in terms of a linear response of the quantum host to some external perturbation. In the adiabatic limit that response is in fact instantaneous ($\omega = 0$) and therefore referred to as the static perturbation. Some classical magnetic perturbation $\boldsymbol{S}_q$ coupling with interaction strength J to the local magnetic moment $\langle s_{i_q}\rangle$ of the quantum host causes a response of the quantum system at site i_r mediated via the magnetic susceptibility. As that response is instantaneous in the adiabatic limit, it is described by $\chi_{i_r\beta,i_q\alpha}(\omega = 0)$. With $\langle s_{i_r\beta}\rangle_0^{(0)}$ as the local magnetic moment of the unperturbed $(...^{(0)})$ host in its ground state $(..._0)$ we expand

$$\langle s_{i_r\beta}\rangle = \langle s_{i_r\beta}\rangle_0^{(0)} + J\sum_{q\alpha}\chi_{i_r\beta,i_q\alpha}(0)S_{q\alpha} + \mathcal{O}(J^2). \tag{4.32}$$

On that account, the exchange interaction up to second order in J can be expressed as

$$\begin{aligned} H_{ex} =& J\sum_q \langle\hat{\boldsymbol{s}}_{i_q}\rangle\boldsymbol{S}_q \\ =& J\sum_q \langle\hat{\boldsymbol{s}}_{i_q}\rangle_0^{(0)}\boldsymbol{S}_q + J^2\sum_{q\alpha,r\beta}\chi_{i_q\alpha,i_r\beta}(0)S_{r\beta}S_{q\alpha} + \mathcal{O}(J^3) \\ =& J\sum_q \langle\hat{\boldsymbol{s}}_{i_q}\rangle_0^{(0)}\boldsymbol{S}_q + \sum_{qr}J^{RKKY}_{q\alpha,r\beta}S_{r\beta}S_{q\alpha} + \mathcal{O}(J^3) \end{aligned} \tag{4.33}$$

with $J^{RKKY}_{q\alpha,r\beta} := J^2\chi_{i_q\alpha,i_r\beta}(0)$ [73–75,86]. Since $\chi_{i_q\alpha,i_r\beta}(0) = \chi_{i_r\beta,i_q\alpha}(0)$ is implied by eq. 4.28, the RKKY-coupling constant is invariant under exchange of its indices. For spin-rotation invariant quantum systems the magnetic susceptibility is furthermore diagonal in the spin indices $\chi_{i_r\beta,i_q\alpha}(0) = \chi_{i_r,i_q}(0)\delta_{\alpha\beta}$. Arguments hereto are analogue to those presented in section 4.1.3.1 and in appendix A.2.2.2 for the spin Berry curvature. For host systems that are magnetically unpolarized when not perturbed by impurities ($\langle\hat{s}_{i\alpha}\rangle_0 = 0$), the exchange up to second order in J takes the compact form of

$$H^{RKKY}_{ex} = \sum_{qr}J^{RKKY}_{q,r}\boldsymbol{S}_r\boldsymbol{S}_q, \text{ with } J^{RKKY}_{q,r} := J^2\chi_{i_q,i_r}(0). \tag{4.34}$$

This effective impurity Hamiltonian comprises the host characteristics that account for the indirect impurity interaction into an effective coupling parameter $J^{RKKY}_{q,r}$, similar to the indirect coupling of magnetic moments in metals initially introduced by Ruderman-Kittel-Kasuya-Yosida (RKKY) [73–75]. The dynamics of the impurities due to H^{RKKY}_{ex}

is defined by

$$\dot{\boldsymbol{S}}_q^N = \frac{\partial H_{ex}^{RKKY}}{\partial \boldsymbol{S}_q} \times \boldsymbol{S}_q \tag{4.35}$$

and is referred to as the naive approach to adiabatic spin dynamics, analog to the purely classical case in 3.1.2.1. Naive adiabatic spin dynamics is obtained from a conceptually incorrect approach, that considers the adiabatic constraint solely via the Hamiltonian. This naive approach dismisses the geometrical spin torque obtained by the conceptually correct derivation, where the constraint is coped with in the Lagrangian formalism.

4.1.3.1 $\boldsymbol{\Omega}^{(0)}$ for Spin-Rotation Invariant Host Systems

In the limit of weak exchange between impurities and the host system, the spin Berry curvature $\boldsymbol{\Omega}^{(0)}$ is, up to second order in the host-impurity coupling, a property of the quantum host only (see eq. 4.30). Thus, the spin Berry curvature is expected to be affected by symmetries of the host model.
In the following we evaluate the effect that spin-rotation invariance of the host has on $\boldsymbol{\Omega}^{(0)}$. To this end we recall $\hat{H} = \hat{H}_Q + \hat{H}_{ex}$ and choose $\hat{H}_{ex} = J \sum_q \hat{\boldsymbol{s}}_{i_q} \boldsymbol{S}_q$. First, we define spin rotations on Fock space by the unitary operator $\hat{U} = \hat{U}(\boldsymbol{n}, \varphi) = \exp(-i\hat{\boldsymbol{s}}_T \boldsymbol{n}\varphi)$, which acts as a spin rotation by angle φ around axis $\boldsymbol{n}$ [48]. Components of the total spin $\hat{\boldsymbol{s}}_T = \sum_i \hat{\boldsymbol{s}}_i$ are generators of these rotations. If the quantum Hamiltonian $\hat{H}_Q$ is invariant under spin rotations, i.e., $[\hat{H}_Q, \hat{\boldsymbol{s}}_T] = 0$, its eigenstates $\{|\psi_n^{(0)}\rangle\}$ can simultaneously be chosen as an eigenbasis of $\hat{U}$. Since the norm of the eigenvalues of an unitary operator equals one, we note $\hat{U}|\psi_n^{(0)}\rangle = e^{i\phi_n}|\psi_n^{(0)}\rangle$. Rotations of the spin operator $\hat{s}_{i_q\alpha}$ can also be constructed via the defining SO(3) matrix representation $\boldsymbol{R} = \boldsymbol{R}(\boldsymbol{n}, \varphi)$, thus, spin components transform as $\hat{U}^\dagger \hat{s}_{i_q\alpha} \hat{U} = \sum_{\alpha'} R_{\alpha\alpha'} \hat{s}_{i_q\alpha'}$. By inserting identities $\hat{I} = \hat{U}\hat{U}^\dagger$ in the matrix elements that build up the spin Berry curvature (eq. 4.30) we find

$$\begin{aligned}
&\langle\psi_0^{(0)}|\hat{U}\hat{U}^\dagger \hat{s}_{i\alpha} \hat{U}\hat{U}^\dagger|\psi_n^{(0)}\rangle\langle\psi_n^{(0)}|\hat{U}\hat{U}^\dagger \hat{s}_{j\beta} \hat{U}\hat{U}^\dagger|\psi_0^{(0)}\rangle \\
&= \sum_{\alpha'\beta'} \langle\psi_0^{(0)}|e^{i\phi_0} R_{\alpha\alpha'} \hat{s}_{i\alpha'} e^{-i\phi_n}|\psi_n^{(0)}\rangle\langle\psi_n^{(0)}|e^{i\phi_n} \hat{s}_{j\beta'} R^T_{\beta'\beta} e^{-i\phi_0}|\psi_0^{(0)}\rangle \\
&= \sum_{\alpha'\beta'} R_{\alpha\alpha'} \langle\psi_0^{(0)}|\hat{s}_{i\alpha'}|\psi_n^{(0)}\rangle\langle\psi_n^{(0)}|\hat{s}_{j\beta'}|\psi_0^{(0)}\rangle R^T_{\beta'\beta}.
\end{aligned} \tag{4.36}$$

Consequently, $\left(\boldsymbol{\Omega}_{ij}^{(0)}\right)_{\alpha\beta} = \Omega^{(0)}_{i\alpha,j\beta} = \sum_{\alpha'\beta'} R_{\alpha\alpha'} \Omega^{(0)}_{i\alpha',j\beta'} R^T_{\beta'\beta}$ is true since $\boldsymbol{R}^T = \boldsymbol{R}^{-1}$, which expressed in matrix notion takes the form $[\boldsymbol{R}, \boldsymbol{\Omega}_{ij}^{(0)}] = 0$. The defining representation of a group, however, is always irreducible, so due to the vanishing commutator and irreducibility of $\boldsymbol{R}$ we find $\Omega^{(0)}_{i\alpha,j\beta} = \Omega^{(0)}_{ij}\delta_{\alpha\beta}$ as a result of Schur's lemma [48, 94, 131] (see appendix A.2.2.2 for an alternative derivation without the use of Schur's lemma).

Recapitulating, we just showed that host Hamiltonians $\hat{H}_Q$ which are invariant under spin rotations lead to spin-diagonal blocks $\mathbf{\Omega}_{ij}^{(0)} = \Omega_{ij}^{(0)}\mathbf{1}$ in the spin Berry curvature as long as impurities couple sufficiently weak to the quantum host. Furthermore, the spin Berry curvature in general is antisymmetric $\Omega_{i\alpha,j\beta} = -\Omega_{j\beta,i\alpha}$ as can easily be seen from its definition in equation 4.16. Hence, $\mathbf{\Omega}_{ij}^{(0)} = -\mathbf{\Omega}_{ji}^{(0)}$ has to be true for spin-rotation invariant host Hamiltonians. Combining the requirements of skew-symmetry and spin-diagonality, the weak coupling spin Berry curvature $\mathbf{\Omega}^{(0)}$ with elements $\Omega_{i\alpha,j\beta}^{(0)}$ takes the form of

$$\mathbf{\Omega}^{(0)} = \Omega \begin{pmatrix} 0 & 1 \\ -1 & 0 \end{pmatrix} \otimes \mathbf{1}_{spin} \tag{4.37}$$

for a setup with two impurities. Spin-diagonality is accounted for by the 3×3 identity matrix $\mathbf{1}_{spin}$, while anti-symmetry has to be ensured by the an impurity-coefficient matrix $\left(\begin{smallmatrix} 0 & 1 \\ -1 & 0 \end{smallmatrix}\right)$ of dimension $N_S \times N_S$. Notably, the entire spin Berry curvature is determined by just a single real number Ω in that case. For a single impurity, however, the combination of anti-symmetry and spin-rotation invariance enforces $\mathbf{\Omega}^{(0)}$ to be zero. Thus, a single impurity interacting with a spin-rotation invariant quantum Hamiltonian can lead to a non-zero spin Berry curvature only beyond the weak coupling limit.

The gained insight in the structure of the spin Berry curvature is not only beneficial for numerical concerns, e.g. as the number of independent components of $\mathbf{\Omega}^{(0)}$ is significantly reduced by exploiting spin-rotation invariance of the host system. Also analytical predictions of the dynamics can become accessible, when the structure of the spin Berry curvature is well understood.

4.1.3.2 Time-Reversal Symmetry and some Motivation to Break it

Turning our attention to time-reversal, we will now explore how it affects the spin Berry curvature. A nontrivial geometric spin torque in the adiabatic spin dynamics (eq. 4.18 and eq. 4.19) demands a non-zero spin Berry curvature. The latter, however, vanishes if time-reversal symmetry is not broken in the setup under consideration. Weak exchange coupling between impurities and host, where the perturbation theory presented in section 4.1.3 is applicable, requires the host model to break time reversal inherently whenever H_{ex} is odd or even under time reversal, which is demonstrated hereinafter. Non-perturbative coupling, on the other hand, breaks time reversal explicitly, since the classical spins can be seen as local magnetic fields. Thus, also time-reversal invariant host models combined with exchange coupling which are symmetric or antisymmteric under time-reversal can lead to finite topological spin torques for exchange interaction beyond the weak coupling limit. When the exchange coupling is linear in the impurity parameters $\boldsymbol{S}$ and for weak coupling strength J, the spin Berry curvature is a property

of the free ($J = 0$) host subsystem only (see eq. 4.30).
To show the necessity of broken time reversal symmetry to obtain finite spin Berry curvatures when the exchange coupling defined by H_{ex} is odd or even under time reversal. We define the anti-unitary time reversal operator $\mathcal{T}$ in Fock space whose action reverses time ($t \mapsto -t$). A system is classified as time reversal invariant if $[\hat{H}, \mathcal{T}] = 0$, which we also referred to as even under time reversal. Impurities $\boldsymbol{S}$ take the role of external parameters to the quantum states in Fock space and are therefore unaffected by $\mathcal{T}$. The spin $\hat{\boldsymbol{s}}$, as an internal angular momentum, is odd under time reversal and flips its sign under time reversal, thus,

$$\mathcal{T}\hat{\boldsymbol{s}}\mathcal{T}^{\dagger} = -\hat{\boldsymbol{s}}. \tag{4.38}$$

Accordingly, the interaction Hamiltonian between impurities and electrons $\hat{H}_{ex} = J\sum_q \boldsymbol{S}_q \hat{\boldsymbol{s}}_{i_q}$ changes sign under the action of $\mathcal{T}$ as well. Time reversal in this case can bee seen as a rotation by π around some arbitrary axis, which we choose to be the y-axis (further can be found in [19,48]). The action of time reversal on the commutator $\mathcal{T}[\hat{x}, \hat{p}] = -i\hbar$, however, requires $\mathcal{T}$ to act as a complex conjugation $\mathcal{K}$ as well, so here the time reversal operator takes the form of $\mathcal{T} = e^{-i\pi \boldsymbol{s}_y}\mathcal{K}$. This explicit form easily illustrates that applying time reversal twice has a fundamentally different effect on a boson than on a fermion. While a rotation by 2π equals the identity ($\mathcal{T}^2 = +1$) for integer spin particles, it results in an additional sign ($\mathcal{T}^2 = -1$) for particles with half-integer spin. Within this thesis we consider host models with non-degenerate ground states, in particular half-filled lattice models with an even number of spin-$\frac{1}{2}$ particles. For these cases the time reversal operator squares to unity ($\mathcal{T}^2 = +1$) and we do not exhibit Kramers degeneracy [19].
For now, we assume the quantum host system to be invariant under time reversal, $[\hat{H}_Q, \mathcal{T}] = 0$. In that case one can choose an orthonormal time-reversal-symmetric (real) basis of eigenstates $|\psi_n^{(0)}\rangle$ to the Hamiltonian, where $\mathcal{T}|\psi_n^{(0)}\rangle = |\psi_n^{(0)}\rangle$ holds for the ground state ($n = 0$) and all excited states ($n > 0$). Next, we consider one of the matrix elements from which $\boldsymbol{\Omega}^{(0)}$ (see eq. 4.16 and eq. 4.30) is constituted. Time reversal invariance yields $\langle\psi_0^{(0)}|\hat{s}_{i\alpha}|\psi_n^{(0)}\rangle = \langle\mathcal{T}\psi_0^{(0)}|\hat{s}_{i\alpha}|\mathcal{T}\psi_n^{(0)}\rangle$. On the other hand, anti-linearity of the time reversal operator $\mathcal{T}$ implies $\langle\mathcal{T}\psi_0^{(0)}|\hat{s}_{i\alpha}|\mathcal{T}\psi_n^{(0)}\rangle = \big(\langle\psi_0^{(0)}|\mathcal{T}^{\dagger}\hat{s}_{i\alpha}\mathcal{T}|\psi_n^{(0)}\rangle\big)^*$ [48, 132] which leads to

$$\langle\psi_0^{(0)}|\hat{s}_{i\alpha}|\psi_n^{(0)}\rangle = -\big(\langle\psi_0^{(0)}|\hat{s}_{i\alpha}|\psi_n^{(0)}\rangle\big)^*. \tag{4.39}$$

Consequently, the matrix element has to be purely imaginary, i.e., $\langle\psi_0^{(0)}|\hat{s}_{i\alpha}|\psi_n^{(0)}\rangle \in i\mathbb{R}$, which is analogously true for $\langle\psi_n^{(0)}|\hat{s}_{i\alpha}|\psi_0^{(0)}\rangle$. As $\Omega^{(0)}_{q\alpha,r\beta}$ is constructed from summands containing $\mathrm{Im}\big(\langle\psi_0^{(0)}|\hat{s}_{i\alpha}|\psi_n^{(0)}\rangle\langle\psi_n^{(0)}|\hat{s}_{j\beta}|\psi_0^{(0)}\rangle\big)$ (eq. 4.30), our demonstration establishes that the spin Berry curvature and the associated geometrical spin torque vanish in the

weak coupling regime for time-reversal-invariant host systems when the host-impurity exchange $\hat{H}_{ex}$ is odd under time reversal.

The same result holds for $\hat{H}_{ex}$ that are even under time reversal as can easily be seen from an exemplary exchange coupling $\hat{H}_{ex} = \sum_q \boldsymbol{S}_q \hat{\boldsymbol{h}}_q^+(\hat{\boldsymbol{s}})$ with some operator $\hat{\boldsymbol{h}}_q^+(\hat{\boldsymbol{s}})$ that is even under time reversal ($\mathcal{T}\hat{\boldsymbol{h}}_q^+\mathcal{T}^\dagger = \hat{\boldsymbol{h}}_q^+$). In this case $\langle\psi_0^{(0)}|\hat{h}_{q\alpha}^+|\psi_n^{(0)}\rangle = \big(\langle\psi_0^{(0)}|\hat{h}_{q\alpha}^+|\psi_n^{(0)}\rangle\big)^*$ is true, requiring the matrix elements to be real ($\langle\psi_0^{(0)}|\hat{h}_{q\alpha}^+|\psi_n^{(0)}\rangle \in \mathbb{R}$), which results in trivial spin Berry curvatures as well. One could envision an adaptation of the Dzyaloshinsky-Moriya interaction [133, 134] with $\hat{\boldsymbol{h}}_q^+(\hat{\boldsymbol{s}}) = \sum_{i,j} D_{q,ij}\hat{\boldsymbol{s}}_i \times \hat{\boldsymbol{s}}_j$ as a potential candidate that couples to the impurities which is even under time reversal.

If, however, the exchange coupling is neither even nor odd under time reversal ($\mathcal{T}\hat{H}_{ex}\mathcal{T}^\dagger \neq \pm\hat{H}_{ex}$), a finite spin Berry curvature can, even in the weak coupling limit, be obtained for time reversal symmetric host systems. Exemplary hereto one can imagine a linear combination of some exchange contribution $\hat{\boldsymbol{h}}_q^+(\hat{\boldsymbol{s}})$ that is even and some exchange contribution $\hat{\boldsymbol{h}}_q^-(\hat{\boldsymbol{s}})$ that is odd ($\mathcal{T}\hat{\boldsymbol{h}}_q^-\mathcal{T}^\dagger = -\hat{\boldsymbol{h}}_q^-$) under time reversal (e.g. $\hat{\boldsymbol{h}}_q^-(\hat{\boldsymbol{s}}) = \sum_i J_{q,i}\hat{\boldsymbol{s}}_i$). Assuming $\hat{H}_{ex} = \sum_q \boldsymbol{S}_q\big(\hat{\boldsymbol{h}}_q^+(\hat{\boldsymbol{s}}) + \hat{\boldsymbol{h}}_q^-(\hat{\boldsymbol{s}})\big)$ and utilizing the time reversal invariance of $|\psi_0^{(0)}\rangle$ and $|\psi_n^{(0)}\rangle$ ($n > 0$) as well as the anti-linearity of the time reversal operator we obtain

$$\begin{aligned}\langle\psi_0^{(0)}|\frac{\partial\hat{H}_{ex}}{\partial S_{q\alpha}}|\psi_n^0\rangle =& \langle\psi_0^{(0)}|\hat{\boldsymbol{h}}_{q\alpha}^+|\psi_n^{(0)}\rangle + \langle\psi_0^{(0)}|\hat{\boldsymbol{h}}_{q\alpha}^-|\psi_n^{(0)}\rangle \\ =& \Big(\langle\psi_0^{(0)}|\hat{\boldsymbol{h}}_{q\alpha}^+|\psi_n^{(0)}\rangle - \langle\psi_0^{(0)}|\hat{\boldsymbol{h}}_{q\alpha}^-|\psi_n^{(0)}\rangle\Big)^* \\ =& a_{q\alpha}^{0n} + ib_{q\alpha}^{0n}, \quad a_{q\alpha}^{0n}, b_{q\alpha}^{0n} \in \mathbb{R} \end{aligned} \tag{4.40}$$

with $a_{q\alpha}^{0n} = \langle\psi_0^{(0)}|\hat{\boldsymbol{h}}_{q\alpha}^+|\psi_n^{(0)}\rangle$ and $ib_{q\alpha}^{0n} = \langle\psi_0^{(0)}|\hat{\boldsymbol{h}}_{q\alpha}^-|\psi_n^{(0)}\rangle$. The spin Berry curvature is formed by terms containing

$$\begin{aligned}-\mathrm{Im}\big(\langle\psi_0^{(0)}|\frac{\partial\hat{H}_{ex}}{\partial S_{q\alpha}}|\psi_n^0\rangle\langle\psi_n^{(0)}|\frac{\partial\hat{H}_{ex}}{\partial S_{r\beta}}|\psi_0^0\rangle\big) &= \mathrm{Im}\big((a_{q\alpha}^{0n} + ib_{q\alpha}^{0n})(a_{r\beta}^{n0} + ib_{r\beta}^{n0})\big) \\ &= i\langle\psi_0^{(0)}|\hat{\boldsymbol{h}}_{q\alpha}^+|\psi_n^{(0)}\rangle\langle\psi_n^{(0)}|\hat{\boldsymbol{h}}_{r\beta}^-|\psi_0^{(0)}\rangle \\ &\quad + i\langle\psi_0^{(0)}|\hat{\boldsymbol{h}}_{q\alpha}^-|\psi_n^{(0)}\rangle\langle\psi_n^{(0)}|\hat{\boldsymbol{h}}_{r\beta}^+|\psi_0^{(0)}\rangle. \end{aligned} \tag{4.41}$$

These terms generally have non-zero values. Thus, one can in general obtain a finite spin Berry curvature in the weak coupling limit even when the host system is time-reversal symmetric.

As demonstrated, an exchange coupling that is just odd or even under time reversal demands a host system that breaks time reversal symmetry to possibly feature a finite spin Berry curvature in the weak coupling limit. One canonical choice of the exchange interaction is to locally couple the impurities to the local magnetic moments of the host, $\hat{H}_{ex} = J\sum_q \boldsymbol{S}_q\hat{\boldsymbol{s}}_{i_q}$, which is odd under time reversal. Beyond the weak coupling

limit the classical impurities break time reversal explicitly.

4.1.3.3 Analytical Exploration of the Adiabatic Dynamics of Two Impurities in the Weak-J Limit

Without external magnetic fields a minimum of two impurities is required to initiate nontrivial dynamics. We assume applicability of the adiabatic theorem, so the host system is assumed to be in its ground state to the impurity configuration at all times. A setup involving two classical impurities coupled to a quantum-mechanical host is prototypical for assessing the fundamental characteristics of adiabatic spin dynamics, which is analytically studied in this section. Here, we discuss the limit of weak and local exchange interaction J, so taking terms up to $\mathcal{O}(J^2)$ into account is sufficient. We assume a host of zero total magnetic moment, which leads to an impurity only formulation of the dynamics for small J.

The adiabatic equation of motion (eq. 4.19) in its explicit form is recalled as the matrix product of $(\mathbf{1}+\boldsymbol{T})^{-1}$ with $T_{r\kappa,q\alpha} := \sum_{\mu\lambda} \Omega_{r\mu,q\alpha} m_{r\lambda} \varepsilon_{\mu\lambda\kappa}$ and the constraint Hamiltonian dynamics. The latter, also referred to as naive adiabatic dynamics, originates from an effective Hamiltonian, which takes the form of $H_{ex}^{RKKY} = \sum_{qr} J_{q,r}^{RKKY} \boldsymbol{S}_r \boldsymbol{S}_q$ (eq. 4.34) for host systems that do not feature local magnetic moments in their free ground state and which are invariant under spin rotations (see section 4.1.3). As a consequence of the spin rotation invariance of the host model combined with the general symmetry of $\boldsymbol{\chi}(\omega = 0)$ (eq. 4.28) in a setup of only two impurities, the effective impurity coupling has to be symmetric under exchange of the impurity labels. Thus, $J_{1,2}^{RKKY} = J_{2,1}^{RKKY} = J^{RKKY}$ is noted. The effective Hamiltonian yields the naive adiabatic dynamics

$$\dot{\boldsymbol{m}}_q^N = \frac{\partial H_{ex}^{RKKY}}{\partial \boldsymbol{m}_q} \times \boldsymbol{m}_q. \tag{4.42}$$

For now, we consider impurities $\boldsymbol{S}_q = S_q \boldsymbol{m}_q$ of magnitude one ($\boldsymbol{S}_q^2 = 1 \, \forall q$), but generalization to arbitrary impurity magnitudes is straight forward.

Since we assume spin rotational invariance of the free ($J = 0$) host model, so $\boldsymbol{\Omega}^{(0)}$ takes the generic form of equation 4.37. Utilizing that predetermined structure of $\boldsymbol{\Omega}^{(0)}$ and $\boldsymbol{J}^{RKKY}$ the adiabatic equations of motion for two impurities up to $\mathcal{O}(J^2)$ take the from

$$\begin{pmatrix} \dot{\boldsymbol{m}}_1^{(0)} \\ \dot{\boldsymbol{m}}_2^{(0)} \end{pmatrix} = (\mathbf{1} + \boldsymbol{T}^{(0)})^{-1} \begin{pmatrix} \dot{\boldsymbol{m}}_1^N \\ \dot{\boldsymbol{m}}_2^N \end{pmatrix} = (\mathbf{1} + \boldsymbol{T}^{(0)})^{-1} \begin{pmatrix} J^{RKKY} \boldsymbol{m}_2 \times \boldsymbol{m}_1 \\ J^{RKKY} \boldsymbol{m}_1 \times \boldsymbol{m}_2 \end{pmatrix} \tag{4.43}$$

with

$$\boldsymbol{T}^{(0)} = \Omega \begin{pmatrix} \mathbf{0} & \boldsymbol{\mathcal{M}}_1 \\ -\boldsymbol{\mathcal{M}}_2 & \mathbf{0} \end{pmatrix} \text{ and } \boldsymbol{\mathcal{M}}_q = \sum_\alpha \boldsymbol{\mathcal{R}}_\alpha m_{q\alpha} = \begin{pmatrix} 0 & -m_{qz} & m_{qy} \\ m_{qz} & 0 & -m_{qx} \\ -m_{qy} & m_{qx} & 0 \end{pmatrix}. \quad (4.44)$$

The $\boldsymbol{\mathcal{R}}_\alpha$ are the generators of rotations in three dimensions and an explicit representation is given in equation A.15. We point out that $\boldsymbol{\mathcal{M}}_q \boldsymbol{m}_r$ is nothing but a matrix-vector product representation for $\boldsymbol{m}_q \times \boldsymbol{m}_r$. To finally obtain an explicit analytical adiabatic equation of motion we need to invert $\mathbf{1} + \boldsymbol{T}^{(0)}$, which requires its determinant

$$\begin{aligned} \det\left(\mathbf{1} + \boldsymbol{T}^{(0)}\right) =& \det\left(\mathbf{1} + \Omega^2 \boldsymbol{\mathcal{M}}_2 \boldsymbol{\mathcal{M}}_1\right) \\ =& 1 - 2\Omega^2 \boldsymbol{m}_1 \boldsymbol{m}_2 + \Omega^4 (\boldsymbol{m}_1 \boldsymbol{m}_2)^2 \end{aligned} \quad (4.45)$$

to be non-zero. Thus, the required matrix inversion can be performed, unless $\Omega^2 \boldsymbol{m}_1 \boldsymbol{m}_2 = 1$. If existing, the analytical inversion results in

$$\left(\mathbf{1} + \boldsymbol{T}^{(0)}\right)^{-1} = \frac{1}{1 - \Omega^2 \boldsymbol{m}_1 \boldsymbol{m}_2} \begin{pmatrix} \mathbf{1} - \Omega^2 \boldsymbol{m}_2 \otimes \boldsymbol{m}_1 & \Omega \boldsymbol{\mathcal{M}}_1 \\ -\Omega \boldsymbol{\mathcal{M}}_2 & \mathbf{1} - \Omega^2 \boldsymbol{m}_1 \otimes \boldsymbol{m}_2 \end{pmatrix}, \quad (4.46)$$

where we denote the outer (dyadic) product of $\boldsymbol{m}_1$ and $\boldsymbol{m}_2$ by $\boldsymbol{m}_1 \otimes \boldsymbol{m}_2$. Evaluating the adiabatic equations of motion by use of the just obtained matrix inverse (eq. 4.46) a set of coupled differential equations is obtained, that is

$$\begin{aligned} \dot{\boldsymbol{m}}_1 =& \frac{J^{RKKY}}{1 - \Omega^2 \boldsymbol{m}_1 \boldsymbol{m}_2} \left[\boldsymbol{m}_2 \times \boldsymbol{m}_1 + \Omega \boldsymbol{m}_1 \times (\boldsymbol{m}_1 \times \boldsymbol{m}_2)\right] \\ \dot{\boldsymbol{m}}_2 =& \frac{J^{RKKY}}{1 - \Omega^2 \boldsymbol{m}_1 \boldsymbol{m}_2} \left[\boldsymbol{m}_1 \times \boldsymbol{m}_2 - \Omega \boldsymbol{m}_2 \times (\boldsymbol{m}_2 \times \boldsymbol{m}_1)\right]. \end{aligned} \quad (4.47)$$

For $\Omega = 0$ the well known RKKY-dynamics (eq. 4.34 and eq. 4.42) is reacquired, where impurities precess around the conserved total spin with frequency $\omega_{prec} = J^{RKKY} |\boldsymbol{m}_1 + \boldsymbol{m}_2|$. Valid non-zero Ω, however, result in dynamics of the total impurity spin $\boldsymbol{m}_T = \boldsymbol{m}_1 + \boldsymbol{m}_2$ itself. Throughout the adiabatic spin dynamics magnitudes $|\boldsymbol{m}_1|$ and $|\boldsymbol{m}_2|$ as well as angle ϑ enclosed by the impurities are conserved for any valid Ω. A non-zero $\dot{\boldsymbol{m}}_T$ can be regarded as a hallmark of the non-Hamiltonian nature of the adiabatic dynamics in our scenario, as it cannot be solely governed by any RKKY-like theory. Yet, we find vector

$$\begin{aligned} \boldsymbol{\Sigma} :=& \boldsymbol{m}_1 + \boldsymbol{m}_2 - \Omega \boldsymbol{m}_1 \times \boldsymbol{m}_2 \\ =& \boldsymbol{m}_T - \Omega \boldsymbol{m}_1 \times \boldsymbol{m}_2 \end{aligned} \quad (4.48)$$

as a constant of motion of the adiabatic spin dynamics in the weak coupling limit.

Impurities as well as the total spin undergo a precession around this axis. The equations of motion (eq. 4.47) can therefore be rewritten in the compact form of $\dot{\boldsymbol{m}}_q = \frac{J^{RKKY}}{1-\Omega \boldsymbol{m}_1 \boldsymbol{m}_2} \boldsymbol{\Sigma} \times \boldsymbol{m}_q$ with $q \in \{1, 2\}$. Thus, the dynamics of the total impurity spin is

$$\begin{aligned} \dot{\boldsymbol{m}}_T =& \frac{J^{RKKY}}{1 - \Omega^2 \boldsymbol{m}_1 \boldsymbol{m}_2} \boldsymbol{\Sigma} \times \boldsymbol{m}_T \\ =& \frac{\Omega J^{RKKY}}{1 - \Omega^2 \boldsymbol{m}_1 \boldsymbol{m}_2} (\boldsymbol{m}_2 \times \boldsymbol{m}_1) \times \boldsymbol{m}_T. \end{aligned} \tag{4.49}$$

Furthermore, the modulus of conserved vector $\boldsymbol{\Sigma}$ determines the precession frequency

$$\omega_{prec} = \sqrt{\boldsymbol{\Sigma}^2} = \sqrt{4 \cos^2(\vartheta/2) + \Omega^2 \sin^2(\vartheta)} \tag{4.50}$$

in the inverse dimensionless timescale $t' = t/\tau$ with τ defined in equation 4.51 and ϑ as the conserved angle enclosed by the impurities. In units of t the precession frequency is thus simply given by $\omega_{prec} = \sqrt{\boldsymbol{\Sigma}^2}/\tau = J^{RKKY}\sqrt{\boldsymbol{\Sigma}^2}/(1 - \Omega \boldsymbol{m}_1 \boldsymbol{m}_2)$. Some further details on conserved quantities in the given setup are presented in A.2.2.3.
Finally, we discuss two qualitative effects finite Ω cause in the impurity dynamics. Firstly, an overall renormalization of the effective RKKY-coupling $J^{RKKY} \mapsto J^{RKKY}/(1 - \Omega^2 \boldsymbol{m}_1 \boldsymbol{m}_2)$ is observed. In essence, this renormalization describes a re-scaling of the timescale of the dynamics by

$$\frac{1}{\tau} := \frac{J^{RKKY}}{1 - \Omega^2 \boldsymbol{m}_1 \boldsymbol{m}_2} = \frac{J^2 \chi_{i_1 i_2}(0)}{1 - \Omega^2 \boldsymbol{m}_1 \boldsymbol{m}_2}. \tag{4.51}$$

For $\Omega^2 \boldsymbol{m}_1 \boldsymbol{m}_2 > 1$ the direction of motion opposes the direction of the naive RKKY-dynamics. Formulating the equations of motion (eq. 4.47) in the dimensionless time scale $t' = t/\tau$ yields

$$\begin{aligned} \frac{d\boldsymbol{m}_1}{dt'} =& \boldsymbol{m}_2 \times \boldsymbol{m}_1 + \Omega (\boldsymbol{m}_2 \times \boldsymbol{m}_1) \times \boldsymbol{m}_1 \\ \frac{d\boldsymbol{m}_2}{dt'} =& \boldsymbol{m}_1 \times \boldsymbol{m}_2 - \Omega (\boldsymbol{m}_1 \times \boldsymbol{m}_2) \times \boldsymbol{m}_2. \end{aligned} \tag{4.52}$$

The just obtained formulation of the adiabatic equations of motion emphasizes the second contribution non-zero Ω cause in the dynamics. That is an additional torque perpendicular to the naive RKKY dynamics (eq. 4.42). This adiabatic spin torque contribution causes the dynamics of $\boldsymbol{m}_T$. We interpret Ω as the coupling strength of e.g. $\boldsymbol{m}_1$ coupling to $\boldsymbol{m}_2 \times \boldsymbol{m}_1 \sim \dot{\boldsymbol{m}}_1^N$ (see 4.52), which leads to the adiabatic spin torque. This torque cannot originate from an effective Hamiltonian $H_{eff}(\boldsymbol{m}_1, \boldsymbol{m}_2)$ and interchanging labels $1 \leftrightarrow 2$ does not lead to an invariant set of equations of motion, but changes the sign of the non-Hamiltonian contribution. That sign changes can be traced back to the anti-symmetry of the spin Berry curvature (see eq. 4.37), which requires $\boldsymbol{\Omega}_{12} = -\boldsymbol{\Omega}_{21}$ in the given scenario of spin-rotation invariant host systems. Both effects

are determined by Ω as well as $\vartheta \sphericalangle \boldsymbol{m}_1, \boldsymbol{m}_2$.

The non-Hamiltonian spin torque can, however, not outweigh the renormalization of the timescale in the limit of large Ω for generic $\vartheta \neq \pi/2$. Furthermore, we observe a critical value of $\Omega_c = 1/\sqrt{\boldsymbol{m}_1 \boldsymbol{m}_2}$. As Ω surpasses Ω_c, the dynamics decelerates until reaching a point of complete cessation in the limit of $\Omega \to \infty$. Comparing dynamics with $\Omega < \Omega_c$ and $\Omega > \Omega_c$, the impurities change the direction of their precessional motion due to a sign change in overall prefactor $J^{RKKY}/(1 - \Omega^2 \boldsymbol{m}_1 \boldsymbol{m}_2)$. An Ω close to Ω_c triggers the strongest renormalization effect, but to ensure a valid application of the adiabatic theorem, the exchange coupling J has to satisfy

$$J^2 \frac{\chi_{i_1 i_2}(0)}{1 - \Omega^2 \boldsymbol{m}_1 \boldsymbol{m}_2} \ll \Delta E, \tag{4.53}$$

with ΔE as the insulating energy gap of the host [48]. Hence, a setup with constant ΔE requires weaker and weaker coupling between impurities and host to assure adiabatic dynamics as Ω approaches Ω_c. For $\Omega = \Omega_c$ the renormlization by τ^{-1} (eq 4.51) diverges for any finite J^{RKKY}, but equations 4.47 and 4.52 do not describe the dynamics correctly in that case. Under the circumstances of $\Omega = \Omega_c = 1/\sqrt{\boldsymbol{m}_1 \boldsymbol{m}_2}$, the theory breaks down as $\det(\mathbf{1} + \boldsymbol{T}^{(0)}) = 0$ in that case, thus, $(\mathbf{1} + \boldsymbol{T}^{(0)})^{-1}$ exploited in equation 4.43 does not exist.

4.1.4 – Strong-J Perturbation Theory of the Constraint Equation of Motion and an Effective Impurity Hamiltonian

In the limit of strong exchange coupling between impurities and host system, local physics dominates the spin Berry curvature. We assume a local and spin-symmetric exchange interaction $\hat{H}_{ex} = \sum_{i\alpha,q\beta} J_{i\alpha,q\beta} \hat{s}_{i\alpha} S_{q\beta} = J \sum_q \hat{\boldsymbol{s}}_{i_q} \boldsymbol{S}_q$ and $|\boldsymbol{S}_q| = 1$. The structure of $\boldsymbol{\Omega}$ changes qualitatively as compared to the previously discussed weak coupling limit. In the weak-J limit, only non-local elements $\Omega^{(0)}_{q\alpha,r\alpha}$ with $q \neq r$ (see eq. 4.37) of the spin Berry curvature are non-zero for spin-diagonal host models. Contrarily, only elements $\Omega_{q\alpha,q\beta}$ of the local blocks are non-zero in the strong coupling limit.

These on-site elements result form an effective local two-spin model $\hat{H}_{2-spin} = J \sum_q \hat{\boldsymbol{s}}_{i_q} \boldsymbol{S}_q$ as the low energy expansion for $J \to \infty$, where $\hat{\boldsymbol{s}}_{i_q}$ is a quantum spin of magnitude $|\hat{\boldsymbol{s}}_{i_q}| = s = 1/2$. The Berry curvature to that two spin model is well known in literature, as it is analog to the prime example of a quantum spin in an external magnetic field that can be solved analytically [19, 47]. To the lowest order, each impurity localizes one electron at the site it couples to the host and the spin Berry curvature takes the

form

$$\boldsymbol{\Omega}^{(\infty)}_{q,r} = \frac{1}{2}\delta_{qr}\sum_{\alpha}\mathcal{R}_{\alpha}S_{q\alpha} = \frac{1}{2}\delta_{qr}\begin{pmatrix} 0 & -S_{qz} & S_{qy} \\ S_{qz} & 0 & -S_{qx} \\ -S_{qy} & S_{qx} & 0 \end{pmatrix}. \tag{4.54}$$

Again, $\mathcal{R}_{\alpha}$ are the generators of spatial rotations in three dimension as defined in equation A.15. In this context of a local two spin model it is convenient to rewrite the on-site blocks of spin Berry curvature tensor in form of the vector $\boldsymbol{\Omega}^{(\infty)}_{q} = (1/2)\sum_{\alpha\beta\gamma}\Omega^{(\infty)}_{q\alpha,q\beta}\boldsymbol{e}_{\gamma}\varepsilon_{\alpha\beta\gamma}$ with $\boldsymbol{e}_{\gamma}$ as the unit vector in $\gamma \in \{x, y, z\}$ direction. That vector takes the form of

$$\boldsymbol{\Omega}^{(\infty)}_{q} = -\frac{1}{2}\frac{\boldsymbol{S}_q}{|\boldsymbol{S}_q|^3} = -\frac{1}{2}\boldsymbol{S}_q \tag{4.55}$$

for $J > 0$. This is nothing but the field generated by a magnetic monopole of magnetic charge $1/2$ at the origin [19,48]. Nontrivial dynamics, however, requires an effective interaction between the impurities, which we again denote by $H_{RKKY} = \sum_{qr} J^{RKKY}_{qr}\boldsymbol{S}_q\boldsymbol{S}_r$ for spin-rotation invariant models. In the strong coupling limit, the indirect magnetic exchange scales as $J^{RKKY} \sim J^{-2}$, which is of second order again, but the proportionality is inverse to the weak coupling limit where $J^{RKKY} \sim J^2$ (see eq. 4.34). The effective Hamiltonian H^{RKKY} yields naive dynamics of the same form as in the weak coupling limit (eq. 4.42), just the coupling constant J^{RKKY} is of a different nature.

Next, we derive an explicit form of the adiabatic equation of motion in the $J \to \infty$ limit by going through the same steps as in subsection 4.1.3.3, but with a spin Berry curvature of the strong coupling form (eq. 4.54). Since we consider local host-impurity exchange interaction, we introduce an abbreviated notation of $\langle \hat{s}_{i_q\alpha}\rangle \equiv s_{q\alpha}$ for the sake of clarity. Matrix $\boldsymbol{T}$ with elements $T_{r\kappa,q\alpha} := \sum_{\mu\lambda}\Omega_{r\mu,q\alpha}m_{r\lambda}\varepsilon_{\mu\lambda\kappa}$ is diagonal in the site indices r, q due to the block-diagonal character of $\Omega_{r,q}$ (see eq. 4.54). The blocks take the form

$$\boldsymbol{T}_{rq} = \delta_{rq}\begin{pmatrix} -s_{qy}S_{qy} - s_{qz}S_{qz} & s_{qx}S_{qy} & s_{qx}S_{qz} \\ s_{qy}S_{qx} & -s_{qx}S_{qx} - s_{qz}S_{qz} & s_{qy}S_{qz} \\ s_{qz}S_{qx} & s_{qz}S_{qy} & -s_{qx}S_{qx} - s_{qy}S_{qy} \end{pmatrix}. \tag{4.56}$$

As determinant of a block diagonal matrix is given by the product of determinants of its diagonal blocks, the overall determinant of $\mathbf{1} + \boldsymbol{T}$ vanishes if the determinant of at least one block $(\mathbf{1} + \boldsymbol{T})_{qq} = \mathbf{1} + \boldsymbol{T}_{qq}$ is zero. These blocks become independent from each other in the strong coupling limit, since $\langle \hat{s}_{i_q\alpha}\rangle$ depends solely on $\boldsymbol{S}_q$ to the lowest nontrivial order in $1/J$. In fact, for $J \to +\infty$ one electron gets not just localized, but also fully polarized at each site that a classical impurity couples to host. Accordingly, $\langle \hat{\boldsymbol{s}}_{i_q}\rangle = -S_q/2$ is exactly antiparallel (parallel for $J \to -\infty$) to the classical spin of its

causation. Accordingly, we find

$$\det(\mathbf{1}+\boldsymbol{T}) = \prod_q \det(\mathbf{1}+\boldsymbol{T}_{qq}) = \prod_q (1+\boldsymbol{s}_q\boldsymbol{S}_q)^2. \tag{4.57}$$

As a single orbital per lattice site is considered, the magnitude of the polarized local magnetic moment at one site of the quantum system is bound by $|\langle\hat{\boldsymbol{s}}_i\rangle| \leq 1/2$. Therefore, the determinant never vanishes in our scenario of $S_q = 1$. If, however, any $\langle\hat{\boldsymbol{s}}_{i_q}\rangle = -\boldsymbol{S}_q$ were to occur, the inversion of $\mathbf{1}+\boldsymbol{T}$ would not be possible since $\det(\mathbf{1}+\boldsymbol{T}) = 0$ in that case. In fact, $\boldsymbol{s}_q\boldsymbol{S}_q = \langle\hat{\boldsymbol{s}}_{i_q}\rangle\boldsymbol{S}_q = -1$ is a condition that is incompatible with the displayed theory of adiabatic spin dynamics.
Next, we invert $\mathbf{1}+\boldsymbol{T}$, which is a straight forward analytically calculation. Similar to the determinant considerations above, the inverse of a block diagonal matrix is obtained by its blockwise inversion, which is derived to be

$$\begin{aligned}\left((\mathbf{1}+\boldsymbol{T})^{-1}\right)_{qq} =& (\mathbf{1}+\boldsymbol{T}_{qq})^{-1} = \frac{1}{1+\boldsymbol{s}_q\boldsymbol{S}_q}\begin{pmatrix} 1+s_{qx}S_{qx} & s_{qx}S_{qy} & s_{qx}S_{qz} \\ s_{qy}S_{qx} & 1+s_{qy}S_{qy} & s_{qy}S_{qz} \\ s_{qz}S_{qx} & s_{qz}S_{qy} & 1+s_{qz}S_{qz}\end{pmatrix} \\ =& \sum_{\alpha\beta}\frac{\delta_{\alpha\beta}+s_{q\alpha}S_{q\beta}}{1+\boldsymbol{s}_q\boldsymbol{S}_q}\boldsymbol{e}_\alpha\otimes\boldsymbol{e}_\beta.\end{aligned} \tag{4.58}$$

Finally, we recombine the naive dynamics and $(\mathbf{1}+\boldsymbol{T})^{-1}$. The explicit adiabatic equations of motion of two impurities strongly coupled to the host in a local and homogeneous way are

$$\begin{aligned}\begin{pmatrix}\dot{\boldsymbol{S}}_1^{(\infty)} \\ \dot{\boldsymbol{S}}_2^{(\infty)}\end{pmatrix} =& (\mathbf{1}+\boldsymbol{T}^{(\infty)})^{-1}\begin{pmatrix}\dot{\boldsymbol{S}}_1^{N} \\ \dot{\boldsymbol{S}}_2^{N}\end{pmatrix} = (\mathbf{1}+\boldsymbol{T}^{(\infty)})^{-1}\begin{pmatrix}J^{RKKY}\boldsymbol{S}_2\times\boldsymbol{S}_1 \\ J^{RKKY}\boldsymbol{S}_1\times\boldsymbol{S}_2\end{pmatrix} \\ =& \begin{pmatrix}\frac{J^{RKKY}\boldsymbol{S}_2\times\boldsymbol{S}_1}{1+\langle\hat{\boldsymbol{s}}_{i_1}\rangle\boldsymbol{S}_1} \\ \frac{J^{RKKY}\boldsymbol{S}_1\times\boldsymbol{S}_2}{1+\langle\hat{\boldsymbol{s}}_{i_2}\rangle\boldsymbol{S}_2}\end{pmatrix} = 2\begin{pmatrix}J^{RKKY}\boldsymbol{S}_2\times\boldsymbol{S}_1 \\ J^{RKKY}\boldsymbol{S}_1\times\boldsymbol{S}_2\end{pmatrix},\end{aligned} \tag{4.59}$$

where the last equality exploits $\langle\hat{\boldsymbol{s}}_{i_q}\rangle = -\boldsymbol{S}_q/2$. The deduced rescaling of the precession frequency $\omega_{prec} = J^{RKKY}|\boldsymbol{S}_1+\boldsymbol{S}_2|/(1+\langle\hat{\boldsymbol{s}}_{i_q}\rangle\boldsymbol{S}_q)$ is a generalization to the strong coupling limit obtained in [47] for a single impurity driven by an external magnetic field. The presented derivation, however, does not assume a single impurity coupled to a linear chain of non-interacting itinerant electrons. It is valid for generic models that fulfill the aforementioned assumptions (e.g. $\langle\hat{\boldsymbol{s}}_{i_q}\rangle\boldsymbol{S}_q \neq -1$) and is universal to an arbitrary number of impurities.

4.1.5 – Technical Realization: Host System States Expressed via Hopping Matrix Eigenstates

To numerically evaluate the dynamics of a quantum-classical hybrid model, may it be the full dynamics of the impurities and the host (section 4.1.1) or dynamics within the adiabatic approximation (section 4.1.2), computation of its eigenstates is required. We obtain them by numerical diagonalization of the (effective) hopping matrix (eq. 4.4). This section provides detailed instructions on the computation of spin expectation values, and it outlines the steps involved in evaluating the spin Berry curvature. We omit $\hat{\cdot}$ as the context resolves the nature of operators.

Since we consider non-interacting quantum systems only, the many body quantum state factorizes into a product of single particle states. These one particle states and energies are labeled by super index k, which comprises wave vector κ (single particle energy level) and spin index σ. The one particle creation operator is denoted by $c_k^\dagger$ and the annihilation operator by $c_k^\dagger$. They obey the fermionic anticommutation relation $[c_k^\dagger, c_{k'}]_+ = \delta_{kk'}$, so single particle states form an orthonormal basis. Accordingly, the many body ground state $|0\rangle$ of N_p particles is

$$|0\rangle = \prod_k c_k^\dagger |vac\rangle = \prod_{\substack{0\leq\kappa<N_p \\ \sigma\in\{\uparrow,\downarrow\}}} c_{\kappa\sigma}^\dagger |vac\rangle, \tag{4.60}$$

where $|vac\rangle$ denotes the vacuum. Single particle states are filled up to the Fermi level labeled by k_F. An excited state $|n_{kk'}\rangle$ can be generated by promoting a particle from the k-th to the k'-th single particle state

$$|n_{kk'}\rangle = c_{k'}^\dagger c_k |0\rangle, \tag{4.61}$$

with $k < k_F$ and $k' \geq k_F$. The set of the ground and all excited states $\{|0\rangle, |n_{kk'}\rangle\}$ form an orthonormal basis for the many body states. Implication of the introduced notion is, that $|n_{kk'}\rangle$ is not the ground state for $k \neq k'$, but for any $k = k' < k_F$ we have $|n_{kk}\rangle = |0\rangle$ and we note $|n_{kk}\rangle = 0$ if $k = k' \geq k_F$.

The effective hopping matrix $\boldsymbol{T}$ (eq. 4.4) is diagonalized by a unitary ($\boldsymbol{U}^{-1} = \boldsymbol{U}^\dagger$) matrix $\boldsymbol{U}$, so $\boldsymbol{U}^\dagger \boldsymbol{T} \boldsymbol{U} = \boldsymbol{\epsilon}$. Diagonal matrix $\boldsymbol{\epsilon}$ contains the single particle eigenenergies ϵ_k, which are the eigenvalues of $\boldsymbol{T}$. The eigenvectors $\boldsymbol{U}_k$ of $\boldsymbol{T}$ form the columns of $\boldsymbol{U}$. For a system of n sites and spin degree $\sigma \in \{\uparrow, \downarrow\}$ per site, $\boldsymbol{U}$ and $\boldsymbol{\epsilon}$ are $2n \times 2n$ matrices. Accordingly, half filling is achieved for $N_p = n$. Aiming for the thermodynamic limit ($n \to \infty$) it is, however, convenient to fix a chemical potential μ instead of a predetermined number of particles. For a given chemical potential the ground state is $|0\rangle = \prod_k \theta(\mu - \epsilon_k) c_k^\dagger |vac\rangle$, where θ is the Heaviside step function. As we consider non-interacting lattice models, the many body ground state is the tensor product of

all single particle states with energies ϵ_k below the chemical potential. Single particle states with $\epsilon_k > \mu$ are unoccupied in the many body ground state. Generically, we assume half filling if not specified otherwise. The aforementioned remarks can, however, serve as a straightforward guide for arbitrary filling.

Moreover, we can use $\boldsymbol{U}$ for a basis transformation from real-space to a single particle energy-level formulation. A formulation in terms of k is convenient [86] to evaluate the one particle reduced density matrix (eq. 4.2) and matrix elements like $\langle n_{kk'}|s_{i\alpha}|0\rangle$. In the preceding consideration sums rum over all possible values of the summation indices if not specified otherwise. The relation between operators in real space and k-space is given by

$$c_{i\sigma} = \sum_k U_{i\sigma,k} c_k \,, \quad c^\dagger_{i\sigma} = \sum_k U^\dagger_{k,i\sigma} c^\dagger_k = \sum_k U^\star_{i\sigma,k} c^\dagger_k. \tag{4.62}$$

Elements $\rho_{i\sigma,i'\sigma'} = \langle \hat{c}^\dagger_{i'\sigma'} \hat{c}_{i\sigma}\rangle$ of the one-particle reduced density matrix are consequently determined by

$$\langle c^\dagger_{i'\sigma'} c_{i\sigma}\rangle = \langle n_{kk'}|c^\dagger_{i'\sigma'} c_{i\sigma}|n_{kk'}\rangle = \sum_{l'l} U^\dagger_{l',i'\sigma'} U_{i\sigma,l} \langle n_{kk'}|c^\dagger_{l'}\, c_l|n_{kk'}\rangle. \tag{4.63}$$

To initialize the reduced one-particle density matrix in the quantum system's ground state, we set $k = k' < k_F$ so $|n_{kk}\rangle = |0\rangle$ and express its elements as

$$\begin{aligned} \rho^0_{i\sigma,i'\sigma'} = \langle 0|c^\dagger_{i'\sigma'} c_{i\sigma}|0\rangle &= \sum_{l'l} U^\dagger_{l',i'\sigma'} U_{i\sigma,l} \langle 0|c^\dagger_{l'}\, c_l|0\rangle \\ &= \sum_{l'l} U^\dagger_{l',i'\sigma'} U_{i\sigma,l} \langle 0|n_{ll'}\rangle. \end{aligned} \tag{4.64}$$

For any $l = l'$ we have $\langle 0|n_{ll}\rangle = \langle 0|c^\dagger_l\, c_l|0\rangle = \langle n_l\rangle_0$. All single particle states with $\epsilon_k < \mu$ are occupied in the many body ground state, which are the energetically lowest N_p single particle states at half filling. The expectation value of the l-th single particle state to be occupied is therefore one, if $l < N_p$ and equals zero if $l \geq N_p$. Any $l \neq l'$ does not contribute, since the ground state is orthogonal to all excited states, thus $\langle 0|n_{ll'}\rangle = 0$. Accordingly, the reduced one-particle density matrix for the ground state of the quantum system is given by

$$\rho^0_{i\sigma,i'\sigma'} = \sum_{l=0}^{N_p} U^\dagger_{l,i'\sigma'} U_{i\sigma,l} = \sum_{l=0}^{N_p} U^\star_{i'\sigma',l} U_{i\sigma,l}. \tag{4.65}$$

In order to evaluate expectation values of local magnetic moments (eq 4.3), an effective impurity coupling $J^{RKKY}_{q\alpha,r\beta}$ (eq. 4.34 or eq. 4.28) and the spin Berry curvature $\boldsymbol{\Omega}$ (eq. 4.16), matrix elements like $\langle n_{kk'}|s_{i\alpha}|0\rangle$ have to be determined. Again, $\sigma^\alpha_{\sigma\sigma'}$ denotes the

(σ, σ')-component of the α Pauli matrix, so

$$\begin{aligned}\langle n_{kk'}|s_{i\alpha}|0\rangle =& \sum_{\sigma\sigma'} \frac{1}{2}\langle n_{kk'}|c^\dagger_{i\sigma}\sigma^\alpha_{\sigma\sigma'}c_{i\sigma'}|0\rangle \\ =& \frac{1}{2}\sum_{\sigma\sigma'}\sum_{ll'} U^\dagger_{l,i\sigma}U_{i\sigma',l'}\sigma^\alpha_{\sigma\sigma'}\langle 0|c^\dagger_k c_{k'}c^\dagger_l c_{l'}|0\rangle. \end{aligned} \tag{4.66}$$

Next, we make use of Wick's theorem [135, 136] to expand the quadruple-product in terms of pairs of creation and annihilation operators. Only particle-number conserving terms can be non-zero here, as many body states of different particle numbers do not overlap, which leads to

$$\begin{aligned}\langle 0|c^\dagger_k c_{k'}c^\dagger_l c_{l'}|0\rangle =& \langle 0|c^\dagger_k c_{k'}|0\rangle\langle 0|c^\dagger_l c_{l'}|0\rangle + \langle 0|c^\dagger_k c_{l'}|0\rangle\langle 0|c_{k'}c^\dagger_l|0\rangle \\ =& \langle 0|c^\dagger_k c_{k'}|0\rangle\langle 0|c^\dagger_l c_{l'}|0\rangle + \langle 0|c^\dagger_k c_{l'}|0\rangle(\delta_{lk'} - \langle 0|c^\dagger_l c_{k'}|0\rangle) \\ =& \delta_{kk'}\delta_{ll'}\langle n_k\rangle\langle n_l\rangle + \delta_{kl'}\delta_{lk'}\langle n_k\rangle(1-\langle n_{k'}\rangle). \end{aligned} \tag{4.67}$$

For now, we are interested in non-diagonal matrix elements $\langle n_{kk'}|s_{i\alpha}|0\rangle$ where $k \neq k'$, thus $|n_{kk'}\rangle \neq |0\rangle$ and the first summand vanishes.

In the adiabatic limit the host remains in its ground state, so at half filling the lowest N_p single particle states are occupied ($k_F = N_p$). Accordingly, $\langle n_k\rangle = 1$ if $k < k_F$ and $\langle n_k\rangle = 0$ if $k \geq k_F$, so

$$\begin{aligned}\langle n_{kk'}|s_{i\alpha}|0\rangle =& \frac{1}{2}\sum_{\sigma\sigma'}\sum_{ll'} U^\dagger_{l,i\sigma}U_{i\sigma',l'}\sigma^\alpha_{\sigma\sigma'}\delta_{kl'}\delta_{lk'}\langle n_k\rangle(1-\langle n_{k'}\rangle) \\ =& \frac{1}{2}\sum_{\sigma\sigma'} U^\dagger_{k'i\sigma}U_{i\sigma',k}\sigma^\alpha_{\sigma\sigma'} \quad \forall\, k < k_F, k' \geq k_F. \end{aligned} \tag{4.68}$$

The ground state expectation value, i.e., $k = k' < k_F$ so $|n_{kk}\rangle \neq |0\rangle$ and $\langle n_k\rangle = 1$, is entailed by the first summat in the last line of eq. 4.67. It can be evaluated via

$$\begin{aligned}\langle 0|s_{i\alpha}|0\rangle =& \langle n_{kk}|s_{i\alpha}|0\rangle = \frac{1}{2}\sum_{\sigma\sigma'}\sum_{ll'} U^\dagger_{l,i\sigma}U_{i\sigma',l'}\sigma^\alpha_{\sigma\sigma'}\delta_{ll'}\langle n_l\rangle \\ =& \frac{1}{2}\sum_{\sigma\sigma'}\sum_{l<k_F} U^\dagger_{l,i\sigma}U_{i\sigma',l}\sigma^\alpha_{\sigma\sigma'}. \end{aligned} \tag{4.69}$$

Subsequently, an exemplary application of the derived expressions is presented. We formulate the spin Berry curvature in terms of quantities that can straightforwardly be accessed through numerical diagonalization of the (effective) hopping matrix. When assuming local exchange interaction $H_{ex} = J\sum_q \boldsymbol{S}_q \boldsymbol{s}_{i_q}$, elements of the spin Berry

curvature (eq. 4.16) can be expressed via

$$\begin{aligned}\Omega_{q\alpha,r\beta}(\boldsymbol{S}) =& -2\,\mathrm{Im}\sum_{n\neq 0}\frac{\langle 0|\nabla_{q\alpha}H|n\rangle\langle n|\nabla_{r\beta}H|0\rangle}{(E_n-E_0)^2}\\ =& -2J^2\,\mathrm{Im}\sum_{\substack{k<k_F\\ k'\geq k_F}}\frac{\langle 0|s_{i_q\alpha}|n_{kk'}\rangle\langle n_{kk'}|s_{i_r\beta}|0\rangle}{(E_{n_{kk'}}-E_0)^2}\\ =& -\frac{J^2}{2}\,\mathrm{Im}\sum_{\substack{k<k_F\\ k'\geq k_F}}\sum_{\substack{\sigma\sigma'\\ \varsigma\varsigma'}}\frac{U^\dagger_{k,i_q\sigma}\sigma^\alpha_{\sigma\sigma'}U_{i_q\sigma',k'}U^\dagger_{k',i_r\varsigma}\sigma^\beta_{\varsigma\varsigma'}U_{i_r\varsigma',k}}{(\epsilon_{k'}-\epsilon_k)^2}.\end{aligned} \tag{4.70}$$

As discussed in section 4.1.3, the spin Berry curvature becomes a quantity of the host system only in the weak coupling limit up to $\mathcal{O}(J^2)$. The leading non-vanishing order $\Omega^{(0)}_{q\alpha,r\beta}$ (see eq. 4.30) is determined by eigenstates of the free host Hamiltonian. Consequently, $\Omega^{(0)}_{q\alpha,r\beta}$ is formulated in terms of eigenvectors $\boldsymbol{U}^{(0)}_k$ and eigenvalues $\epsilon^{(0)}_k$ of the quantum hopping matrix $\boldsymbol{T}^Q$ (see eq. 4.1). When the host is not explicitly time dependent, $\epsilon^{(0)}_k$ and $\boldsymbol{U}^{(0)}_k$ are constant in time, thus $\boldsymbol{\Omega}^{(0)}$ is static. Contrarily, $\boldsymbol{\Omega}$ has to be re-evaluated at each instance of time, as it is a function of $\boldsymbol{U}_k$ and ϵ_k. Eigenvalues and eigenvectors of the effective hopping matrix (eq. 4.4) are generically time dependent due to the dynamics of the impurities $\boldsymbol{S}(t)$.

Furthermore, symmetries can be exploited to enhance numerical performance. As an example, we assume translational invariance in the free ($J = 0$) quantum system. To take advantage of the translational invariance, the Hamiltonian is transformed to reciprocal space. At first, the real space Hamiltonian is formulated in terms of unit cells, which periodically repeat after translation vectors $\boldsymbol{I}$. Super index r specifies details within a unit cell (first line of eq. 4.71). This super index runs over all degrees of freedom within a unit cell, which are sublattices (A-, and B-sites) and spin indices ($\sigma \in \{\uparrow,\downarrow\}$) in our case. Next, Fourier transformation by unitary operator $U_{\boldsymbol{Ik}} = L^{-1/2}e^{i\boldsymbol{Ik}}$ reformulates the Hamiltonian in reciprocal space. The number of unit cells are labeled by L and $\boldsymbol{k}$ is a wave vector of reciprocal space. Generically, the exchange Hamiltonian is not translational invariant, thus here we focus on the quantum Hamiltonian only. With $t_{\boldsymbol{I}r,\boldsymbol{I}'r'} = \sum_k U_{\boldsymbol{Ik}}t_{rr'}(\boldsymbol{k})U^\dagger_{\boldsymbol{kI}'}$ and $c^\dagger_{\boldsymbol{k}r} = \sum_{\boldsymbol{I}} U_{\boldsymbol{Ik}}c^\dagger_{\boldsymbol{I}r}$ the Hamiltonian of the quantum system can be expressed by

$$\begin{aligned}H_Q =& \sum_{i\sigma,i'\sigma'}t_{i\sigma,i'\sigma'}c^\dagger_{i\sigma}c_{i'\sigma'} = \sum_{\boldsymbol{I}r,\boldsymbol{I}'r'}t_{\boldsymbol{I}r,\boldsymbol{I}'r'}c^\dagger_{\boldsymbol{I}r}c_{\boldsymbol{I}'r'}\\ =& \sum_{\boldsymbol{k},rr'}t_{rr'}(\boldsymbol{k})c^\dagger_{\boldsymbol{k}r}c_{\boldsymbol{k}r'} = \sum_{\boldsymbol{k}\nu}\epsilon_\nu(\boldsymbol{k})c^\dagger_{\boldsymbol{k}\nu}c_{\boldsymbol{k}\nu}\\ =& \sum_{\boldsymbol{I}r,\boldsymbol{I}'r'}\sum_{\boldsymbol{k}\nu}W_{\boldsymbol{I}r,\boldsymbol{k}\nu}\epsilon_\nu(\boldsymbol{k})W^\dagger_{\boldsymbol{k}\nu,\boldsymbol{I}'r'}c^\dagger_{\boldsymbol{I}r}c_{\boldsymbol{I}'r'}.\end{aligned} \tag{4.71}$$

Furthermore, as denoted in the second line of eq. 4.71, the intra unit cell hopping matrix $t_{rr'}(\boldsymbol{k}) = \sum_\nu V_{r\nu}(\boldsymbol{k})\epsilon_\nu(\boldsymbol{k})V^\dagger_{\nu r'}(\boldsymbol{k})$ is diagonalized by the $\boldsymbol{k}$-dependent unitary transformation $c^\dagger_{\boldsymbol{k}\nu} = \sum_r V_{r\nu}(\boldsymbol{k})c^\dagger_{\boldsymbol{k}r}$. The band index ν is associated with all degrees of freedom within a unit cell (e.g. site and spin degrees of freedom). Moreover, ν labels the single particle energy bands at all $\boldsymbol{k}$. In the last line of eq. 4.71 we used the combined transformation $W_{\boldsymbol{I}r,\boldsymbol{k}\nu} = U_{\boldsymbol{I}\boldsymbol{k}}V_{r\nu}(\boldsymbol{k})$ to express $t_{\boldsymbol{I}r,\boldsymbol{I}'r'} = \sum_{\boldsymbol{k}\nu} W_{\boldsymbol{I}r,\boldsymbol{k}\nu}\epsilon_\nu(\boldsymbol{k})W^\dagger_{\boldsymbol{k}\nu,\boldsymbol{I}'r'}$.
The unit cell of a translation-invariant lattice is naturally much smaller than the entire lattice, resulting in a dimension of $\boldsymbol{t}(\boldsymbol{k})$ with elements $t_{rr'}(\boldsymbol{k})$ that is significantly smaller than the dimension of $\boldsymbol{t}$ with elements $t_{i\sigma,i'\sigma'}$. When considering a finite lattice with periodic boundary conditions, which is build up by a large number of unit cells, the diagonalization of the unit cell hopping matrix $\boldsymbol{t}(\boldsymbol{k})$, even thought it has to be performed for all $\boldsymbol{k}$, is in general significantly faster than diagonalizing the full real space hopping matrix $\boldsymbol{t}$ once. Taking advantage hereof typically enhances numerical performance substantially.
One application that exploits translational invariance is a formulation of the spin Berry curvature in the weak coupling limit in terms of $W_{\boldsymbol{I}r,\boldsymbol{k}\nu}$. Evaluation of the required matrix elements is straight forward and analogue to what has been presented above. With $(\boldsymbol{I}, r) = i_q$ and $(\boldsymbol{I}', r') = i_{q'}$ and assuming a spin-diagonal host, elements of the weak coupling $\boldsymbol{\Omega}^{(0)}$ (eq. 4.37) are

$$\Omega^{(0)}_{q\alpha,q'\beta} = -\frac{J^2}{2}\delta_{\alpha\beta}\mathrm{Im}\sum_{\boldsymbol{k}\nu}^{\text{occ.}}\sum_{\boldsymbol{k}'\nu'}^{\text{unocc.}}\sum_{rr'}\frac{W^\dagger_{\boldsymbol{k}\nu,\boldsymbol{I}r}W_{\boldsymbol{I}r,\boldsymbol{k}'\nu'}W^\dagger_{\boldsymbol{k}'\nu',\boldsymbol{I}'r'}W_{\boldsymbol{I}'r',\boldsymbol{k}\nu}}{\big(\epsilon_{\nu'}(\boldsymbol{k}') - \epsilon_\nu(\boldsymbol{k})\big)^2}. \tag{4.72}$$

Periodic boundary conditions do not necessarily have to be applied in all dimensions of the lattice. A two dimensional lattice, for example, might be subject to periodic boundary conditions in one direction only. The resulting geometry is cylinder-like and features one-dimensional open boundaries at the rims. Conceptually, the transformation to reciprocal space is analogue to the procedure described above. The unit cell, however, is of the dimension of the hight of the cylinder, which generically leads to a much larger number of (sub-)bands.

4.2 – Haldanes Model of a Chern Insulator

The theory of adiabatic spin dynamics in quantum-classical hybrid models has been developed on rather general terms of non-interacting lattices models. Our interest, however, is in the interplay of topology and magnetism. In section 4.1, non-Hamiltonian dynamics is derived as a consequence of a finite spin Berry curvature $\mathbf{\Omega}$. But in the weak coupling limit (section 4.1.3) the host is required to be neither symmetric nor anti-symmetric under time reversal to feature finite $\mathbf{\Omega}$ for common exchange Hamiltonians (for example eq. 4.21). Furthermore, the host has to be an insulator, so the adiabatic theorem can apply.

A suitable candidate, that meets these conditions is Haldane's model of a Chern insulator [28]. Historically, it is the first model of a quantum anomalous Hall insulator without external fields and contributed significantly to the development and understanding of topological band insulators [49, 137]. The Haldane model breaks time reversal symmetry inherently. The conjunction of symmetries and topological invariants is commonly documented in the ten fold way via the Altland-Zirnbauer classification [31, 138]. In this classification, the two-dimensional Haldane model is classified as a topological insulator of class A, where time reversal, particle-hole, and chiral symmetry are broken for generic model parameters [19, 48]. The Chern number (eq. 2.22) is the topological invariant used to identify distinct topological phases in topological insulators of this class. A prototypical hybrid model involving classical spins coupled to a topological insulator may provide insights into the topological properties of the host by analyzing the dynamics of the impurities in the context of adiabatic spin dynamics. To this end, this section introduces the Haldane model and discusses its most relevant features for the forthcoming studies, where the Haldane model serves as the quantum host.

The Haldane model (fig. 4.1) is defined on a two-dimensional hexagonal lattice, respectively a two-dimensional triangular Bravais lattice with a biatomic unit cell. $\boldsymbol{v}_1 = (\sqrt{3}, 0)^T$ and $\boldsymbol{v}_2 = (-\sqrt{3}/2, \sqrt{3}/2)^T$ are basis vectors of the lattice, when we set the spatial distance of neighboring sites (e.g. within one unit cell) to unity. Originally, Haldane defined this model [28] for spinless particles, but to enable spin-exchange interaction with the impurities we duplicate the model and consider one copy of the Haldane model for each spin projection $\sigma =\uparrow$ and $\sigma =\downarrow$. The two copies are coupled via interaction with the impurities ($\hat{H}_{ex} = \sum_{q\alpha,i\beta} J_{q\alpha,i\beta} S_{q\alpha} \hat{s}_{i\beta}$). We refer to the spin-$\frac{1}{2}$ particles occupying the host lattice as non-interacting electrons (e.g. no Coulomb or spin-spin interaction). The two sites of a unit cell differ in the sign of a staggered onsite potential $\pm M$. This staggered nature is encoded by sign-factor z_i, which takes values $+1$ on the A-sublattice and -1 on the B-sublattice. Accordingly, any $M \neq 0$ breaks sublattice invariance. Note, that in the wording we use, next-nearest neighbors

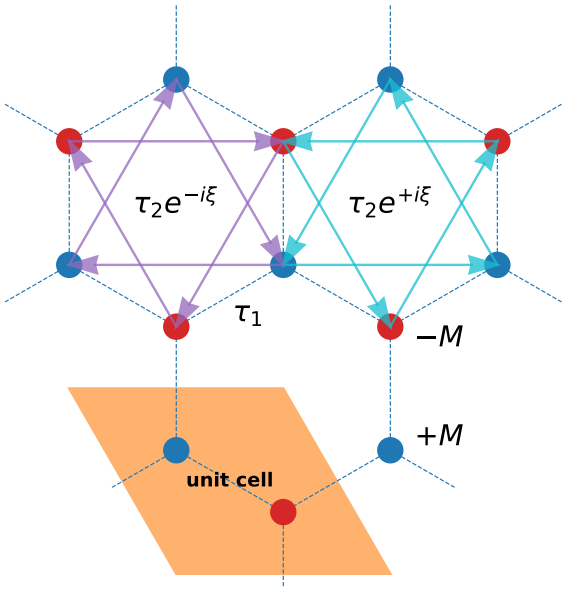

Figure 4.1: Scheme of the Haldane model on a honeycomb lattice. Blue dots indicate sites of the A-sublattice with positive onsite potential $+M$, while red dots mark sites of the B-sublattice with negative onsite potential $-M$. Dashed lines display nearest-neighbor hopping with amplitude τ_1 and purple arrows illustrate clockwise next-nearest neighbor hopping $\tau_2 e^{-i\xi_{ij}}$ where the Peierls factor has negative phase $\xi_{ij} = -\xi$, whereas the counter-clockwise cyan colored arrows depict next-nearest neighbor hopping with positive Peierls phase $\xi_{ij} = +\xi$.

are always of the same sublattice. Nearest neighbors, however, are conceivably constituents of the same unit cell and always of different sublattices (see fig 4.1). Electrons can transition between adjacent sites $\langle ij \rangle$ of the hexagon by nearest-neighbor hopping amplitude τ_1. Further hopping between next-nearest neighbors $\langle\langle ij \rangle\rangle$ is quantified by transition amplitude $e^{i\xi_{ij}}\tau_2$ with real weight τ_2 and direction-dependent phase factor ξ_{ij} of magnitude $-\pi \leq \xi_{ij} < \pi$. For clockwise hopping from site j to site i, as indicated by the purple arrows in figure 4.1, the phase $\xi_{ij} = -\xi$ is negative. Counter-clockwise hopping, on the other hand, is of positive phase $\xi_{ij} = +\xi$ and indicated by the cyan-colored arrows. The net flux of the orbital magnetic field corresponding to next-nearest neighbor hopping (Peierls factors $\tau_2 e^{-i\xi_{ij}}$) vanishes within a unit cell. It is exactly this direction-dependent complex phase factor that breaks time-reversal symmetry for any $\tau_2 \neq 0$ when $\xi \neq 0$ and $\xi \neq \pm\pi$.

The tight-binding Hamiltonian of the Haldane model is given by

$$\hat{H}_H = M \sum_{i\sigma} z_i \hat{c}^\dagger_{i\sigma} \hat{c}_{i\sigma} - \tau_1 \sum_{\langle ij \rangle, \sigma} \hat{c}^\dagger_{i\sigma} \hat{c}_{j\sigma} - \tau_2 \sum_{\langle\langle ij \rangle\rangle, \sigma} e^{i\xi_{ij}} \hat{c}^\dagger_{i\sigma} \hat{c}_{j\sigma} \tag{4.73}$$

which is trivially invariant under spin rotations. That invariance is, however, broken by

the exchange interaction with the impurities. In the bulk $\hat{H}_H$ is translational invariant and the real space Hamiltonian (eq. 4.73) can be Fourier-transformed to reciprocal space by $\hat{c}_j = \frac{1}{\sqrt{2\pi}} \int d\boldsymbol{k} \hat{c}_k e^{-i\boldsymbol{k}\boldsymbol{r}_j}$ respectively $\hat{c}_j^\dagger = \frac{1}{\sqrt{2\pi}} \int d\boldsymbol{k} \hat{c}_k^\dagger e^{i\boldsymbol{k}\boldsymbol{r}_j}$, where the trivial replication related to the spin degree of freedom is neglected for now. Here, $\boldsymbol{r}_j$ is the real space location of the j-th lattice site and $\boldsymbol{k}$ a reciprocal lattice vector. In the two dimensional basis due to the two sites per unit cell, Fourier transformation of eq. 4.73 leads to

$$\hat{H}_H = \int d\boldsymbol{k} \begin{pmatrix} \hat{a}_{\boldsymbol{k}}^\dagger \\ \hat{b}_{\boldsymbol{k}}^\dagger \end{pmatrix} \mathcal{H}(\boldsymbol{k}) \begin{pmatrix} \hat{a}_{\boldsymbol{k}} & \hat{b}_{\boldsymbol{k}} \end{pmatrix}, \tag{4.74}$$

with $\hat{a}_{\boldsymbol{k}}^\dagger$ as the creation operator of an electron with momentum $\boldsymbol{k}$ on the A-sublattice. $\hat{a}_{\boldsymbol{k}}$ is its annihilator and $\hat{b}_{\boldsymbol{k}}^\dagger$, $\hat{b}_{\boldsymbol{k}}$ act correspondingly on the B-sublattice. Disregarding spin-degeneracy, the two-level Hamiltonian $\mathcal{H}(\boldsymbol{k})$ takes the convenient form of

$$\begin{aligned} \mathcal{H}(\boldsymbol{k}) = &- 2\tau_2 \cos(\xi) \left(\sum_{i=1}^{6} \cos(\boldsymbol{k}\boldsymbol{v}_i) \right) \mathbf{1} + \left(M + 2\tau_2 \sin(\xi) \sum_{i=1}^{6} \sin(\boldsymbol{k}\boldsymbol{v}_i) \right) \boldsymbol{\sigma}^z \\ &- \tau_1 \left(\sum_{j=1}^{3} \cos(\boldsymbol{k}\boldsymbol{e}_j) \boldsymbol{\sigma}^x + \sum_{j=1}^{3} \sin(\boldsymbol{k}\boldsymbol{e}_j) \boldsymbol{\sigma}^y \right). \end{aligned} \tag{4.75}$$

The $\boldsymbol{e}_j$ are the real space displacements from a B-site to its three neighboring A-sites and $\boldsymbol{v}_i$ describe the displacements of some site to its six next-nearest neighbors [19,28]. Again, $\boldsymbol{\sigma}^x$, $\boldsymbol{\sigma}^y$, $\boldsymbol{\sigma}^z$ are the Pauli matrices and $\mathbf{1}$ the identity in two dimensions. Since the model is invariant under spatial rotations of 120°, respectively Hamiltonians 4.73 and 4.75 are C_3 symmetric, the two twofold spin degenerate energy bands have to respect the same symmetry. Thus, a gap closure as required for a topological phase transition, occurs at the $\boldsymbol{K} = 2\pi/3\big(1/\sqrt{3}, 1\big)^T$ and $\boldsymbol{K'} = 2\pi/3\big(2/\sqrt{3}, 0\big)^T$ point of the first Brillouin zone [19]. We note that the Haldane model does not have an inversion center and breaks time reversal symmetry when $M \neq 0$ and $\tau_2 \sin(\xi) \neq 0$. For that reason, the spectrum is not invariant under an inversion $\boldsymbol{k} \to -\boldsymbol{k}$ [28]. To set an energy scale we fix $\tau_1 = 1$.

The band structure is gapped for generic model parameters M, ξ and $|\tau_2/\tau_1| < 1/3$, except for the topological phase transition determined by

$$\frac{|M|}{|\tau_2|} = 3\sqrt{3} |\sin(\xi)|. \tag{4.76}$$

Figure 4.2 shows an examplary bulk band-structure close to the topological phase transition. The gap-closure condition is derived from an expansion of eq. 4.75 at the $\boldsymbol{K}$ and $\boldsymbol{K'}$ point as shown in appendix A.2.3. That expansion also entails us to read

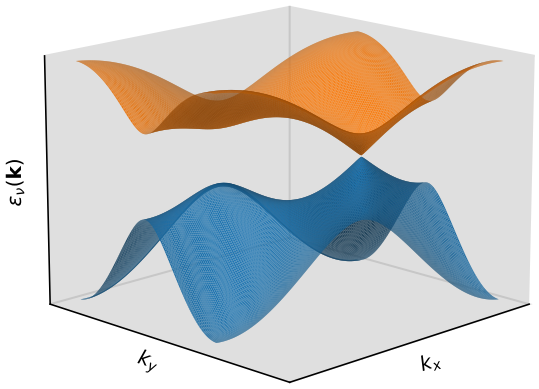

Figure 4.2: Typical bulk band structure of the Haldane model close to the topological phase transition with $\tau_1 = 1$, $\tau_2 = 0.1$, $\xi = \frac{\pi}{4}$ and $M = 0.95 M_{crit} \approx 0.35$. Depicted are the two, in case of the spinful Haldane model twofold degenerate, bands of a square ($l_1 = l_2$ unit cells) slab with periodic boundary conditions, thus periodic continuation results in the well known hexagonal representation of the first Brillouin zone of a honeycomb lattice.

off the gap at the $\boldsymbol{K}$-point (see eq. A.19) for $M > 0$, $\tau_2 > 0$ and $0 < \xi < \pi$, which is

$$\Delta E = 2|M - 3\sqrt{(3)}\tau_2 \sin(\xi)|. \tag{4.77}$$

The topological phase diagram of the Haldane model (fig. 4.3), is deduced from analysis of the topological band index for generic model parameters in each region where the gap does not close. The classifying topological invariant to this model is the Chern number (see 2.3). Since a change of the Chern number requires the spectrum to undergo a gap closing and reopening transition [19], the Chern number remains the same for all model parameters in a region where the bulk gap remains non-zero [28,137]. A straight forward analysis is the integration of the Berry curvature

$$\Omega_{\alpha\beta}(\boldsymbol{k}) = \frac{\partial\langle\psi_0|}{\partial k_\alpha}\frac{\partial|\psi_0\rangle}{\partial k_\beta} - \frac{\partial\langle\psi_0|}{\partial k_\beta}\frac{\partial|\psi_0\rangle}{\partial k_\alpha} \tag{4.78}$$

over the first Brillouin zone. In this case, the first Brillouin zone, respectively the base manifold, is a two-torus $\mathcal{T}^2 = \mathcal{S}^1 \otimes \mathcal{S}^1$, as the bulk can be described by an infinite two dimensional slab in real space (with periodic boundary conditions). Accordingly, topological phases are characterized by the first Chern number

$$C = \frac{1}{2\pi}\int_{\mathcal{T}^2}\sum_{\alpha<\beta}\Omega_{\alpha,\beta}(\boldsymbol{k})dk_\alpha dk_\beta. \tag{4.79}$$

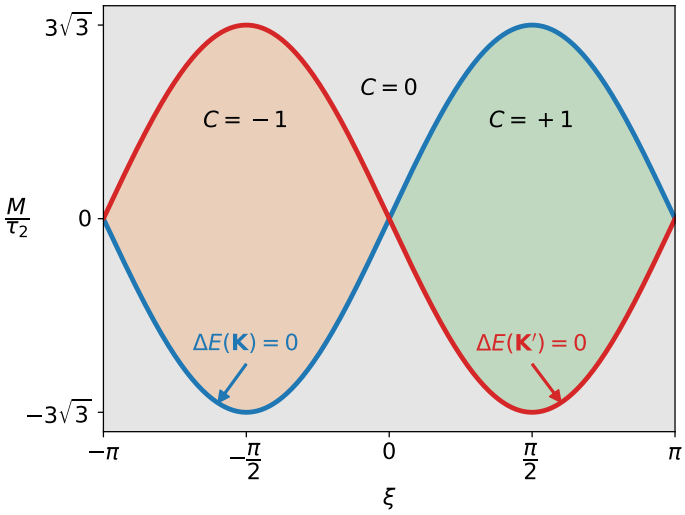

Figure 4.3: Topological phase diagram of the Haldane model, $\tau_1 = 1$ sets the energy scale and the first Chern numbers C are declared for positive τ_2. The blue line indicates a gap-closure at the $\boldsymbol{K}$ and the red line at the $\boldsymbol{K}'$ point in the first Brillouin zone.

Distinct topological phases lead to different integers C.

Even though the spin Berry curvature (eq. 4.16) is of similar structure as the Berry curvature (eq. 4.78), the subtle difference in the wording hints towards central difference in its meaning. While the spin Berry curvature encodes information of the response of a quantum system to an external perturbation via the classical spins, the Berry curvature is an intrinsic quantity of the quantum system itself. As we consider the Haldane model alone here, we stick to the bulk band Chern number for now.

A change of the first Chern number through a gap closing and reopening transition is equivalent to the total change of the Hall conductance ($e = 1$, $\hbar = 1$) during that transition [19, 137]. So another approach to the topological phase diagram is to start in a parameter regime where the first Chern number is known and to trace its change via the Hall conductance through the gap closures from there. In general, the Hall conductance of non-interacting electron systems equals the first Chern number and thus takes integer values, which is known as the (integer) quantum Hall effect [19, 28]. In the Haldane model, three topologically different phases can be identified [28]. A topologically trivial phase with $C = 0$ for $\frac{|M|}{|\tau_2|} > 3\sqrt{3}|\sin(\xi)|$ and two topologically nontrivial phases with $C = \pm 1$ for $\frac{|M|}{|\tau_2|} < 3\sqrt{3}|\sin(\xi)|$. The sign of the topological index depends on the sign of $\tau_2 \sin(\xi)$, which are exactly the contributions that break time-reversal invariance. For positive τ_2 the first Chern number is $C = 1$ if $0 < \xi < \pi$ and $C = -1$ if $-\pi < \xi < 0$, which results the topological phase diagram shown in fig. 4.3. Along the blue line, a topological phase transition is assigned with a gap-closure at the $\boldsymbol{K}$-point and for the red line with a gap-closure at the $\boldsymbol{K}'$-point. For negative τ_2 all C change sign and the gap-closure transition lines (red and blue lines in fig. 4.3) interchange. Moreover, a spinful extension consisting of two similar copies of the

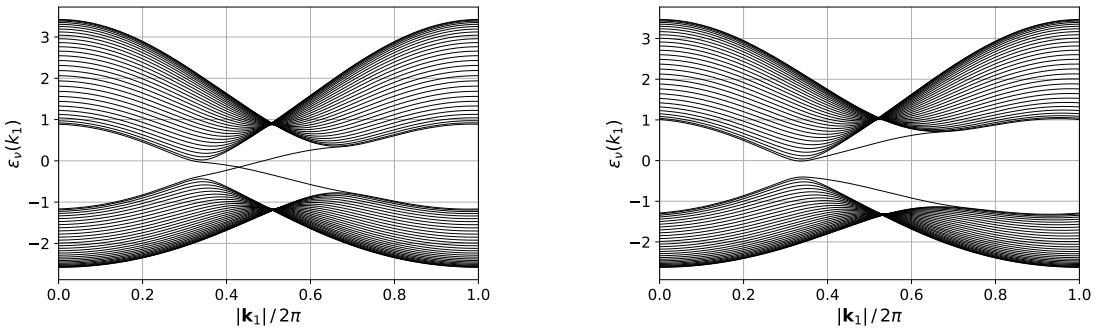

(a) Topologically nontrivial phase with $M = 0.5M_{crit} \approx 0.18$ and $C = 1$.

(b) Topologically trivial phase ($C = 0$) with $M = 1.5M_{crit} \approx 0.55$.

Figure 4.4: Typical band structure of a Haldane ribbon with open zigzag edges. Exemplary width is $l_2 = 30$ unit cells while periodic boundary conditions are assumed along the $\boldsymbol{v}_1$ direction. Further parameters are $\tau_2 = 0.1$ and $\xi = \frac{\pi}{4}$.

Haldane model, one for $\sigma =\uparrow$ and one for $\sigma =\downarrow$, doubles all C [28].

Topological insulators in general exhibit gapless states at the interfaces of regions, where the topological quantum number changes [49]. A prime example of such an interface is the edge of a topological insulator when the bulk is in a topological nontrivial state, as it is a surface to the topologically trivial vacuum outside. For that reason the existence of gapless edge states at surfaces of topological insulators is also referred to as bulk-boundary correspondence. In two dimensional Chern insulators, like the Haldane model, the number of gapless edge modes corresponds to the total change of the Chern number across that surface [139]. The existence of gapless states which are exponentially localize at the edges of topological insulators in a any dimension, are direct consequence of the fact that a topological invariant cannot change its value unless the energy gap closes [19, 49].

Figure 4.4 depicts the band structure of the Haldane model in a ribbon geometry, with open boundaries are along zigzag-edges and periodic boundary conditions applied in the $\boldsymbol{v}_1$ direction. Any finite number of unit cells along the $\boldsymbol{v}_1$ direction results in a finite grid of $k_1 = |\boldsymbol{k}_1|$. The two bands of that system are formed by a finite number of sub-bands. The count of unit cells along the $\boldsymbol{v}_2$-expansion (open boundaries) determines the number of sub-bands. Each sub-band is trivially twofold degenerate in the spinful Haldane model. Since the surface states are exponentially localized at the zigzag edge, a rather narrow expansion in the $\boldsymbol{v}_2$-direction is sufficient to ensure non-substantial overlap of the edge modes. Figure 4.4a shows a band structure of a Haldane ribbon in the topological phase. Two major energy band are separated by a bulk band gap and two modes bridge that bulk band gap. As they bridge the bulk band gap and eventually cross each other, they degenerate and are therefore named gapless modes or zero modes. States of the two crossing bands are exponentially localized at the open boundaries. The observation of two modes crossing the gap is due to the two edges

of the chosen geometry, where the Chern number changes at the upper as well as the lower zigzag edge of the nano-ribbon. For a lattice model at half filling, the crossing of these two modes takes place at the Fermi energy. Model parameters τ_2, ξ and M tune the band gap as well as the k-dependence of all subbands, including the gapless modes. For generic model parameters, the band structure is neither particle hole, nor inversion ($\epsilon_\nu(k_1) = \epsilon_\nu(-k_1)$) symmetric and the bandwidth exceeds the bulk band gap considerably. The specific choice of $\xi = \pm\pi/2$ restores particle-hole symmetry. In the topologically trivial phase, however, the Chern number does not change at the edges. A corresponding band structure is displayed in figure 4.4b, where gapless modes are absent. One can still identify two distinct modes near the bulk band gap and they are still associated with the edges of the models geometry, but they do not cross the band gap and the model is all insulating.

4.3 – Numerical Results of the Quantum-Classical Adiabatic Spin Dynamics

After deriving the (adiabatic) equations of motion of a quantum classical hybrid model in section 4.1 and an introduction of Haldanes model of a Chern insulator in section 4.2, we study the interplay of bulk band topology and classical impurities within this section. The Hamiltonian of the Haldane-impurity model with local and isotropic host-impurity exchange reads

$$\begin{aligned}\hat{H} =&\hat{H}_H + J\sum_q \boldsymbol{S}_q \hat{\boldsymbol{s}}_{i_q} \\ =&M\sum_{i\sigma} z_i \hat{c}^\dagger_{i\sigma}\hat{c}_{i\sigma} - \tau_1 \sum_{\langle ij\rangle,\sigma} \hat{c}^\dagger_{i\sigma}\hat{c}_{j\sigma} - \tau_2 \sum_{\langle\langle ij\rangle\rangle,\sigma} e^{i\xi_{ij}}\hat{c}^\dagger_{i\sigma}\hat{c}_{j\sigma} \\ &+ \frac{J}{2}\sum_{q,\sigma\,\sigma'} \boldsymbol{S}_q \boldsymbol{\sigma}_{\sigma\sigma'} \hat{c}^\dagger_{i_q\sigma}\hat{c}_{i_q\sigma'},\end{aligned} \tag{4.80}$$

where $\boldsymbol{\sigma} = (\boldsymbol{\sigma}_x, \boldsymbol{\sigma}_y, \boldsymbol{\sigma}_z)^T$ is the vector of Pauli matrices.
Applying the adiabatic constraint, a geometric spin torque emerges in the adiabatic equation of motion for the classical spins coupled to a quantum host (eq. 4.18). This contribution beyond the conventional RKKY-like coupling of impurities is featured by the spin Berry curvature (eq. 4.16), which is the central quantity of interest here. Without external fields and with the quantum system initialized in the ground state to a given impurity configuration, the minimal example to induce nontrivial dynamics requires two impurities. We apply the theory of adiabatic spin dynamics, derived on general terms for gapped quantum systems and an arbitrary number of impurities, to a prototypical setup. This setup involves two classical spins coupled to a spinful Haldane model that serves as the quantum host.
We investigate weak host-impurity exchange in the bulk of the (topological) insulator in section 4.3.1. The host lattice is subject to periodic boundary conditions to emulate a bulk and evade edge modes. Spatial extensions, however, are chosen such that the $\boldsymbol{K}$ and the $\boldsymbol{K}'$ point are contained in the discretized first Brillouin zone. We study the geometry of impurity positions (sections 4.3.1.1 and 4.3.1.2) and finite size effects, in particular related to the τ_2-parameter of the Haldane host (section 4.3.1.3). Moreover, we evaluate the spin Berry curvature in the Haldane phase diagram (section 4.3.1.4) and discuss Ω at the topological phase transition of the host (section 4.3.1.5). In section 4.3.2 we address the question on whether topological edge states feed back to the spin Berry curvature. To achieve this, impurities are coupled to the edge of a lattice where periodic boundary conditions apply in one direction only.
Furthermore, real time dynamics of two impurities is considered in section 4.3.3. On the one hand, this section addresses the weak coupling impurity dynamics, where effects

due to the spin Berry curvature are explicitly displayed. On the other hand, the dynamics obtained from effective equations of motion is compared to the dynamics obtained via the full set of equations of motion. By analyzing the impurity dynamics, we assess the accuracy of the adiabatic approximation, the perturbative weak coupling approach to adiabatic spin dynamics, and the naive Hamiltonian approach. To this end we probe a setup in which impurities are coupled to the edge of a Haldane ribbon, and vary the host-impurity exchange coupling. Finally, the effect of the topological phase of the host on the dynamics of the impurities is studied.
In the following discussion of numerical results, the energy scale is set by the nearest-neighbor hopping $\tau_1 = 1$. Most of the presented results have been published in [48].

4.3.1 – Weak Coupling in the Bulk

The geometric spin torque in the adiabatic dynamics of two impurities, $\boldsymbol{S}_q$ and $\boldsymbol{S}_r$, coupled to the local magnetic moments at sites i_q and i_r of a lattice of itinerant electrons originates form the spin Berry curvature tensor $\boldsymbol{\Omega}_{q,r}$. Here we focus on the limit of weak host-impurity exchange coupling. The unperturbed spinful Haldane model is a spin-rotation invariant system, thus, $\Omega_{q\alpha,r\beta} = -\Omega_{r\beta,q\alpha} = \Omega_{q,r}\delta_{\alpha\beta}$ (eq. 4.37). The first equality is due to the anti symmetry of $\boldsymbol{\Omega}$ and the second equality is a result of the weak coupling limit as discussed in section 4.1.3.1. When rescaling the equations of motion as in equation 4.52, a single real number Ω determines the geometric spin torque for a pair of impurities. The host is also translation invariant in the weak coupling limit, so the spin Berry curvature is numerically evaluated via equation 4.72.
Before discussing numerical results, we briefly analyze symmetries of the Haldane host (eq. 4.73) and their consequences for the spin Berry curvature. For $\tau_2 \neq 0$ and $\xi \neq n\pi$ the host breaks time reversal symmetry. Local spin expectation values, however, transform as $\langle\psi_0^{(0)}|s_{i\alpha}|\psi_0^{(0)}\rangle \mapsto -\langle\psi_0^{(0)}|s_{i\alpha}|\psi_0^{(0)}\rangle^\star$ under time reversal, which implies $\Omega^{(0)}_{q\alpha,r\beta} \mapsto \Omega^{(0)}_{r\beta,q\alpha}$ (eq. 4.30) under time reversal in the weak coupling limit. Thus, for this spin rotation invariant host, we deduce $\Omega \mapsto -\Omega$ for the defining element of the two-impurity weak coupling spin Berry curvature (eq. 4.37) under time reversal. Reflection at a mirror axis of the hexagonal lattice that respects the staggered onsite potential ($\pm M$ within a unit cell), transforms the Haldane Hamiltonian in the same way as time reversal. These axes are actually the mirror axes of the triangular Bravais lattice, which forms the hexagonal grid when using a two-atomic unit cell. The onsite potential and the nearest neighbor hopping (first two terms in eq. 4.73) remain unchanged under reflection at these axis. To the next-nearest neighbor hopping (third term in eq. 4.73), however, reflection has the same effect as the complex conjugation of the phase, since $\xi_{ij} = -\xi_{ji}$ and $\xi_{ij} \mapsto \xi_{ji}$ under that transformation. Consequently, the spin Berry curvature transform as $\Omega \mapsto -\Omega$ under such reflections. Accordingly, Ω and the Haldane Hamiltonian are invariant under the combined action of time reversal

and a reflection of the aforementioned type. Moreover, the (spinful) Haldane model is invariant under discrete spatial rotations of $2\pi/3$ around a fixed site, thus, it is C_3 invariant. Consequently, Ω remains invariant under such rotations.

4.3.1.1 Positioning of the Impurities in the Bulk

At first, we investigate the geometry of a two-impurity setup. As we fix the models parameters, so Ω depends on the position of the impurities only. Since we consider weak coupling and the Haldane host to be translation invariant, one can fix the position of the first impurity and compute Ω for any other position of the second impurity to cover the entire geometry of impurity locations. To mimic the bulk of a topological insulator, we apply periodic boundary conditions to a lattice extending l_1 unit cells in $\boldsymbol{v}_1$ direction and l_2 unit cells in $\boldsymbol{v}_2$ direction. Computations are performed with $J = 0.01$ as the weak coupling host-impurity exchange.

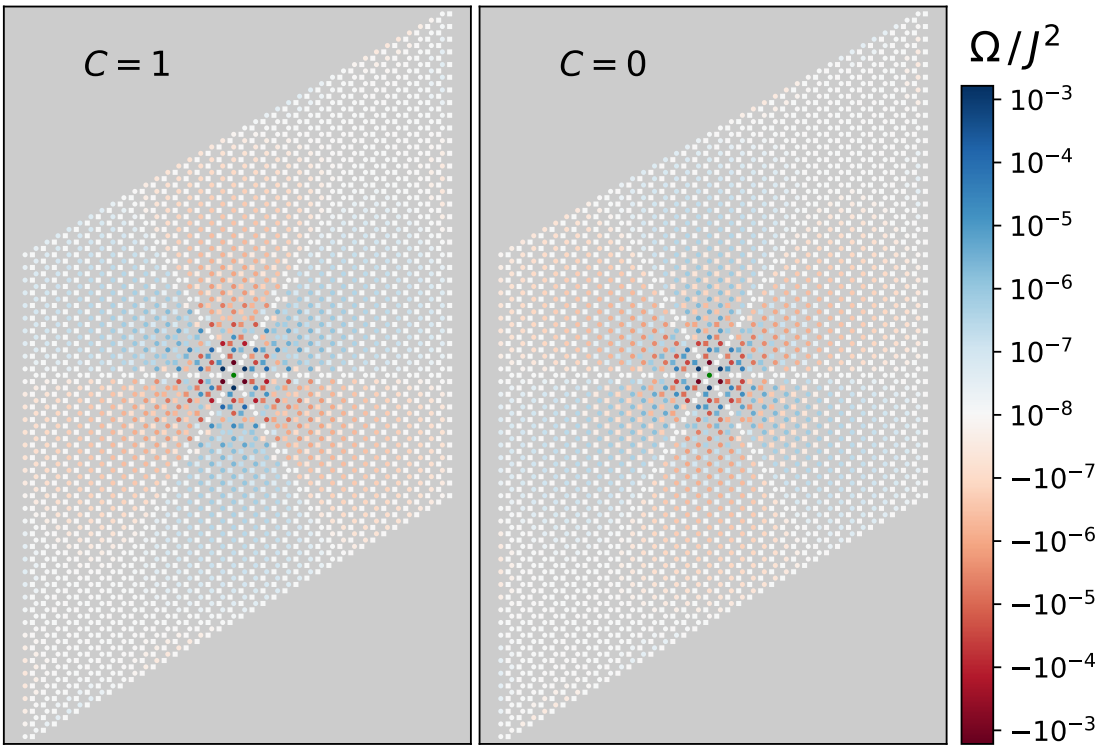

Figure 4.5: Defining element Ω of the two-impurity weak coupling spin Berry curvature $\Omega_{q\alpha,r\beta} = \Omega_{qr}\delta_{\alpha\beta}$ (eq.4.37) for all impurity positions i_r and $i_q = i_{\text{center}}$. Two classical spins are locally coupled to the bulk of the Haldane host by weak $J = 0.01$. We fix the location of the first impurity in the center (green dot) and vary the position of the second impurity over all remaining $2l_1l_2 - 1$ lattice sites to cover all distinct impurity locations The color code displays the value of Ω/J^2 in a lattice of $l_1 = l_2 = 39$ unit cells. Further model parameters are $\tau_2 = 0.1$, $\xi = \pi/4$ and $M = 0.8M_{crit}$ (topologically nontrivial, $C = 1$) in the left and $M = 1.2M_{crit}$ (topologically trivial, $C = 0$) in the right panel. The energy gap is the same for both panels.

In figure 4.5 the position of the fixed impurity is marked by the green circle in the center of each panel. Since we consider the weak coupling limit where $\mathbf{\Omega} \sim J^2$ (eq. 4.30) and a spin rotation invariant host model (see section 4.1.3.1) the generic quantity Ω/J^2 is color coded for all other positions of the second impurity on lattices of 39×39 unit cells. The two sublattices of the Haldane model are indicated by circles for the A-sites and squares for the B-sites. Parameters are chosen such, that the host is in a topologically nontrivial phase in the left and in a topologically trivial phase in the right panel. The energy gap, however, is the same for both panels, i.e., $\Delta E(0.8M_{crit}) = \Delta E(1.2M_{crit})$, since the gap is linear in M (eq. 4.77). In the considered scenario ($\tau_2 = 0.2$, $\xi = \pi/4$), the topological phase transition takes place at $M_{crit} \approx 0.37$ (eq. 4.76) for the chosen parameter.

At first, the set of discrete spatial lattice rotations by multiples of $2\pi/3$ around the fixed site is clearly visible. Invariance of Ω under C_3-rotations originates from the symmetry of the Haldane model. These spatial rotations by multiples of $2\pi/3$ about a site-centered axis perpendicular to the plane of the lattice are actions of elements of the symmetry group of the Haldane Hamiltonian. Furthermore, reflections at symmetry-axes containing the fixed impurity site cause Ω to change sign, as such reflections have the same effect as time reversal. In figure 4.5 these are reflections at a horizontal axis through the anchored central site (green marker) as well as the two in-plane axes rotated by $2\pi/3$ and $-2\pi/3$ relative to the horizontal one. As a consequence, Ω at sites directly on these axis has to vanish, which is clearly visible by the white 'rays' extending from the fixed site marked by the green circle. Indirectly, also the anti symmetry of the spin Berry curvature tensor $\mathbf{\Omega}$ can be recognized. For spin-rotation invariant host systems in the weak coupling limit (eq. 4.37) this anti-symmetry manifests in a sing change of the non-local blocks $\mathbf{\Omega}_{qr} = -\mathbf{\Omega}_{rq}$. That sign change is recognizable when fixing the position of one impurity q to the site $i_q = i_{center}$ (green in fig. 4.5), and denoting the position of the second impurity r at any other site by i_r. We define a coordinate system where i_q is at the origin and determine the position of i_r by $\boldsymbol{I}_r$, which is the index vector of elementary translations, thus in the mentioned coordinate system i_r is at $\boldsymbol{I}_r\boldsymbol{v} = I_{r,1}\boldsymbol{v}_1 + I_{r,2}\boldsymbol{v}_2$ where $\boldsymbol{v}_1$ and $\boldsymbol{v}_2$ are the two primitive translation vectors of the Honeycomb lattice. Interchanging the impurity labels $q, r \leftrightarrow r, q$ corresponds to negation of $\boldsymbol{I}_r$. When comparing Ω at site $\boldsymbol{I}_r\boldsymbol{v}$ with that at $-\boldsymbol{I}_r\boldsymbol{v}$ in figure 4.5, we find $\Omega(\boldsymbol{I}_r) = -\Omega(-I_r)$, i.e., them being of equal magnitude and opposing sign.

Next, we briefly touch on the dependency of Ω/J^2 on the distance between the impurities. More detailed considerations hereto are discussed in section 4.3.1.2. One can distinguish between two regions, a close range region where the proximity of the impurities leads to an oscillatory distance dependence of Ω and a far range region, where Ω does not change sign and decreases monotonically with increasing distance between the impurities. In figure 4.5, the close range region extends about three to four unit cells

in each direction. The spatial structure of Ω is in general rather complicated within this proximity region. Next-nearest neighbors of the central site, however, show a clear pattern of alternating signs in the topological (left panel) as well as the trivial (right panel) phase. In the far range region, on the other hand, the sign of Ω for sites of the same sublattice as the central site changes when transitioning from the topological to the trivial Haldane phase (see fig. 4.5). The spin Berry curvature here is to some degree sensitive to the topological phase of the host and might act as an indicator of topological properties in this sense. However, we have to point out, that even though in the weak coupling limit the spin Berry curvature and thus Ω is a property of the host model and the geometry of the setup only (eq. 4.30), it is not apparent, that Ω is directly related to its band topology. Although the k-space curvature and the spin Berry curvature $\boldsymbol{\Omega}$ originate from the same Bloch states, $\boldsymbol{\Omega}$ (eq. 4.16) is constructed by different matrix elements as compared to the k-space Berry curvature (eq. 4.78). But, only the latter determines the band topology of the Haldane model. Nonetheless, both curvatures can be expressed in a form where they share the same energy differences in the denominator. The band topology appears to influence the spin Berry curvature more in cases of smaller overall energy gaps, e.g. caused by smaller τ_2, where finite size effects become a major factor. An example in this regard is shown in Appendix A.2.5.

4.3.1.2 Distance Dependence

Impurity dynamics in the adiabatic limit is determined by an effective impurity-impurity coupling $\boldsymbol{J}^{RKKY}$ and the spin Berry curvature $\boldsymbol{\Omega}$. Within this section, the dependence of $\boldsymbol{\Omega}$ and $\boldsymbol{J}^{RKKY}$ on the distance of the impurities in the bulk is analyzed in the weak coupling regime. Again, the bulk is modeled by a finite slab of the spinful Haldane model with periodic boundary conditions, here extending 150×150 unit cells in both directions of primitive translations. Further parameters are the same as in the preceding consideration of Ω and the general spatial impurity geometry (see fig. 4.5), that is $\tau_2 = 0.1$ and $\xi = \pi/4$.

In figure 4.6, the defining elements of the weak coupling spin Berry curvature Ω (eq. 4.37) and the effective indirect impurity coupling J^{RKKY} (eq. 4.34) are displayed as functions of the Euclidean impurity distance d. The first non-vanishing term in a weak J expansion of both quantities is of order $\mathcal{O}(J^2)$, thus scaling both by $1/J^2$ eliminates the explicit dependence on the weak host-impurity interaction parameter J. For small distances both quantities change sign multiple times and the generic distance dependence is intricate. On larger distances, with $40 \lesssim d \lesssim 100$, the dependence of $\ln|\Omega|$ is virtually linear with d (fig. 4.6a), thus one can assume $|\Omega| \sim \exp(-d/\lambda)$ with $\lambda > 0$. Figure 4.6b shows a similar trend for $\ln|J^{RKKY}|$ as well. When comparing situations of equal gap size ΔE in the topological and the trivial phase of the Haldane model ($M_{top} = 0.8 M_{crit}$, $M_{tri} = 1.2 M_{crit}$), we observe a sign-change of Ω in the distant

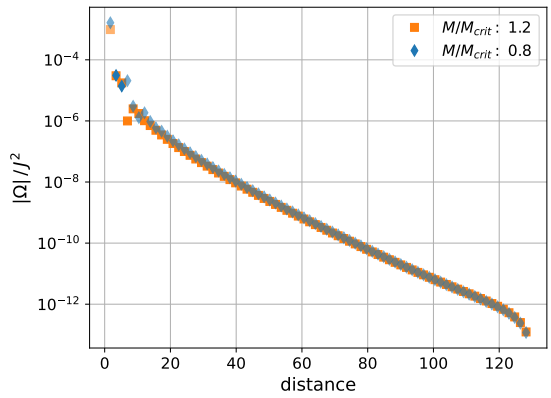

(a) Dimensionless defining element of the spin Berry curvature Ω/J^2 as a function of distance in the topological ($M = 0.8M_{crit}$) and trivial ($M = 1.2M_{crit}$) phase of the Haldane model.

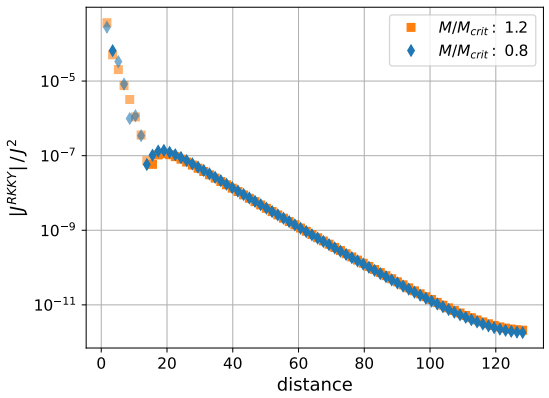

(b) Dimensionless defining element of the coupling constant J^{RKKY}/J^2 as a function of distance in the topological ($M = 0.8M_{crit}$) and trivial ($M = 1.2M_{crit}$) phase of the Haldane model.

Figure 4.6: Distance dependence of Ω and J^{RKKY} in the limit where impurities are weakly coupled to the bulk of the spinful Haldane model. Distance is the real spatial separation of impurities of the same sublattice in direction of the primitive translation vector $\boldsymbol{v}_1 = (0, \sqrt{3})$. System parameters are the same as in fig. 4.5, that is $\tau_2 = 0.1$ and $\xi = \pi/4$, but on a lattice of 150 unit cells in both directions of primitive translations, again with periodic boundary conditions. Signs of the respective quantities are indicated with full symbols for positive and light symbols for negative signs.

region of figure 4.6a. The absolute values of Ω are the same in the topological phase with M_{top} and the trivial phase with M_{tri}. On very large distances $d \gtrsim 100$, that linear trend breaks down due to finite size effects.

The slope $-1/\lambda$ in the linear region of figure 4.6a depends on the insulating gap ΔE of the host model. We vary the gap size in the Haldane model by performing similar calculations for numerous M and deduce a linear dependence of $1/\lambda \sim \Delta E$ as shown in figure 4.7. The linear dependence is similar in the topological and the trivial phase as we compare setups with gaps of equal magnitude. We find that the spin Berry curvature becomes exponentially smaller with increasing distance and the decay rate is controlled by the bulk band gap, i.e. $\Omega \sim \exp(-\Delta E\, d)$. These characteristics are similar to the RKKY-exchange observed in insulating systems [140], which is known to decline exponentially with distance as well. An example hereof is displayed in figure 4.6b, where J^{RKKY}/J^2 is given as a function of distance d in the same model as in figure 4.6a and the exponential behavior is well recognizable in the same range of $40 \lesssim d \lesssim 100$.

The exponential decay of Ω and J^{RKKY} coincides with the far range region discussed in figure 4.5. In the close range region, the Ω dependence on the distance of the impurities appears to be less smooth and sign changes are common. To some degree this is reminiscent of the distance dependent oscillatory behavior of RKKY-interactions

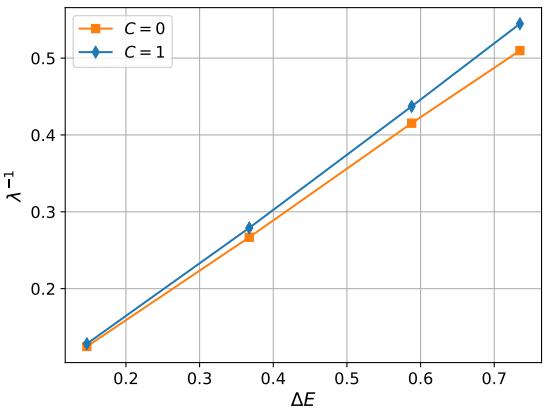

Figure 4.7: Slope $-1/\lambda$ of the distance dependence of Ω as a function of the energy gap ΔE. The gap is controlled by varying M in analogue to setups to 4.6 of 150×150 unit cells.

in semimetals and metals [73–75, 117, 141–143]. A qualitative understanding of the decay of Ω and J^{RKKY} is given by the fact, that both quantities result from virtual second-order-in-J processes, which require excitations of electrons across the energy gap ΔE. Thus, it is not surprising, that larger gaps result in a faster decay (fig. 4.7). Furthermore, the virtual excitations are exponentially suppressed the longer they last. As a result, both Ω and J^{RKKY} decrease exponentially as the distance between impurities increases.

The topology of the host model does not have a major impact on Ω and J^{RKKY} in the presented study (figures 4.5, 4.6 and 4.7) as we find ΔE being the primary factor. When comparing results of the topological and trivial phase, we therefore choose the same ΔE in both phases. In the far range region the sign of Ω changes between the trivial and nontrivial phase, but the absolute values of Ω/J^2 and J^{RKKY}/J^2 are rather small in the setup under investigation. Weak indirect impurity coupling, i.e. small J^{RKKY}, lead to a slow impurity dynamics in general. Furthermore, a small magnitude of $|\Omega|$ leads to a weak geometric spin torque, and thereby does not refine the naive approach to adiabatic spin dynamics significantly.

4.3.1.3 Finite Systems Sizes and Small τ_2

The limit of small τ_2 is interesting as large absolute values of the spin Berry curvature can be observed. Furthermore, weak next-nearest neighbor hopping τ_2 features pronounced differences of the spatial structure of Ω in the topologically trivial ($C = 0$) and the nontrivial ($C = \pm 1$) phases of the host. In figure 4.8 we set $M = 0$, therefore any finite $0 < \tau_2 < 1/3$ and $\xi \neq n\pi$ with $n \in \mathbb{Z}$ leads to a topologically nontrivial phase in the Haldane host. Adiabatic dynamics of the impurities in the discussed setup is described by eq. 4.47 and the limiting case of weak host-impurity exchange is analytically discussed in section 4.1.3.3. We compare host models that are finite spinful

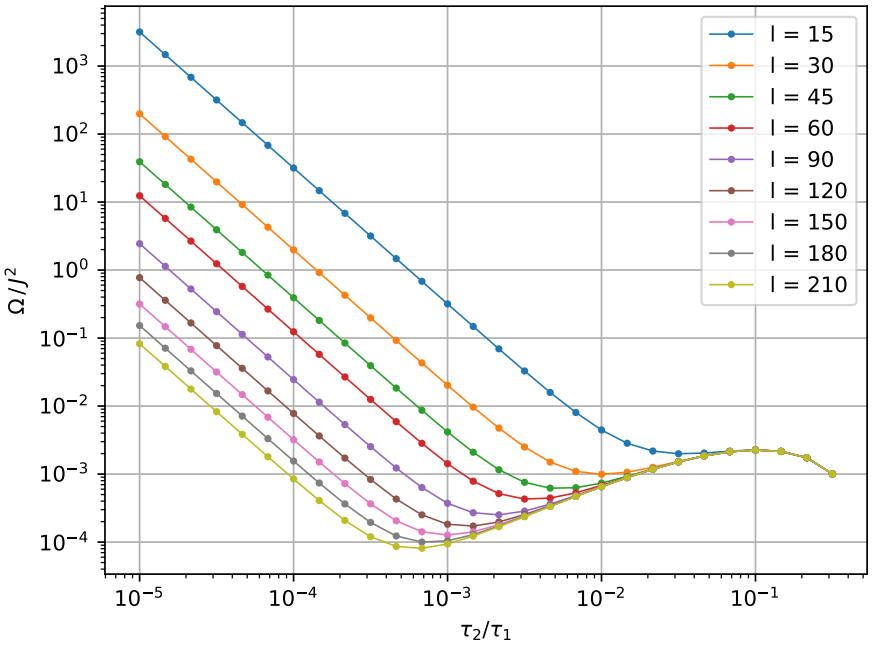

Figure 4.8: Ω/J^2 for impurities at next-nearest neighbor sites as a function of τ_2 for $\xi = \pi/4$ and $M = 0$. Finite lattices with periodic boundary conditions extent l unit cells in both directions of primitive translations.

Haldane slabs with periodic boundary conditions, extending $l = l_1 = l_2$ unit cells in the two directions of primitive translations. Thus, the overall number of sites ranges up to $2l^2 = 88200$ in figure 4.8.

For these 'finite' lattices we deduce $\Omega \sim 1/\tau_2^2$ in the limit of $\tau_2 \to 0$. In the adiabatic equations of motion large Ω dominate the dynamics due to the geometric spin torque (see eq. 4.47) and in the limit of diverging Ω the dynamics slows down as $\dot{\boldsymbol{m}}_q \sim 1/\Omega^2$. Moreover, one can tune Ω via τ_2, e.g. to be in the order of magnitude one, where the rescaling effect of the adiabatic spin dynamics as compared to the naive RKKY-dynamics is most pronounced.

The near range regime, previously mentioned in the discussion of figure 4.6, becomes larger with smaller τ_2. Ultimately, the staggered sign signature of the close range region spreads over the entire lattice, as exemplarily depicted in figure A.4 in the appendix. The lack of the far range region, where Ω decays exponentially with distance, is an indicator for an incomplete description of the bulk of a topological insulator. The divergence $\Omega \sim 1/\tau_2^2$ as $\tau_2 \to 0$ is symptomatic for finite lattices with periodic boundary conditions. In the thermodynamic limit ($l \to \infty$) one inevitably observes a far range region of exponentially declining Ω in the insulating bulk. From figure 4.8 we infer $\Omega \sim \tau_2$ for impurities on next-nearest neighbor sites as $l \to \infty$ and consequently, $\Omega = 0$ for $\tau_2 = 0$ in the thermodynamic limit. The latter is consistent with the fact, that for $M = 0$ and $0 < \xi < \pi$ (or $\pi < \xi < 2\pi$) the Haldane model undergoes a topological phase transition from $\tau_2 = 0$ to any finite $0 < \tau_2 < 1/3$. For these ξ, finite next-nearest

neighbor hopping breaks time reversal symmetry and gives rise to nontrivial bulk band topology, while vanishing τ_2 results in a time-reversal symmetric model and therefore $\Omega = 0$ in the weak coupling limit (see section 4.1.3.2).
An intuitive understanding of the finite size artifact is deduced when discussing the situation in reciprocal space. The smaller the slab with periodic boundaries, the rougher the grid in k-space. All lattice extensions we choose include the K and K' point in their manifold of reciprocal lattice vectors. It is exactly these two points, where the energy gap closes at $\tau_2 = 0$. Their relative contribution in the sum over all $\boldsymbol{k}$ vectors of the first Brillouin zone (see eq. 4.72) becomes more pronounced the rougher the k-space is discretized. Close to the topological phase transition, contributions of $\boldsymbol{k} = \boldsymbol{K}$ and $\boldsymbol{k} = \boldsymbol{K'}$ dominate the sum over $\boldsymbol{k}$ (and $\boldsymbol{k'}$), as they account for the smallest gaps. Ultimately, these summands lead to the divergence of Ω, since no $\boldsymbol{k} = \boldsymbol{K} + \delta\boldsymbol{k}$ ($\boldsymbol{k} = \boldsymbol{K'} + \delta\boldsymbol{k}$, and the same for $\boldsymbol{k'}$) regularize these singular contributions. Furthermore, we can deduce the rate of the divergence from this k-grid argument, since the matrix elements in the numerator of the spin Berry curvature are smooth functions of τ_2. The τ_2 dependence of Ω in this scenario is essentially given by the square of the closing energy gap in the denominator. The latter scales as $\Delta E \sim \tau_2$ (eq. 4.77) at the K- and the K'-point (also see eq. A.19 and eq. A.17), thus $\Omega \sim 1/\tau_2^2$. In the thermodynamic limit, however, reciprocal space is continuous and the contributions from K and K' are regularized.
Similar considerations as for $\tau_2 \to 0$ apply for $\xi \to n\pi$ with $n \in \mathbb{Z}$ and generically for a 'parametric vicinity' to a topological phase transition. One avoids the discussed finite size divergence by sufficient large lattices for the desired parameters. An example of a lattice that is large enough to fulfill these criteria is displayed in figure 4.5. From figure 4.8 we deduce that the smaller τ_2, and with that the closer to the topological phase transition the models parameters are ($M = 0$, $\xi \neq n\pi$ with $n \in \mathbb{Z}$), the larger the lattice has to be to be able to capture features of the Haldane model in the thermodynamic limit appropriately. If the lattice becomes too small, actual host characteristics are overshadowed by finite size effects. Further details on the spin Berry curvature at the topological phase transition of the Haldane model are discussed in section 4.3.1.5.

4.3.1.4 Spin Berry Curvature Dependence on Parameters of the Haldane Model

Following the prior discussion on Ω/J^2 concerning τ_2, our next focus is on a thorough analysis of the impact of parameters M and ξ on the weak coupling spin Berry curvature.
The next-nearest neighbor hopping is fixed to $\tau_2 = 0.1$ on a lattice of 27×27 unit cells, which is of sufficient extent so that finite size effects are of minor relevance for the majority of the $M - \xi$-parameter manifold (compare fig. 4.8 and fig. 4.5). Some hints of finite size effects are, however, inevitable in our setup. The increase of $|\Omega|$ for

$M = 0$ as $\xi \to n\pi$ with $n \in \mathbb{Z}$ in 4.9b as well as the seeming discontinuity of the spin Berry curvature at the topological phase boundary are still related to a finite extension of the periodically bounded lattice. A 'boost' of Ω for $\xi \to n\pi$ and $M = 0$ has been considered in section 4.3.1.3 and is explained analogously to the $\tau_2 \to 0$ scenario. The apparent discontinuity of Ω at the topological phase boundary is discussed in detail in section 4.3.1.5.

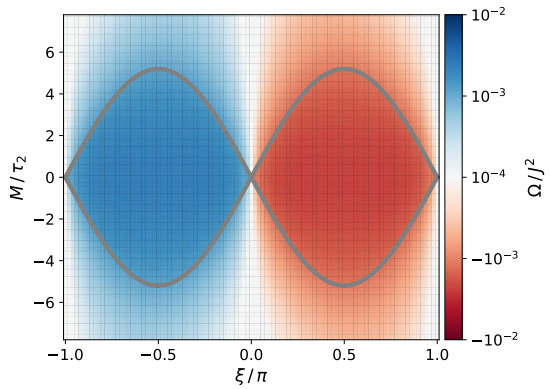

(a) Phase diagram for impurities on next-nearest-neighbor sites ($d = \sqrt{3}$), i.e. impurities couple to host sites of the same sublattice at adjacent unit cells.

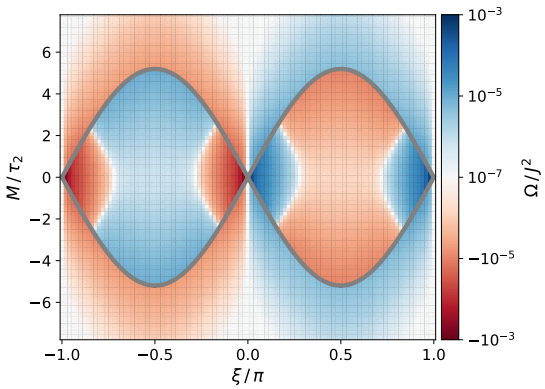

(b) Phase diagram for impurities that are five primitive lattice translation apart ($d = 5\sqrt{3}$), i.e. impurities couple to host sites of the same sublattice at unit cells $5\boldsymbol{v}_1$ apart.

Figure 4.9: Parametric dependence of Ω/J^2 in the $\xi - M/\tau_2$ plane. Thick gray lines indicate the topological phase boundaries of the hosting Haldane model (see fig. 4.3). The defining element of the spin Berry curvature in the weak coupling limit is color coded for a lattice of 27×27 unit cells with periodic boundary conditions and $\tau_2 = 0.1$.

In figure 4.9 we vary the on-site potential M and phase ξ which comes with the next-nearest neighbor hopping (see eq. 4.73 and fig. 4.1). Topological phase boundaries of the host model are indicated by the gray lines. Within the regions of the parameter manifold enclosed by these lines, the Haldane model is in a topologically non-tivial phase ($C = \pm 1$), and outside it is a conventional ($C = 0$) band insulator (see fig. 4.3). First of all, figure 4.9 shows, that Ω changes the sign as $\xi \mapsto -\xi$, while the sign of M does not influence the spin Berry curvature in the weak coupling limit. As the magnitude of M increases, Ω decreases in the trivial phase for $M \to \pm\infty$. This is explained by the associated increase in the insulating gap (eq. 4.77). Other than that, figure 4.9a displays no further features and Ω/J^2 is at most $\mathcal{O}(10^{-3})$ in all of the parameter manifold. As discussed previously (fig. 4.5 and fig. 4.6a), absolute values of the spin Berry curvature become smaller with increasing distance of the impurities. Therefore, the scale of the color bars in figure 4.9a and 4.9b is adjusted to the respective magnitudes of Ω/J^2. While impurities are positioned on next-nearest neighbor sites in figure 4.9a, they are five primitive lattice translations in $\boldsymbol{v}_1$ direction apart in figure 4.9b. Impurities separated by more than $d = \sqrt{3}$ can lead to more complicated parametric

dependencies of Ω. An example thereof is given by figure 4.9b, which exhibits a richer structure of the spin Berry curvature as compared to figure 4.9a. Further examples to various d are displayed in figure A.6.
Study of the parametric dependence of Ω on quantities of the Haldane model suggests, that the spin Berry curvature in the weak coupling regime is a smooth function of the model parameters. Although $\Omega \sim [\epsilon_+(\boldsymbol{k}') - \epsilon_-(\boldsymbol{k})]^{-2}$ (eq. 4.72) in the two band model at hand and the gap closing at the topological phase transition (fig. A.5), the weak coupling spin Berry curvature does not diverge at the host's topological phase transition in the thermodynamic limit. In fact, Ω is actually smooth across the topological phase transition, since the gap closes only at the K or K' point in the first Brillouin zone (fig. 4.2). A detailed discussion on this subject is subsequently given in section 4.3.1.5. Although finite size effects become more pronounced close to a topological phase transition, a lattice extension of $l = l_1 = l_2 = 27$ unit cells and next-nearest neighbor hopping fixed to $\tau_2 = 0.1$ is sufficient to observe a clear gap closing and re-opening transition across the topological phase transition (fig. A.5). In a vast regime of model parameters deficiencies due to the finite extension of the lattice are negligible. Commonly, finite size gaps are of minor relevance as compared to the insulating gap. Furthermore, we argue that the overall small absolute values of the spin Berry curvature are a consequence of the weak magnetic response of the spinful Haldane model in the weak coupling regime. Also, non-zero Ω necessitate virtual second-order-in-J processes, but these processes are suppressed by the bulk band gap.

4.3.1.5 Spin Berry Curvature at the Topological Phase Transition

Sections 4.3.1.3 and 4.3.1.4 indicate the need for a thorough study of the spin Berry curvature at the topological phase transition of the Haldane model. Strictly speaking, topology is associated with a continuous k-space, presuming the thermodynamic limit of $l \to \infty$. And indeed, approximating the bulk of the Haldane model by a finite lattice with periodic boundary conditions leads to a jump $\Delta\Omega$ of the defining element of the spin Berry curvature in the weak coupling limit (eq. 4.37). We define that jump by

$$\Delta\Omega = |\Omega_{triv} - \Omega_{topo}| = |\Omega(M_{crit} + \Delta M) - \Omega(M_{crit} - \Delta M)| \tag{4.81}$$

with $M_{crit} = 3\sqrt{3}\tau_2 \sin(\xi)$. Right at the topological phase boundary the gap closes at the K or K' point, which implies degenerate eigenenergies at the Fermi level. As we consider lattices at half filling that contain the K and the K' point in their discontinuous k-grid, the degeneracy of conduction and valence band at the topological phase transition leads to numerical intricacies. Hence numerically $\Omega(M_{crit})$ is not readily accessible.
In figure 4.10 we study the finite size discontinuity of Ω by variation of the on site

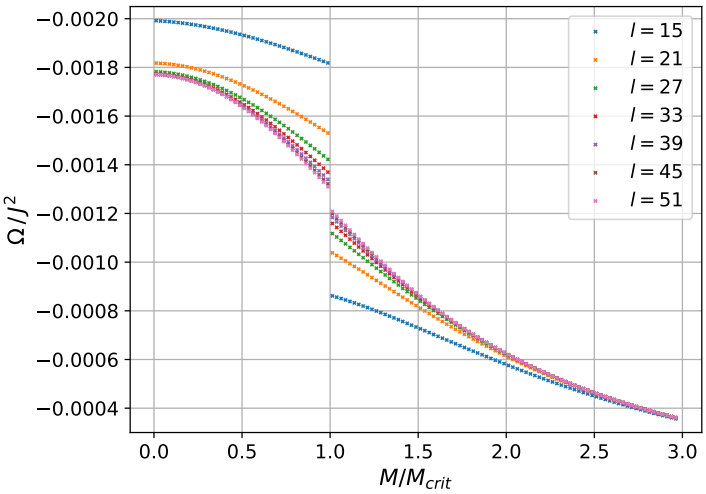

Figure 4.10: Spin Berry curvature Ω for impurities on next-nearest neighbor sites as a function of the relative onsite potential M/M_{crit} across the topological phase transition of the Haldane model. $M_{crit} \approx 0.16$ marks the phase boundary for $\tau_2 = 0.1$, $\xi = 0.1\pi$. Periodic boundary conditions are applied for lattices of l unit cells in both directions of primitive lattice translations.

potential M across the topological phase boundary for various l while maintaining constant values for the other model parameters. We opt for $\tau_2 = 0.1$ and $\xi = 0.1\pi$, where finite size effects are prominent (see discussion in 4.3.1.3 and 4.3.1.4). Lattices extend $l \times l$ unit cells and we apply periodic boundary conditions. Two impurities are locally coupled to next-nearest neighbor sites of the host. Figure 4.81 shows a decreasing jump $\Delta\Omega$ with increasing lattice size. However, linear increase of l leads to a diminishing decline of $\Delta\Omega$, the larger the lattices become. Since Ω is inherently a function of M, one reason we observe finite $\Delta\Omega$ is a constant interval ΔM that fixes the parametric vicinity to the topological phase boundary.

An improved numerical approach to the characteristics of Ω at the topological phase transition of the Haldane host is made by investigating the thermodynamic limit $l \to \infty$ and approaching the phase boundary by $\Delta M \to 0$ at the same time. A study of this twofold limit is depicted in figure 4.11. Following the trends of both limits we conclude, that $\Delta\Omega$ vanishes when taking the two limits ($l \to \infty$ and $\Delta M \to 0$) simultaneously. Hence, based on this numerical study, it can be inferred that the spin Berry curvature remains continuous at the topological phase transition of the Haldane model when impurities are weakly coupled to the bulk.

In fact, one can give an analytical argument to this issue. Close to the topological phase transition in the Haldane host, the contributions from $\boldsymbol{k} = \boldsymbol{K}$ (respectively $\boldsymbol{k} = \boldsymbol{K}'$) dominate the spin Berry curvature. Right at the topological phase transition the energy gap closes at one of these two k-points, i.e. $\epsilon_+(\boldsymbol{K}) = \epsilon_-(\boldsymbol{K})$ or $\epsilon_+(\boldsymbol{K}') = \epsilon_-(\boldsymbol{K}')$. Since $\Omega \sim [\epsilon_+(\boldsymbol{k}') - \epsilon_-(\boldsymbol{k})]^{-2}$ (eq. 4.72) a divergence of the Ω is conceivable. Expanding the dispersion of the Haldane model at the K or the K' point when the

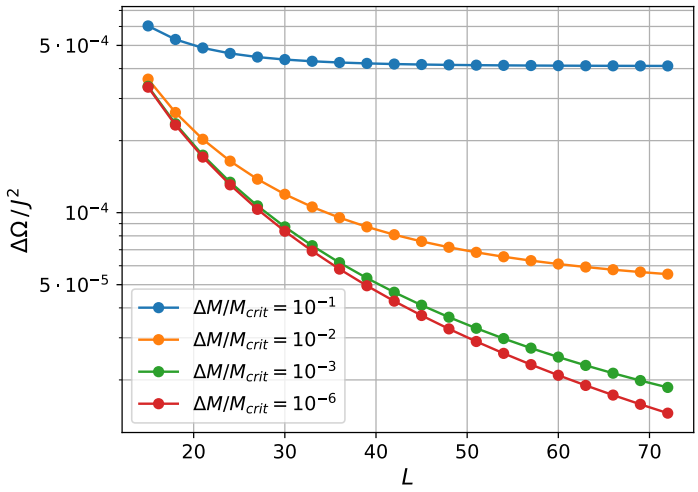

Figure 4.11: Finite size dependence of the jump $\Delta\Omega$ of the spin Berry curvature at the topological phase transition of the Haldane model, considered upon the proximity to the phase boundary with $M = M_{crit} \pm \Delta M$. Impurities are on next-nearest neighbor sites of periodically bounded lattices of $l \times l$ unit cells, with $\tau_2 = 0.1$ and $\xi = 0.5\pi$.

model is parametrically close to a topological phase transition leads to a band structure $\epsilon_{\pm}(\boldsymbol{\kappa}) \sim \pm\sqrt{m + \boldsymbol{\kappa}^2}$ which takes the form of a relativistic Dirac theory [19, 28, 48]. Wave vector $\boldsymbol{\kappa}$ with $|\boldsymbol{\kappa}| << 1$ is taken relative to the k-point of the gap closure. Since $m \sim \Delta E$ is linearly related to the gap (see A.17 and A.19), approaching the topological phase transition is equivalent to $m \to 0$. In fact, the Haldane Hamiltonian in the thermodynamic limit ($l \to \infty$) takes the form of a relativistic Dirac Hamiltonian $H_D \sim \kappa_x \boldsymbol{\sigma}_x + \kappa_y \boldsymbol{\sigma}_y + m\sigma_z$ [28] when expanded around a gap closing point. A Hamiltonian of this form leads to the aforementioned dispersion. Furthermore, the two eigenstates $|\psi_0(\boldsymbol{k})\rangle$ and $|\psi_1(\boldsymbol{k})\rangle$ of H_D, are smooth functions of $\boldsymbol{k} = \boldsymbol{K} + \boldsymbol{\kappa}$ (respectively $\boldsymbol{k} = \boldsymbol{K}' + \boldsymbol{\kappa}$). State $|\psi_0(\boldsymbol{k})\rangle$ refers to the eigenstate related to the occupied valence band (blue in figure 4.2) and $|\psi_1(\boldsymbol{k})\rangle$ to the one of the unoccupied conduction band (orange in figure 4.2) as we assume half filling. Hence, matrix elements $\langle\psi_0|\hat{s}_{i_q\alpha}|\psi_1\rangle$ are finite and smooth functions in $\boldsymbol{k}$.

To analyze a conceivable divergence of Ω for impurities in the bulk at the topological phase transition in the Haldane model we compute I_{bulk}. The contributions to I_{bulk} are the possibly diverging terms for wave vectors in sufficiently small spherical vicinity A with radius Λ around $\boldsymbol{\kappa} = 0$. The sum over occupied and unoccupied single particle states become integrals in the thermodynamic limit, so we obtain

$$I_{bulk} \sim \int_A d^2\kappa \int_A d^2\kappa' \frac{1}{(\sqrt{m + \boldsymbol{\kappa}^2} + \sqrt{m + \boldsymbol{\kappa}'^2})^2}. \tag{4.82}$$

Detailed calculations on the evaluation of the integral are presented in A.2.4. The limit $m \to 0$ of I_{bulk} exists and is proportional to Λ^2. Our focus is on the contributions to Ω

at $\boldsymbol{\kappa} = 0$, so we take the limit of $\Lambda \to 0$ where I_{bulk} vanishes. Consequently, we do not expect a divergence of the weak coupling spin Berry curvature even though the energy gap closes at a singular point of the two dimensional k-space when the Haldane model transitions between distinct topological phases. The result of this analytical proceeding emphasizes that the weak coupling Ω is continuous at topological phase transitions in the Haldane host.

4.3.2 – Weak Coupling at the Edge

So far we discussed various aspects of the spin Berry curvature for impurities coupled to the bulk of a spinful Haldane model. As this host model is a topological insulator, the situation of impurities coupled to the edge of the host can be fundamentally different. For the purpose of studying edge effects in the spinful Haldane model, we consider a host geometry with periodic boundary conditions in l_1-direction and open boundaries in l_2-direction. This geometry leads to an open zig-zag edge and here impurities are coupled to lattice sites at this edge. Due to the bulk boundary correspondence [32, 49, 52], there must be a gapless boundary mode at any edge when the bulk is in a topological nontrivial phase, as the Chern numbers changes from $C = \pm 1$ in the bulk to $C = 0$ in the surrounding vacuum. Consequently, this edge state is featured by the topological Haldane phases only and is absent in the topologically trivial region of the phase diagram (fig. 4.3). Sensitivity of the spin Berry curvature on the band structure of the underlying host model poses the question on the feedback of the host model's topology on $\boldsymbol{\Omega}$ in this setup.

Here, we consider lattices of large but finite extension with open boundaries in one and periodic boundaries in the second direction of primitive translations. The host geometry is defined by l_2 unit cells in $\boldsymbol{v}_2$ direction, bounded by an open zig-zag edge, and l_1 unit cells in $\boldsymbol{v}_1$ direction where periodic boundary conditions apply. An example of this cylinder-like geometry with a zig-zag rim is depicted in figure 4.16a (section 4.3.3). We define a unit cell of finite extension l_2 in $\boldsymbol{v}_2$ direction and a one-dimensional k-space by $k = 2\pi n/l_1$, since analytically utilizing translational invariance enables numerical computations on larger lattices. The number of one-particle eigenstates equals $4l_2$ (A- and B-site per unit cell and spin $\sigma \in \{\uparrow, \downarrow\}$), so half filling requires the lowest $2l_2$ band to be filled. For large, but finite extension in $\boldsymbol{v}_2$ direction, the one particle dispersions $\epsilon_\nu(k)$ with $\nu = 1, ..., 4l_2$ form two quasi-continua, separated by a band gap ΔE (see fig. 4.4). As we label the single particle eigenenergies from the lowest $\nu = 1$ to the highest $\nu = 4l_2$, the dispersion of the edge states $\epsilon_{2l_2} = \epsilon_-$ and $\epsilon_{2l_2+1} = \epsilon_+$ cross is the bulk band gap if $C = \pm 1$. In the topologically trivial phase of the Haldane model ($C = 0$) but close to the topological phase transition ϵ_+ and ϵ_-

take the form of an avoided crossing

$$\epsilon_{\pm} \sim \pm\sqrt{\kappa^2 + m^2}. \tag{4.83}$$

We define $\kappa = k - k_{crit}$ as the distance from k_{crit}, which is the wave vector at which ϵ_+ and ϵ_- cross when $C = \pm 1$.

Once more, our focus is on Ω when the gap closes. In this setup, however, not due to the topological phase transition in the Haldane model, but because impurities are coupled to an open boundary, i.e., an edge of the host lattice with nontrivial bulk band topology. For $C = \pm 1$ there are two effects that can regularize the spin Berry curvature. These are associated with finite l_1 on the one and with finite l_2 on the other hand. Concerning the latter, finite overlap of the edge states leads to a dispersion which takes the form of an avoided crossing in the $C = \pm 1$ phase as well. In this scenario, m and the finite size gap that comes with finite m are associated with (significant) overlap of the edge states, which are exponentially localized at the zig-zag boundaries. Accordingly, such an in-gap gap $\Delta\epsilon = \epsilon_+(k_{crit}) - \epsilon_-(k_{crit}) = 2m < \Delta E$ vanishes for $l_2 \to \infty$. For sufficient large l_2 that overlap becomes inconsequential and it is save to assume $m = 0$.

Concerning finite l_1 and $C = \pm 1$, we calculate the contribution I_{rib} to the weak coupling spin Berry curvature in a small vicinity Λ around the gap closure ($\kappa = 0$) for impurities coupled to the edge of a Haldane ribbon. We then take the limit of $l_1 \to \infty$, thus $m \to 0$, similar to eq. 4.82. Vanishing energy differences in the denominator (see eq. 4.72) might cause Ω to diverge, analog to the more detailed arguments given in section 4.3.1.5. The contribution I_{rib} yields

$$\begin{aligned} I_{rib} &= \int_{-\Lambda}^{\Lambda} d\kappa \int_{-\Lambda}^{\Lambda} d\kappa' \frac{1}{(\sqrt{\kappa^2 + m^2} + \sqrt{\kappa'^2 + m^2})^2}\bigg|_{m=0} \\ &= \int_{-\Lambda}^{\Lambda} d\kappa \int_{-\Lambda}^{\Lambda} d\kappa' \frac{1}{(|\kappa| + |\kappa'|)^2} \\ &\sim \lim_{\varepsilon \to 0} \int_{\varepsilon}^{\Lambda} d\kappa \int_{\varepsilon}^{\Lambda} d\kappa' \frac{1}{(\kappa + \kappa')^2} \\ &\sim -\ln(\epsilon). \end{aligned} \tag{4.84}$$

Any finite l_1 leads to a discrete k-space with $\delta_k = 2\pi/l_1$ and $\varepsilon \sim \delta_k \sim 1/l_1$. Consequently, we derived a weak logarithmic divergence $\Omega \sim \ln(l_1)$ when the Haldane model is in the topological phase and opposing open boundaries are sufficiently far apart.

In figure 4.12 the defining element of the weak coupling spin Berry curvature is displayed as a function of l_1 for various l_2. Impurities are coupled to next-nearest neighbor sites at the same edge and we set $M = 0$, which nullifies sublattice imbalance. Fixing the other parameters, this choice of the on-site potential leads to the largest bulk band

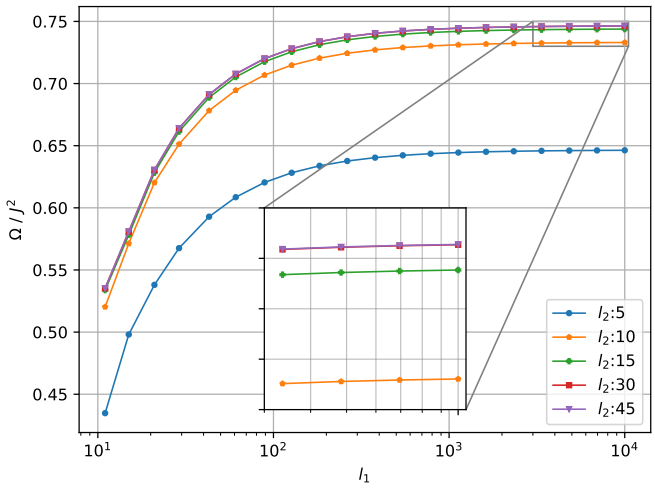

Figure 4.12: Ω/J^2 depending on the extension of the slab. l_1 labels the number of unit cells in the direction with periodic boundary conditions and l_2 the width of the slab between open zig-zag boundaries. Impurities are positioned as next-nearest neighbors on the same zig-zag edge of a Haldane ribbon with $\xi = 0.1\pi$, $M = 0$ and $\tau_2 = 0.1\pi$.

gap in the topologically nontrivial phase, thus, most localized boundary modes. Furthermore, ξ close to $n\pi$ emphasizes finite size effects, so we choose $\xi = 0.1\pi$. Fixing l_1, an increase of l_2 reduces the overlap of edge states localized at opposing boundaries and the associated finite-size m decreases exponentially with l_2. Already for $l_2 = 30$ and $l_2 = 45$ there is no perceptible difference observable in figure 4.12. Hence, Ω quickly converges as a function of l_2 . However, the finite size regularization of Ω is still depending on l_1. The slope of Ω decreases with increasing l_1, but even at $l_1 = \mathcal{O}(10^4)$ the spin Berry curvature still rises with increasing l_1, albeit with a small slope (see insert of fig. 4.12). We observe a close to linear dependence of Ω on $\ln(l_1)$. We do not observe a perfect consensus of the analytical and the numerical study as any non-zero overlap of the edge states impedes the analytically predicted $\Omega \sim \ln(l_1)$ divergence.

By figure 4.12 we confirm, that finite size effects become of minor relevance to Ω when increasing the extension of the lattice. As absolute values of Ω/J^2 are in the order of unity, effects of the geometric spin torque caused by the spin Berry curvature are expected to be of major relevance to the adiabatic impurity dynamics for adequate J. Furthermore, we emphasize, that a zero-dimensional gap closure (singular point) in a 1-dimensional k-manifold boosts Ω. In this sense, a reduction of the phase space is favorable for large Ω. Such a scenario is realized when impurities are weakly coupled to the edge of a topological insulator, where gapless boundary modes are accessible. A zero-dimensional gap closure in a two-dimensional $\boldsymbol{k}$-manifold, however, does not boost Ω, as discussed in section 4.3.1.5. The latter is realized by impurities coupled to the bulk of a Haldane model, where Ω turned out to be continuous at the topological phase transition in the thermodynamic limit.

4.3.2.1 Positioning with One Impurity Coupled to the Edge

To investigate the influence of the gapless edge states featured by the Haldane model in its nontrivial topological phases, we choose a slab geometry for the host lattice. It extends l_1 unit cells in $\boldsymbol{v}_1$ direction to which we apply periodic boundary conditions and l_2 unit cells in the direction of $\boldsymbol{v}_2$ where the boundary is an open zig-zag edge. An example of the described geometry is depicted in section 4.3.3 (fig. 4.16a). We choose the width in the direction of open boundaries to be $l_2 = 15$ unit cells, so there is insignificant overlap of the edge states for the numerical results presented within this section. The topological phase of the Haldane model is controlled by the on-site potential M while any other parameter is kept constant. For the chosen M-values the bulk band gap is the same in the trivial and the topological phase.

In the upper panel of figure 4.13 the Haldane model is in a topologically trivial phase and the modulus of the defining element of the weak coupling spin Berry curvature (eq. 4.37) decreases approximately radial-symmetric. The sign of Ω changes under reflection at the mirror axis containing the fixed central site (green dot) as discussed in section 4.3.1.1. Directly on that axis Ω has to vanish, which is noticeable by a ray

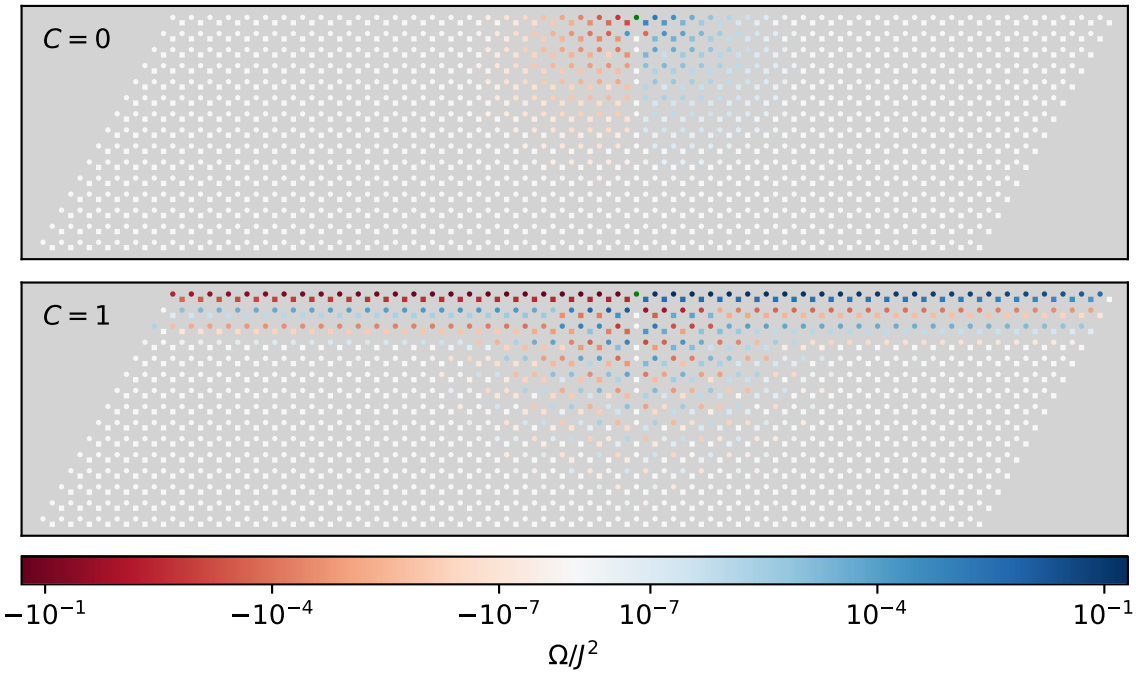

Figure 4.13: Positional dependence of Ω/J^2 (eq. 4.37) when one impurity, marked by the green dot, is locally exchange coupled to an edge site of a Haldane ribbon. The position of the second impurity varies over all remaining lattice sites. In the upper panel with $M = 2M_{crit}$ the host is topologically trivial ($C = 0$), while $M = 0$ in the lower panel gives rise to nontrivial host topology ($C = 1$). The bulk band gap is the same in both panels. Further model parameters are $l_1 = 51$, $l_2 = 15$, $\tau_2 = 0.1$ and $\xi = \pi/4$.

of uncolored lattice sites originating at the fixed green lattice site. For positions of the non-fixed impurity reaching into the bulk, the decay of Ω is consistent with fig. 4.5 in either phase.

In the lower panel of figure 4.13 the host is in a topologically nontrivial state, thus, the host features gapless edge states (see sections 4.2). A signature of these states which are exponentially localized at the open boundaries is the long-range characteristic of Ω. When both impurities are coupled to the same edge, i.e., susceptible to the same gapless boundary mode, the decay of Ω with impurity-distance is significantly slower compared to the scenario where at least one impurity couples to a bulk site. This long-range characteristic of Ω persists for a few unit cells from the edge into the bulk, indicating the spread of the exponentially localized edge modes into the bulk.

Also the absolute values of Ω/J^2 are boosted in the presence of gapless edge modes. The maximal value of the defining element of the spin Berry curvature, divided by the square of the coupling constant, is $\max(\Omega_{triv})/J^2 \approx 1.6 \cdot 10^{-3}$ in the trivial phase ($C = 0$). In the topological phase ($C = 1$), however, it is about two orders of magnitude larger and reaches up to $\max(\Omega_{topo})/J^2 \approx 0.2$ for the parameters of figure 4.13. Interestingly, the largest Ω are obtained for different impurity positions in the topologically trivial and the nontrivial phase. While impurities coupled to next-nearest neighbor sites are the optimal choice when $C = 0$, the largest $|\Omega|$ are observed for impurities $d = 3|\boldsymbol{v}_1| = 3\sqrt{3}$ apart when $C = 1$. When impurities are located far apart at the same zig-zag edge, the relative difference in Ω when transitioning from the topological to the trivial phase is strongly pronounced. For example, the ratio of $\Omega_{topo}/\Omega_{triv}$ for impurities separated by $d = 5\sqrt{3}$ and positioned right at the same edge of the slab exceeds 10^5 in the setup of figure 4.13. This variation of Ω_{top} as compare to Ω_{triv} is a result of the long range characteristic featured solely by the topologically nontrivial ($C = 1$) phase of the host model.

We conclude that the gap less edge modes boost the spin Berry curvature in the weak coupling regime as their dispersion bridges the bulk band gap. Their existence correlates to nontrivial bulk topology and the defining element Ω (eq. 4.37) being sensitive to the gapless modes is therefore suited as marker for the topological phase of the host. In this context, impurities positioned at the edge of a topological insulator, ideally some distance apart, exhibit distinct dynamics (see eq. 4.47) related to the bulk band topology of the host. These differences stem from the disparity between Ω_{top} and Ω_{triv}. Examples hereof are discussed in section 4.3.3.

4.3.2.2 Ω in the Haldane Phase Diagram for Impurities at the Edge

Similar to section 4.3.1.4, we now explore the dependence of the defining element Ω of the weak coupling spin Berry curvature on the parameters of the Haldane model. In this section, however, we focus on impurities coupled to the edge of a Haldane ribbon.

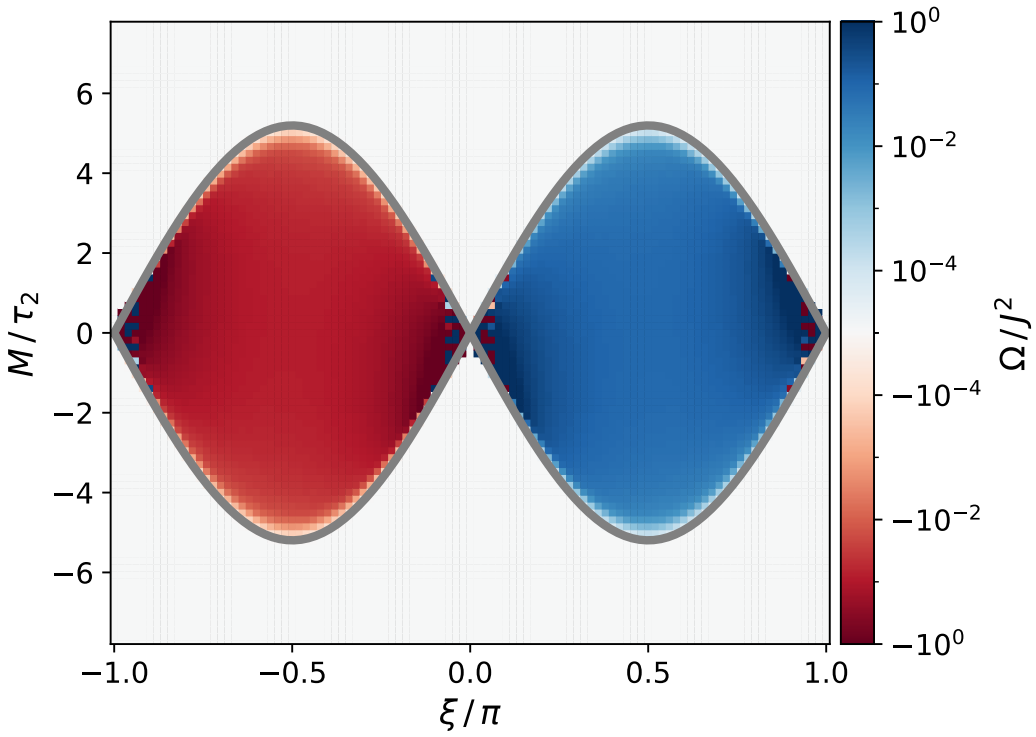

Figure 4.14: Weak coupling spin Berry curvature in the Haldane phase diagram for impurities positioned on next-nearest neighbor sites at the zig zag edge of a $l_1 = 201$, $l_2 = 30$ unit cell ribbon with periodic boundaries in the $\boldsymbol{v}_1$ direction and $\tau_2 = 0.1$.

The most prominent feature of figure 4.14 is the abrupt change of Ω at the topological phase boundary of the host. The Haldane model is in a topologically nontrivial phase ($C = \pm 1$) in the parameter regimes enclosed by the gray lines. We observe near perfect consensus of the topological phase diagram (fig. 4.3) and Ω in the same parameter manifold (fig. 4.14). In the topologically nontrivial parameter regime, the spin Berry curvature is orders of magnitude larger than in areas of trivial bulk band topology, which is caused by the change of the band structure associated with the topological edge states (see section 4.3.2.1).
The link of the topological phase diagram and Ω reaches even further. Altering $\xi \to -\xi$ changes the sign of Ω as well as the sign of the Chern number which defines the topological phases of the Haldane model. In this sense, the spin Berry curvature, and thus the impurity dynamics, is not just sensitive to whether the Haldane model is in a trivial or topological phase, but Ω is also susceptible to the sign of the Chern number featured by the Haldane model. Increasing the distance between the impurities does not result in qualitative changes of the figure 4.14, as long as impurities are located at the same edge. Minor imperfections near $\xi \sim n\pi$ result from the finite k-grid as well as non-zero overlap of the edge states since the slab in this numerical study is of finite extension.

4.3.3 – Dynamics of Two Impurities

In previous sections we discussed the weak (section 4.1.3) and the strong (section 4.1.4) coupling limit of the adiabatic spin dynamics. Here, we display examples of the dynamics and validate the applicability of the adiabatic constraint for two impurities coupled to a spinful Haldane model (see section 4.2) as a quantum host.

4.3.3.1 Dynamics in the Weak Coupling Limit

At first, the weak coupling limit is considered for a host that is invariant under spin rotations, like for example the spinful Haldane model. The adiabatic equation of motion for the two impurities (eq. 4.47) depends on an effective coupling constant J^{RKKY}, the enclosed angle ϑ between the impurities and the defining element Ω of the spin Berry curvature (eq. 4.37).

As this section concentrates on the effects that the spin Berry curvature causes to the adiabatic impurity dynamics, we opt for $J^{RKKY} = 1$, which sets the timescale of the naive adiabatic dynamics, and set Ω to fixed values. In general, J^{RKKY} and Ω are quantities of the host system and the geometry of the setup as derived in section 4.1.3 and with extensive examples discussed in sections 4.3.1 and 4.3.2. Subsequently, we consider dynamics where J^{RKKY} and $\boldsymbol{\Omega}$ follow from the setup of the quantum-classical system in section 4.3.3.2. Furthermore we set $|\boldsymbol{S}_1| = |\boldsymbol{S}_2| = 1$.

Figure 4.15a displays the dynamics of two classical spins in blue and red without geometric spin torque. Both impurities precess around the total spin, which is indicated by the green arrow. $\boldsymbol{S}_T = \boldsymbol{S}_1 + \boldsymbol{S}_2$ is constant of motion (black dot). As we assume a host of zero total magnetic moment and $\Omega = 0$ in this dynamics, we find $\boldsymbol{S}_T = \boldsymbol{\Sigma}$ (eq. 4.48) as a conserved quantity. Here, the modulus of $\boldsymbol{S}_T$ determines the frequency of the precession ($\omega_{prec} = |\boldsymbol{S}_T| \approx 1.8$). This scenario results in an adiabatic spin dynamics $\dot{\boldsymbol{S}}_q$ (eq. 4.47) equal to the naive adiabatic dynamics $\dot{\boldsymbol{S}}_q^N = \frac{\partial H^{RKKY}}{\partial \boldsymbol{S}_q} \times \boldsymbol{S}_q$ with $H^{RKKY} = J^{RKKY}\boldsymbol{S}_1\boldsymbol{S}_2$. In this case, the dynamics is of a Hamiltonian nature and 'symmetric' in the sense that interchanging the impurity labels $1 \leftrightarrow 2$ effectively results in the same dynamics.

Non-zero Ω, on the other hand, result in $\dot{\boldsymbol{S}}_q$ unequal to $\dot{\boldsymbol{S}}_q^N$. Figure 4.15b displays the dynamics of a similar setup, but with a nontrivial $\boldsymbol{\Omega}$. The defining element of the weak coupling spin Berry curvature (eq. 4.37) is set to $\Omega = 0.5$. The total spin is no longer a constant of motion (eq. 4.49), but exhibits a precessional motion around an axis $\boldsymbol{\Sigma} = \boldsymbol{S}_T - \Omega\boldsymbol{S}_1 \times \boldsymbol{S}_2$ (eq. 4.48). This $\boldsymbol{\Sigma}$ is a constant of motion and defines the axis that the impurities $\boldsymbol{S}_q$ precesses around. We note that the precessional axis is tilted compared to the $\Omega = 0$ scenario. The frequency of the $\boldsymbol{S}_q$ and the $\boldsymbol{S}_T$ precession is now determined by $\omega_{prec} = |\boldsymbol{\Sigma}|/(1 - \Omega^2\boldsymbol{S}_1\boldsymbol{S}_2) \approx 2.3$. Here, the nontrivial adiabatic dynamics ($\Omega \neq 0$) is faster than the naive dynamics, i.e. the $\Omega = 0$ scenario. It is to

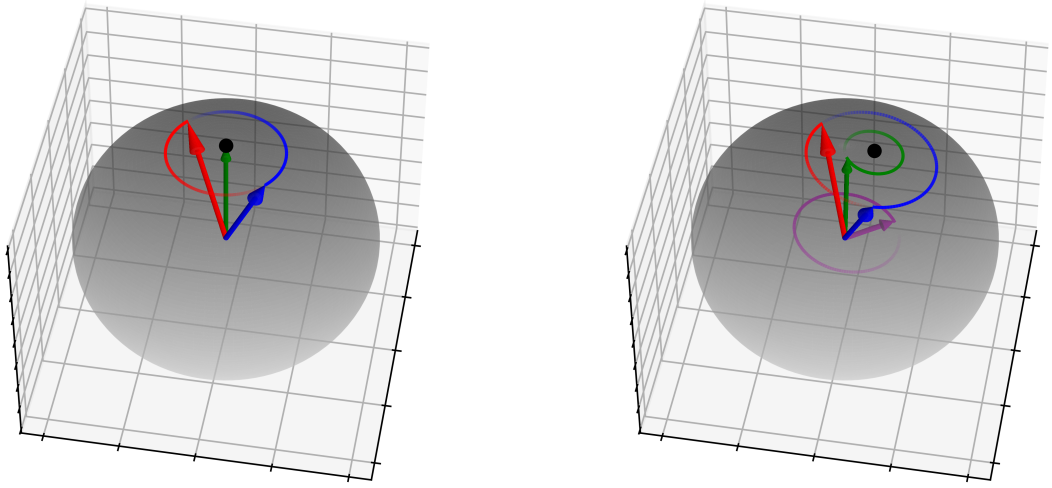

(a) $\Omega = 0$ dynamics with zero adiabatic spin torque.

(b) $\Omega = 0.5$ dynamics with nontrivial adiabatic spin torque.

Figure 4.15: Dynamics of two impurities (red and blue) in the weak coupling limit as derived in section 4.1.3.3. Impurities enclose an angle of $\vartheta = \pi/4$ and $J^{RKKY} = 1$ sets the timescale of the naive adiabatic dynamics (eq. 4.42). Conserved quantity $\mathbf{\Sigma}/|\mathbf{\Sigma}|$ (eq. 4.48) is indicated by the black dot. The normalized total spin $(\boldsymbol{S}_1+\boldsymbol{S}_2)/|\boldsymbol{S}_1+\boldsymbol{S}_2|$ is green and the effective field that leads to the adiabatic spin torque is magenta colored.

mention, that due to the adiabatic spin torque even the direction of motion can change, as compared to the naive adiabatic theory. This change of directionality occurs when $\Omega^2 \boldsymbol{S}_1 \boldsymbol{S}_2 > 1$ (see eq. 4.49).

The adiabatic spin torque is caused by an effective field $\Omega \boldsymbol{S}_2 \times \boldsymbol{S}_1$ (magenta arrow in fig. 4.15b), which leads to non-Hamiltonian dynamics. Interchanging impurity labels $1 \leftrightarrow 2$ requires a simultaneous change of $\Omega \to -\Omega$ to obtain equivalent equations of motion, i.e., observe similar dynamics. In that sense the dynamics is 'asymmetric' for the two impurities and the blue and red trajectory in figure 4.15b are not symmetric around the conserved axis $\mathbf{\Sigma}$ (black dot in figure 4.15b). One cannot formulate a Hamiltonian that results in dynamics of this kind, which is therefore referred to as non-Hamiltonian. Rather, both effects that can be caused by finite Ω (see section 4.1.3.3) are contributing to the dynamics here. That is, a rescaling of the precession frequency ($\sim (1 - \Omega^2 \boldsymbol{S}_1 \boldsymbol{S}_2)^{-1}$) on the one hand and a nontrivial dynamics of $\dot{\boldsymbol{S}}_T$ associated with a tilt of the rotational axis ($\sim \Omega \boldsymbol{S}_2 \times \boldsymbol{S}_1$) on the other hand. Beside the spin Berry curvature these effects depend on the conserved angle ϑ enclosed by the impurities.

4.3.3.2 Applicability of Adiabatic Dynamics in the Presence of Gapless Topological Edge Modes

Next, we approach an example of a specific host model and investigate the applicability of the adiabatic theory. In section 4.3.2 we discussed a setup, where the impurities are at the edge of topological insulator. We argued, that the existence or absence of gapless topological edge states has an effect on the impurity dynamics in the weak coupling limit. Therefore, we propose the observation of spin dynamics (in the adiabatic limit) as a method to detect the topological phase of the host model.

Here, we investigate the dynamics of two classical impurities coupled to next-nearest neighbor sites, i.e. $d = 2\sqrt{3}$, at the zig-zag edge of a spinful Haldane ribbon. Such a setup is sketched in figure 4.16a. Time evolution of the impurities is numerically computed for a $l_1 \times l_2 = 33 \times 10$ unit cell Haldane ribbon with periodic boundaries in $\boldsymbol{v}_1$ direction. In the initial configuration ($t = 0$) impurities enclose $\vartheta = \pi/4$. For now, the Haldane host is set to be in a topologically nontrivial phase with parameters $\tau_2 = 0.1$, $M = 0.5M_{crit} \approx 0.18$ and $\xi = \pi/4$.

Gapless edge modes of the Chern insulator are absent in the topologically trivial phase of the Haldane model, but present in the topologically nontrivial phases. Due to conceivable gapless edge modes of the Haldane host, the question arises of whether the adiabatic spin dynamics, its expansion in the weak J limit and the naive approach to adiabatic spin dynamics are suitable approximations of the impurity dynamics. Strictly speaking, applicability of the adiabatic theorem is not guaranteed when the host features gaples modes which are of non-zero weight at the lattices sites where the impurities interact with the host.

To compare dynamics computed within different approaches (full, adiabatic, adiabatic + weak J, naive) we define

$$\Delta_{XY}(t) = \frac{1}{N_S} \sum_{q=0}^{N_S} \left(\boldsymbol{S}_q^X(t) - \boldsymbol{S}_q^Y(t) \right)^2 \tag{4.85}$$

as a measure of deviation. In the following, abbreviation F relates to dynamics obtained via the full set of equations of motion (eq. 4.5 and eq. 4.6). Moreover, A indicates dynamics which results from the adiabatic equations of motion (eq. 4.19), where the host has no intrinsic degrees of freedom but its dynamics is fully determined by the impurity dynamics by the adiabatic constraint ($|\psi_0\rangle = |\psi_0(\boldsymbol{S}(t)\rangle$). We use P for the dynamics computed within the weak-J perturbation theory of the adiabatic equations of motion (eq. 4.47) and N for dynamics obtained from the naive approach to adiabatic spin dynamics (eq. 4.20). Hence, $X, Y \in \{F, A, P, N\}$ in equation 4.85.

Measure Δ_{XY} describes the mean square deviation of two spin configurations at time t. Deviations are averaged over all impurities, where $\boldsymbol{S}_q^X(t)$ is the configuration of the

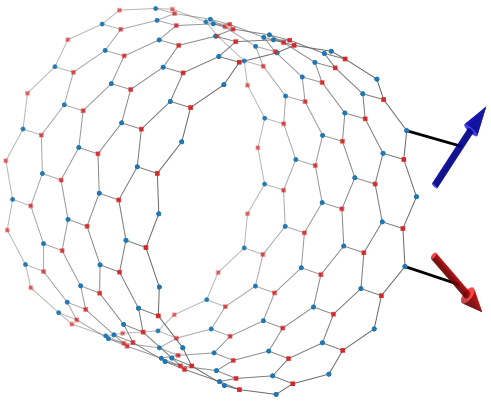

(a) Scheme of a Haldane ribbon with periodic boundaries in $\boldsymbol{v}_1$ direction and impurities coupled to next-nearest neighbor sites ($d = 2\sqrt{3}$) at the open zig-zag edge.

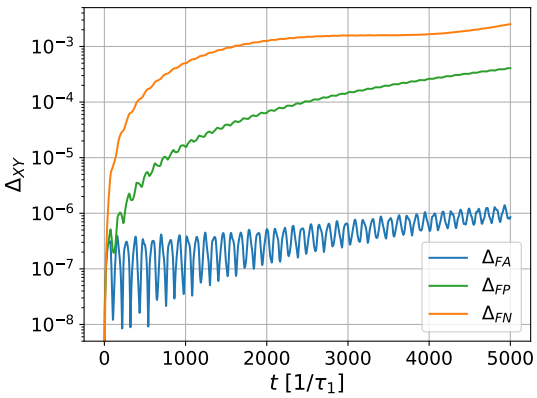

(b) Deviation Δ_{XY} (eq. 4.85) of impurity dynamics for $J = 0.5$. Geometry like fig. 4.16a on a 33×10 Haldane ribbon with $\tau_2 = 0.1$, $M = 0.5 M_{crit}$, $\xi = \pi/4$ and $\vartheta = \pi/4$.

Figure 4.16: Two impurities coupled to the edge of a Haldane ribbon.

q-th impurity at time t computed with equations of motion of theory X. We make use of Δ_{XY} to evaluate the validity and quality of various levels of approximations. The system is initialized identically for all approaches, therefore $\Delta_{XY}(t_0) = 0$. Time propagation of the impurity configuration is obtained by numerically integrating the equations of motion using an explicit eighth-order Runge-Kutta method with a relative numerical error $\Delta_{num} < 10^{-9}$ per time-step. As long as spin-configurations are not too dissimilar and the precession frequencies of different approaches are comparable, Δ_{XY} is a suitable measure to compare impurity dynamics across different approaches. Periods T_0 of the precessional impurity dynamics are determined with a precision of $\Delta T_0 = 1$ throughout this section.

At first, we discuss a rather weak exchange coupling of $J = 0.5$, where impurities just slightly disturb the free ($J = 0$) host. Largest elements of the spin Berry curvature $\boldsymbol{\Omega}$ are the ones of the weak coupling from $\boldsymbol{\Omega}^{(0)}$ (eq. 4.37) with $\Omega \approx 0.03$ ($|\boldsymbol{\Omega} - \boldsymbol{\Omega}^{(0)}| \approx 0.02$). The period time of the precessional impurity dynamics obtained via the respective equations of motion is presented in table 4.1.

Time evolution in the adiabatic theory underestimates T_0 by an relative error

$$\Delta_0^{AF} = (T_0^A - T_0^F)/T_0^F \approx -4.5 \cdot 10^{-4} \tag{4.86}$$

per period and is consequently a very good approximation of the dynamics. Perturbation theory on the other hand overestimates the period time by $\Delta_0^{PF} \approx 5.9 \cdot 10^{-3}$, which is a rather good approximation of the dynamics as well. Worst of the considered approximations is the naive theory of adiabatic spin dynamics, which overshoots T_0 by $\Delta_0^{NF} \approx 3.1 \cdot 10^{-2}$. Comparing the latter indicates relevance of the spin Berry curvature in this quasi adiabatic dynamics. The approach to an effective impurity dynamics is

J	T_0^F	T_0^A	T_0^P	T_0^N
0.5	4425	4423	4451	4565
2	257	243	527	193
5	787	785	253	525

Table 4.1: Period T_0^X of precessional impurity dynamics measured in inverse units of the nearest neighbor hopping, $\tau_1 = 1$, and obtained through time evolution using equations of motion of approach $X \in \{F, A, P, N\}$ for varying values of the host-impurity exchange coupling J. Impurities are coupled to next-nearest neighbor sites ($d = 2\sqrt{3}$) at the edge of a $l_1 \times l_2 = 33 \times 10$ unit cell Haldane ribbon with periodic boundary in $\boldsymbol{v}_1$ direction and an open zig-zag edge in $\boldsymbol{v}_2$ direction. Initially, impurities enclose $\vartheta = \pi/2$. The Haldane host is in a topologically nontrivial phase with parameters $\tau_2 = 0.1$, $\xi = \pi/4$ and $M = 0.5M_{crit}$.

significantly improved by taking even small Ω into account. Agreement of T_0^A, T_0^P and T_0^F advances for even smaller J, as $J = 0.5$ is not strictly weak coupling. For $J = 0.5$ we find $|\langle \hat{\boldsymbol{s}}_{i_q} \rangle| \approx 0.073$, but $|\langle \hat{\boldsymbol{s}}_{i_q} \rangle| = 0$ is assumed in the weak coupling theory. The adiabatic spin torque, however, diminishes for very small J due to the fact that $\Omega \sim J^2$ in the weak coupling limit.

Figure 4.16b displays the accumulated deviations over time. The previous finding, that the adiabatic equations of motion are a well suited approximation to determine the period of the dynamics is affirmed by deviation measure $\Delta_{XY}(t)$. Indeed, the accumulated error over time is $\Delta_{FA} \approx 10^{-6}$ at $t = T_0^F$ appears to follow a linear trend with a rather shallow slope. The much faster electron dynamics, however, feeds back to the impurity dynamics and predominately induces an additional nutational dynamics, which is notable by the oscillatory characteristics of $\Delta_{XY}(t)$ in fig. 4.16b. Such nutational dynamics is somewhat similar to the tight binding dynamics in the purely classical setup (see section 3.1.3). Magnetic moments of the electron system are, however, not just tightly bound. They are neither of uniform magnitude across the entire host, nor necessarily of constant magnitude throughout the dynamics. Moreover, magnetic moments of adjacent host sites can exhibit inherent canting, i.e., might not be collinear. This leads to a more complex overall dynamics, which goes beyond the simple precessional motion with superimposed nutational motion that is associated with the classical tight binding dynamics. Nonetheless, the correction due to nutation in the precessional dynamics can be considered as the leading correction.

The dynamics of the total magnetic moment of the electron system is observed to be of a typical timescale of $t_{\langle \hat{\boldsymbol{s}}_T \rangle} \sim 100$ for the non-precessional dynamics. Hence, the typical inherent dynamics of magnetic moments in the host system are of a significantly faster timescale than the impurity dynamics ($t_{\langle \hat{\boldsymbol{s}}_T \rangle} \ll T_0$). Eventually, the inherent dynamics of host magnetic moments causes minor effects to the overall impurity dynamics. Combining both arguments we conclude, that in our setup the assumption of adiabatic spin dynamics is in general a viable approximation for the impurity dynamics, despite

the lack of a strictly gapped host system.

The perturbative approach to adiabatic spin dynamic is less good of an approximation and accumulates an error $\Delta_{FP} \approx 5 \cdot 10^{-4}$ in the first period. A coupling strength of $J = 0.5$ does, however, not strictly meet the criteria of weak coupling. At this exchange coupling strength the impurities locally polarize the host which contradicts the weak coupling assumption.

Nonetheless, the perturbative approach is a significantly better approximation than the naive approach to adiabatic spin dynamics. Applying the adiabatic constraint solely to the Hamiltonian results is the most erroneous approximation of the impurity dynamics. Deviation Δ_{FN} between the impurity configuration obtained by the full set of equations of motion and the impurity configuration computed via the naive approach to adiabatic impurity dynamics is about an order of magnitude lager than Δ_{FP} after one precessional period, i.e., at $t = T_0^F$. We conclude, that even though elements of $\mathbf{\Omega}$ are of small magnitude in the considered setup, the adiabatic spin torque is an essential contribution to the impurity dynamics. Taking the spin Berry curvature into account in the way the adiabatic equation of motion dos, leads to a significantly better approximation of the impurity dynamics ($\Delta_{FA} \ll \Delta_{FN}$). This improvement arises from a conceptual advancement. Both, the naive and the adiabatic approach, take the same number of dynamic degrees of freedom into account.

Next, we discuss $J = 2$, where exchange coupling is well beyond the perturbative weak coupling regime. Locally, the impurities affect eigenstates and eigenenergies substantially. Angle ϑ enclosed by the impurities is relevant to the aforementioned manipulation of the host by the impurities. In terms of the transition from the weak to the strong J limit, $J = 2$ is in the intermediate regime (see section 5.2.3 and figure 5.7 for impurities in the bulk). In this transition regime elements $\mathbf{\Omega}$ can be of large modulus, here $\max(\mathbf{\Omega}) \approx 0.25$. Moreover, $\mathbf{\Omega}$ takes an intricate form, comparable to the bulk situation shown in fig. 5.7a. As we consider impurity exchange at the open boundary, that intermediate regime is at weaker J in comparison to intermediate the exchange coupling strength in the bulk.

Impurity dynamics is still approximated rather well by the adiabatic theory. For $\vartheta = \pi/4$ impurities precess at $T_0^F = 257$, while adabatic theory predicts $T_0^A = 243$. Dynamics is of a significantly shorter timescale than for $J = 0.5$. Polarization of the host ($|\langle \hat{\boldsymbol{s}}_{i_q} \rangle| \approx 0.26$) has a stronger effect on the impurity dynamics than for $J = 0.5$. This leads to a more pronounced disturbance in the fundamentally adiabatic dynamics. As a consequence, the relative angle enclosed by the impurities oscillates about $\Delta\vartheta \approx \pi/40$. Again, relevance of the spin Berry curvature to the impurity dynamics is emphasized by comparing T_0^F, T_0^A and $T_0^N = 193$. Theory of adiabatic spin dynamics underestimates T_0^F by about 5%. In contrast, the naive approach falls short by nearly 25%, indicating its inadequacy as an approximation.

For large J the adiabatic theory is once more a well suited approximation to evaluate the dynamics of the impurities (see table 4.1). We find $T_0^A/T_0^F \approx 0.997$, and $T_0^N/T_0^F \approx 0.667$ for $J = 5$ and $\vartheta = \pi/4$. Accordingly, adiabatic theory is a good description to approximate the precessional impurity dynamics, while the naive approach to adiabatic dynamics is not. The adiabatic theory predicts the angle enclosed by the impurities to be constant of motion. Upon analyzing the dynamics obtained from the full set of equations of motion, we find $\Delta\vartheta \approx \pi/200$ in full dynamics, indicating that ϑ is essentially conserved. This serves as another indication of the effectiveness of the adiabatic approximation.
Since $|\langle \hat{\boldsymbol{s}}_{i_q} \rangle| \approx 0.41 < 0.5$, exchange coupling $J = 5$ is not strictly in the strong coupling limit. Consequently, T_0^A does not yet equal $2T_0^N$ as derived in section 4.1.4 for the strong coupling limit. Nonetheless, we observe significantly slower dynamics than the naive adiabatic approach suggests. Discrepancy between T_0^N and T_0^F stems from a failure to consider the influence of $\boldsymbol{\Omega}$ on impurity dynamics, which is essential in this setup. The spin Berry curvature is dominated by local blocs ($\Omega_{q\alpha,r\beta}$ with $q = r$), close to the strong coupling limit (eq. 4.54). Non-local blocks ($q \neq r$) are non-zero, but take about one order of magnitude smaller values.
As J approaches the strong coupling limit ($J \to \infty$), the impurity dynamics decelerates, since an electron is increasingly localized at each host site to which an impurity couples. In this limit, $\boldsymbol{\Omega}$ rescales the naive dynamics resulting in $T_0^A = 2T_0^N$ (eq. 4.59). In the limit of $J = \infty$, however, the electrons are strongly bound to the impurity sites, rendering them incapable of mediating spin dynamics through the host. Hence, there is no impurity dynamics at all for infinitely strong host-impurity exchange coupling.

4.3.3.3 Impurity Dynamics Related to the Topological Phase of the Host

Lastly, we take the host's topology into account. Dynamics of the impurities on a topologically nontrivial host ($C = 1$) is compared to dynamics on a trivial band insulator ($C = 0$). To this end, we choose the same setup as before (fig. 4.16a).
We keep the same model parameters $\tau_2 = 0.1$ and $M \approx 0.18$ as in the preceding section. We appoint the topological phase of host by the value of the next-nearest neighbor hopping in the Haldane host. Setting $\xi = 0$ leads to a topologically trivial band insulator ($C = 0$), while $\xi = \pi/4$ results in a topologically nontrivial insulating phase ($C = 1$) for the host system as the topological phase diagram of the Haldane model indicates (fig. 4.3). The bulk band gap is the same in both phases. Furthermore, we set $J = 0.5$ to prevent severe disturbance of the host system's states and ensure reasonably fast dynamics. Details of the impurity dynamics in this setup with a topologically nontrivial host ($\xi = \pi/4$) have previously been discussed in section 4.3.3.2.
In the topologically trivial phase, the period of precessional impurity dynamics obtained using adiabatic spin dynamics matches extremely well with the precessional period

$d/\sqrt{3}$	$T^F_{0,top}$	$T^F_{0,tri}$	J^{RKKY}_{top}	J^{RKKY}_{tri}
1	675	2045	$-4.8 \cdot 10^{-3}$	$1.7 \cdot 10^{-3}$
2	4425	3441	$-7.5 \cdot 10^{-4}$	$9.9 \cdot 10^{-4}$
3	6055	19855	$5.1 \cdot 10^{-4}$	$1.7 \cdot 10^{-4}$
5	3335	>20000	$9.5 \cdot 10^{-4}$	$9.6 \cdot 10^{-6}$
10	3255	>20000	$9.7 \cdot 10^{-4}$	$5.4 \cdot 10^{-8}$

Table 4.2: Period T_0 of precession for impurities coupled to the edge of a $l_1 \times l_2 = 33 \times 10$ unit cell Haldane slab with periodic boundary in $\boldsymbol{v}_1$ direction and an open zig-zag edge in $\boldsymbol{v}_2$ direction. Two impurities couple d apart with $J = 0.5$ at the zig-zag edge. Initially, the impurities enclose angle $\vartheta = \pi/2$. The Haldane host with parameters $\tau_2 = 0.1$, $M = 0.5 M_{crit}$ is in the topological phase for $\xi = \pi/4$ and in the trivial phase for $\xi = 0$.

obtained from the full system's dynamics ($T^F_0 = T^A_0 = 3441$). Since the host model is time-reversal symmetric for $\xi = 0$, the spin Berry curvature in the weak coupling limit $\boldsymbol{\Omega}^{(0)}$ (eq. 4.37) vanishes. Accordingly, the naive approach to adiabatic spin dynamics, with $T^N_0 = 3443$ also serves as a good approximation for impurity dynamics. Minor differences of T^A_0 and T^N_0 result from the fact, that $J = 0.5$ does not strictly resemble the unperturbed host of the weak coupling limit ($|\langle \hat{\boldsymbol{s}}_{i_q} \rangle| \approx 0.05$, $\max(\boldsymbol{\Omega}) \approx 5 \cdot 10^{-4}$). The perturbative approach is the least accurate approximation of the impurity dynamics in this setup, predicting $T^P_0 = 3433$. Nonetheless, perturbation theory is still decent, undershooting the period time by $\Delta^{NF}_0 \approx -2.3 \cdot 10^{-3}$, which is of the same order of magnitude as for the topological host considered earlier (see section 4.3.3.2).

Over all, impurity dynamics for $J = 0.5$ and $\xi = 0$ is about 20% faster than for $\xi = \pi/4$. Thus, precessional motion occurs at a comparable rate across phases of either trivial or nontrivial bulk band topology. We relate the differences to the intricate interplay of local polarization of magnetic momentum and the spatial expansion of the host states that the impurities interact with. Exchange coupling $J = 0.5$ is not strictly weak coupling and for $d = 2\sqrt{3}$ local effects the impurities cause to the host overlap.

However, topological edge modes can affect the impurity dynamics. At large impurity distances d along the edge, we find T_0 for a topologically nontrivial host ($\xi = \pi/4$) to be orders of magnitudes faster than for the trivial host ($\xi = 0$), as shown in table 4.2. Local effects in the host caused by the impurities do no longer overlap when the impurities are sufficiently far apart. Finding $T^{top}_0 \ll T^{tri}_0$ is explained by the long range gapless edge modes featured by a topologically non-tivial host phase. At large impurity distances along the edge, the magnetic susceptibility is drastically enhanced in the presence of topological edge modes ($C = 1$), compared to the topologically trivial phase ($C = 0$) where these edge modes are absent. In the weak coupling limit, the magnetic susceptibility is directly related to the effective coupling of the impurities mediated via the host system (eq. 4.34). But not only J^{RKKY} is amplified by the

gapless edge modes, also the spin Berry curvature is boosted by the topological edge modes (see fig. 4.13). Hence, non-Hamiltonian impurity dynamics is more pronounced when the host system is in a phase of nontrivial bulk topology.
Furthermore, the directionality of the impurity dynamics for small J can be related to the host topology for nearby impurities at the edge. In the considered setup, J^{RKKY} is of different sign for the topological ($C = 1$) and the trivial ($C = 0$) host for $d \leq 2\sqrt{3}$ (see table 4.2).

4.4 – Summary of the Quantum-Classical Adiabatic Spin Dynamics

The focal subject of this thesis is on quantum classical hybrid models, where the local magnetic moment of adatoms is modeled by a classical spin, i.e. a three component vector. Such adatoms are exchange coupled with interaction strength J to a gapped quantum host with a unique ground state. Within this chapter, we discussed analytical and numerical results on adiabatic spin dynamics of local magnetic moments modeled by classical spins coupled to a gapped electron system.
A generic framework for adiabatic spin dynamics in the quantum classical setup is studied in section 4.1.2. The spin Berry curvature $\mathbf{\Omega}$ arises in the equations of motion for the classical degrees of freedom $\boldsymbol{S}$ and generates a non-Hamiltonian adiabatic spin torque in their dynamics. An analytical expression for $\mathbf{\Omega}$ and the adiabatic equations of motion $\dot{\boldsymbol{S}}$ is derived in the weak ($J \to 0$ in section 4.1.3) as well as the strong ($J \to \infty$ in section 4.1.4) coupling limit. On one hand, the spin Berry curvature $\mathbf{\Omega}$ affects impurity dynamics $\dot{\boldsymbol{S}}$ through an overall renormalization of the indirect, $RKKY$-like magnetic exchange. On the other hand, $\mathbf{\Omega}$ leads to an additional coupling of the impurities. For a setup with two impurities and in the weak coupling limit, the adiabatic spin torque leads to a precessional motion of $\boldsymbol{S}_{1,2}$ perpendicular to the axis of an $RKKY$-like dynamics.
We aim to study the interplay of bulk band topology and the dynamics to the magnetic impurities. Hence, a suitable quantum host is constituted by two copies of Haldanes model of a Chern insulator (section 4.2), one for each spin projection $\sigma \in \{\uparrow, \downarrow\}$, which we refer to as the spinful Haldane model.
Extensive studies of the parametric and geometric influences to $\mathbf{\Omega}$ in the weak coupling limit are presented in sections 4.3.1 and 4.3.2. We find $\mathbf{\Omega}$ being smooth across the topological phase transition of the bulk band structure when impurities are weakly coupled to the bulk of the spinful Haldane model. Noteworthy, however, is a boost of the weak coupling spin Berry curvature when impurities couple to the edge of a topological insulator. For two impurities, the defining element Ω of the weak coupling spin Berry curvature can vary over orders of magnitude between phases of trivial and nontrivial

bulk topology. We showed, that for two far-apart impurities weakly coupled along the edge of a topological insulator $\mathbf{\Omega}$ is particularly sensitive to the bulk topology of the host system. This finding is related to the presence or absence of gapless topological edge modes in the quantum host.
In section 4.3.3, dynamics of the impurities is evaluated numerically with a twofold intent. At first, the effects of non-zero geometric spin torque in the weak coupling limit are visualized. Secondly, we validate the fidelity of the adiabatic approximation by comparing adiabatic impurity dynamics with the impurity dynamics obtained via the full set of equations of motion, with the latter accounting for inherent host dynamics. We find, that generically our approach on adiabatic spin dynamics is significantly better than the naive Hamiltonian approach whenever the spin Berry curvature is non-zero. Equation 4.18 is a suitable description of the impurity dynamics not only in the weak, but also towards the strong coupling limit. Moreover, our study of two impurities weakly coupled to the edge of a topological insulator suggests, that adiabatic spin dynamics remains appropriate despite the presence of gapless topological edge modes, which inhibit strict application of the adiabatic theorem. For distant impurities weakly coupled to the edge of the host, we observe significant slower impurity dynamics when the host is in a topologically trivial phase in comparison to phases of nontrivial bulk band topology. Not only the spin Berry curvature, but also an effective $RKKY$-like impurity coupling is boosted by the gapless topological boundary modes. As such gapless modes are featured by a topologically nontrivial phase of the host only, the dynamics of the impurities is found to be sensitive to the topological phase of the host.

5 – Topology of Localized Magnetic Moments on a Chern Insulator

In the theory of topological insulators, the fundamental concept of the bulk-boundary correspondence dictates a gapless boundary mode at the edge of an insulator when the topology of the bulk band structure is nontrivial. The presence and the nature of these boundary modes is determined by topological invariants. An important issue for detecting topological phases of matter is whether there are local signatures of a band insulator's topology. Therefore, we conduct a study to explore the possibility of diagnosing nontrivial bulk band topology by observing changes in the local electronic structure caused by local defects of zero spatial dimension.

Given a topologically nontrivial bulk, the bulk-defect correspondence [20, 32] deduced from the tenfold way outlines in which scenarios zero-energy excitations, exponentially localized at a defect, are guaranteed to exist. In our studies, magnetic impurities are locally coupled to a two-dimensional Chern insulator, specifically the Haldane model. These spatially zero-dimensional defects (codimension 2) are topologically classified as trivial. Hence, for a Haldane model with nontrivial bulk topology the expectation of topologically protected zero modes to be localized at the point defect is unjustified. This does, however, not rule out the potential of a close correlation between localized impurity modes and the topological characteristics of the bulk system.

Several prior studies have investigated the electronic structure in the vicinity of defects in topological insulators [144–154]. Noninteracting models in different Altland-Zirnbauer symmetry classes have been studied under the influence of various types of defects. The aim is to find general conditions, under which eigenenergies of the Hamiltonian cross the bulk band gap or undergo zero-energy crossings in dependence of defect parameters. For example, the response of a time reversal symmetric $\mathbb{Z}_2$ quantum-spin-Hall insulator like the Kane-Mele model [67] to a time-reversal symmetric point impurity has been studied in [146]. In the topologically nontrivial spin-Hall phase they found in-gap states caused by the impurity, but such in-gap states were absent in the topologically trivial phase. The spectral response to site and bond impurities has been studied for the spinless Haldane model in [153]. Again, in-gap states are found to occur for arbitrary strong impurity potentials when bulk topology is nontrivial, but were ab-

sent in the trivial Haldane phase for strong impurity potentials. These characteristics are, however, not generic, which has been demonstrated by models where the impurity cannot distinguish between topologically trivial and nontrivial phases.

In our studies, we employ three-component classical spins of unit length, denoted by $\boldsymbol{S}_q$, to model magnetic impurities. Consequently, the configuration space for these classical spins can be represented as a two-sphere, denoted as $\mathcal{S}^2$. These $\boldsymbol{S}_q$ act as local magnetic fields, which couple to the local magnetic moment at site i_q in a lattice of itinerant electrons. In the numerical studies, the inherent structure of the itinerant electron system is defined by the spinful Haldane model.

For any Hamiltonian $H(\boldsymbol{S})$ with a unique ground state that smoothly depends on a single classical spin $\boldsymbol{S}$ one can compute a first Chern number that characterizes the associated $U(1)$ ground-state bundle over $\mathcal{S}^2$ (see section 2.3). This topological invariant is referred to as the first spin Chern number $C_1^{(S)}$. It characterizes the fiber bundle constructed from the base manifold $\mathcal{S}^2$ and the typical ground-state fiber $|\psi_0(\boldsymbol{S})\rangle$. $C_1^{(S)}$ is a characteristic number of the ground-state bundle that takes values in $\mathbb{Z}$. A change of a topological invariant requires a gap closure, thus the spin Chern number can only change when the ground state becomes degenerate on at least a point of the base manifold $\mathcal{S}^2$, i.e., a subspace of the classical parameter space.

Our aim is to exploit the topological characterization of the S-space in addition to the conventional k-space characterization. For the latter, the base manifold is a 2-torus $\mathcal{T}^2$ formed by the wave vectors in the first Brillouin zone. The associated principal bundle gives rise to the first k-space Chern number C_1, which categorizes, for instance, the topological phases of the Haldane model. The topology of S-space is developed through local interactions, whereas the topology of k-space considers infinite lattice extensions. Hence, they reflect rather complementary physical aspects.

We seek to related these two and trace signatures of k-space topology in the transition characteristics of the spin Chern number. To this end, we study the spectral flow of in-gap states in dependence of the interaction parameter J, which defines the exchange coupling strength between $\boldsymbol{S}$ and the electron system. In the weak coupling limit $J \to 0$, the electron system becomes independent of $\boldsymbol{S}$, so trivially $C_1^{(S)} = 0$. In the strong coupling limit, however, the physics becomes local to the impurity and eventually is gouverned by the magnetic monopole model [15, 16, 33, 38], i.e., a quantum spin-1/2 in an external magnetic field. The spin Chern number in the magnetic monopole model is known to be non-zero for finite external fields, thus, one expects $C_1^{(S)} \neq 0$ in the strong-J limit.

The spin Berry curvature serves a twofold purpose within this thesis, besides its feedback to the adiabatic dynamics of the classical impurity spins, which has previously been discussed in chapter 4, $\boldsymbol{\Omega}$ plays a crucial role in determining the spin Chern number. In fact, the spin Chern number can be calculated by integrating the spin Berry cur-

vature over the base manifold, which, for a single impurity, is $\mathcal{S}^2 \cong \{\boldsymbol{S} \in \mathbb{R}^3 || \boldsymbol{S}| = 1\}$. Moreover, the $\boldsymbol{\Omega}$ is associated with the Berry phase accumulated by the ground state of the electron system as closed loops in $\mathcal{S}^2$ are adiabatically traversed by $\boldsymbol{S}$ [33] (see section 2.2).

In this chapter, we locally couple a number of N_S impurities to different sites of the lattice. Accordingly, the space of calssical spin-configurations is an N_S-fold direct product $\mathcal{S}_1^2 \times ... \times \mathcal{S}_{N_S}^2$. The fiber bundle over this $2N_S$-dimensional base manifold can topologically be classified by the N_S-th spin Chern number $C_{N_S}^{(S)}$. Similar to the single impurity case, $C_{N_S}^{(S)} = 0$ for $J = 0$ and $C_{N_S}^{(S)} = 1$ for $J \to \infty$. In addition to studying the transitions of $C_1^{(S)}$, we investigate the transitions of higher spin Chern numbers ($N_S > 1$) and study the J-spectral flow of single-particle energies ϵ_k. We expound on the computation of spin Chern numbers and argue, that utilizing symmetries of the model can significantly increase numerical efficiency in the computation of $C_{N_S}^{(S)}$.

This section is closely aligned with our paper [155].

5.1 – Computation of Spin Chern Numbers

The Chern number as a topological invariant has been introduced in section 2.3. In this context, our emphasis is on the technical aspects, and we formulate the N-th spin Chern number by employing the spin Berry curvature. The process of computing the spin Berry curvature has previously been detailed in section 4.1.5.

The N-th spin Chern number is defined by

$$C_N^{(S)}(\mathcal{M}^{2N}) := \frac{1}{N!(2\pi)^N} \oint_{\mathcal{M}^{2N}} \mathrm{tr}\left(\omega^N\right) \tag{5.1}$$

with $\omega = dA - iA^2$ as the spin Berry curvature two form. The latter is derived from the spin Berry connection one form A (eq. 5.2) [48]. The trace of ω^N integrated over a $2N$-dimensional closed (compact) orientable manifold $\mathcal{M}^{2N}$ leads to a topological invariant. We note, that any multiplication of n-forms is understood as their exterior (wedge) product and by d we denote the exterior derivative. The integer quantization of $C_N^{(S)}$ may be understood as a consequence of a suitable index theorem, but is generally taken as given by definition [39]. A typical fiber attached to each point of an even-dimensional closed orientable manifold forms a fiber bundle and this fiber bundle can topologically be characterized by a Chen number.

Since $\omega = dA - iA^2$, the curvature two form is a closed differential form, by definition that is $d\omega = 0$. The Abelian spin Berry connection one form is

$$A(\boldsymbol{S}) = i \sum_{q\alpha} \langle \psi_0(\boldsymbol{S})| \frac{\partial}{\partial S_{q\alpha}} |\psi_0(\boldsymbol{S})\rangle dS_{q\alpha}. \tag{5.2}$$

This definition, moreover, causes the Abelian spin Berry curvature to be an exact differential from, i.e. $\omega = dA$ and $A^2 = 0$. Accordingly, the differential two form of that spin Berry curvature is given by

$$\begin{aligned}\omega =& dA = i \sum_{q\alpha, r\beta} \frac{\partial}{\partial S_{r\beta}} \langle \psi_0(\boldsymbol{S}) | \frac{\partial}{\partial S_{q\alpha}} |\psi_0(\boldsymbol{S})\rangle dS_{r\beta} \wedge dS_{q\alpha} \\ =& i \sum_{q\alpha, r\beta} \frac{\partial \langle \psi_0(\boldsymbol{S})|}{\partial S_{r\beta}} \frac{\partial |\psi_0(\boldsymbol{S})\rangle}{\partial S_{q\alpha}} dS_{r\beta} \wedge dS_{q\alpha} \\ =& \sum_{r\beta < q\alpha} \Omega_{r\beta, q\alpha} dS_{r\beta} \wedge dS_{q\alpha}, \end{aligned} \tag{5.3}$$

where terms of the form $\langle \psi_0(\boldsymbol{S})| \frac{\partial^2}{\partial S_{r\beta} \partial S_{q\alpha}} |\psi_0(\boldsymbol{S})\rangle dS_{r\beta} \wedge dS_{q\alpha}$ vanish in the sum.

If one were to consider degenerate ground states, the non-Abelian spin Berry connection (see [69]) would be necessary, which leads to a non-Abelian spin Berry curvature that is still a closed but not necessarily an exact differential form. In the Abelian case of non-degenerate ground states, however, the trace in equation 5.1 becomes trivial, since it is carried out over the degree of freedom of fiber that is one-dimensional in this instance. In our case, the fiber is related to the undetermined phase degree of freedom of the unique many-body ground state the quantum system takes to a given impurity configuration. Thus, the typical fiber is $\mathbb{C}$. Non-Abelian however, that trace runs over the multidimensioal space of states considered in the non-Abelian adiabatic theory [69], e.g. all degenerate ground states. Yet, throughout this thesis, we consistently reference the Abelian spin Berry curvature and henceforth omit the explicit statement of 'Abelian'.

After specifying the typical fiber, we next focus on the base manifold. Each classical impurity spin can point in any direction in three spatial dimensions, but their length is fixed, so the two dimensional parameter space of an impurity is given by the two-sphere $\mathcal{S}_q^2$. Consequently, the overall base manifold

$$\mathcal{M}^{2N_S} = \Pi_{q=0}^{N_S} \mathcal{S}_q^2 \tag{5.4}$$

is the N_S-fold direct product of the two-spheres $\mathcal{S}_q^2$.

The top Chern number is the one that results from pairing the entire $2N_S$-dimensional basis manifold with the $2N_S$-form that is given by the N_S-th Chern character. Hence in our case the N_S-th Chern number is a generic topological index for a setup with N_S impurities and we have $N = N_S$. Since ω itself is a two form (see eq. 5.3), the $2N$-dimensional integral over the $2N$-form ω^N takes the entire base manifold into account.

The factor of $\frac{1}{N!}$ in 5.1 accounts for multi-counting of equivalent contributions when the sum in eq. 5.3 runs over all possible indices. Sufficiently restricting the sum

prevents redundant computation of identical summands and the combinatoric $\frac{1}{N!}$-factor becomes dispensable. This technical detail is a first stake which enhances numerical performance. Furthermore, our definition of the spin Berry curvature in eq. 4.16 requires a restriction of $r\beta < q\alpha$ or an additional factor 1/2 to ensure $C_N^{(S)} \in \mathbb{Z}$ and not twice an integer.

5.1.1 – Exploiting $SO(3)$ Symmetry of the Hamiltonian

Equipped with the preceding considerations we now exemplarily deduce an expression to calculate the top Chern number $C_2^{(S)}$ for two classical impurities coupled to a quantum host. Following up on the computation of the spin Berry curvature (eq. 4.70), a straight forwardly evaluable form of $C_2^{(S)}$ is

$$
\begin{aligned}
C_2^{(S)} &= \frac{1}{2!(2\pi)^2} \oint_{\mathcal{S}_1^2 \otimes \mathcal{S}_2^2} \omega^2(\boldsymbol{S}) \\
&= -\frac{1}{2!(2\pi)^2} \oint_{\mathcal{S}_1^2 \otimes \mathcal{S}_2^2} \sum_{\substack{q\alpha, r\beta \\ q'\alpha', r'\beta'}} \Bigg(\frac{\partial \langle \psi_0(\boldsymbol{S})|}{\partial S_{r\beta}} \frac{\partial |\psi_0(\boldsymbol{S})\rangle}{\partial S_{q\alpha}} \frac{\partial \langle \psi_0(\boldsymbol{S})|}{\partial S_{r'\beta'}} \frac{\partial |\psi_0(\boldsymbol{S})\rangle}{\partial S_{q'\alpha'}} \\
&\qquad dS_{r\beta} \wedge dS_{q\alpha} \wedge dS_{r'\beta'} \wedge dS_{q'\alpha'} \Bigg) \\
&= \frac{1}{(2\pi)^2} \oint_{\mathcal{S}_1^2 \otimes \mathcal{S}_2^2} \sum_{\substack{r\beta < r'\beta' \\ r\beta < q\alpha \\ r'\beta' < q'\alpha'}} \Omega_{r\beta, q\alpha} \Omega_{r'\beta', q'\alpha'} dS_{r\beta} dS_{q\alpha} dS_{r'\beta'} dS_{q'\alpha'} \\
&= \frac{1}{(2\pi)^2} \int_0^{2\pi} d\phi_1 \int_0^{\pi} d\theta_1 \int_0^{2\pi} d\phi_2 \int_0^{\pi} d\theta_2 \sum_{\substack{r\beta < r'\beta' \\ r\beta < q\alpha \\ r'\beta' < q'\alpha'}} \Bigg(\Omega_{r\beta, q\alpha} \Omega_{r'\beta', q'\alpha'} \\
&\qquad \left| \frac{\partial (S_{r\beta}, S_{q\alpha}, S_{r'\beta'}, S_{q'\alpha'})}{\partial (\phi_1, \theta_1, \phi_2, \theta_2)} \right| \Bigg).
\end{aligned}
\tag{5.5}
$$

The first line presents the general formula for the second spin Chern number. In line two, we provided a more explicit expression of the squared Berry curvature two-form in terms of derivatives of the quantum system's ground state and an four-fold wedge product. The orientation of the surface element is fixed by selecting a parametrization (push forward) of the base manifold. Furthermore, we eliminate redundant summands and exploit the definition of the integration of differential forms by choosing a reference order of the base manifold coordinates, which yields the third line. The integrand is an explicit expression of the Pfaffian $\mathrm{Pf}(\boldsymbol{\Omega})$. The Pfaffian specifies the general form of the polynomial that yields all non-redundant summands for any Chern number. Finally, we parameterized the base manifold using the two generic angles θ_q and ϕ_q of spherical coordinates for each $\mathcal{S}_q^2$, resulting in an easily computable expression for the second

spin Chern number.

This formulation, however, does not exploit any symmetries. Utilizing symmetries of the Hamiltonian and ultimately the integrand of the spin Chern number, we can reformulate the integral in a minimal set of generalized coordinates and symmetry based constant factors. The Hamiltonian $\hat{H}(\boldsymbol{S}) = J\sum_q \boldsymbol{S}_q \hat{\boldsymbol{s}}_{i_q} + \hat{H}_H$ where $\hat{H}_H$ (eq. 4.73) is the spinful Haldane model acting as the quantum host, is symmetric under rotations. A rotation of the quantum-classical hybrid model is defined by a spatial rotation of the classical spins alongside a rotation of the quantum spin degrees of freedom in Hilbert space. Thus, $\hat{H}$ is invariant under the aforementioned group action of $SO(3)$ and $\hat{H}(\boldsymbol{S}') = \hat{U}\hat{H}(\boldsymbol{S})\hat{U}^\dagger$. Rotation of the impurities is achieved by $\boldsymbol{S}_q \to \boldsymbol{R}(\boldsymbol{n},\phi)\boldsymbol{S}_q = \boldsymbol{S}'_q \ \forall q$, where $\boldsymbol{R}(\boldsymbol{n},\phi)$ is the matrix causing rotations of angle φ around axis $\boldsymbol{n}$ in three dimensions. The associated rotation of the spin degrees in Hilbert space is described by unitary operator $\hat{U} = \exp(-i\hat{\boldsymbol{s}}_T \boldsymbol{n}\phi)$ with the same $\boldsymbol{n}$ and ϕ. Consequently, three degrees of freedom associated with the thee generators of this symmetry (see eq. A.15) can be eliminated from the integral that determines the spin Chern number.

Since the free ($J = 0$) quantum host is invariant under spin rotations and $\hat{H}$ does not contain external fields, the ground state energy is invariant under simultaneous rotations of the impurities, $E_0(\boldsymbol{S}_1, \boldsymbol{S}_2, ...) = E_0(\boldsymbol{R}\boldsymbol{S}_1, \boldsymbol{R}\boldsymbol{S}_2, ...)$ with $\boldsymbol{R} \in SO(3)$. We shorten the notion of global rotation of all impurities by $\boldsymbol{S} \to \boldsymbol{S}'$ and omit arguments $(\boldsymbol{n},\phi)$ which are set to take the same values for $\boldsymbol{R}(\boldsymbol{n},\phi)$ and $\hat{U}(\boldsymbol{n},\phi)$. Accordingly we find

$$\begin{aligned} E_0(\boldsymbol{S}') =& \langle\psi_0(\boldsymbol{S}')|\hat{H}(\boldsymbol{S}')|\psi_0(\boldsymbol{S}')\rangle \\ =& \langle\psi_0(\boldsymbol{S}')|\hat{U}\hat{H}(\boldsymbol{S})\hat{U}^\dagger|\psi_0(\boldsymbol{S}')\rangle \\ =& \langle\psi_0(\boldsymbol{S})|e^{i\varphi}\hat{H}(\boldsymbol{S})e^{-i\varphi}|\psi_0(\boldsymbol{S})\rangle = E_0(\boldsymbol{S}). \end{aligned} \tag{5.6}$$

We made use of the fact that a non-degenerate ground state has the same symmetry as the Hamiltonian. Furthermore, one can find a common eigenbasis of the Hamiltonian and the unitary operation that characterizes the symmetry, thus $|\psi_0(\boldsymbol{S})\rangle = e^{i\varphi}\hat{U}^\dagger|\psi_0(\boldsymbol{R}\boldsymbol{S})\rangle$. Operator $\hat{U}$ does not depend on $\boldsymbol{S}$, but phase $\varphi = \varphi(\boldsymbol{S},\boldsymbol{n},\phi)$ in principle does.

Next, we show the invariance of the spin Berry curvature two form under simultaneous rotations of all impurities, i.e., $\boldsymbol{S}_q \mapsto \boldsymbol{R}(\boldsymbol{n},\phi)\boldsymbol{S}_q = \boldsymbol{S}'_q \ \forall q$. At first, we recall the consequence of such a rotation on the one form $\sum_\alpha \frac{\partial f(\boldsymbol{S})}{\partial S_\alpha} dS_\alpha$, which is

$$\sum_\alpha \frac{\partial f(\boldsymbol{S}')}{\partial S'_\alpha} dS'_\alpha = \sum_{\alpha\beta} \left(\frac{\partial f(\boldsymbol{S}')}{\partial S_\beta}\frac{\partial S_\beta}{\partial S'_\alpha}\right)\left(\frac{\partial S'_\alpha}{\partial S_\beta} dS_\beta\right) = \sum_\beta \frac{\partial f(\boldsymbol{S}')}{\partial S_\beta} dS_\beta. \tag{5.7}$$

Accordingly, the spin Berry curvature two form $\omega(\boldsymbol{S}')$ of globally rotated impurities is

$$\begin{aligned}\omega(\boldsymbol{S}') =& i\sum_{q\alpha,r\beta}\frac{\partial\langle\psi_0(\boldsymbol{S}')|}{\partial S'_{r\beta}}\frac{\partial|\psi_0(\boldsymbol{S}')\rangle}{\partial S'_{q\alpha}}dS'_{r\beta}\wedge dS'_{q\alpha}\\ =& i\sum_{q\alpha,r\beta}\frac{\partial\langle\psi_0(\boldsymbol{S}')|}{\partial S_{r\beta}}\frac{\partial|\psi_0(\boldsymbol{S}')\rangle}{\partial S_{q\alpha}}dS_{r\beta}\wedge dS_{q\alpha}\\ =& i\sum_{q\alpha,r\beta}\frac{\partial\left(\langle\psi_0(\boldsymbol{S})|\hat{U}^\dagger e^{i\varphi}\right)}{\partial S_{r\beta}}\frac{\partial\left(e^{-i\varphi}\hat{U}|\psi_0(\boldsymbol{S})\rangle\right)}{\partial S_{q\alpha}}dS_{r\beta}\wedge dS_{q\alpha}\\ =& i\sum_{q\alpha,r\beta}\frac{\partial\langle\psi_0(\boldsymbol{S})|}{\partial S_{r\beta}}\frac{\partial|\psi_0(\boldsymbol{S})\rangle}{\partial S_{q\alpha}}dS_{r\beta}\wedge dS_{q\alpha}=\omega(\boldsymbol{S}).\end{aligned}\tag{5.8}$$

Straight forwardly $\left(\frac{\partial}{\partial S_{r\beta}}\langle\psi_0(\boldsymbol{S})|\right)|\psi_0(\boldsymbol{S})\rangle = 0$ vanishes. Furthermore, unitarity ($\hat{U}^\dagger\hat{U} = 1$) of the $\boldsymbol{S}$-independent rotation in Hilbert space $\hat{U}$ yields

$$\sum_{q\alpha,r\beta}\frac{\partial e^{i\varphi}}{\partial S_{r\beta}}\frac{\partial e^{-i\varphi}}{\partial S_{q\alpha}}dS_{r\beta}\wedge dS_{q\alpha}=\sum_{r\beta<q\alpha}\left(\frac{\partial\varphi}{\partial S_{r\beta}}\frac{\partial\varphi}{\partial S_{q\alpha}}-\frac{\partial\varphi}{\partial S_{q\alpha}}\frac{\partial\varphi}{\partial S_{r\beta}}\right)dS_{r\beta}dS_{q\alpha}=0.\tag{5.9}$$

As shown, a simultaneous rotation of all impurities has no effect on the integrand of the second spin Chern number. This statement, in fact, holds analogously for an arbitrary number of impurities, i.e., $C_N^{(S)}$.

Consequently, in case of $C_2^{(S)}$, the integral taking advantage of $SO(3)$ symmetry can be formulated in terms of one angle ϑ enclosed by two impurities as well as α_1, α_2, α_3. The latter account for the three rotations of the entire impurity configuration associated with the generators of $SO(3)$. Transforming the integral to these coordinates leads to an effective one dimensional integration. Hence, exploiting the aforementioned symmetry avoids redundant numerical effort of computing $\boldsymbol{\Omega}$ on the entire four-dimensional base manifold and makes the evaluation of the spin Berry curvature on a one-dimensional submanifold sufficient to compute the second spin Chern number. The integral is taken over

$$\omega^2(\boldsymbol{S}_1,\boldsymbol{S}_2)=\sum_{\substack{r\beta<q\alpha\\ r'\beta'<q'\alpha'}}^{r\beta<r'\beta'}\Omega_{r\beta,q\alpha}\Omega_{r'\beta',q'\alpha'}dS_{r\beta}dS_{q\alpha}dS_{r'\beta'}dS_{q'\alpha'},\tag{5.10}$$

which is denoted as $\tilde{\omega}^2(\vartheta,\alpha_1,\alpha_2,\alpha_3) = f(\vartheta,\alpha_1,\alpha_2,\alpha_3)\sin(\vartheta)\sin(\alpha_2)d\vartheta d\alpha_1 d\alpha_2 d\alpha_3$ in the new set of coordinates. By construction, however, $f(\vartheta,\alpha_1,\alpha_2,\alpha_3)$ does not actually depend on $\alpha_1,\alpha_2,\alpha_3$, as it obeys $SO(3)$ symmetry. Consequently, integration over $\alpha_1,\alpha_2,\alpha_3$ trivially yields a constant factor only. Hence, by exploiting $SO(3)$ symmetry,

the second spin Chern number can be evaluated by

$$\begin{aligned}
C_2^{(S)} =& \frac{1}{(2\pi)^2} \oint_{\mathcal{S}_1^2 \otimes \mathcal{S}_2^2} \omega^2(\boldsymbol{S}_1, \boldsymbol{S}_2) \\
=& \frac{1}{(2\pi)^2} \oint_{\mathcal{S}_1^2 \otimes \mathcal{S}_2^2} \sum_{\substack{r\beta<r'\beta' \\ r\beta<q\alpha \\ r'\beta'<q'\alpha'}}^{r\beta<r'\beta'} \Omega_{r\beta,q\alpha}\Omega_{r'\beta',q'\alpha'} dS_{r\beta} dS_{q\alpha} dS_{r'\beta'} dS_{q'\alpha'} \\
=& \frac{1}{(2\pi)^2} \int_0^{\pi} d\vartheta \int_0^{2\pi} d\alpha_1 \int_0^{\pi} d\alpha_2 \int_0^{2\pi} d\alpha_3 \sum_{\substack{r\beta<r'\beta' \\ r\beta<q\alpha \\ r'\beta'<q'\alpha'}}^{r\beta<r'\beta'} \left(\Omega_{r\beta,q\alpha}\Omega_{r'\beta',q'\alpha'} \right. \\
& \left. \left| \frac{\partial(S_{r\beta}, S_{q\alpha}, S_{r'\beta'}, S_{q'\alpha'})}{\partial(\alpha_1, \alpha_2, \alpha_3, \vartheta)} \right| \right) \\
=& 2 \int_0^{\pi} d\vartheta \sin(\vartheta) f(\vartheta).
\end{aligned} \tag{5.11}$$

5.1.2 – $C_N^{(S)}$ in the Strong Coupling Limit

In the strong coupling limit, it is possible to simplify and analytically perform the calculation of higher spin Chern numbers $C_N^{(S)}$ with $N > 1$. For large J, the model becomes effectively local since we assume local impurity-host interaction. Each impurity polarizes a quantum spin-1/2 at the site it couples to the host, and the host-impurity interaction reduces to a series of uncorrelated monopole models. Recalling the spin Berry curvature in the $J \to \infty$ limit (eq. 4.54)

$$\boldsymbol{\Omega}^{(\infty)} = \mathbf{1}_{NS} \otimes \boldsymbol{\Omega}_{qr}^{(\infty)} \delta_{qr}, \text{ with } \boldsymbol{\Omega}_{qq}^{(\infty)} = \frac{1}{2} \boldsymbol{S}_q \boldsymbol{\mathcal{R}} = \frac{1}{2} \begin{pmatrix} 0 & -S_{qz} & S_{qy} \\ S_{qz} & 0 & -S_{qx} \\ -S_{qy} & S_{qx} & 0 \end{pmatrix} \tag{5.12}$$

we can analytically calculate the top Chern number for an arbitrary number of impurities in the strong coupling limit.

To begin with, we recover the well known result of a single quantum spin-1/2 in an external magnetic field [19] when a single impurity is coupled to the quantum host. Straight forward integration yields $C_1^{(S)}(\boldsymbol{S}) = 1$ for $\boldsymbol{\Omega}$ in the form of eq. 5.12 (see [19] or [53]). As $\boldsymbol{\Omega}$ is of the form of equation 5.12 the spin Berry curvature two from is

$$\omega = -\frac{1}{2} \sum_{q,\alpha\beta\gamma} S_{q\gamma}\, \epsilon_{\alpha\beta\gamma}\, dS_{q\alpha} \wedge dS_{q\beta}. \tag{5.13}$$

The N-th spin Chern number $C_N^{(S)}$ can be obtained through the N-fold exterior product of ω. On the other hand, the N-th power of the spin Berry curvature two-form takes

the factorized form

$$\begin{aligned}
\omega^N &= \left(-\frac{1}{2}\right)^N \left(\sum_{q,\alpha\beta\gamma} S_{q\gamma}\,\epsilon_{\alpha\beta\gamma}\,dS_{q\alpha}\wedge dS_{q\beta}\right)\wedge\left(\sum_{q',\alpha'\beta'\gamma'} S_{q'\gamma'}\,\epsilon_{\alpha'\beta'\gamma'}\,dS_{q'\alpha'}\wedge dS_{q'\beta'}\right)... \\
&= \left(-\frac{1}{2}\right)^N \left(\sum_{\alpha\beta\gamma} S_{q\gamma}\,\epsilon_{\alpha\beta\gamma}\,dS_{q\alpha}\wedge dS_{q\beta}\right)\wedge\left(\sum_{\alpha'\beta'\gamma'} S_{q'\gamma'}\,\epsilon_{\alpha'\beta'\gamma'}\,dS_{q'\alpha'}\wedge dS_{q'\beta'}\right)... \\
&= \left(-\frac{1}{2}\right)^N N!\left(\sum_{\alpha\beta\gamma} S_{1\gamma}\,\epsilon_{\alpha\beta\gamma}\,dS_{1\alpha}\wedge dS_{1\beta}\right)\cdot\left(\sum_{\alpha'\beta'\gamma'} S_{2\gamma'}\,\epsilon_{\alpha'\beta'\gamma'}\,dS_{2\alpha'}\wedge dS_{2\beta'}\right)... \\
&= \left(-\frac{1}{2}\right)^N N!\,2^N\left(\sum_{\alpha<\beta,\gamma} S_{1\gamma}\,\epsilon_{\alpha\beta\gamma}\,dS_{1\alpha}dS_{1\beta}\right)\cdot\left(\sum_{\alpha'<\beta',\gamma'} S_{2\gamma'}\,\epsilon_{\alpha'\beta'\gamma'}\,dS_{2\alpha'}dS_{2\beta'}\right)...
\end{aligned} \tag{5.14}$$

The exterior products of equal one forms vanish, hence all $(q, q', ...)$ have to be pairwise different. For $q = q'$ indices $\alpha, \beta, \alpha', \beta' \in \{x, y, z\}$ have to take at least one value twice. Thus, any $q = q'$ inevitably leads to some $dS_{q\alpha} \wedge dS_{q\alpha} = 0$, which is exploited from the second to the third line. Sufficiently restricting the sums to avoid repeated summation of equivalent contributions brings up a factor of $N!$ which cancels the $1/N!$ in the definition of the spin Chern number (eq. 5.1). It is only a combinatorial factor, as there are $N!$ equivalent arrangements to order the two-forms of different q. For example $dS_{1\alpha_1} \wedge dS_{1\beta_1} \wedge S_{2\alpha_2} \wedge dS_{2\beta_2} = dS_{2\alpha_2} \wedge dS_{2\beta_2} \wedge dS_{1\alpha_1} \wedge dS_{1\beta_1}$, which has been utilized from the third to the fourth line. Furthermore, restricting the sum to $\alpha < \beta$ yields another factor of 2 for each q and finally we choose a parametrization. The acquired equation yields N independent factors.

Next, we substitute obtained result for ω^N (eq. 5.14) in the definition of the spin Chern number, which leads to

$$\begin{aligned}
C_N^{(S)} =& \frac{1}{(2\pi)^N N!}\oint_{\prod_q \mathcal{S}_q^2}\omega^N \\
=& \frac{(-1)^N}{(2\pi)^N}\oint_{\prod_q \mathcal{S}_q^2}\left(\sum_{\alpha<\beta,\gamma} S_{1\gamma}\,\epsilon_{\alpha\beta\gamma}\,dS_{1\alpha}dS_{1\beta}\right)\cdot\left(\sum_{\alpha'<\beta',\gamma'} S_{2\gamma'}\,\epsilon_{\alpha'\beta'\gamma'}\,dS_{2\alpha'}dS_{2\beta'}\right)... \\
=& (-1)^N\left(\frac{1}{2\pi}\oint_{\mathcal{S}_1^2}\sum_{\alpha<\beta,\gamma} S_{1\gamma}\,\epsilon_{\alpha\beta\gamma}\,dS_{1\alpha}dS_{1\beta}\right) \\
& \left(\frac{1}{2\pi}\oint_{\mathcal{S}_2^2}\sum_{\alpha'<\beta',\gamma'} S_{2\gamma'}\,\epsilon_{\alpha'\beta'\gamma'}\,dS_{2\alpha'}dS_{2\beta'}\right)... \\
=& (-1)^N\; C_1^{(S)}(\mathcal{S}_1^2)\; C_1^{(S)}(\mathcal{S}_2^2) = (-1)^N\prod_q C_1^{(S)}(\mathcal{S}_q^2).
\end{aligned} \tag{5.15}$$

In summary, we conclude, that the N-th spin Chern number $C_N^{(S)}$ factorizes into a

product of the first spin Chern numbers $C_1^{(S)}$ in the strong coupling limit. We derived this explicitly for a spin Berry curvature of the strong coupling form (eq. 5.12). However, the specific structure of $\mathcal{M}^{2N} = \prod_q \mathcal{S}_q^2$ has to be pointed out. The factorization is not valid for an arbitrary decomposition of $\mathcal{M}^{2N}$ into sub-manifolds. Simultaneous decomposition of the product manifold $\mathcal{M}^{2N}$ and a matching local block structure of $\mathbf{\Omega}$, i.e., uncorrelated local Hilbert spaces, enable the factorization derived in equation 5.15. It comes down to a coherent factorization of the base manifold and the ground state. For $J = \infty$, the latter becomes a product of the local single particle states localized at the impurity sites and a state that accounts for the rest of the electron system which is disconnected from the impurities. The fiber bundle can be decomposed into independent sub-bundles when no quantum state has spectral weight at impurity sites associated with different subsets of the base manifold. In fact, any spin Chern number over sub-manifolds other than products of the generic Bloch spheres has to be zero in the strong-J limit.

Ultimately, the top Chern number is the topological index suited to characterize the system. In general, 'minor' Chern numbers, e.g. $C_1^{(S)}(\mathcal{M}^2)$ over submanifold $\mathcal{M}^2 \subset \mathcal{M}^{2N}$ for $N \geq 2$, yield little characterizing information on the entire model. The previously discussed scenario is a specific case where the first spin Chern number, $C_1^{(S)}(\mathcal{S}_q^2)$, eminently qualifies as a reference for higher spin Chern numbers $C_N^{(S)}(\mathcal{M}^{2N})$.

5.2 – Spin Chern Transition in the Haldane-Impurity Model

Subsequent to the findings of section 5.1 and equipped with analytical insight in the weak (section 4.1.3.1) and the strong (section 4.1.4) coupling limit, we now consider the spin Chern transition in the Haldane-impurity model. For now we assume that all $J \geq 0$, as negative J result in similar physics, but change the sign of e.g. $C_1^{(S)}(\boldsymbol{S})$ when choosing the same parametrization.

Exchange interaction between the impurities and the host model beyond the weak coupling limit affects the eigenstates and eigenenergies of the unperturbed host. As we assume local host-impurity exchange coupling at sites i_q, only eigenenergies associated with eigenstates of non-zero spectral weight at i_q are affected by the classical spins. We emphasize, that only for $\xi = n\pi/2$ with $n \in \mathbb{Z}$ the Fermi energy E_F is zero. In general, however, the center of the bulk band gap of the Haldane model is a function of the complex phase of the next-nearest neighbor hopping ξ. We choose $\xi = \pi/4$, to account for a generic situation. Moreover, the onsite potential M determines the magnitude of the bulk band gap ΔE (eq. 4.77) as we fix $\tau_2 = 0.1$ and $\xi = \pi/4$. At $M = \pm M_{crit}$ the Haldane model is right at the topological phase transition ($\Delta E = 0$), consequently, for $|M| < |M_{crit}|$ the model is in an insulating phase with nontrivial bulk band topology and for $|M| > |M_{crit}|$ it is in an insulating phase with trivial k-space topology. The

electronic structure of the model as a function of the host-impurity exchange coupling J is obtained by numerical diagonalization of the effective hopping matrix (eq. 4.4), since its eigenvalues are the single particle eigenenergies of the quantum-classical model.
The chemical potential μ is set midway through the bulk band gap. At zero temperature, μ approaches the center of the bulk band gap even for an unequal density of states near the upper edge of the valence and the lower edge of the conduction band (see fig. A.8). For a chemical potential within the bulk band gap, the model is at half filling in the weak coupling limit.

5.2.1 – Single Impurity

At first, a single impurity ($N_S = 1$) is coupled to site i_0 of the A-sublattice in the bulk of the Haldane host. Generally, results for an impurity at a B-site will be different. However, swapping $M \to -M$ and $\xi \to -\xi$ interchanges the roles of the A- and the B-sublattice. Thus, we expect only quantitative differences for an impurity coupled to a site of either sublattice. For the sake of simplicity, we label the single impurity that couples to the host at site i_0 by $\boldsymbol{S}$ within this section and omit further labels.

5.2.1.1 Low-Energy Electronic Structure

For now, we examine the low-energy electronic structure and analyze the eigenenergies within the bulk band gap as the coupling strength J is increased from the weak to the strong coupling limit. We utilize generic parameters $\xi = \pi/4$ and $\tau_2 = 0.1$ in units of τ_1 for this analysis. Under this set of parameters, the Haldane model lacks both particle-hole and time-reversal symmetry.
All panels of figure 5.1 are truncated in their energy range to visualize the situation in and around the bulk band gap ΔE. The energy range with no background color indicates the bulk band gap. A gray line in the center of ΔE refers to the Fermi energy $\mu \approx -0.21$. Red background color indicates the valence band of bandwidth $W_{val} \approx 2.2$ and blue the conduction band of bandwidth $W_{cond} \approx 3.5$. The varying onsite potentials M among the three panels all result in the same bulk band gap $\Delta E \approx 0.37$. The bulk band gap (eq. 4.77) remains unaffected by J. A finite lattice of 39×39 unit cells yields distinct eigenenergies in both the conduction and valence bands, resulting from finite size gaps. In the thermodynamic limit, i.e., in a lattice of macroscopic extension, eigenenergies would densely form both bands. Figure 5.1 illustrates the main characteristics of the J-dependent single-particle eigenenergies ϵ_k, in particular within the bulk band gap. The ϵ_k within the gap show a dependence on the electronic structure of the host, as indicated by different M.
In the left panel with $M = -0.5M_{crit}$, the Haldane model is in a topological nontrivial phase ($C = 1$). The negative onsite potential favors occupation of the A-sublattice,

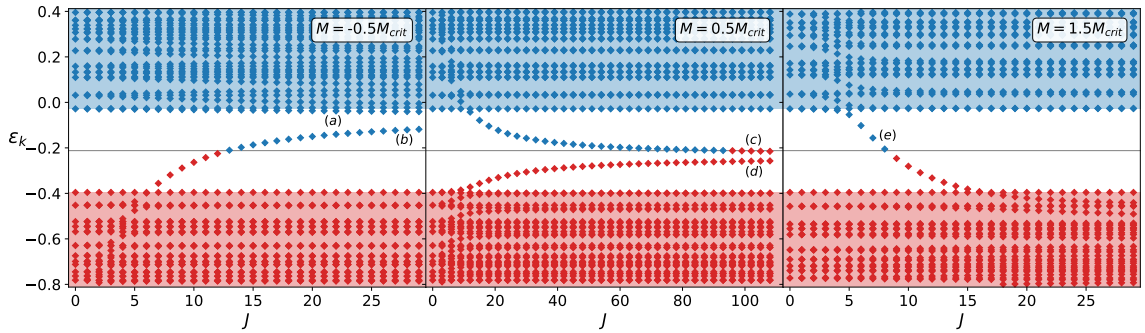

Figure 5.1: One particle eigenenergies depending on the coupling strength J for a single impurity coupled to the bulk of a Haldane model. The panels display situations for different onsite potentials M. Occupied energy levels are depicted by red markers and the bulk valence band is indicated by the red background color, while blue color refers to empty energy levels and the bulk conductance band. The Fermi energy E_F centered in the bulk band gap (uncolored background) is marked by the gray line. Computations are performed on a 39×39 unit cell lattice with periodic boundary conditions, $\tau_2 = 0.1$ and $\xi = \pi/4$.

so $\langle \hat{n}_{i_0} \rangle = \langle \psi_0 | \sum_\sigma \hat{c}^\dagger_{i_0\sigma} \hat{c}_{i_0\sigma} | \psi_0 \rangle > 1$ for finite J. The central panel displays a situation where the Haldane model is in the same topological phase, but with $M = 0.5 M_{crit}$, so occupation of the A-sublattice is energetically disadvantageous, i.e., $\langle \hat{n}_{i_0} \rangle < 1$ for finite J. Moreover, $M = 1.5 M_{crit}$, as displayed in the right panel, yields trivial bulk band topology for the Haldane model ($C = 0$).

For $J = 0$, the first spin Chern number $C_1^{(S)} = 0$ always vanishes, since the parameter manifold $\mathcal{S}$ of the classical impurity spin does not affect the quantum system and the unperturbed spinful Haldane model is trivial concerning the spin Chern number $C_1^{(S)}(\mathcal{S})$. For small but finite J, we find $C_1^{(S)} = 0$ as well, which is easily concluded from the perturbative relation $\mathbf{\Omega} \sim J^2$ (eq. 4.30) in the weak coupling limit. Since $\mathbf{\Omega} = 0$ for $J \to 0$ also $C_1^{(S)} = 0$. Moreover, $\mathbf{\Omega}$ is a continuous function of J in the weak coupling limit, but since $C_1^{(S)}$ is quantized, the spin Chern number cannot change continuously with J. Consequently, $C_1^{(S)} = 0$ holds for small but finite J as well.

When increasing J, the system undergoes a topological phase transition at some finite critical coupling strength J_{crit}. The spin Chern number discontinuously changes from $C_1^{(S)} = 0$ to $C_1^{(S)} = 1$ at this phase transition. The quantum-classical model remains in that spin-topologically nontrivial phase for any $J > J_{crit}$. An in-gap state crossing the chemical potential leads to a degeneracy of the many-electron ground state right at the topological phase transition. Accordingly, the coupling strength where one $\epsilon_k(J) = \mu$ defines J_{crit}.

Due to $SO(3)$-symmetry of the Haldane-impurity model (see section 5.1), single particle energies $\epsilon_k(\boldsymbol{S}) = \epsilon_k$ are the same on the entire manifold of impurity configurations. This $\mathcal{S}^2$ is the base manifold of the fiber bundle that defines the first spin Chern number for a single impurity. To each non-degenerate ϵ_k one can assign a single particle spin

Chern number $c_1^{(S)}$. The single particle energy crossing the chemical potential is non-degenerate in all panels of figure 5.1. The single electron Chern number of the in-gap state crossing μ is nontrivial, i.e., $c_1^{(S)} \neq 0$.
Since the model is non-interacting, single-electron spin Chern numbers are additive, thus, there is a change in the total spin Chern number $C_1^{(S)}$ at J_{crit} determined by the $c_1^{(S)}$ of the in-gap states. As we consider half filling, all $\epsilon_k < \mu$ are occupied. Consequently, the total spin Chern number changes by $\Delta C_1^{(S)} = -c_1^{(S)}$ when a single particle energy crosses μ from below, i.e., the in-gap state becomes unoccupied, and by $\Delta C_1^{(S)} = +c_1^{(S)}$ when a single particle energy crosses μ from above, i.e., the corresponding state gets occupied. Single particle spin Chern number $c_1^{(S)} = +1$ are assigned to in-gap states (a), (c), (e) and $c_1^{(S)} = -1$ to in-gap states (b), (d) in figure 5.1. In all cases, $\Delta C_1^{(S)} = +1$ at J_{crit}.
An exception, where $\epsilon_k \neq \mu$ for any finite J, i.e., no single particle energy crosses the chemical potential, will be subject of a latter discussion. A final remark in this section concerns the choice of μ. If the chemical potential was, for example, set just above the conduction band rather than in the middle of the bulk band gap, possibly a different energy level ϵ_k would intersect with the chemical potential. For example in the central panel of figure 5.1, state (c) would never cross μ and be unoccupied for all J. Instead, state (d) would cross μ from below. However, $\Delta C_1^{(S)} = +1$ would still be the case, although at a then different J_{crit}.

5.2.1.2 The Magnetic Monopole in the Strong-J Limit and the Spin Chern Transition at J_{crit}

The spinful Haldane model is unpolarized at $J = 0$, i.e., $\langle \hat{\boldsymbol{s}}_i \rangle = 0$ at all sites. As the coupling strength J increases, a local magnetic moment $\langle \hat{\boldsymbol{s}}_{i_0} \rangle \neq 0$ forms in the electron system at impurity site i_0. With rising J, this spin moment forms a rigid quantum spin-1/2, i.e., $\langle \hat{\boldsymbol{s}}_{i_0}^2 \rangle \to 3/4$. Thus, the occupation at site i_0 approaches half filling $\langle \hat{n}_{i_0} \rangle \to 1$ for $J \to \infty$. One can assume a single electron being localized at the impurity site for infinite J. Furthermore, the impurity polarizes the local magnetic moment $\langle \hat{\boldsymbol{s}}_{i_0} \rangle \to -0.5\boldsymbol{S}$ in the limit of strong J. Without loss of generality we set $\boldsymbol{S} = \boldsymbol{e}_z$ for now.
Right before the topological spin Chern transition, i.e., $J \to J_{crit}$ from below, we find $\langle \hat{s}_{i_0,z} \rangle \approx -0.46$ and $\langle n_{i_0} \rangle \approx 0.99$ for the left panel in figure 5.1 with $M = -0.5M_{crit}$ where $J_{crit} \approx 12.9$. Moreover, $\langle \hat{s}_{i_0,z} \rangle \approx -0.5$, $\langle n_{i_0} \rangle \approx 1.00$ and $J_{crit} \approx 94.8$ when $M = 0.5M_{crit}$ (central panel in fig. 5.1, and $\langle \hat{s}_{i_0,z} \rangle \approx -0.40$, $\langle n_{i_0} \rangle \approx 0.92$ and $J_{crit} \approx 8.2$ when $M = 1.5M_{crit}$ (right panel in fig. 5.1). The local occupation $\langle n_{i_0} \rangle$ as well as the local spin polarization $\langle \hat{s}_{i_0} \rangle$ are close to the $J \to \infty$ saturation values in all three cases. Yet, as we approach J_{crit} from below, $C_1^{(S)} = 0$.
In the extreme limit of very strong host-impurity exchange ($J \to \infty$), hopping of elec-

trons from and to the impurity site is suppressed. In this case, one can assume a single electron at site i_0 being fully localized and polarized by the impurity. Accordingly, the local physics at i_0 is effectively described by a single quantum spin-1/2 in an external magnetic field in that limit. Hence, $J\boldsymbol{S}$ takes the role of an external magnetic field to the electron and the effective local Hamiltonian reads

$$\hat{H}_{mono} = J\boldsymbol{S}\hat{\boldsymbol{s}}_{i_0}. \tag{5.16}$$

This well-known Hamiltonian serves as the paradigmatic model for a magnetic monopole [15, 33]. The spin Berry curvature of this model is easily derived (see e.g. [33]) and takes the form we refer to as the strong coupling $\boldsymbol{\Omega}$ (eq. 5.12) for a single impurity.

Next, we emphasize an analogy of this magnetic monopole picture to magnetostatics, which proofs to be enlightening in the proceeding discussion. We touched upon the monopole picture in section 2.2 already, but discuss its characteristics in more detail hereinafter. To strengthen the analogy, we apply the notion of $\boldsymbol{R} = J\boldsymbol{S}$ with $\boldsymbol{R} \in \mathbb{R}^3$.

In this single impurity - single electron picture, the spin Berry curvature can be interpreted as a three-component vectorfield (see eq. 2.17) resulting from the curl of the spin Berry connection $\boldsymbol{A}(\boldsymbol{R})$, which itself takes the role of a vector potential. $\boldsymbol{A}(\boldsymbol{R})$ takes the form of the vector potential of a magnetic point charge located at $\boldsymbol{R} = 0$ (see eq. 2.18). Accordingly, the magnetic charge density is $\rho_{mag}(\boldsymbol{R}) = q_{mag}\delta(\boldsymbol{R})$. The Berry curvature, correspondingly, takes the form of the magnetic field induced by this point charge. In case of the magnetic monopole, the spin Berry connection $\boldsymbol{A}(\boldsymbol{R}) = i\langle\psi_0(\boldsymbol{R})|\nabla_{\boldsymbol{R}}|\psi_0(\boldsymbol{R})\rangle$ is the connection of the $U(1)$ bundle of ground states $|\psi_0\boldsymbol{R}\rangle$ over base manifold $\boldsymbol{R}$ and one obtains

$$\boldsymbol{B}(\boldsymbol{R}) = \nabla_{\boldsymbol{R}} \times \boldsymbol{A}(\boldsymbol{R}) = \frac{\mu_0}{4\pi} q_{mag} \frac{\boldsymbol{R}}{|\boldsymbol{R}^3|} \tag{5.17}$$

for the spin Berry curvature.

Integrating the magnetic flux through a closed two-dimensional surface yields the spin Chern number in this picture. Hence, when e.g. a sphere of radius R_0 encloses the magnetic charge, we get

$$C_1^{(S)} = \frac{1}{2\pi} \oint_{|\boldsymbol{R}|=R_0} \boldsymbol{B}(\boldsymbol{R}) R^2 dR = 1, \tag{5.18}$$

for a magnetic charge of $q_{mag} = 2\pi/\mu$.

The monopole model predicts an ill-defined spin Chern number due to the two-fold degenerate ground state of H_{mono} (eq. 5.16) at $J = 0$, i.e., $\boldsymbol{R} = 0$, and $C_1^{(S)} = 1$ for all $J > 0$. In the full Haldane-impurity model, however, the topological phase transition and its concomitant gap closure generically takes place at some finite exchange coupling

$J_{crit} > 0$. Contrary to the monopole model, the Haldane-impurity model requires the impurity to localize electrons and polarize magnetic momentum. While any finite J fully polarizes the single electron in the monopole model, electron states in the spinful Haldane model remain delocalized and are only marginally polarized at small J. Hence, in the Haldane-impurity model the gap closes on the surface $R = |\boldsymbol{R}| = J_{crit}S$ ($S = |\boldsymbol{S}|$) and not only in a singular point $\boldsymbol{R} = 0$ in the space of the external magnetic field. $SO(3)$ symmetry of the Hamiltonian (eq. 4.80) leads to infinitely degenerate eigenenergies $\epsilon_k(\boldsymbol{S}) = \epsilon_k$ on the entire critical surface. Consequently, the N-electron ground state energy $E = \sum_{\epsilon_k<\mu} \epsilon_k$ is equally degenerate, which is apparent at the topological phase transition at J_{crit}.

Relating this to the analogy with magnetostatics, one conceives a magnetic charge q_{mag} uniformly spread over a 2-sphere with radius $R = J_{crit}S$ in $\boldsymbol{R}$ space. Hence, the magnetic charge surface density reads

$$\sigma_{mag} = \frac{q_{mag}}{4\pi J_{crit}^2 S^2}, \tag{5.19}$$

and the magnetic charge density

$$\rho_{mag} = \sigma_{mag}\delta(R - J_{crit}S). \tag{5.20}$$

By help of the divergence theorem and $SO(3)$ symmetry, solving $\nabla_{\boldsymbol{R}}\boldsymbol{B}(\boldsymbol{R}) = \mu_0\rho_{mag}(\boldsymbol{R})$ for the envisioned magnetic field, i.e., the spin Berry curvature, yields

$$\boldsymbol{B}(\boldsymbol{R}) = \frac{\mu_0}{4\pi} q_{mag} \frac{\boldsymbol{R}}{|\boldsymbol{R}|^3}\Theta(R - J_{crit}S). \tag{5.21}$$

Herein Θ is the Heaviside step function. Since $\boldsymbol{R} = J\boldsymbol{S}$, we note $\Theta(R - J_{crit}S) = \Theta(J - J_{crit})$. Accordingly, in the interior of the critical sphere with $|\boldsymbol{R}| = J_{crit}S$ the field $\boldsymbol{B}(\boldsymbol{R})$ vanishes, i.e., for $J < J_{crit}$. Outside of this critical sphere, that is for $J > J_{crit}$, the field takes the same form as for a magnetic point charge at the origin. In this picture one understands, why the single impurity spin Berry curvature, which takes the role of a magnetic field in this monopole analogy, jumps at J_{crit} from $\boldsymbol{\Omega}(J < J_{crit}) = 0$ to its strong coupling form, given by equation 4.54, for $J > J_{crit}$. This jump of $\boldsymbol{\Omega}$ at J_{crit} is of topological origin and is observed in the numerically computation of $\boldsymbol{\Omega}(J)$ as well. The Chern number as the magnetic flux through a sphere of radius $|\boldsymbol{R}| = JS$ is consequently given by $C_1^{(S)} = \Theta(J - J_{crit})$. Thus, it changes discontinuously from $C_1^{(S)} = 0$ for $J < J_{crit}$ to $C_1^{(S)} = 1$ for $J > J_{crit}$ and is ill-defined right at $J = J_{crit}$.

Since hopping from and to the impurity site is suppressed for $J \to \infty$, the rest of the host model is decoupled from the impurity site and therefore also from the locally coupled $\boldsymbol{S}$. Consequently, the Haldane model excluding impurity site i_0 yields $C_{1,rest}^{(S)} =$

0, since it is unrelated to $\mathcal{S}^2$.
For a single impurity, we reasoned that the spin Chern number of the full model (eq. 5.1) can analytically be computed via the magnetic monopole model (eq. 5.16) in the $J \to \infty$ limit. Combining this insight with the fact that $C_1^{(S)} = 0$ for $J \to 0$ (see eq. 4.30), the necessity for a topological phase transition at some intermediate $J = J_{crit}$ becomes apparent. Such a transition requires an in-gap state to cross the chemical potential μ as a function of J, i.e., one $\epsilon_k(J_{crit}) = \mu$. We also calculate $C_1^{(S)} = 0$ and $C_1^{(S)} = 1$ numerically for various J. In the numerical studies, the spin Chern number is obtained from equation 5.1, with the spin Berry curvature being computed via equation 4.70.

5.2.2 – Connecting the Spin Chern Transition and k-Space Topology

Transitions of the spin Chern number are driven by the host's electronic structure that is localized in the vicinity of the impurity. Acting like a local magnetic field $J\boldsymbol{S}$, the impurity locally spin-polarizes the electron system, which lifts the spin $SU(2)$-symmetry of total-spin multiplets of the spinful Haldane model, i.e., at $J = 0$. This local Zeeman effect forms two high-energy states for large J, which are not visible in figure 5.1, since therein only the low energy regime of eigenenergies close to the bulk band gap are displayed.
Assuming an impurity spin orientation $\boldsymbol{S} \sim \boldsymbol{e}_z$ in the $+z$ direction, a spin-down state decreases in energy as coupling strength J increases. This spin-down state separates from the lower edge of the valence band as the coupling strength reaches approximately the energy of the valence band bandwidth W_{val}. Similarly, a spin-up state increases in energy, separating from the upper edge of the conduction band at $J \sim W_{cond}$. Such Zeeman-splitting characteristics occur irrespective of the electron system's parameters. Both of these high-energy states, with $\epsilon_k \sim \pm J$ for sufficiently large J, are exponentially localized in the vicinity of i_0. In the limit of $J \to \infty$, they become fully localized at the impurity site and constitute the magnetic-monopole model of equation 5.16.
Concerning the localized low-energy states within the bulk band gap (see fig. 5.1), the physical reasoning is more intricate. Their nature very much depends on the k-space topology of the Haldane host, which is characterized by the first bulk band Chern number C_1 (see fig. 4.3). Disregarding trivial spin-duplication, the topologically nontrivial Haldane phase has $C_1 = \pm 1$.
We find two in-gap states for sufficiently large J whenever k-space topology is nontrivial, examples hereof are states (a), (b) and (c), (d) in figure 5.1. Their eigenenergies lie in the bulk band gap for sufficiently large J. With J increasing from the weak towards the strong coupling limit, one eigenenergy splits off the upper edge of the valence band and one off the lower edge of the conduction band. Both do not merge back into the continuum again, instead, their energies degenerate in the bulk band gap for $J \to \infty$.

Contrarily, in the trivial Haldane phase ($C_1 = 0$) the bulk band gap is completely bridged by a single in-gap state as a function of J. Depending on parameters of the electron system, a single particle state splits of the continuum of the valence or the conduction band as a function of J. It merges, however, back into the respective other continuum at finite J. Consequently, there is no in-gap state at $J \to \infty$ as the example of state (e) in figure 5.1 illustrates.

At infinite host-impurity exchange, the impurity acts like a hard, zero-dimensional defect to the host. In our scenario, that is a point-defect in both the spin-up and the spin-down copy of the Haldane model. The Haldane model belongs to class A in the Altland-Zirnbauer classification [31] and since it is a two-dimensional model, a point-defect is of codimension two (codimension = bulk dimension - defect dimension) [20]. According to the ten-fold way which relates bulk topology to gapless modes localized at topological defects [32], a model of class A in two spatial dimensions is topologically classified trivial for a defect of codimension two. Consequently, referring to the bulk-boundary correspondence, there is no reason to expect a topologically protected zero mode localized at i_0 for the topologically nontrivial host ($C_1 = \pm 1$).

For 'soft defects', i.e., finite impurity strengths, is it known that bound states around a defect can serve as a local signature of a topologically nontrivial bulk, even though the ten-fold way classifies a defect of the considered codimension as trivial for the respective system under consideration [146, 149]. Hence, one might also expect a close relation between the bulk Chern number and the occurrence of topological edge modes for the presented setup of a magnetic point impurity in a spinful Haldane model. In fact, the existence of edge states in the Haldane model subject to various nonmagnetic local impurity potentials was found to be associated with the bulk band topology [153]. In the subsequent proceedings, we provide a comprehensible understanding why a localized spin-up and spin-down mode must exist in the strong J-limit for a host of nontrivial bulk topology. Such an ingap mode is predominately localized at the nearest neighbor sites of i_0 and is absent in the topologically nontrivial host phase.

We start the discussion by noting that in the limit of $J \to \infty$ the low-energy structure around the bulk band gap is determined solely by the spinful Haldane model with a hole at i_0. If one assumes a macroscopically large hole, the bulk-boundary correspondence demands a topologically protected zero mode at the one-dimensional boundary of that hole if the k-space topology of the Haldane model is nontrivial, i.e., $C_1 = \pm 1$. In that case, there is a dispersive chiral edge mode bridging the bulk band gap for both spin projections. As this in-gap mode inevitably crosses the chemical potential μ within the bulk band gap, it is also referred to as a gapless zero mode. Due to its dispersion, the number of in-gap states forming this gap-bridging edge mode is determined by a fraction of the number of unit cells N_{edge} along the edge, as any finite number of unit cells along the open boundary results in a finite k-grid. For a Haldane model in a

cylinder like geomertry, i.e., with two edges, figure 4.4a displays the two topologically protected zero modes that bridge the bulk band gap. This figure also illustrates that the in-gap modes occur in a finite k-range only. The number of unit cells along the edge of the hole is proportional to the hole's radius r, i.e., $N_{edge} \propto 2\pi r$. Reducing the radius of the hole essentially means increasing the discretization of the edge in real space. Consequently, the coarser k-grid leads to fewer in-gap states forming the edge mode. Ultimately, when shrinking the hole to a single site, the finite-size thinning of the edge mode leads to just a single in-gap state per spin projection. Generically, this single in-gap state is not located at μ, i.e., the system is not gapless.

In the limit of infinite J, the spin-up and spin-down edge states degenerate, as the impurity site i_0 decouples energetically from the Haldane model. Thus, the lattice without i_0 is unaffected by the impurity. At large but finite J, however, the spin-up and the spin-down in-gap states are non-degenerate, as the classical spin feeds back to the edge-state due to finite hopping between i_0 and its adjacent lattice sites. We observe exactly these Zeeman-split edge modes for sufficiently large J in the left and central panel of figure 5.1, where k-space topology of the spinful Haldane model is nontrivial.

Moreover, we investigate the characteristics of finite holes in the lattice of the Haldane model. In figure 5.2, finite clusters of lattice sites centered around i_0 are (energetically) removed from the Haldane model. Each cluster includes site i_0 and all sites linked to i_0 by r or less nearest neighbor hoppings on the honeycomb lattice. We refer to this specification of distance, framed in terms of nearest-neighbor hoppings, as the 'honeycomb metric.' Hence, we may think of r as the radius of the hole with respect the honeycomb metric.

As previously argued for a single-site hole, the hole sites are dynamically decoupled from the low-energy electronic structure when classical spins couple to all sites of a hole by infinite J. Hence, in the limit of infinitely strong exchange coupling ($J \to \infty$), the low-energy sector of a Haldane-impurity model is the same as for a Haldane model where the hole-sites are removed from the lattice. Here, the eigenenergy spectra in figure 5.2 are numerically evaluated for $J = 10^3$ and impurities at all the hole-site are co-aligned ($\boldsymbol{S}_q = \boldsymbol{e}_z \, \forall q$), which effectively removes the hole sites from the electronic structure in and around the bulk band gap.

The left panels of figure 5.2 display the low-energy electronic structure of the Haldane model with a hole of the respective radius r. A honeycomb lattice is displayed in the right panels, where green sites mark the holes, violet sites indicate the edge and gray illustrates further sites of the Haldane model. All sites at the edge of the Haldane model belong to the same sublattice. A-sites are indicated by full colored circles and B-sites by pale colors. For the largest displayed hole with $r = 9$, a number of 136 sites (green) are removed from the lattice and the outer shell, i.e., the edge of the Haldane

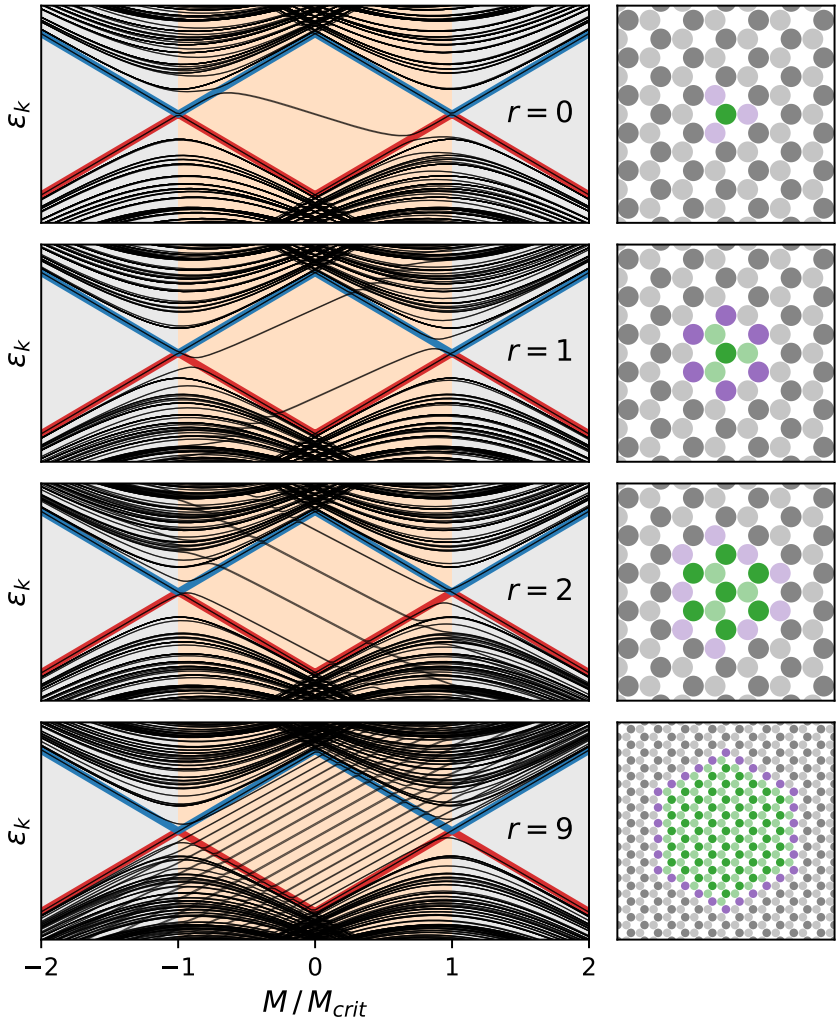

Figure 5.2: Single particle eigenenergies ϵ_k of the Haldane model with a 'hole' as a function of the on-site potential M (left panels). Holes are centered around site i_0 with radii $r = 0, 1, 2, 9$ (from top to bottom) in the honeycomb metric, which is specified in the text. Blue and red lines indicate the bulk band gap in the right panels and the orange background the topologically nontrivial Haldane phase. Right panels display the hole sites (green) and the first shell, i.e., the boundary of the Haldane model to the hole (violet). Further sites of the Haldane model are gray. Full colored circles in the right panels indicate A-sites and pale circles B-sites. Hopping between the Haldane model (violet and gray sites) and the hole (green sites) is effectively prevented by exchange coupling impurities with $J = 10^3$ to all hole-sites. Computations are performed on a 39×39 unit cell lattice with periodic boundary conditions, $\tau_2 = 0.1$ and $\xi = \pi/2$.

model at $r+1=10$ from i_0 (violet), is formed by $3(r+1)=30$ A-sites.

In the lowest left panel of figure 5.2, in-gap states between the red and the blue bold lines are found for nearly all $-M_{crit} < M < M_{crit}$, which corresponds to the topologically nontrivial phase indicated by an orange background color. In the limit $r \to \infty$, these in-gap states would densely fill the entire bulk band gap in the M-range that corresponds to nontrivial k-space topology. Besides a decrease in the number of in-gap states, the spectral flow with M remains qualitatively unchanged for holes of smaller radii r. Based on the aforementioned arguments, we relate this reduction in the number of in-gap states to the diminishing number of edge sites, which implies an increasing discretization of the edge for smaller r.

In-gap states are predominately localized at the edge sites at $r+1$ (violet). Their weight reduces significantly and ultimately declines exponentially further away from the hole. Even though the honeycomb lattice is bipartite, the edge sites of any hole constructed via the honeycomb metric are assigned to the same sublattice. Due to their exponential localization at the edge, the in-gap states' energies increase (decrease) about linearly with increasing M for holes of odd (even) radius, where the edge is formed solely by A (B) sites. Figure 5.2 displays a neat numerical verification of this pattern.

When shrinking the hole to a single site, a single spin-degenerate edge mode is primarily localized on the three nearest neighbor sites of i_0 (violet sites in the upper right panel of fig. 5.2). It is exactly this edge mode that we observe as in-gap states (a), (b) and (c), (d) in figure 5.1, albeit slightly spin split due to finite J. Such in-gap states are observed as a remnant of the topologically protected chiral edge mode of a hypothetical one-dimensional defect within the two-dimensional Chern insulator belonging to Altland-Zirnbauer class A. Its existence is rooted in the nontrivial topology of the bulk system and the bulk-boundary correspondence, i.e., a defect of codimension-1. Consequently, these in-gap states can be interpreted as remnants of the topologically protected gapless zero mode that is bound to exist for an infinitely large hole ($r \to \infty$).

The single in-gap mode ($r=0$), however, must not be understood as a 'real' topologically protected zero mode of a point defect at i_0. If it was a topologically protected edge mode of a zero-dimensional defect, that mode would have to reside at the chemical potential μ within the bulk band gap. But the top left panel of figure 5.2 shows, that the energy of the in-gap mode of a point defect changes depending on M. A topologically protected zero mode, however, has to exist throughout the entire phase of nontrivial bulk topology. The dispersion of such a topologically protected edge mode may be deformed by model parameters, but when remaining in the same topological phase, it must always coincide with μ. The energy of an individual in-gap state, however, depends on M about linearly. Consequently, it cannot coincide with any fixed μ throughout the entire topological phase. Hence, our reasoning is consistent with the necessary absence of a topologically protected zero mode for a point-defect

(codimension 2) in the Haldane model, as established by the tenfold-way [32].

Next, the situation in the topologically trivial Haldane phase ($C_1 = 0$) is discussed. In this scenario, no edge state forms around i_0 at strong J and no states are observed within the bulk band gap for $M < -M_{crit}$ or $M > M_{crit}$ (see fig. 5.2). Such characteristics corresponds to the absence of a dispersive topologically protected zero mode at the one-dimensional boundary of a Chern insulator that is in a topologically trivial phase, i.e., when $C_1 = 0$ in the Haldane model. The spin Chern number, however, needs to change from $C_1^{(S)} = 0$ at $J = 0$ to $C_1^{(S)} = 1$ at $J = \infty$, which enforces an in-gap mode at some intermediate J-range. Indeed, we observe a mode bridging the bulk band gap as a function of J, labeled by (e) in the right panel of figure 5.1. The state associated with that in-gap mode is localized at i_0 and its vicinity. However, its weight at i_0 is less than that of the high-energy bound states. The in-gap state in the topologically trivial Haldane phase features weight at impurity site i_0 itself, unlike the in-gap states in the topologically nontrivial Haldane phase at large J. The latter, as remnants of a topological edge mode, are predominantly localized at the boundary of i_0, i.e., its nearest neighbor sites.

We argued earlier, that the Haldane-impurity model has to undergo a topological phase transition as a function of J, since the spin Chern number $C_1^{(S)}$ changes from the trivial weak coupling limit ($C_1^{(S)} = 0$) to the nontrivial strong coupling limit ($C_1^{(S)} = 1$). The critical exchange coupling J_{crit}, where the spin Chern number jumps from $C_1^{(S)} = 0$ to $C_1^{(S)} = 1$, is determined by the J-dependence of the in-gap states, hence, the bulk electronic structure of the spinful Haldane mode. Figure 5.3 displays the numerical computation of J_{crit}, on a finite grid in the ξ-M-parameter space with fixed next-nearest neighbor hopping $\tau_2 = 0.1$. The critical coupling strength J_{crit} at which the transition of the first spin Chern number takes place is color-coded.

In general, the spin Chern transition from $C_1^{(S)} = 0$ to $C_1^{(S)} \neq 0$ demands strong local exchange interaction between the host and the impurity. We find that J_{crit} is typically of the order of the band width or stronger. One would expect from the preceding discussion, that, in consideration of the spin-split in-gap state in the strong coupling picture, the typical critical exchange coupling is stronger if the Haldane host is in a topologically nontrivial phase ($C_1 = \pm 1$). In the topologically trivial Haldane phase ($C_1 = 0$), on the other hand, there is not particular mechanism at hand, that demands further features in the strong-J limit. Hence, we argue that due to the strong-J signature when bulk band topology is nontrivial, J_{crit} typically takes larger values when $C_1 = \pm 1$. In fact, the numerical results displayed in figure 5.3 support this expectation. The gray lines depicted in this figure serve to separate parameter regimes of distinct bulk band topology. Within the $C_1 = \pm 1$ parameter regimes, indicated by the regions enclosed by the gray lines, J_{crit} is typically about an order of magnitude larger, than in the phase of trivial k-space topology ($C_1 = 0$).

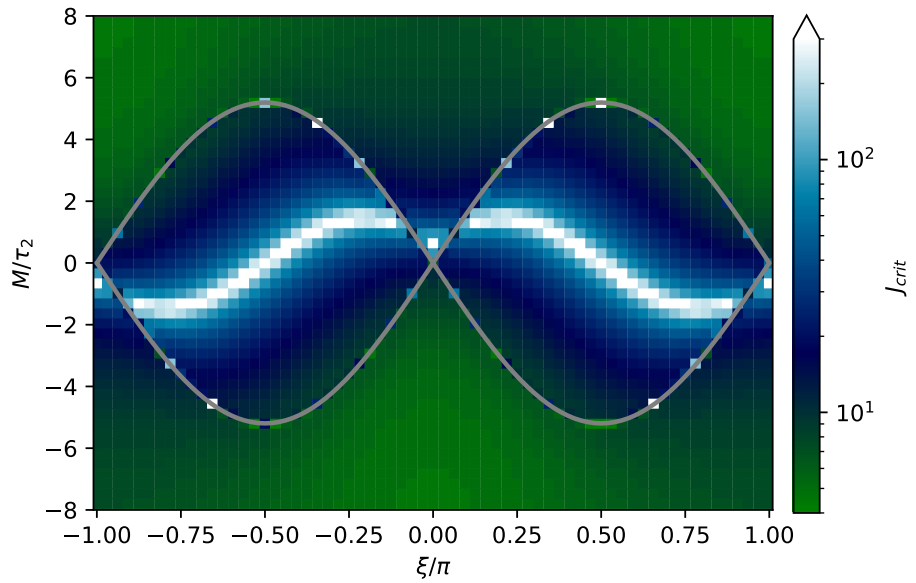

Figure 5.3: Critical coupling strength J_{crit} in the plane of parameters of the Haldane model. At J_{crit} a single particle eigenenergy ϵ_k intersects with the Fermi energy μ. A single impurity is coupled to a bulk site of the A-sublattice of a 39×39 unit cell Haldane lattice with periodic boundary conditions and $\tau_2 = 0.1$. Topological phase boundaries of the Haldane model are indicated by gray lines.

The lines of white pixels in figure 5.3 indicate, that for specific parameters in the ξ-M-plane, the spin Chern transition takes place at infinite J_{crit}. For these parameters, the Zeeman-pair of spin-up and spin-down in-gap states in the band-topologically nontrivial phase converge symmetrically around the chemical potential μ as $J \to \infty$. Hence, no in-gap state crosses μ at any finite J. Such characteristics are, for instance, observed at $\xi = \pi/2$ and $M = 0$. The model is particle-hole symmetric at these parameter values, i.e., $\mu = 0$ and large but finite J results in symmetric spin-splitting of the in-gap states around μ. Similarly, for $\xi \neq \pi/2$ a unique M ($|M| < |M_{crit}|$) is found such that in-gap states do not cross μ at finite J.

5.2.3 – Multiple Impurities

The upcoming section concerns the spin Chern transition when multiple impurities couple to the bulk of the Haldane host. In figure 5.2, the $J \to \infty$ limit is already displayed, but for finite J the relative angle between impurities has to be taken into account. All impurities are of unit magnitude, but each impurity can take any orientation, i.e., the parameter space of each impurity is a two-sphere $\mathcal{S}^2$. Accordingly, the parameter manifold of classical spins is $\mathcal{S} = \prod_q \mathcal{S}_q^2$ with $\mathcal{S}_q^2 \cong \{\boldsymbol{S}_q \in \mathbb{R}^3 \mid |\boldsymbol{S}_q| = 1\}$. We parameterize each two-sphere by a polar angle ϑ_q and an azimuthal angle φ_q. Analogously to the single-impurity discussion, the manifold $\mathcal{S}$ of impurity configurations decouples from the electron system when the exchange coupling is zero. Hence,

for any number of impurities N_S, the spin Chern number $C^{(S)}_{N_S}$ must vanish for $J = 0$. In the strong coupling limit $J \to \infty$, on the other hand, physics related to the classical parameter manifold becomes local to the impurity sites i_q. Impurity sites decouple from the rest of the Haldane model and the local electron states at i_q become independent from one another. Hence, the host-impurity exchange becomes a sum of local magnetic monopole models

$$\hat{H}_{N_S-mono} = J \sum_q \boldsymbol{S}_q \hat{\boldsymbol{s}}_{i_q}. \tag{5.22}$$

As demonstrated in equation 5.15, higher spin Chern numbers factorize into a product of first spin Chern numbers, which can be associated with the isolated magnetic monopoles at infinite J. The spin Chern number of the rest, i.e., the host model without $\{i_q\}$, is trivially zero since the base manifold fully decouples from these sites. Hence, $C^{(S)}_{N_S,rest} = 0$ and the total spin Chern number of such a multi-impurity model with local interaction in the strong coupling limit is $C^{(S)}_{N_S} = \left(C^{(S)}_1(\mathcal{S}_q)\right)^{N_S} = 1$. Consequently, since the weak coupling limit is spin Chern trivial ($C^{(S)}_{N_S} = 0$) and the strong coupling limit is not ($C^{(S)}_{N_S} = 1$), a phase transition between the topologically distinct phases has to take place as a function of J.

5.2.3.1 Two Impurities in the Topologically Trivial Haldane phase

Next, we consider two impurities ($N_S = 2$) coupled to the host at sites i_0 and i_1. To begin with, the Haldane model is considered to be in a topologically trivial ($C_1 = 0$) phase. Aside from the influential factors discussed in the weak coupling limit (sections 4.3.1 and 4.3.2), now the relative angle ϑ between impurities affects the single particle eigenenergies as well. Accordingly, also $\boldsymbol{\Omega}$ depends on ϑ in the J-regime between weak and strong coupling. Due to the $SO(3)$ symmetry, only one angle $0 \leq \vartheta \leq \pi$ is required to describe genuinely distinct impurity configurations. This symmetry leads to $\epsilon_k(\boldsymbol{S}_0, \boldsymbol{S}_1) = \epsilon_k(\vartheta)$ and can also be exploited in the numerical calculation of the spin Chern number (eq. 5.11).

Figure 5.4 displays single-particle eigenenergies for two impurities at i_0 and i_1 at nearest neighbor sites on the A-sublattice, i.e., next-nearest neighbor sites of the honeycomb lattice. Model parameters are the same as in the single-impurity case (see fig. 5.1) and all panels display energies around $\mu \approx 0.21$ as functions of J. In the top panels of figure 5.4 we set $M = 1.5M_{crit}$ and the bulk band topology of the host is trivial ($C_1 = 0$). The lower panels with $M = 0.5M_{crit}$, however, depict a scenario of nontrivial bulk band topology of the host ($C_1 = 1$). The case of nontrivial k-space topology is subsequently discussed in section 5.2.3.2.

For a topologically trivial Haldane host, we find two in-gap states (a) and (b) fully

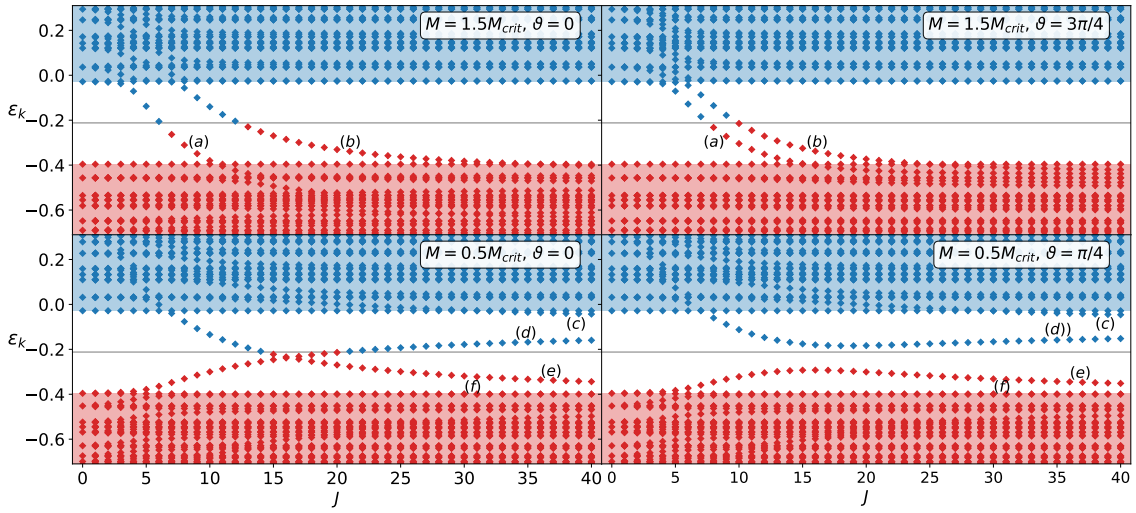

Figure 5.4: Single particle eigenenergies ϵ_k of the hybrid model when two impurities interact via exchange coupling J with the bulk of a Haldane model. The two impurities enclose angle an ϑ and couple to next-nearest neighbor sites. Onsite potential M is positive on the impurity A-sites. Red color marks occupied single particle energies (diamond markers) and the bulk valence band (background color), while blue refers to empty energy levels and the bulk conductance band. The chemical potential μ is indicated by the gray line centered in the bulk band gap (uncolored background). Computations are performed on a 39×39 unit cell lattice with periodic boundary conditions, $\tau_2 = 0.1$ and $\xi = \pi/4$.

bridging the bulk band gap as a function of J in the upper left ($\vartheta = 0$) as well as the upper right ($\vartheta = 3\pi/4$) panel of figure 5.4. When impurities are aligned, these in-gap states cross the chemical potential at $J_1(\vartheta = 0) \approx 6.0$ and $J_2(\vartheta = 0) \approx 12.3$. As ϑ increases, $J_1(\vartheta)$ increases and $J_2(\vartheta)$ decreases, until they coincide at $\vartheta = \pi$.

We can explain $J_1(\pi) = J_2(\pi)$ for $\vartheta = \pi$ through separation of the Hamiltonian in a spin-up and a spin-down sector ($H = H_\uparrow + H_\downarrow$). Without loss of generality, one can assume that the electron spins at i_0 and i_1 are polarized in $\pm z$ direction for $\vartheta = \pi$. Hence, the two impurity bound states have well-defined and opposite spin-projection quantum numbers. Accordingly, hybridization of the bound states is prevented, since the opposing spin-projections do not mix. By the combination of a spin flip $\uparrow\leftrightarrow\downarrow$ and a reflection at a mirror axis perpendicular to and in the middle of the connection line between the impurities, the states can be mapped onto each other. Trivially, symmetric setups cannot lead to distinct energies. Consequently, the eigenenergies must be degenerate for any J, which implies crossing μ at the same critical J. Any $\vartheta \neq \pi$ leads to non-zero hybridization at finite J. For $\vartheta = 0$ hybridization is the strongest since localized eigenstates are in the same spin sector. In this scenario with parallel aligned impurities, the difference between J_1 and J_2 is the largest.

The critical exchange couplings J_1 and J_2 in dependence of ϑ when $C_1 = 0$ are displayed in figure 5.5a. The system becomes gapless whenever the color in the plot changes.

Hence, we see coupling strengths $J_{crit,1} = J_1(\vartheta = 0) \approx 6.0$ and $J_{crit,2} = J_2(\vartheta = 0) \approx 12.3$ defining a transition regime. For all $J_{crit,1} < J < J_{crit,2}$ some ϑ leads to a gapless system. As the system is not gapped on the entire base manifold, i.e., the gap closes for certain ϑ, the second spin Chern number remains undefined in that J-range. The spin Chern trivial phase with $C_2^{(S)} = 0$ for $J < J_{crit,1}$ is separated from the phase of nontrivial spin Chern number $C_2^{(S)} = 1$ for $J > J_{crit,2}$ by the gapless transition phase $J_{crit,1} < J < J_{crit,2}$.

Moreover, the gapless transition phase is located around J_{crit} for a single impurity ($N_S = 1$), which can be seen by comparing the right panel of figure 5.1 with the upper panels of figure 5.4. This similarity becomes apparent in the limit of an infinite distance between the impurities. The electronic structure of the host is locally affected by the impurities, i.e., in a vicinity around i_q. As the distance between i_0 and i_1 increases, the electronic structure around the impurity sites disentangles. Hence, the gap-closure becomes independent of ϑ and the two in-gap states degenerate. Effectively, single-impurity spin Chern transitions take place at each impurity site, thus, $J_{crit,1} = J_{crit,2} = J_2$ and the gapless transition regime vanishes.

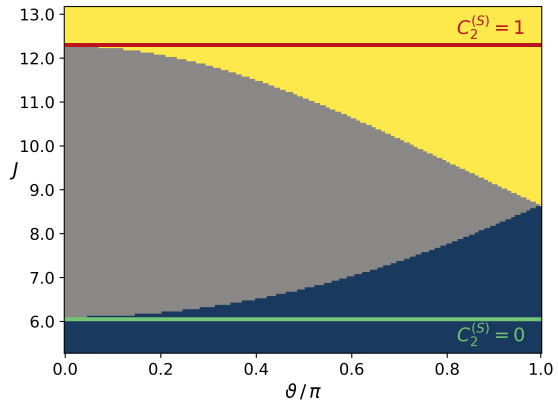

(a) $M = 1.5M_{crit}$ resulting in a host of trivial k-space topology ($C_1 = 0$).

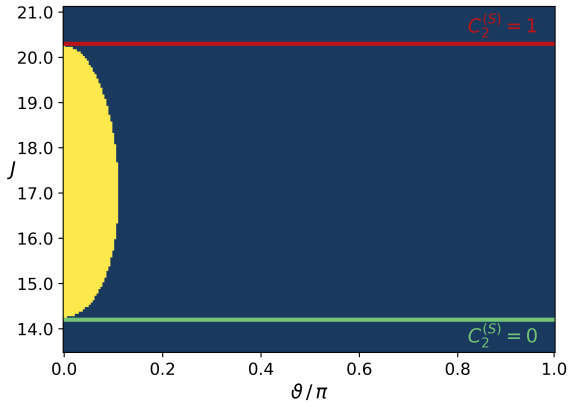

(b) $M = 0.5M_{crit}$ resulting in a host of nontrivial k-space topology ($C_1 = 1$).

Figure 5.5: Transition of the second spin Chern number $C_2^{(S)}$ as a function of the exchange coupling J. Two impurities are coupled to the host, thus the base manifold is $\mathcal{S}_1^2 \times \mathcal{S}_2^2$. Due to $SO(3)$ symmetry all distinct impurity configurations can be parameterized by the angle $0 \leq \vartheta \leq \pi$ enclosed by the impurities. Whenever the color changes, the system becomes gapless. The host is a spinful Haldane model of 27×27 unit cells with periodic boundaries and $\tau_2 = 0.1$, $\xi = 45$. Impurities are positioned on the A-sublattice as next-nearest neighbors of the honeycomb lattice. Both panels feature the same bulk band gap $\Delta E \approx 0.37$. The green line indicates $J_{crit,1}$ and the red line $J_{crit,2}$.

5.2.3.2 Two Impurities in the Topologically Nontrivial Haldane Phase

Let us now discuss the spin Chern transition with two impurities in a setup where k-space topology is nontrivial ($C_1 = 1$). In the limit of infinite distance between the impurities, the strong-J limit features four in-gap states. These are two slightly spin-split modes localized around each impurity, i.e., around i_0 and i_1. As discussed in section 5.2.2, each Zeeman pair is the remnant of a topologically protected boundary mode for a discretized hole, i.e., a one-dimensional boundary shrunk to a single site. The boundaries of both macroscopic holes are assumed to be equivalent and so are the remnant in-gap states. Hence, when i_0 and i_1 are of the same sublattice, the energies of in-gap states located around different impurities are degenerate in the infinite-distance limit.

Bringing the impurities closer to each other increases the overlap of the bound in-gap states around i_0 and i_1 which lifts the aforementioned degeneracy. Bonding and antibonding linear combinations of the in-gap states result in two Zeeman pairs of in-gap states at different energies. However, these Zeeman pairs remain in the bulk band gap for strong J. Bringing i_0 and i_1 closer together and ultimately to nearest neighbor sites results in a single two-site hole. Depending on the parameters of the Haldane model, however, Zeeman pairs can energetically merge with the continuum of delocalized bulk states. An example thereof can be seen in figure 5.2, where for $r = 1$ and $M = 0.5M_{crit}$ we find a single in-gap Zeeman pair for a four-site hole.

We consider two impurities on next-nearest neighbor sites, which is on the brink of a merged single two-site hole and two separated holes. Since the edge modes are predominantly localized on boundary sites of each hole and i_0 and i_1 share one common nearest neighbor, there is considerable overlap of the respective edge modes in the two single-site hole picture. In the lower panels of figure 5.4 we identify three in-gap states for large but finite J in both cases, for $\vartheta = 0$ (lower left panel) and for $\vartheta = \pi/4$ (lower right panel). States (c) and (d) form a Zeeman pair and their energies, which remain in the bulk band gap, become degenerate for $J \to \infty$. On the other hand, states (e) and (f), which form a Zeeman pair of their own, approach each other in the bulk continuum from $J \to \infty$, even though (e) is an in-gap state for finite J-range. In the range of roughly $7 \lesssim J \lesssim 30$, only the eigenenergies of the spin-$\uparrow$ state (d) of the first Zeeman pair and the spin-$\downarrow$ state (e) of the second Zeeman pair take values within the bulk band gap. For parallel impurity alignment ($\vartheta = 0$, lower left panel of fig. 5.4), we observe a crossing of these states at $J \approx 16$. For non-collinear impurity orientations, however, these states form an avoided crossing, which is illustrated for $\vartheta = \pi/4$ in the lower right panel of figure 5.4. This avoided crossing is associated with the mixing of spin-polarizations. When the first impurity at site i_0 sets the polarization axis, that defines the spin-$\uparrow$ and spin-$\downarrow$ projection, the second impurity polarizes electron spin

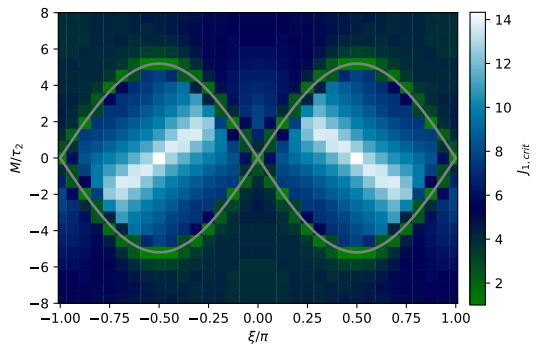

(a) Critical coupling strength $J_{1,crit}$ up to which the system is in a trivial spin Chern state with $C_2^{(S)} = 0$.

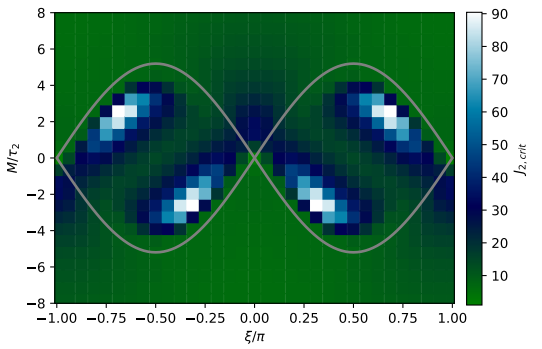

(b) Critical coupling strength $J_{2,crit}$ from which the system is in a nontrivial spin Chern state with $C_2^{(S)} = 1$.

Figure 5.6: Parametric dependence of the critical coupling strength in the $\xi - M/\tau_2$ plane. Thick gray lines mark the topological phase boundaries of the hosting Haldane model (see fig. 4.3). Impurities are positioned on next-nearest neighbor sites in the bulk of a 9×9 unit cell lattice with periodic boundary conditions and $\tau_2 = 0.1$.

of both spin-polarizations at site i_1 and its surrounding. Therefore, the increases or decreases in single-particle energies are no longer solely related to pure spin-$\uparrow$ or spin-$\downarrow$ states. Instead, they are associated with states that comprise a mixture of both spin projections.

To realize the spin Chern transition from $C_2^{(S)} = 1$ at $J \to \infty$ to $C_2^{(S)} = 0$ at $J = 0$, there must be a gap closure on $\mathcal{S} = \mathcal{S}_0^2 \times \mathcal{S}_1^2$ when J decreases from the strong to the weak coupling limit. In the lower left panel of figure 5.4, we find a gap-closure at $J = J_{crit,2} = J(\vartheta = 0) \approx 20.3$. Decreasing J further, we find a second gap-closure at $J = J_{crit,1} = J(\vartheta = 0) \approx 14.2$. Unlike the scenario of trivial k-space topology, gap-closures are not observed at any ϑ when bulk band topology is non-trivial. An example thereof is displayed in the lower right panel of figure 5.4.

A comprehensive picture of the spin Chern transition when k-space topology is non-trivial is shown in figure 5.5b. We see that up to $\vartheta \approx 0.11\pi$ one generically finds a gap-closure at $J_1(\vartheta)$ and $J_2(\vartheta)$. It is worth mentioning that due to the $SO(3)$ symmetry figure 5.5 captures the full information on the transition of the second spin Chern number. Accordingly, aforementioned gap closures take place on three-dimensional submanifolds of the four-dimensional manifold $\mathcal{S}$ of classical spin configurations.

All in all, we find a transition regime for all $J_{crit,1} < J < J_{crit,2}$, where the system is not gapped on the entire base manifold, i.e., the top spin Chern number $C_2^{(S)}$ is not defined. For $J < J_{crit,1}$ we find $C_2^{(S)} = 0$ and $C_2^{(S)} = 0$ for $J > J_{crit,2}$, which is also validated by numerical evaluation of the second spin Chern number via equation 5.11. Furthermore, critical coupling strengths $J_{crit,1}$ and $J_{crit,2}$ depend on parameters of the Haldane model. Figure 5.6 shows the critical coupling strengths in the M/τ_2-ξ plane. These numerical calculations are done for a small lattice of 9×9 unit cells. Finite

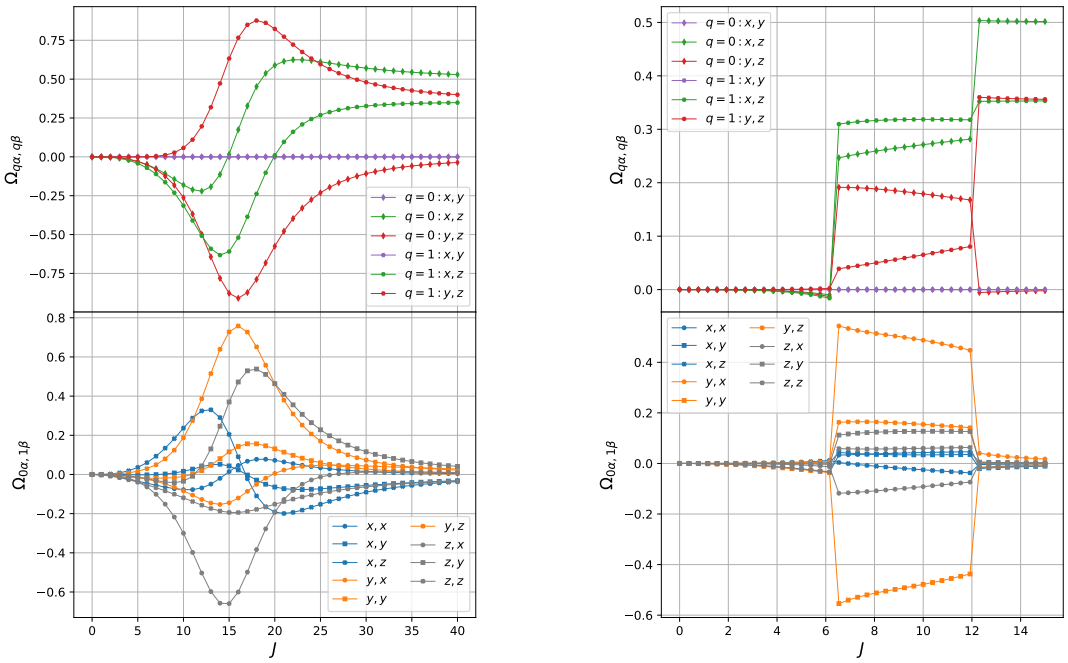

(a) Topological Haldane phase with $M = 0.5M_{crit}$.

(b) Trivial Haldane phase with $M = 1.5M_{crit}$.

Figure 5.7: Elements of the spin Berry curvature $\mathbf{\Omega}$ from the weak towards the strong coupling limit. Upper panels depict elements of the diagonal blocks with $q = r \in \{0, 1\}$ and lower panels elements of the off-diagonal block $(q, r) = (0, 1)$. Computations are performed for two impurities on next-nearest neighbor A-sites in the bulk emulated by a 39×39 unit cell lattice with periodic boundary conditions. Further parameters of the Haldane host are $\tau_2 = 0.1$ and $\xi = \pi/4$. Impurity orientations are $\boldsymbol{S}_1 = (0, 1, 0)^T$ and $\boldsymbol{S}_2 = (-1/\sqrt{2}, 1/\sqrt{2}, 0)^T$, i.e., $\vartheta = \pi/4$.

size effects affect the absolute values of $J_{crit,1}$ and $J_{crit,2}$, but characteristic features of the transition of the second spin Chern number are consistent with computations performed for larger lattices. As discussed previously, a crossing of in-gap states is observed for $\vartheta = 0$. When in-gap states cross right at the chemical potential, one finds $J_{crit,1} = J_{crit,2}$. For a chemical potential located in the middle of the bulk band-gap, a degeneracy of in-gap states at finite J occurs at μ for $M = 0$ and $\xi = \pm\pi/2$. Similar to the discussion of the white pixels in figure 5.3, $J_{crit,2}$ becomes infinite when a Zeeman pair converges symmetrically around μ in the limit of $J \to \infty$ (see white pixels in figure 5.6b). Typically, the topological transition to a nontrivial second spin Chern number requires stronger J in phases of nontrivial k-space topology ($C_1 = \pm 1$) as compared to the phase of trivial bulk band topology ($C_1 = 0$).

A final remark on the transition from weak to strong J when $N_S = 2$ is to be made on the spin Berry curvature itself. The spin Berry curvature may contain large elements and takes an intricate form in the J-range where single particle eigenenergies intersect or come close to E_F. Generically, non-zero $\Omega_{q\alpha,r\beta}$ are discontinuous whenever some ϵ_k crosses the Fermi energy, but $\mathbf{\Omega}$ cannot be evaluated right where the single particle gap

vanishes ($\epsilon_k = \mu$). Exemplary $\mathbf{\Omega}$ are displayed in figure 5.7, where we vary the exchange coupling from the weak coupling limit (see section 4.1.3) to the strong coupling limit (see section 4.1.4). Due to the anti-symmetry of $\mathbf{\Omega}$, the off-diagonal blocks are related via $\mathbf{\Omega}_{01} = -\mathbf{\Omega}_{10}$. Hence, all non-redundant elements of $\mathbf{\Omega}$ are expressed in figure 5.7. Large $\Omega_{q\alpha,r\beta}$ can be achieved through the spin Chern transition, which result in large geometric spin-torque in the impurity dynamics (eq. 4.18). Contrary to the topological phase transition of the k-space Chern number, where $\mathbf{\Omega}$ is found to be smooth across the closure of the bulk band gap (see section 4.3.1.5), $\Omega_{q\alpha,r\beta}$ is discontinuous at gap-closures associated with a spin Chern transition. In fact, elements of $\mathbf{\Omega}$ can even diverge at the spin Chern transition when k-space topology of the Haldane host is nontrivial. Linking figure 5.5 and 5.7, we notice, that a nontrivial spin Chern number $C_2^{(S)} = 1$ can be obtained, even though $\mathbf{\Omega}$ is not strictly of its strong coupling form (eq. 5.12). Exemplary $\mathbf{\Omega}$ can be read off from figure 5.7 at J just slightly stronger than $J_{crit,2}^{topo} \approx 20$ and $J_{crit,2}^{triv} \approx 12$. As discussed previously, there is more to the transition of the second spin Chern number than the mere superposition of two magnetic monopoles. Considering the $\mathbf{\Omega}$-elements of large magnitude in the spin Chern transition regime, the impurity dynamics is expected to exhibit pronounced non-Hamiltonian behavior within a suitably fine-tuned parameter regime.

5.2.3.3 Three Classical Impurity Spins

Next, we address the spin Chern transition for three impurities, with the central arguments being analogous to the analysis of the two-impurity setup. In the strong coupling limit $C_3^{(S)} = (C_1^{(S)})^3 = 1$, since $C_1^{(S)} = 1$ results from the magnetic monopole picture that applies for $J \to \infty$ (see section 5.2.1.2). On the other hand, $C_3^{(S)} = 0$ for $J = 0$, so there must be a spin Chern transition when J increases from the weak to the strong coupling limit.

The base manifold of the Haldane-impurity model when $N_S = 3$ is the six-dimensional manifold $\mathcal{S} = \mathcal{S}_0^2 \times \mathcal{S}_1^2 \times \mathcal{S}_2^2$ with $\mathcal{S}_q^2 \cong \{\boldsymbol{S}_q \in \mathbb{R}^3 \mid |\boldsymbol{S}_q| = 1\}$. Again, the model obeys $SO(3)$ symmetry, hence single particle eigenenergies $\epsilon_k(\boldsymbol{S}_0, \boldsymbol{S}_1, \boldsymbol{S}_2)$ are degenerate on a three dimensional submanifold of $\mathcal{S}$ since global $SO(3)$ rotations form a class of '$SO(3)$-equivalent' spin configurations. In fact, this $SO(3)$-equivalence applies not only to the spin Berry curvature two-form $\boldsymbol{\omega}$, but also to $\boldsymbol{\omega}^3$. Within a class of equivalent spin configurations, one might choose $\boldsymbol{S}_0$ pointing in $+z$ direction and $\boldsymbol{S}_1$ lying in the y-z plane as a representative of this class. This way, the minimal set of three variables to describe representative spin configurations of different classes is given by ϑ enclosed by $\boldsymbol{S}_0$ and $\boldsymbol{S}_1$ together with polar angle ϑ' and azimuthal angle φ' of $\boldsymbol{S}_2$ relative to $\boldsymbol{S}_0$ and the y-z plan.

In our numerical studies, impurities are coupled to next-nearest neighbor A-sites within one hexagon of the honeycomb lattice. Similar to the two-impurity setup studied

previously (see sections 5.2.3.1 and 5.2.3.2), the regime with a trivial spin Chern number $C_3^{(S)} = 0$ is separated from the nontrivial $C_3^{(S)} = 1$ regime by a transition phase. In that intermediate J-regime, the model is never gapped on the entire base manifold, so $C_3^{(S)}$ is ill-defined.

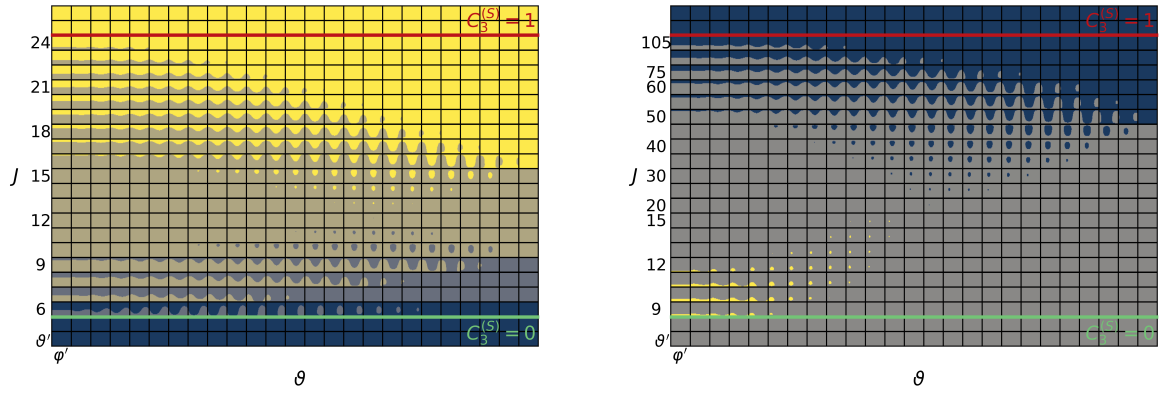

(a) $M = 1.5M_{crit}$ resulting in a host of trivial k-space topology ($C_1 = 0$).

(b) $M = 0.5M_{crit}$ resulting in a host of nontrivial k-space topology ($C_1 = 1$).

Figure 5.8: Transition of the spin Chern number $C_3^{(S)}$ as a function of the exchange coupling J. Three impurities couple to next-nearest neighbor A-sites within one hexagon of the honeycomb lattice. The base manifold is $\mathcal{S}_1^2 \times \mathcal{S}_2^2 \times \mathcal{S}_3^2$. Due to $SO(3)$ symmetry all distinct impurity configurations can be parameterized by an angle $0 \leq \vartheta \leq \pi$ enclosed by $\boldsymbol{S}_0$ and $\boldsymbol{S}_1$ together with polar angle ϑ' and azimuthal angle φ' of $\boldsymbol{S}_2$. Whenever the color changes the system becomes gapless. The host is a spinful Haldane model of 27×27 unit cells with periodic boundaries and $\tau_2 = 0.1$, $\xi = 45$. The bulk band gap is the same for $M = 0.5M_{crit}$ and $M = 1.5M_{crit}$, i.e., in both panels. The green line indicates $J_{crit,1}$ and the red line $J_{crit,2}$.

Figure 5.8 shows these three regimes and visualizes gap-closures on the parameter manifold in the transition regime of $C_3^{(S)}$. Angle ϑ runs from zero in the leftmost column to π in the rightmost column and each small frame is spanned by $0 \leq \vartheta' \leq \pi$ on the y-axis and $0 \leq \varphi' \leq 2\pi$ on the x-axis. In figure 5.8a, the Haldane host is in the k-space topological trivial phase ($C_1 = 0$, $M = 1.5M_{crit}$). We find $C_3^{(S)} = 0$ for $J < J_{crit,1} \approx 5.5$ and $C_3^{(S)} = 0$ for $J > J_{crit,2} \approx 24.5$. In the transition regime $J_{crit,1} < J < J_{crit,2}$, the model is not gapped everywhere on the base manifold, thus, the spin Chern number of top degree, here $C_3^{(S)}$, is ill-defined. Fixing J corresponds to a line of small ϑ'-φ' frames. For any fixed $J_{crit,1} < J < J_{crit,2}$ one finds at least one small frame in each line, where a change in color can be observed. Note, that for $J = 12$, one finds a hardly visible gap closure in the small frame corresponding to $\vartheta = 2\pi/3$.

Further more, we find exactly three gap closures as a function of J for any fixed impurity configuration, i.e., to any fixed set of $(\vartheta, \vartheta', \varphi')$. This can be seen by focusing on a single column, which fixes ϑ. Focusing on any fixed pixel within a small frame furthermore fixes ϑ' and φ'. Along any column, this chosen pixel changes its color three

times. This finding is again in line with previous discussions on the $N_S = 1$, where a single mode crosses μ as a function of J (see right panel in fig. 5.1) and the $N_S = 2$ setup (see upper panels in fig. 5.4), where two modes were found to cross the chemical potential as J increases from the weak to the strong coupling limit. Such regularity can be understood from the infinite distance limit, where one mode is localized at each impurity and $C_3^{(S)}(\mathcal{S}) = C_1^{(S)}(\mathcal{S}_1^2) \cdot C_1^{(S)}(\mathcal{S}_2^2) \cdot C_1^{(S)}(\mathcal{S}_3^2)$. Decreasing the distance between the impurities increases the overlap between the in-gap states, which lifts their degeneracy. Hence we find a 'continuous transformation' of the impurity geometry might change the J-dependent characteristics of in-gap states, but their number is a topological invariant and remains unchanged.

Figure 5.8b illustrates the spin Chern transition of $C_3^{(S)}$ when the bulk band topology of the host is nontrivial. Again similar to the two-impurity setup, the transition of $C_3^{(S)}$ does not feature a three-fold gap closure on the entire base manifold when k-space topology is nontrivial ($C_1 = 1$). We do not find a threefold change in color for any fixed pixel within a ϑ'-φ' frame along all columns of constant ϑ. Furthermore, the intermediate regime seems to expand over larger J-range with an increasing number of impurities.

A final remark is to be made on 'lower' spin Chern numbers, i.e., $C_N^{(S)}$ with $2N < \dim(\mathcal{S})$. When the model is gapped on a closed orientable submanifold of $\mathcal{S}$, say a two sphere $\mathcal{S}^2 \subset \mathcal{S} = \mathcal{S}_1^2 \times \mathcal{S}_2^2 \times \times \mathcal{S}_2^3$, one could evaluate a spin Chern number $C_1^{(S)}(\mathcal{S}^2)$ on this submanifold. By these lower spin Chern numbers one classifies a sub-bundle of the full fiber bundle. Such sub-bundles can transition somewhere within $J_{crit,1} < J < J_{crit,2}$ of the full system, since the model is fully gapped, i.e., does not change any topological invariant, for $J < J_{crit,1}$ and $J > J_{crit,2}$.

As an example, we computed $C_1^{(S)}(\mathcal{S}^2)$ over the two-sphere parameterized by ϑ' and φ' for a host of trivial k-space topology ($M = 1.5M_{crit}$). This first spin Chern number is well defined within any single-colored small frame of figure 5.8. For $\vartheta = 5\pi/6$ (fifth column from the right in figure 5.8a), we obtained $C_1^{(S)}(J = 5) = C_1^{(S)}(J = 7) = 0$. While the $C_1^{(S)}(J = 5) = 0$ is a trivial statement ($J < J_{crit,1}$), $C_1^{(S)}(J = 7) = 0$ is not obvious, since there has been a gap-closure on $\mathcal{S}^2(\vartheta', \varphi')$ when increasing the exchange coupling from $J = 5$ (dark blue frame color) to $J = 7$ (gray-blue frame color). Increasing J further, we find $C_1^{(S)}(J = 12) = 1$ and the color of the frame has again changes and the ϑ'-φ' frame becomes ocher. For even stronger J the gap closes on $\mathcal{S}^2(\vartheta', \varphi')$ again. Finally, after another regime where $C_1^{(S)}$ is ill-defined, we find $C_1^{(S)}(J > 18) = 1$ (yellow frames), which is consistent to the strong-coupling limit. This example illustrates, that multiple J regimes of well defined lower spin Chern numbers, can be separated by various gap-closures and not every gap-closure necessarily changes the spin Chern number. In principle, this could also be the case for the spin Chern number of top degree, but only two regimes of well defined $C_N^{(S)}$ separated by a

single transition regime are found in our setups of the Haldane-impurity model.
The preceding example highlights, that knowledge of $C_1^{(S)}(\mathcal{S}^2)$ alone is not sufficient to classify the full model, even though $C_3^{(S)} = \left(C_1^{(S)}\right)^3$ factorizes into a product of first spin Chern numbers $C_1^{(S)}(\mathcal{S}^2)$ in the limit of $J \to \infty$. This mathematically trivial statement is supported by an physical example, which emphasizes the necessity to evaluate higher spin Chern numbers to characterize a multi-impurity setup. Whenever quantum states of non-zero spectral weight at multiple impurity sites exist, a spin Chern number taking the combined manifold of impurity configurations into account is required. Moreover, one could define an infinite number of $\mathcal{S}^2 \subset \mathcal{S}$ and other two dimensional submanifolds of $\mathcal{S}$ that offer the possibility to evaluate different $C_1^{(S)}(\mathcal{S}^2)$. However, only the unique top spin Chern number, i.e., $C_N^{(S)}(\mathcal{S})$ with $2N = \dim(\mathcal{S})$, takes the entire base manifold into account. For that reason, only the top spin Chern number is sufficient to generically classify the entire system by the means of its spin Chern topology.

5.2.4 – Summary of the Topology of Localized Magnetic Moments on a Chern Insulator

The configuration space of a single impurity with fixed magnitude is a two-sphere $\mathcal{S}^2$. This closed orientable parameter manifold serves as a base manifold to a fiber bundle formed by $\mathcal{S}^2$ and the ground state of the quantum system. The first spin Chern number $C_1^{(S)} \in \mathbb{Z}$ is exploited to classify topologically distinct bundles of this kind. The first k-space Chern number C_1, on the other hand, is defined as a fiber bundle of electron system's ground state over the two-torus $\mathcal{T}^2$ associated with the first Brillouin zone of a translation invariant lattice. Here, the bulk band Chern number C_1 is utilized to identify topologically distinct phases of the Haldane model. Unlike C_1, which addresses global bulk topology, $C_1^{(S)}$ is related to spatially local topological properties.
We emphasized that there must be a spin Chern transition as a function of the exchange coupling strength J, with which local magnetic impurities are coupled to the spinful Haldane model. This is evident since the analytically accessible limiting cases $C_1^{(S)}(J = 0) = 0$ and $C_1^{(S)}(J \to \infty) = 1$ are distinct. A similar argument holds for any number N_S of impurities, when considering the N_S-th spin Chern number $C_{N_S}^{(S)}$. A Chern number is obtained by a suiting integral over the base manifold of a fiber bundle (eq. 5.1). To obtain top Chern number $C_{N_S}^{(S)}$ for a number of N_S impurities, this is a $2N_S$-dimensional integral over the N_S-fold direct product of two-spheres $\mathcal{S} = \mathcal{S}^2 \times ... \times \mathcal{S}^2$.
At first, we discussed the spin Chern transition with a single impurity ($N_S = 1$). Since a gap closure is necessary for a topological invariant to change its value, a single electron state ϵ_k crosses the chemical potential μ when $C_1^{(S)}$ transitions from its weak to its strong coupling value. This implies a degeneracy of the (N and $N \pm 1$) multi-electron state at a critical coupling strength J_{crit}. The Hamiltonian that describes

our system is symmetric under $SO(3)$ rotations of the classical impurity $\boldsymbol{S}$ and the quantum-spin degrees of freedom. Consequently, the 'magnetic charge' inducing the spin Berry curvature is uniformly distributed over the two-sphere $J_{crit}\boldsymbol{S} \subset \mathbb{R}^3$.

The necessity of an in-gap state with $\epsilon_k = \mu$ at some critical coupling strength J_{crit} is unrelated to the bulk band topology in k-space, as J_{crit} characterizes the spin Chern transition. In fact, the requirement of $\epsilon_k = \mu$ holds for any choice of the chemical potential within the bulk band gap irrespective of C_1. The critical coupling strength, however, typically depends on the choice of the chemical potential, i.e., $J_{crit} = J_{crit}(\mu)$. Hence, $J \mapsto \mu_{crit}(J)$ maps to the full range of in-gap energies between the J-independent valence band maximum and the conduction band minimum. Consequently, in-gap states must fully bridge the bulk band gap ΔE between $J = 0$ and $J = \infty$. Yet, in-gap states do not have to span ΔE on the entire base manifold $\mathcal{S}$, since a gap closure on a submanifold of the base manifold is sufficient for a topological phase transition. For a single impurity, in-gap states are displayed in figure 5.1. The right panel shows a single in-gap state crossing ΔE when k-space topology is trivial ($C_1 = 0$). The left and the centered panels, on the other hand, display a setup with $C_1 = 1$. When k-space topology is nontrivial two in-gap states of opposing spin-projection converge in the bulk band gap for $J \to \infty$, thus ΔE is fully bridged by $\{\epsilon_k\}$ as well.

In the strong coupling limit, the distinct characteristics of the in-gap states associated with trivial and nontrivial k-space topology are most evident. An intuitive yet not mathematically rigorous thought to explain in-gap state characteristics based on k-space topology is deduced from the idea of a one-dimensional boundary in the Haldane model. Such a topological defect can be generated by a macroscopic circular hole of radius r, where an infinitely strong impurity potential ($J \to \infty$) couples to all sites within the hole. For a one-dimensional defect the bulk-boundary correspondence enforces a topologically protected zero mode when $C_1 = \pm 1$ for the Haldane model. This zero mode bridges the bulk band gap and is spin-degenerate in the spinful Haldane model. Shrinking the hole to a single site corresponds to thinning of the dispersive spectrum of the boundary mode, which leads to a decreasing number of in-gap states in the infinite J limit until only a single spin-degenerate in-gap state remains for a single-site hole. The remnant in-gap model of the topologically protected edge-mode of a hypothetical one-dimensional boundary is absent when k-space topology is trivial. This intuitive argument based on the bulk-boundary correspondence of k-space topology is numerically verified. Furthermore, the absence of an in-gap mode for $J \to \infty$ when $C_1 = 0$ supports this argument. Rather, a single in-gap mode fully bridges ΔE in a finite J-range when $C_1 = 0$.

Next, we increased the number of independent impurities. Qualitatively similar results were obtained for $N_S = 2$ and $N_S = 3$, where the strong coupling limit is found to

feature one or more Zeeman pairs of in-gap states when k-space topology is nontrivial ($C_1 = \pm 1$). When $C_1 = 0$, however, in-gap states are absent for $J \to \infty$. At finite J, the Zeeman pairs are spin-split, and the details of the in-gap states generally depend on model parameters. Furthermore, when the sites to which the impurities couple are close to each other, the geometry of the impurity configuration becomes relevant, since in-gap modes hybridize. Only at infinite distance between the impurities, exactly N_S pairs of degenerate in-gap modes form for $C_1 = \pm 1$ when J increases from the weak to the strong coupling limit. In the phase of trivial k-space topology, N_S in-gap modes are found to fully bridge the gap in a finite J-range. The necessity of in-gap states to fully bridge the gap is again enforced by spin Chern transition, since $C^{(S)}_{N_S} = 0$ for $J = 0$ and $C^{(S)}_{N_S} = \left(C^{(S)}_1\right)^{N_S} = 1$ at infinite J. In fact, one can deduce that the number of gap closures ($\epsilon_k = \mu$) and with that the number of gap bridging modes when $C_1 = 0$ corresponds to the number of impurities. The following argument supports this fact: The exchange coupling of the q-th impurity is labeled by J_q. Starting from $J_q = 0$ we successively increase the local exchange couplings. First we increase $J_0 \to \infty$ of one impurity while any other J_q with $q \in \{1, ..., N_S - 1\}$ remains zero. The first spin Chern number associated with the 0-th impurity ($C^{(S)}_1(\mathcal{S}^2_0)$) changes from zero to one and a single in-gap energy crosses μ, since a magnetic monopole at i_0 is created in the process. Subsequently increasing $J_q \to \infty$ one after the other creates N_S monopoles. The corresponding $C^{(S)}_1(\mathcal{S}^2_q)$ all transition from zero to one. Consequently, the full process generates exactly N_S gap closures when carried out adiabatically.

For $N_S = 1$ and $N_S = 2$ we numerically evaluated the local topological spin Chern transitions on a M-ξ parameter manifold spanning the Haldane phase diagram ($\tau_2 = 0.1$). With uniform $J_q = J$, the topological spin Chern transition is found to take place at coupling strengths roughly of the order of the band width when k-space topology is trivial. In phases of nontrivial k-space topology, the spin Chern transition typically requires stronger J, since the additional requirement of in-gap states in the strong coupling limit applies. When fine tuning the Haldane parameters, e.g. $M = 0$, $\xi = \pm\pi/2$, the spin-split in-gap states present in the $C_1 = \pm 1$ phases can converge right at μ. In these particular scenarios, no ϵ_k crosses μ at finite J.

For $N_S \geq 2$, the topological transition in $\mathcal{S}$-space generically takes place in a finite range of coupling strength $J_{crit,1} < J < J_{crit,2}$, unlike the spin Chern transition for a single impurity, which takes place at a distinct critical coupling strength $J = J_{crit}$. In the entire range of $J_{crit,1} < J < J_{crit,2}$, the system is gapless on a J-dependent submanifold of $\mathcal{S} = \mathcal{S}^2_0 \times ... \times \mathcal{S}^2_{N_S-1}$. In this transition regime the top Chern number $C^{(S)}_{N_S}$ is undefined. We note, that the gap closures at $J_{crit,1}$ and $J_{crit,2}$ take place at high-symmetry impurity spin configurations, i.e., ferro- or antiferromagentic impurity alignment.

6 – Summarizing Conclusion

The theme of this thesis is a study of unconventional properties of localized magnetic moments modeled by classical spins. The first of three major subjects is the idea of investigating adiabatic dynamics, i.e., dynamics under the 'adiabatic constraint', when slow degrees of freedom are coupled to a fast host system. At first, a model of fast and slow classical Heisenberg spins was investigated in chapter 3. Secondly, in chapter 4 we studied classical impurities exchange coupled to a lattice model of non-interacting itinerant electrons. In the numerical studies of this chapter, Haldane's model of a Chern insulator serves as the quantum host and we find a correlation between the dynamics of the impurities and the topological phase of the host. Finally, the spin Chern topology arising from the classical magnetic moments coupled to an electron system was analyzed and related to the bulk band topology of the Haldane host, which is the subject of chapter 5. Remarkably, the low-energy electronic structure surrounding the impurities proofs to be sensitive to the bulk band topology of the Chern insulator, which is argued to originate from an interplay of the global k-space and the local $\boldsymbol{S}$-space topology.

A central role in our studies is taken by the spin Berry curvature $\boldsymbol{\Omega}$ (eq. 4.16), respectively its classical counterpart in chapter 3. In its dual role, $\boldsymbol{\Omega}$ influences the dynamics of the impurities (chapters 3 and 4) on one hand, and serves the definition of a topological invariant, the spin Chern number, on the other hand (chapter 5).

First, we analyze the dynamics of classical impurities. When studying atomistic spin dynamics in condensed matter or molecular systems, it is common to opt for classical Heisenberg spins. The classical approximation enables computation of long-time dynamics for a large number of spins and is well-justified in the context of large local magnetic moments [42]. As expected for nonlinear ergodic systems, microscopic spin trajectories obtained for generic model parameters are generically chaotic and cover the entire accessible phase space in the long-time limit. For systems with a clear separation of intrinsic time scales, however, more regular dynamics is to be expected, which calls for an effective low-energy theory.

An effective low-energy theory for the dynamics was initially derived in a purely classical system of slow and fast classical spins. This simple model fulfills our theoretical objectives without aiming to describe any real materials. Nonetheless, the main con-

clusions drawn from our studies carry over in a consistent and qualitative manner to more realistic setups. Primary finding of this initial study is, that the dynamics of the slow impurity degrees of freedom cannot be derived from an effective Hamiltonian relying exclusively on the slow impurity degrees of freedom. This is due to the emergence of a geometric spin torque, which can affect the impurity dynamics profoundly, such as influencing the typical timescale. This non-Hamiltonian adiabatic spin dynamics is derived via the Lagrange formalism, where the 'adiabatic' constraint is imposed. We exploited the constraint of the fast subsystem remaining in its ground state to the momentary configuration of the slow subsystem. For the adiabatic spin dynamics to apply, the validity of the imposed constraint is, however, vital. We find that even for well-separated time scales, the adiabatic constraint is not generically satisfied throughout the system's dynamics. Unlike quantum mechanics, there is no direct classical equivalent to the adiabatic theorem that provides certainty for dynamics to be adiabatic under specific conditions. We have therefore relaxed the constraint by assuming that the fast host spin system always remains in its ground state, i.e., it is tightly bound, but this ground state's orientation is not required to correspond to the ground state of the momentary impurity configuration at all times. Rather, the tightly bound ground state of the host system has an inherent dynamical axis. The tight-binding dynamics adequately describes the dynamics when the slow and the fast timescale differ significantly. The adequacy of the tight-binding dynamics is, however, not generically guaranteed for nonmagnetic host models. A potential ground state ambiguity can lead to an inadmissible singular effective Lagrangian.

The classical low energy theory could be refined by further relaxation of the constraint, e.g. by allowing controlled tilting between the host spins. Incorporating additional dynamical degrees of freedom that facilitate spin-wave-like excitations in the host system can lead to an improved effective description for a wider range of timescales. Such inherent collective modes within the host can be seen as a classical magnon mode, similar to the the quantum-classical concepts discussed in [156].

Subsequent to the initial study of a purely classical model, we focused on quantum-classical models, where local magnetic moments are still described by classical spins, but these impurities are coupled to a gapped quantum system of (non-interacting) itinerant electrons. Typically, the exchange coupling between an electron system and local magnetic impurities is significantly weaker than the characteristic inherent energy scales of the electron system, often by several orders of magnitude. This causes the local magnetic moments to be slow as compared to the characteristic timescale of the electron system. Hence, the adiabatic theorem typically applies, particularly when the exchange coupling is weak in comparison to the energy gap of the insulating electron system. Consequently, when initially prepared in its ground state, the electron system remains in its ground state corresponding to the momentary impurity configuration

during slow variations of the impurity configuration $\boldsymbol{S}$. This ground-state constraint $|\psi(t)\rangle \to |\psi_0(\boldsymbol{S}(t))\rangle$ is refer to as the adiabatic constraint.

Utilizing the adiabatic constraint, we derived an effective semi-classical low-energy theory for the dynamics of the classical impurities for a quantum-classical Lagrangian. The adiabatic equation of motion relies solely on the electron system's ground state properties, and thus eliminates any intrinsic host dynamics. Accordingly, the number of dynamic degrees of freedom is substantially reduced compared to the dynamics of the full semi-classical model. This adiabatic equation of motion contains a adiabatic spin torque in addition to the indirect $RKKY$-like interaction between local magnetic impurities. The adiabatic spin torque arises from the spin Berry curvature $\boldsymbol{\Omega}$, so it is typically non-zero when time-reversal symmetry is broken. We explicitly discussed anomalous dynamics in the minimal setup of two impurities and worked out differences between the effective adiabatic dynamics and an effective Hamiltonian dynamics, particularly in the weak and the strong coupling limit. In general, the spin Berry curvature causes a renormalization of the indirect magnetic exchange and facilitates additional coupling between impurities. Such a geometric torque is similarly encountered in molecular dynamics, where a geometric force can occur when coordinates of the nuclei are treated as classical parameters and electrons are assumed to adapt to the position of the nuclei adiabatically [43–45].

The primary model studied numerically is the spinful Haldane-impurity model. This prototypical setup benefits from the inherently broken time-reversal symmetry of the electron system and enables the exploration of spin Berry curvature effects concerning the bulk band topology of a Chern insulator. In the Haldane model, bulk band topology is described by the k-space Berry curvature.

We systematically analyzed the spin Berry curavture $\boldsymbol{\Omega}$ for impurities in the bulk and at the edge of a Haldane host in phases of trivial and nontrivial k-space topology. In the weak coupling limit, the spin Berry curvature is found to equal the frequency derivative of the magnetic susceptibility at zero frequency. For impurities that are coupled to the bulk and when the exchange coupling J is weak obtaining sizable $\boldsymbol{\Omega}$ values is not easily achievable. This issue stems from the host model's weak magnetic response along with virtual second-order-in-J processes that are suppressed by the bulk's band gap ΔE. Hence, large $\boldsymbol{\Omega}$ values are to be expected when the model is parametrically close to a topological phase transition, where the bulk band gap closes. Analytical studies supported by numerical results revealed, that the spin Berry curvature remains finite and in fact is continuous at a topological phase transition when impurities couple to an infinitely extended bulk. For edge-coupled impurities, a significant $\boldsymbol{\Omega}$ can be attained in the thermodynamic and weak J limit due to a gapless edge mode when k-space topology is nontrivial.

For distant impurities along the edge, the weak coupling $\boldsymbol{\Omega}$ exhibits values that are

several orders of magnitude larger when bulk band topology is nontrivial in comparison to a trivial k-space topology. Moreover, the $RKKY$-like exchange is amplified in the presence of gapless edge modes. These characteristics are expected to be generic, since the bulk boundary correspondence enforces boundary zero modes at interfaces between systems of different bulk band topology. It is the dispersion related to theses gapless edge modes that boosts the weak coupling spin Berry curvature and the indirect $RKKY$-like impurity coupling. Thus, the dynamics of local magnetic moments can in general serve as a signature of bulk band topology.

Boundary zero modes, however, prevent strict application of the adiabatic theorem, which relies on a fully gapped host model. To evaluate the quality of the adiabatic approximation, we compared it to dynamics obtained from the full set of equations of motion. We find an overall good agreement for a large range of exchange coupling strengths. Moreover, already for rather small spin Berry curvatures the adiabatic equations of motion are significantly better of an approximation for the impurity dynamics than an effective Hamiltonian approach that neglects the geometric spin torque. Dynamics of local magnetic moments can be measured by scanning tunneling microscopy methods, which may provide picosecond temporal and nanometer spatial resolution [157].

For a single impurity driven by an external magnetic field, anomalous quantum-classical dynamics resulting from a geometrical torque has also been observed in a correlated quantum host model [158] and for a single quantum impurity coupled to a non-interacting host [47]. Non-Hamiltonian dynamics due to a geometric spin torque is a generic concept and the framework of adiabatic dynamics derived in chapter 4 could easily be applied to other systems where classical control parameter adiabatically steer a gapped quantum system. Similar concepts apply analogously to systems with degenerate ground states, thermal excitations or dynamics that is not strictly adiabatic. To this end, the presented approach has been be extended to a non-Abelian adiabatic dynamics outlined in publication [69].

The presented studies provide a basis for future research and the gained insight raises appealing questions. Future studies could address adiabatic dynamics of local magnetic moments that couple to spin-polarized helical edge modes, for instance in the Kane-Mele model [67, 108]. Here, the impact of the host's topological phase on impurity dynamics may vary with the geometry of the impurity setup. Furthermore, adiabatic impurity dynamics in systems with spontaneous magnetic order could result in a spin Berry curvature of large magnitude, and thus lead to highly non-Hamiltonian dynamics. Moreover, magnetic frustration in the host systems may feed back to the adiabatic dynamics of local impurities. The identification of topological bulk states via the dynamics of local magnetic impurities is foreseen to be generic, so it may also be used to identify topological phases in topological insulators of various spatial dimension, higher

order topological insulators [159], Chern insulators with $C_1 > 1$ and $\mathbb{Z}_2$ topological insulators. These proposals, however, highlight only a fraction of the vast range of potential applications involving adiabatic spin dynamics.

In the final chapter of the presented research, the spectral flow pertaining the host-impurity exchange coupling J is investigated. We studied the interrelation between the J-spectral flow and the k-space topology of the electron system. The main inferences of previous research [144–146, 149, 151, 153, 160] on a singular impurity in spinless models are confirmed by our studies. We find, that the spectral response to a local impurity and the associated in-gap states can indicate bulk topology as proposed in [144, 149, 153]. In accordance with their research, it has been observed that a sufficiently strong impurity potential induces in-gap states. When bulk topology is nontrivial, these in-gap states persist up to infinite impurity strength, which is explained by the descriptive argument of a rigged one-dimensional defect [144]. When k-space topology is, however, trivial, in-gap states induced by an impurity bridge the bulk band gap in a finite range of impurity-potential strength. Consequently, we find a correspondence between the existence of in-gap states in the strong coupling limit and bulk band topology. Moreover, in-gap states at a single impurity are spin-split when k-space topology is nontrivial, while trivial k-space topology entails an in-gap states of only one spin projection for sufficiently strong but finite J. Furthermore, chiral currents associated with the in-gap states induced by an impurity are sensitive bulk band topology [151].

Experimental control of an impurity potential is for instance attained by locally applying a tuneable gate voltage as proposed in [149]. The presence or absence of in-gap states, which can be probed using scanning tunneling spectroscopy, then serves as an indicator for bulk band topology. Spin-split in-gap states, which have been proposed in our study [155], can be detected by spin-sensitive scanning tunneling spectroscopy [161]. The Zeeman-like characteristic of in-gap states induced by a magnetic impurity at any sufficient but finite exchange coupling strength relates to nontrivial bulk topology. Single-atom precision in the deposition of magnetic adatoms [162, 163] enables spatial impurity engineering. A sufficient density of magnetic impurities [154] in a two-dimensional topological insulator is expected to induce in-gap states detectable via photo emission spectroscopy [164]. It has, however, been pointed out that for fundamental reasons local probes cannot serve to detect global topological properties unambiguously [153]. The proposed diagnostics has been demonstrated to yield false results for bulk Hamiltonians which break lattice symmetries via anisotropic or modulated hopping terms. Nonetheless, local indicators for topological phases of matter are of great practical interest.

Furthermore, we studied the spin Berry curvature in a second facet, which concerns the N-th spin Chern number $C_N^{(S)}$ defined through $\mathbf{\Omega}$. As the local interaction J is increased from the weak to strong coupling limit, a spin Chern transition from $C_N^{(S)} = 0$

to $C_N^{(S)} = 1$ takes place. The topological phase transition specified via the spin Chern number necessitates the J-spectral flow of eigenenergies ϵ_k to fully bridge the bulk band gap. Since we considered an $SO(3)$ invariant model, eigenergies for a single magnetic impurity are independent of $\boldsymbol{S}$. Consequently, at J_{crit} the spectrum becomes gapless for an arbitrary orientation of the single impurity $\boldsymbol{S}$, since $\epsilon_k(J_{crit}) = \mu$ for a particular k. With $\boldsymbol{S}$ oriented along the z-direction, the spin Chern transition requires the J-spectral flow associated with the eigenstates of the spin-$\uparrow$ copy of the Haldane model to fully bridge the bulk band gap in the full range of coupling strength $-\infty < J < \infty$. This necessity carries over to the spectral flow of eigenstates of the spinless Haldane model under the influence of a non-magnetic impurity potential. Hence, by utilizing the symmetry of the spinful model, the gap closure for a critical impurity potential in the spinless model may be interpreted as being topologically enforced by a transition of the spin Chern number associated with a virtual $\mathcal{S}^2$ base manifold. A demonstration of this remarkable transfer to non-magnetic impurity potentials is depicted in figure A.9 for a local on-site potential.

Our study of the spin Chern transition and the J-spectral flow provides valuable insight to the local indication of topological phases of matter, which is highly desirable for experimental applications. Furthermore, we propose the topological charge distribution over the base manifold of the fiber bundle as a subject of further studies. In particular in the gapless regime of a multi impurity model, it provides insight to the details of the spin Chern transition. Such insight can be fruitful for forthcoming studies of correlated impurities in topological insulators [165–167], for instance realized by a quantum spin-1/2 coupled to a spinful topological insulator. However, the construction of a fiber bundle lacks the classical parameter manifold when a quantum impurity is locally coupled to a host model. Hence, is is unclear how to define a spin Chern number in the quantum impurity model. Yet, the discussed characteristics of in-gap states related to k-space topology are anticipated to translate qualitatively to correlated local impurities.

A variety of aspects in the considered quantum classical model are also worth further research. For instance higher values of the spin Chern number $C_N^{(S)} > 1$, which can be achieved by non-local short-range host-impurity exchange. Furthermore, unequal host-impurity exchange coupling among different impurities might yield a path to a spin Chern bulk-boundary correspondence. Moreover, anisotropic host-impurity exchange breaks $SO(3)$-symmetry, since $\boldsymbol{J} = (J_x, J_y, J_z)$ can be interpreted as a deformation of the classical parameter manifold. In fact, an XY-like interaction $\boldsymbol{J} = (J, J, 0)$ implies that each impurity contributes a configuration subspace $\mathcal{S}^1$ to the base manifold for the fiber bundle that defines the spin Chern number. Hence, tuning the exchange coupling can alter the dimensionality of the base manifold.

Studying in-gap states in a range of topologically nontrivial materials with various local defects can provide insights to the local detection of topological phases of matter.

Moreover, impurities, vacancies, or disorder are unavoidable in real materials and can impact topological-insulator devices. Thus, comprehension of vacancy effects is necessary for practical applications. The robustness of topological phases against a finite vacancy density, i.e., bulk defect density, has been studied in [154]. Similar studies of a magnetic impurity density bridge the path to Kondo-lattice type models. Vice versa, a topologically nontrivial phase, i.e., quantum spin Hall phase, could be induced by vacancies in a topologically trivial insulator [168]. Applications of topological insulators for potential future devices, for instance exploiting an intriguing interplay of magnetic and electric properties, are explored in [169]. Control over impurities is a path to control localized and possibly gapless in-gap modes, which could serve a wide range of applications. By adiabatically controlling local magnetic impurities, it could even be possible to tune the phase of the localized states through the Berry phase, which holds potential value for the engineering of quantum bits.

A – Appendix

A.1 – Classical Systems

A.1.1 – Derivation of the Classical Adiabatic Equation of Motion

A detailed derivation of the classical adiabatic equation 3.10 of motion is presented by applying the stationary-action principle which results in the Euler-Lagrange equations

$$\frac{\partial L}{\partial m_{r\mu}} - \frac{d}{dt}\frac{\partial L}{\partial \dot{m}_{r\mu}} = 0 \tag{A.1}$$

to the effective Lagrangian

$$L^{\text{eff}}\big(\boldsymbol{m}, \dot{\boldsymbol{m}}; \boldsymbol{n}^0(\boldsymbol{m})\big) = \sum_{q\alpha} S_q A_\alpha(\boldsymbol{m}_q)\dot{m}_{q\alpha} + \sum_{i\beta} F_i A_\beta\big(\boldsymbol{n}_i^0(\boldsymbol{m})\big) \sum_{q\alpha} \frac{\partial n_{i\beta}^0}{\partial m_{q\alpha}}\dot{m}_{q\alpha} \tag{A.2}$$

$$- H^{\text{eff}}(\boldsymbol{m}; \boldsymbol{n}^0(\boldsymbol{m})) - \sum_q \lambda_q(\boldsymbol{m}_q^2 - 1). \tag{A.3}$$

The holonomic constraint of the fast spins $\boldsymbol{F} = F\boldsymbol{n}$ adiabatically following the dynamics of the slow spins $\boldsymbol{S} = S\boldsymbol{m}$ is indicated by $\boldsymbol{n}^0(\boldsymbol{m})$. Note that only the directionality $\boldsymbol{m} = \boldsymbol{m}(t)$ and the velocity $\dot{\boldsymbol{m}} = \frac{d}{dt}\boldsymbol{m}$ of the slow spins are dynamical variables in this context. Even though, since their magnitudes are fixed, unit vectors $\boldsymbol{m}_q$ are defined by only two independent quantities each, the Lagrange multipliers $\{\lambda_q\}$ explicitly ensure that variation of all three $m_{q\alpha}$ for any fixed q does not change the modulus of the unit vectors. The conservation of the length of the classical impurities could also be formulated via $\sum_q \tilde{\lambda}_q(\boldsymbol{S}_q^2 - S_q^2)$ which is equivalent to the re-scaling of the Lagrange multipliers in equation 3.2 ($\lambda_q = \tilde{\lambda}_q S_q^2$). Hereinafter arguments will be omitted for the sake of clarity, $A_{q\alpha} := A_\alpha(\boldsymbol{m}_q)$ and $A_{i\beta}^0 := A_\beta\big(\boldsymbol{n}_i^0(\boldsymbol{m})\big)$ are going to be used since the detailed dependencies are unambiguous from the effective Lagrangian.

$$\begin{aligned}\frac{\partial L_{eff}}{\partial m_{r\mu}} =& S_r \sum_\alpha \frac{\partial A_{r\alpha}}{\partial m_{r\mu}}\dot{m}_{r\alpha} + \sum_{i\alpha,q\beta,\gamma} F_i \frac{\partial A_{i\beta}^0}{\partial n_{i\gamma}^0}\frac{\partial n_{i\gamma}^0}{\partial m_{r\mu}}\frac{\partial n_{i\beta}^0}{\partial m_{q\alpha}}\dot{m}_{q\alpha} \\ &+ \sum_{i\alpha,q\beta} F_i A_{i\beta}^0 \frac{\partial^2 n_{i\beta}^0}{\partial m_{r\mu}\partial m_{q\alpha}}\dot{m}_{q\alpha} - \frac{\partial H^{\text{eff}}}{\partial m_{r\mu}} - 2\lambda_r m_{r\mu}\end{aligned}$$

$$\begin{aligned}\frac{d}{dt}\frac{\partial L_{eff}}{\partial \dot{m}_{r\mu}} =& \frac{d}{dt}\left(S_r A_{r\mu} + \sum_{i\beta} F_i A^0_{i\beta}\frac{\partial n^0_{i\beta}}{\partial m_{r\mu}}\right)\\ =& S_r \sum_{\alpha}\frac{\partial A_{r\mu}}{\partial m_{r\alpha}}\dot{m}_{r\alpha} + \sum_{q\alpha,i\beta,\gamma} F_i \frac{\partial A^0_{i\beta}}{\partial n^0_{i\gamma}}\frac{\partial n^0_{i\gamma}}{\partial m_{q\alpha}}\dot{m}_{q\alpha}\frac{\partial n^0_{i\beta}}{\partial m_{r\mu}}\\ &+ \sum_{q\alpha,i\beta} F_i A^0_{i\beta}\frac{\partial^2 n^0_{i\beta}}{\partial m_{q\alpha}\partial m_{r\mu}}\dot{m}_{q\alpha}\end{aligned}$$

When recombining the previous two auxiliary equations according to the Euler-Lagrange equation the $\sum_{q\alpha,i\beta} F_i^2 A_\beta \frac{\partial^2 n^0_{i\beta}}{\partial m_{q\alpha}\partial m_{r\mu}}\dot{m}_{q\alpha}$ terms cancel each other. Furthermore terms with equivalent $\dot{m}$ dependencies are merged.

$$\begin{aligned}0 =& S_r \sum_{\alpha}\left(\frac{\partial A_{r\alpha}}{\partial m_{r\mu}} - \frac{\partial A_{r\mu}}{\partial m_{r\alpha}}\right)\dot{m}_{r\alpha} + \sum_{i\alpha,q\beta,\gamma} F_i \frac{\partial A^0_{i\beta}}{\partial n^0_{i\gamma}}\left(\frac{\partial n^0_{i\gamma}}{\partial m_{r\mu}}\frac{\partial n^0_{i\beta}}{\partial m_{q\alpha}} - \frac{\partial n^0_{i\gamma}}{\partial m_{q\alpha}}\frac{\partial n^0_{i\beta}}{\partial m_{r\mu}}\right)\dot{m}_{q\alpha}\\ &- \frac{\partial H^{\text{eff}}}{\partial m_{r\mu}}\end{aligned}$$

The first summand is simplified by explicitly utalizing $\boldsymbol{A}$ as the vector potential of a Dirac monopole [15, 16, 47] and hence satisfies $\boldsymbol{\nabla}_{m_q} \times \boldsymbol{A}(\boldsymbol{m}_q) = -\frac{\boldsymbol{m}_q}{|\boldsymbol{m}_q|^3}$. Note that by construction the directional vectors are of unit length, hence $|\boldsymbol{m}_q|^3 = |\boldsymbol{n}_i|^3 = 1$ can be omitted.

$$\begin{aligned}\frac{\partial A_{r\alpha}}{\partial m_{r\mu}} - \frac{\partial A_{r\mu}}{\partial m_{r\alpha}} =& \sum_{\beta\gamma}\frac{\partial A_{r\beta}}{\partial m_{r\gamma}}(\delta_{\alpha\beta}\delta_{\mu\gamma} - \delta_{\alpha\gamma}\delta_{\mu\beta}) = \sum_{\beta\gamma\nu}\frac{\partial A_{r\beta}}{\partial m_{r\gamma}}\varepsilon_{\alpha\mu\nu}\varepsilon_{\beta\gamma\nu}\\ =& -\sum_{\nu}\varepsilon_{\alpha\mu\nu}\sum_{\beta\gamma}\frac{\partial A_{r\beta}}{\partial m_{r\gamma}}\varepsilon_{\gamma\beta\nu} = -\sum_{\nu}\varepsilon_{\alpha\mu\nu}\left(\boldsymbol{\nabla}_{m_r}\times\boldsymbol{A}_r\right)_\nu\\ =& \sum_{\nu} m_{r\nu}\,\varepsilon_{\alpha\mu\nu}\end{aligned}$$

The second summand can be simplified in a similar fashion, to expose the curl of the vector potential indices β and γ are interchanged in the latter term.

$$\begin{aligned}&\sum_{\substack{i,q\\ \alpha\beta\gamma}} F_i \frac{\partial A^0_{i\beta}}{\partial n^0_{i\gamma}}\frac{\partial n^0_{i\gamma}}{\partial m_{r\mu}}\frac{\partial n^0_{i\beta}}{\partial m_{q\alpha}}\dot{m}_{q\alpha} - \underbrace{\sum_{\substack{i,q\\ \alpha\beta\gamma}} F_i \frac{\partial A^0_{i\beta}}{\partial n^0_{i\gamma}}\frac{\partial n^0_{i\gamma}}{\partial m_{q\alpha}}\frac{\partial n^0_{i\beta}}{\partial m_{r\mu}}\dot{m}_{q\alpha}}_{\beta\leftrightarrow\gamma}\\ &= \sum_{\substack{i,q\\ \alpha\beta\gamma}} F_i\left(\frac{\partial A^0_{i\beta}}{\partial n^0_{i\gamma}} - \frac{\partial A^0_{i\gamma}}{\partial n^0_{i\beta}}\right)\frac{\partial n^0_{i\gamma}}{\partial m_{r\mu}}\frac{\partial n^0_{i\beta}}{\partial m_{q\alpha}}\dot{m}_{q\alpha} = \sum_{\substack{i,q\\ \alpha\beta\gamma\nu}} F_i n^0_{i\nu}\varepsilon_{\beta\gamma\nu}\frac{\partial n^0_{i\gamma}}{\partial m_{r\mu}}\frac{\partial n^0_{i\beta}}{\partial m_{q\alpha}}\dot{m}_{q\alpha}\end{aligned}$$

Summing up the previous considerations the Euler-Lagrange equations now take the form

$$0 = S_r \sum_{\alpha\nu} m_{r\nu}\dot{m}_{r\alpha}\varepsilon_{\alpha\mu\nu} + \sum_{\substack{i,q \\ \alpha\beta\gamma\nu}} F_i n^0_{i\nu} \frac{\partial n^0_{i\gamma}}{\partial m_{r\mu}} \frac{\partial n^0_{i\beta}}{\partial m_{q\alpha}} \dot{m}_{q\alpha}\varepsilon_{\beta\gamma\nu} - \frac{\partial H^{\text{eff}}}{\partial m_{r\mu}} - 2\lambda_r m_{r\mu}. \tag{A.4}$$

Here the definition

$$\Omega_{r\mu,q\alpha} := \sum_{\substack{i \\ \beta\gamma\nu}} F_i \frac{\partial n^0_{i\beta}}{\partial m_{q\alpha}} \frac{\partial n^0_{i\gamma}}{\partial m_{r\mu}} n^0_{i\nu}\varepsilon_{\beta\gamma\nu}$$

is made. In a next step contributions of this equation that are parallel and perpendicular to $\boldsymbol{m}_r$ are evaluated individually. On one hand the parallel contribution is obtained by the scalar product of the Euler-Lagrange equation and its variational quantity. Ensured by the Lagrange parameter $|\boldsymbol{m}_r| = 1\,\forall t$ can be used.

$$\begin{aligned} 0 &= \sum_{\mu} m_{r\mu}\left(S_r \sum_{\alpha\nu} m_{r\nu}\dot{m}_{r\alpha}\varepsilon_{\alpha\mu\nu} + \sum_{\substack{q \\ \alpha}} \Omega_{r\mu,q\alpha}\dot{m}_{q\alpha} - \frac{\partial H^{\text{eff}}}{\partial m_{r\mu}} - 2\lambda_r m_{r\mu}\right) \\ &= \sum_{\substack{q \\ \alpha\mu}} \Omega_{r\mu,q\alpha} m_{r\mu}\dot{m}_{q\alpha} - \sum_{\mu} \frac{\partial H^{\text{eff}}}{\partial m_{r\mu}} m_{r\mu} - 2\lambda_r \end{aligned}$$

This determines the Lagrange parameters to be $\lambda_r = \sum_\mu \frac{m_{r\mu}}{2}\big(\sum_{q\alpha}\Omega_{r\mu,q\alpha}\dot{m}_{q\alpha} - \sum_\mu \frac{\partial H^{\text{eff}}}{\partial m_{r\mu}}\big)$, which is a consequence of the fact that each $\boldsymbol{m}_r$ actually depends on only two independent variables, since $|\boldsymbol{m}_{r\mu}| = 1$ is fixed, but the Euler Lagrange equations yield three components per impurity spin. On the other hand the perpendicular contribution is obtained by the vector product of A.4 and $\boldsymbol{m}_r$. The sums over μ as well as α and ν are executed in the first term and subsequently simplified by again using that $\boldsymbol{m}_r$ is of constant unit magnitude.

$$\begin{aligned} 0 &= \sum_{\mu\lambda} \varepsilon_{\mu\lambda\kappa}\, m_{r\lambda}\left(S_r \sum_{\alpha\nu} m_{r\nu}\dot{m}_{r\alpha}\varepsilon_{\alpha\mu\nu} + \sum_{\substack{q \\ \alpha}} \Omega_{r\mu,q\alpha}\dot{m}_{q\alpha} - \frac{\partial H^{\text{eff}}}{\partial m_{r\mu}} - 2\lambda_r m_{r\mu}\right) \\ &= S_r\dot{m}_{r\kappa} + \sum_{\substack{q \\ \alpha\mu\lambda}} \Omega_{r\mu,q\alpha} m_{r\lambda}\dot{m}_{q\alpha}\varepsilon_{\mu\lambda\kappa} - \sum_{\mu\lambda} \frac{\partial H^{\text{eff}}}{\partial m_{r\mu}} m_{r\lambda}\varepsilon_{\mu\lambda\kappa} \\ &= S_r\dot{m}_{r\kappa} + \sum_{\substack{q \\ \alpha}} S_q T_{r\kappa,q\alpha}\dot{m}_{q\alpha} - \sum_{\mu\lambda} \frac{\partial H^{\text{eff}}}{\partial m_{r\mu}} m_{r\lambda}\varepsilon_{\mu\lambda\kappa} \end{aligned}$$

Here the definition

$$T_{r\kappa,q\alpha} := \frac{1}{S_q}\sum_{\mu\lambda}\Omega_{r\mu,q\alpha}m_{r\lambda}\epsilon_{\mu\lambda\kappa}$$

is applied in the last line. It is to mention that the Lagrange parameter vanish in the equation of motion and thus do not impact the dynamics since they are of no physical meaning but just imposed for technical reasons. As a final step this implicit differential equation is brought to an explicit form, which can formally be obtained straight forwardly when a matrix and vector notion is used. To that end the final term is written as $\left(\frac{\partial H^{eff}}{\partial \boldsymbol{m}} \times \boldsymbol{m}\right)_r = \sum_{\mu\lambda}\frac{\partial H^{\text{eff}}}{\partial m_{r\mu}}m_{r\lambda}\varepsilon_{\mu\lambda\kappa}$ where the vector product is meant to be taken for each impurity site r.

$$\begin{aligned}\mathbf{0} =& \dot{\boldsymbol{S}} + \boldsymbol{T}\cdot\dot{\boldsymbol{S}} - \frac{\partial H^{\text{eff}}}{\partial \boldsymbol{m}} \times \boldsymbol{m} \\ \Rightarrow \dot{\boldsymbol{S}} =& \left(\mathbf{1}+\boldsymbol{T}\right)^{-1}\cdot\left(\frac{\partial H^{\text{eff}}}{\partial \boldsymbol{m}} \times \boldsymbol{m}\right) = \frac{\frac{\partial H^{\text{eff}}}{\partial \boldsymbol{S}} \times \boldsymbol{S}}{\mathbf{1}+\boldsymbol{T}}\end{aligned}$$

Note that bold letters indicate matrices of dimension $3N_S \,\mathrm{x}\, 3N_S$ where N_S is the total number of impurities.

A.1.2 – Auxiliary Calculations for the Analytical Collinear Hostsystem's Ground State

An analytical expression of a collinear host spins groundstate is given by equation 3.20. Eventually the impurity quantity $\boldsymbol{m}_0 = \sum_{q,i} J^K_{qi} z_i \boldsymbol{m}_q$ is used to express the groundstate of the host system. In various considerations it is useful to have an analytical expression for $\frac{\partial m_{0\beta}}{\partial m_{q\alpha}}$, $\frac{\partial m_0}{\partial m_{q\alpha}}$ and $\frac{\partial m_0^{-1}}{\partial m_{q\alpha}}$ at hand. These straight forward calculations are shown in some detail below, note that $z_q = \sum_i J^K_{qi} z_i$ is used for a more compact notion.

$$\frac{\partial m_{0\beta}}{\partial m_{q\alpha}} = \frac{\partial}{\partial m_{q\alpha}}\sum_{r,i} J^K_{ri} z_i m_{r_\beta} = z_q \delta_{\alpha\beta}$$

$$\begin{aligned}\frac{\partial m_0}{\partial m_{q\alpha}} =& \frac{\partial}{\partial m_{q\alpha}}\sqrt{\sum_\beta\Big(\sum_{r,i} J^K_{ri} z_i m_{r\beta}\Big)^2} \\ =& \frac{1}{2m_0}\sum_\beta \frac{\partial}{\partial m_{q\alpha}}\Big(\sum_{r,i} J^K_{ri} z_i m_{r\beta}\Big)^2 \\ =& \frac{1}{m_0}\sum_\beta\Big(\sum_{r,i} J^K_{ri} z_i m_{r\beta}\Big)\Big(\sum_{r,i} J^K_{ri} z_i \frac{\partial m_{r\beta}}{\partial m_{q\alpha}}\Big) \\ =& z_q \frac{m_{0\alpha}}{m_0}\end{aligned}$$

$$\begin{aligned}\frac{\partial m_0^{-1}}{\partial m_{q\alpha}} =& \frac{\partial}{\partial m_{q\alpha}} \frac{1}{\sqrt{\sum_\beta m_{0\beta}^2}} \\ =& -\frac{1}{m_0^3} \sum_\beta m_{0\beta} \frac{\partial m_{0\beta}}{\partial m_{q\alpha}} \\ =& -z_q \frac{m_{0\alpha}}{m_0^3}\end{aligned}$$

A.1.3 – Analytical Solution to Coupled Ordinary Differential Equations

The dynamics of $\boldsymbol{m}_0$ (eq. 3.33) and $\boldsymbol{m}_T$ (eq. 3.34) is defined by a set of coupled differential equations. An analytical solution to such a set of dynamical variables is easily obtained as demonstrated within this subsection by following the thoughts we published in [88]. Let $\boldsymbol{x}_1$ and $\boldsymbol{x}_2$ be two classical three component vectors, which evolve according to the coupled differential equations

$$\begin{aligned}\dot{\boldsymbol{x}}_1 =& c_1 \boldsymbol{x}_2 \times \boldsymbol{x}_1 \\ \dot{\boldsymbol{x}}_2 =& c_2 \boldsymbol{x}_1 \times \boldsymbol{x}_2\end{aligned}$$

with $c_1, c_2 \in \mathbb{R}$. These equations of motion imply that $x_1 = |\boldsymbol{x}_1|$, $x_2 = |\boldsymbol{x}_2|$, and $\boldsymbol{x_1 x}_2$ are constants throughout the dynamics. A simple scaling transformation

$$\begin{aligned}\boldsymbol{y}_1 =& \alpha_1 \boldsymbol{x}_1 \\ \boldsymbol{y}_2 =& \alpha_2 \boldsymbol{x}_2\end{aligned}$$

is imposed with real coefficients α_1, α_2 which leads to

$$\begin{aligned}\dot{\boldsymbol{y}}_1 =& \frac{c_1}{\alpha_2} \boldsymbol{y}_2 \times \boldsymbol{y}_1 \\ \dot{\boldsymbol{y}}_2 =& \frac{c_2}{\alpha_1} \boldsymbol{y}_1 \times \boldsymbol{y}_2.\end{aligned}$$

For our purposes the choice of $\alpha_1 = \sqrt{\left|\frac{c_2}{c_1}\right|}$ and $\alpha_2 = \sqrt{\left|\frac{c_1}{c_2}\right|} = \frac{1}{\alpha_1}$ comes in handy for these coefficients, so one obtains

$$\begin{aligned}\dot{\boldsymbol{y}}_1 =& s_1 \sqrt{|c_1 c_2|} \boldsymbol{y}_2 \times \boldsymbol{y}_1 \\ \dot{\boldsymbol{y}}_2 =& s_2 \sqrt{|c_1 c_2|} \boldsymbol{y}_1 \times \boldsymbol{y}_2.\end{aligned}$$

The sign coefficients $s_1 = \frac{c_1}{|c_1|}$ and $s_2 = \frac{c_2}{|c_2|}$ take values of ± 1. Depending on $s_1 = \pm s_2$ or vector

$$\boldsymbol{y} := \boldsymbol{y}_1 \pm \boldsymbol{y}_2 = \sqrt{\left|\frac{c_2}{c_1}\right|}\boldsymbol{x}_1 \pm \sqrt{\left|\frac{c_1}{c_2}\right|}\boldsymbol{x}_2$$

is a constant of motion. As we distinguish these two cases the set of differential equations can be expressed via

$$\begin{aligned}\dot{\boldsymbol{y}}_1 =& \pm s_1\sqrt{|c_1c_2|}\boldsymbol{y} \times \boldsymbol{y_1}\\ \dot{\boldsymbol{y}}_2 =& s_2\sqrt{|c_1c_2|}\boldsymbol{y} \times \boldsymbol{y_2}\end{aligned}$$

and one can read off that $\boldsymbol{y_1}$ and $\boldsymbol{y_1}$ precess unidirectional around $\boldsymbol{y}$ with $\omega_p = \sqrt{|c_1c_2|}|\boldsymbol{y}|$. Using $\alpha_1\alpha_2 = 1$ the length of $y = |\boldsymbol{y}|$ is set by

$$\begin{aligned}|\boldsymbol{y}|^2 =& |\boldsymbol{y}_1|^2 + |\boldsymbol{y}_2|^2 \pm 2\boldsymbol{y}_1\boldsymbol{y}_2\\ =& \left|\frac{c_2}{c_1}\right| x_1^2 + \left|\frac{c_1}{c_2}\right| x_2^2 \pm 2\boldsymbol{x}_1\boldsymbol{x}_2\end{aligned}$$

and as function of conserved quantities only a constants of motion itself. Finally the precession frequency takes the from of

$$\omega_p = \sqrt{c_2^2x_1^2 + c_1^2x_2^2 \pm 2|c_1c_2|\boldsymbol{x}_1\boldsymbol{x}_2}. \tag{A.5}$$

With an analytical expression for the precession frequency of coupled differential equations of this kind at hand, we can now substitute $\boldsymbol{x}_1 = \boldsymbol{m}_0$ and $\boldsymbol{x}_2 = \boldsymbol{m}_T$ by choosing the coefficients

$$\begin{aligned}c_1 =& c_{m_0} = \frac{1}{\frac{m_0}{F(J^K)^2} + \frac{F\Delta}{Sm_0^2}\boldsymbol{m}_0\boldsymbol{m}_T}\\ c_2 =& c_{m_T} = \frac{\frac{F\Delta}{Sm_0}}{\frac{m_0}{F(J^K)^2} + \frac{F\Delta}{Sm_0^2}\boldsymbol{m}_0\boldsymbol{m}_T}\end{aligned}$$

accordingly. Noting that $\frac{c_{m_T}}{c_{m_0}} = \frac{F\Delta}{Sm_0}$ the precession takes place around axis

$$\boldsymbol{y} = \sqrt{\frac{F\Delta}{Sm_0}}\boldsymbol{m}_0 \pm \sqrt{\frac{Sm_0}{F\Delta}}\boldsymbol{m}_T = \text{const}$$

which might be rescaled to

$$\pm\frac{F\Delta}{m_0}\boldsymbol{m}_0 + S\boldsymbol{m}_T = \text{const}.$$

The latter expression of the rotational axis is recognized as total spin $\boldsymbol{F}_T + \boldsymbol{S}_T$ when the "$-$"-sign applies to $\Delta < 0$ and the "$+$"-sign to $\Delta > 0$, since $\boldsymbol{F}_T = F \sum_i z_i \boldsymbol{\eta} = \frac{F\Delta}{m_0} \boldsymbol{m}_0$.

A rather simple analytical expression for the precession frequency is obtained when specifying to a case of just two impurities with local and homogeneous interaction. To ensure $\Delta \neq 0$ the sign factors then have to fulfill $z_{i_1} = -z_{i_2}$ which implies $\boldsymbol{m}_0 \boldsymbol{m}_T = 0$. Without loss of generality one can parameterize the impurity unit vectors within the plane they span by

$$\boldsymbol{m}_1 = \begin{pmatrix} 1 \\ 0 \\ 0 \end{pmatrix}, \quad \boldsymbol{m}_2 = \begin{pmatrix} \cos(\theta) \\ \sin(\theta) \\ 0 \end{pmatrix}$$

when choosing the coordinate system accordingly and with θ as the enclosed angle of the impurities. This parameterization leads to in $m_T = |\boldsymbol{m}_1 + \boldsymbol{m}_2| = \sqrt{2 + 2\cos(\theta)}$ and $m_0 = J^K |\pm \boldsymbol{m}_1 \mp \boldsymbol{m}_2| = J^K \sqrt{2 - 2\cos(\theta)}$. Using those terms we obtain

$$\begin{aligned} \omega_p =& \sqrt{c_{m_T}^2 m_0^2 + c_{m_0}^2 m_T^2} \\ =& \frac{F(J^K)^2}{m_0} \sqrt{\frac{\Delta^2 F^2}{S^2} + m_T^2} \\ =& F J^K \sqrt{\frac{\Delta^2 F^2}{2S^2(1-\cos(\theta))} + \cot^2\left(\frac{\theta}{2}\right)} \end{aligned}$$

A.1.4 – Derivation of the Classical Tight Binding Equations of Motion

To the spin Lagrangian $L(\boldsymbol{m}, \dot{\boldsymbol{m}}, \boldsymbol{n}, \dot{\boldsymbol{n}})$ (eq. 3.2) the tight binding constraint $\boldsymbol{n}(t) \to \boldsymbol{n}^0(\boldsymbol{\eta}(t))$ is applied. The host spin system is enforced to be in it's ground state at all times, with some axis $\boldsymbol{\eta}(t)$ defining the orientation of the $SO(3)$ degenerate ground state manifold. That axis, however, is a dynamical quantity itself and not a function of the impurities as it was in the adiabatic case. The effective Lagrangian

$$\begin{aligned} L^{\text{eff}}\big(\boldsymbol{m}, \dot{\boldsymbol{m}}, \boldsymbol{\eta}, \dot{\boldsymbol{\eta}}; \boldsymbol{n}^0(\boldsymbol{\eta})\big) =& \sum_{q\alpha} S_q A_\alpha(\boldsymbol{m}_q) \dot{m}_{q\alpha} + \sum_{i\alpha\beta} F_i A_\beta\big(\boldsymbol{n}_i^0(\boldsymbol{\eta})\big) \frac{\partial n_{i\beta}^0}{\partial \eta_\alpha} \dot{\eta}_\alpha \\ & - H^{\text{eff}}\big(\boldsymbol{m}, \boldsymbol{\eta}; \boldsymbol{n}^0(\boldsymbol{\eta})\big) - \sum_q \lambda_q(\boldsymbol{m}_q^2 - 1) - \lambda(\boldsymbol{\eta}^2 - 1) \end{aligned}$$

leads to the tight binding equations of motion for the impurities $\dot{\boldsymbol{m}} = \{\dot{\boldsymbol{m}}_q\}$ as well as $\dot{\boldsymbol{\eta}}$ by using the Euler Lagrange equations ($\frac{\partial L}{\partial x} - \frac{d}{dt}\frac{\partial L}{\partial \dot{x}} = 0$ with $x \in \{m_{q\alpha}, \eta_\alpha\}$). First the contributions are calculated individually, similar to A.1.1 the notion of $A_{r\mu} := A_\mu(\boldsymbol{m}_r)$

and $A^{\eta}_{i\mu} := A_\mu(\boldsymbol{n}^0_i(\boldsymbol{\eta}))$ is exploit.

$$\frac{\partial L_{eff}}{\partial m_{r\mu}} = \sum_\alpha S_r \frac{\partial A_{r\alpha}}{\partial m_{r\mu}} \dot{m}_{r\alpha} - \frac{\partial H_{eff}}{\partial m_{r\mu}} - 2\lambda_r m_{r\mu}$$

$$\frac{\partial L_{eff}}{\partial \eta_\mu} = \sum_{i\alpha\beta\gamma} F_i \frac{\partial A^{\eta}_{i\beta}}{\partial n^0_{i\gamma}} \frac{\partial n^0_{i\gamma}}{\partial \eta_\mu} \frac{\partial n^0_{i\beta}}{\partial \eta_\alpha} \dot{\eta}_\alpha + \sum_{i\alpha\beta} F_i A^{\eta}_{i\beta} \frac{\partial^2 n^0_{i\beta}}{\partial \eta_\mu \partial \eta_\alpha} \dot{\eta}_\alpha - \frac{\partial H_{eff}}{\partial \eta_\mu} - 2\lambda \eta_\mu$$

$$\frac{\partial L_{eff}}{\partial \dot{m}_{r\mu}} = S_r A_{r\mu}, \quad \frac{d}{dt}\frac{\partial L_{eff}}{\partial \dot{m}_{r\mu}} = S_r \sum_\alpha \frac{\partial A_{r\mu}}{\partial m_{r\alpha}} \dot{m}_{r\alpha}$$

$$\frac{\partial L_{eff}}{\partial \dot{\eta}_\mu} = \sum_{i\beta} F_i A^{\eta}_{i\beta} \frac{\partial n^0_{i\beta}}{\partial \eta_\mu}, \quad \frac{d}{dt}\frac{\partial L_{eff}}{\partial \dot{\eta}_\mu} = \sum_{i\alpha\beta\gamma} F_i \frac{\partial A^{\eta}_{i\beta}}{\partial n^0_{i\alpha}} \frac{\partial n^0_{i\alpha}}{\partial \eta_\gamma} \dot{\eta}_\gamma \frac{\partial n^0_{i\beta}}{\partial \eta_\mu} + \sum_{i\alpha\beta} F_i A^{\eta}_{i\beta} \frac{\partial^2 n^0_{i\beta}}{\partial \eta_\alpha \partial \eta_\mu} \dot{\eta}_\alpha$$

Combining these terms and simplifying the expressions, the Euler Lagrange equations are obtained in an explicit form.

$$0 = \frac{\partial L_{eff}}{\partial m_{r\mu}} - \frac{d}{dt}\frac{\partial L_{eff}}{\partial \dot{m_{r\mu}}} = \sum_\alpha S_r \left(\frac{\partial A_{r\alpha}}{\partial m_{r\mu}} - \frac{\partial A_{r\mu}}{\partial m_{r\alpha}} \right) \dot{m}_{r\alpha} - \frac{\partial H_{eff}}{\partial m_{r\mu}} - 2\lambda_r m_{r\mu} \tag{A.6}$$

$$0 = \frac{\partial L_{eff}}{\partial \eta_\mu} - \frac{d}{dt}\frac{\partial L_{eff}}{\partial \dot{\eta}_\mu} = \sum_{i\alpha\beta\gamma} F_i \left(\frac{\partial A^{\eta}_{i\beta}}{\partial n^0_{i\gamma}} - \frac{\partial A^{\eta}_{i\gamma}}{\partial n^0_{i\beta}} \right) \frac{\partial n^0_{i\gamma}}{\partial \eta_\mu} \frac{\partial n^0_{i\beta}}{\partial \eta_\alpha} \dot{\eta}_\alpha - \frac{\partial H_{eff}}{\partial \eta_\mu} - 2\lambda \eta_\mu \tag{A.7}$$

To compensate for the independently treated $m_{r\mu}$ of which only two are independent due to $|\boldsymbol{m}_r| = 1$, equation A.7 is projected into contributions unidirectional (scalar product) as well as perpendicular (cross product) to $\boldsymbol{m}_r$. Furthermore the defining property of the vector potential $\boldsymbol{\nabla}_{m_r} \times \boldsymbol{A}(\boldsymbol{m}_r) = -\frac{\boldsymbol{m}_r}{m_r^3} \rightarrow \frac{\partial A_{r\alpha}}{\partial m_{r\mu}} - \frac{\partial A_{r\mu}}{\partial m_{r\alpha}} = \sum_\nu m_{r\nu}\, \varepsilon_{\alpha\mu\nu}$ is used.

$$\begin{aligned} 0 &= \sum_\mu \left(\frac{\partial L_{eff}}{\partial m_{r\mu}} - \frac{d}{dt}\frac{\partial L_{eff}}{\partial \dot{m_{r\mu}}} \right) m_{r\mu} \\ \rightarrow \lambda_r &= -\frac{1}{2} \sum_\mu \frac{\partial H_{eff}}{\partial m_{r\mu}} m_{r\mu} \end{aligned} \tag{A.8}$$

$$\begin{aligned} 0 &= \sum_{\mu\kappa} \left(\frac{\partial L_{eff}}{\partial m_{r\mu}} - \frac{d}{dt}\frac{\partial L_{eff}}{\partial \dot{m_{r\mu}}} \right) m_{r\kappa} \varepsilon_{\mu\kappa\xi} \\ \rightarrow \dot{m}_{r\xi} &= \frac{1}{S_r} \sum_{\mu\kappa} \frac{\partial H_{eff}}{\partial m_{r\mu}} m_{r\kappa} \varepsilon_{\mu\kappa\xi} \end{aligned} \tag{A.9}$$

We obtain a condition for the Lagrange multipliers λ_r (eq. A.8)and recover the Hamiltonian equation of motion for the impurities (eq. A.9).

To proceed in a similar fashion with eq. A.7 again $\boldsymbol{\nabla}_\eta \times \boldsymbol{A}(\boldsymbol{\eta}) = -\frac{\boldsymbol{\eta}}{\eta^3}$ as well as $|\boldsymbol{\eta}| = 1$ are exploited and the tensor

$$\Omega_{\mu\alpha} := \sum_{i\beta\gamma\nu} F_i \frac{\partial n^0_{i\beta}}{\partial \eta_\alpha} \frac{\partial n^0_{i\gamma}}{\partial \eta_\mu} n^0_{i\nu}\, \varepsilon_{\beta\gamma\nu} \tag{A.10}$$

is defined. Note that this is a purely host-dependent quantity in the tight binding framework, whereas $\Omega_{r\mu,q\alpha}$ (eq. 3.8) from the adiabatic approach is contingent on the impurities.

$$\begin{aligned} 0 =& \sum_\mu \left(\frac{\partial L_{eff}}{\partial \eta_\mu} - \frac{d}{dt} \frac{\partial L_{eff}}{\partial \dot{\eta}_\mu} \right) \eta_\mu \\ \rightarrow \lambda =& \frac{1}{2} \sum_{\alpha\mu} \Omega_{\mu\alpha} \eta_\mu \dot{\eta}_\alpha - \frac{1}{2} \sum_\mu \frac{\partial H_{eff}}{\partial \eta_\mu} \eta_\mu \end{aligned} \tag{A.11}$$

$$\begin{aligned} 0 =& \sum_{\mu\kappa} \left(\frac{\partial L_{eff}}{\partial \eta_\mu} - \frac{d}{dt} \frac{\partial L_{eff}}{\partial \dot{\eta}_\mu} \right) \eta_\kappa \varepsilon_{\mu\kappa\xi} \\ =& \sum_{\alpha\mu\kappa} \Omega_{\mu\alpha} \dot{\eta}_\alpha \eta_\kappa \varepsilon_{\mu\kappa\xi} - \sum_{\mu\kappa} \frac{\partial H_{eff}}{\partial \eta_\mu} \eta_\kappa \varepsilon_{\mu\kappa\xi} \end{aligned} \tag{A.12}$$

The equation of motion derived for $\boldsymbol{\eta}$ (eq. A.12) is rather unconventional, since the only dependency on $\dot{\boldsymbol{\eta}}$ comes with Ω. The definition of some tensor

$$\tilde{T}_{\xi\alpha} := \sum_{\mu\kappa} \Omega_{\mu\alpha} \eta_\kappa \varepsilon_{\mu\kappa\xi}$$

allows for an explicit formulation of $\dot{\boldsymbol{\eta}}$, given $\tilde{\boldsymbol{T}}$ is invertible.

$$\dot{\boldsymbol{\eta}} = \tilde{\boldsymbol{T}}^{-1} \left(\frac{\partial H_{eff}}{\partial \boldsymbol{\eta}} \times \boldsymbol{\eta} \right) \tag{A.13}$$

A.1.5 – Further Numerical Results for the Classical Spin System

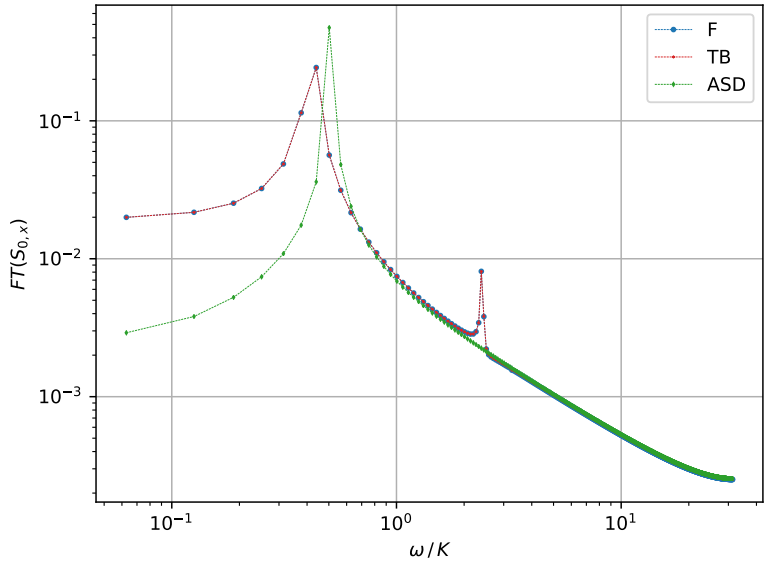

Figure A.1: Fourier transformed of the x-component of $\boldsymbol{S}_0 = S\boldsymbol{m}_0$ obtained from the dynamics of two slow impurity spins coupled to a linear chain of $l = 5$ host spins at site $i_1 = 0$, $i_2 = 3$. The time-evolution is performed for an initial configuration where $\vartheta = 0.95\pi$ is close to the overall ground state and $K/J = 10^{-5}$.

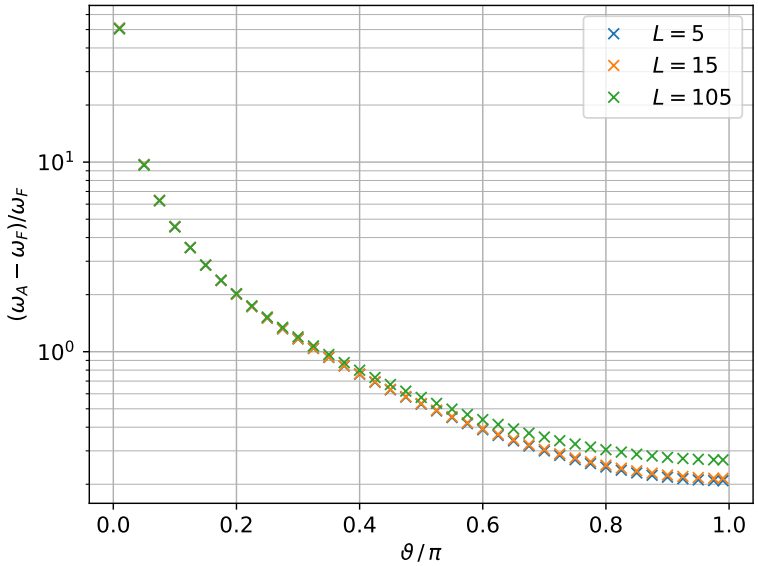

Figure A.2: Difference of the precession frequency ω_A obtained via the adiabatic equation of motion and ω_F obtained from the full set of equation of motion as a function of ϑ enclosed by two impurities. Slow impurity spins couple at sites $i_1 = 1$ and $i_2 = L-1$ for various system sizes of $L = 5, 15, 105$ with $K/J = 10^{-3}$.

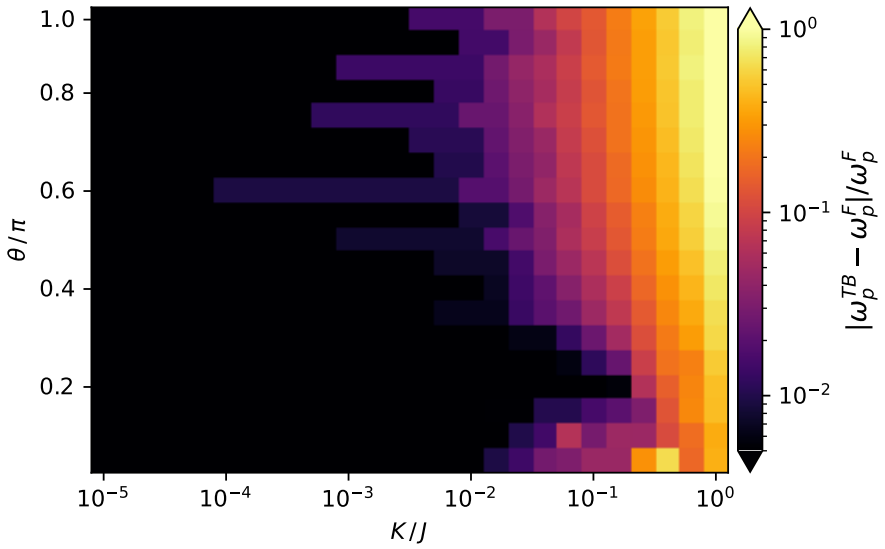

Figure A.3: Color-coded relative difference of the precession frequency ω_{TB} of the real time dynamics of $\boldsymbol{m}_0$ obtained via tight-binding spin dynamics and dynamics ω_F obtained via the full set of equations of motion. Precession frequencies are determined via the main peak in the Fourier spectrum for model parameters in the θ-K/J plane.

A.2 – Quantum-Classical Systems

A.2.1 – Unconstrained Dynamics of Classical and Quantum Degrees of Freedom

Applying the stationary action principle or respectively the Euler Lagrange equations

$$\begin{aligned}\frac{\partial L}{\partial m_{r\mu}} - \frac{d}{dt}\frac{\partial L}{\partial \dot{m}_{r\mu}} &= 0 \\ \frac{\delta L}{\delta \langle\psi|} - \frac{d}{dt}\frac{\delta L}{\delta(\frac{d}{dt}\langle\psi|)} &= 0\end{aligned}$$

to the quantum-classical Lagrangian (eq. 4.7) leads to a set of coupled differential equations that governs the dynamics of quantum as well as classical degrees of freedom.

$$\begin{aligned}L(\langle\psi|, |\psi\rangle, \frac{d}{dt}\langle\psi|, \frac{d}{dt}|\psi\rangle, \boldsymbol{S}, \frac{d}{dt}\boldsymbol{S}) =& \langle\psi| i\frac{d}{dt}|\psi\rangle + \sum_q \boldsymbol{A}(\boldsymbol{m}_q)\frac{d}{dt}\boldsymbol{S}_q \\ & - \langle\psi|\hat{H}(\boldsymbol{S})|\psi\rangle - \sum_q \lambda_q(\boldsymbol{m}_q^2 - 1)\end{aligned}$$

The short notion of $A_{q\alpha} = A_\alpha(\boldsymbol{m}_q)$ as well as $\langle \hat{H} \rangle = \langle \psi | \hat{H} | \psi \rangle$ is used, so for the classical degrees of freedom we get

$$\begin{aligned}\frac{\partial L}{\partial m_{r\mu}} =& \sum_\alpha \frac{\partial A_{r\alpha}}{\partial m_{r\mu}} S_r \dot{m}_{r\alpha} - \frac{\partial \langle \hat{H} \rangle}{\partial m_{r\mu}} - 2\lambda_r m_{r\mu} \\ \frac{d}{dt}\frac{\partial L}{\partial \dot{m}_{r\mu}} =& S_r \frac{d}{dt} A_{r\mu} = S_r \sum_\alpha \frac{\partial A_{r\mu}}{\partial m_{r\alpha}} \dot{m}_{r\alpha}\end{aligned}$$

Explicitly using $\boldsymbol{\nabla}_r \times \boldsymbol{A}_r = -\boldsymbol{m}_r$ and $\frac{\partial A_{r\alpha}}{\partial m_{r\mu}} - \frac{\partial A_{r\mu}}{\partial m_{r\alpha}} = \sum_\nu m_{r\nu}\, \varepsilon_{\alpha\mu\nu}$ leads to

$$0 = S_r \sum_{\alpha\nu} \dot{m}_{r\alpha} m_{r\nu}\, \varepsilon_{\alpha\mu\nu} - \frac{\partial \langle \hat{H} \rangle}{\partial m_{r\mu}} - 2\lambda_r m_{r\mu}.$$

By taking the cross product of the previous expression and $\boldsymbol{m}_r$ the classical equations of motion, equivalent to the once obtained by exploiting the Hamiltonian formalism, are obtained.

$$0 = S_r \dot{m}_{r\kappa} - \sum_{\mu\lambda} \frac{\partial \langle \hat{H} \rangle}{\partial m_{r\mu}} m_{r\lambda} \epsilon_{\mu\lambda\kappa}$$

Similarly varying the Lagrangian with respect to $\langle \psi |$ results in the equation of motion for $|\psi\rangle$

$$0 = i\frac{d}{dt}|\psi\rangle - \hat{H}(\boldsymbol{S})|\psi\rangle$$

which is nothing but the well known Schrödinger equation and vice versa variation of the Lagrangian with respect to $|\psi\rangle$ leads to the Schrödinger equation of $\langle \psi |$.

A.2.2 – Constrained Dynamics of the Classical Impurities

In some detail the application of the stationary action principle or respectively the Euler Lagrange equations to the effective spin-only quantum-classical Lagrangian (eq. 4.17) is presented within this subsection. The resulting equations of motion are a set of coupled differential equations of the classical impurity degrees of freedom, containing the spin Berry curvature of the map $\boldsymbol{S} \to |\psi_0(\boldsymbol{S})\rangle$. The explicit time dependence $\boldsymbol{S} = \boldsymbol{S}(t)$ is omitted as it is obvious from the context.

$$\begin{aligned}L_{eff}(\boldsymbol{S}, \dot{\boldsymbol{S}}) =& \sum_{q\alpha} \langle \psi_0(\boldsymbol{S}) | i \frac{\partial}{\partial S_{q\alpha}} | \psi_0(\boldsymbol{S}) \rangle \dot{S}_{q\alpha} + \sum_q \boldsymbol{A}(\boldsymbol{m}_q) \dot{\boldsymbol{S}}_q \\ & - \langle \psi_0(\boldsymbol{S}) | \hat{H}(\boldsymbol{S}) | \psi_0(\boldsymbol{S}) \rangle - \sum_q \lambda_q (\boldsymbol{m}_q^2 - 1).\end{aligned}$$

In a first auxiliary step the derivatives

$$\begin{aligned}\frac{\partial L_{eff}}{\partial m_{r\mu}} =& \sum_{q\alpha} i\frac{\partial\langle\psi_0|}{\partial m_{r\mu}}\frac{\partial|\psi_0\rangle}{\partial m_{q\alpha}}\dot{m}_{q\alpha} + \sum_{q\alpha} i\langle\psi_0|\frac{\partial^2|\psi_0\rangle}{\partial m_{r\mu}m_{q\alpha}}\dot{m}_{q\alpha} + \sum_{\alpha} S_r\frac{\partial A_{r\alpha}}{\partial m_{r\mu}}\dot{m}_{r\alpha} \\ & - \frac{\partial\langle\psi_0|}{\partial m_{r\mu}}\hat{H}|\psi_0\rangle - \langle\psi_0|\frac{\partial\hat{H}}{\partial m_{r\mu}}|\psi_0\rangle - \langle\psi_0|\hat{H}\frac{\partial|\psi_0\rangle}{\partial m_{r\mu}} - 2\lambda_r m_{r\mu} \\ \frac{d}{dt}\frac{\partial L_{eff}}{\partial\dot{m}_{r\mu}} =& \frac{d}{dt}\left(\sum_{r\mu}\langle\psi_0|i\frac{\partial}{\partial m_{r\mu}}|\psi_0\rangle + S_r A_{r\mu}\right) \\ =& \sum_{q\alpha} i\frac{\partial\langle\psi_0|}{\partial m_{q\alpha}}\frac{\partial|\psi_0\rangle}{\partial m_{r\mu}}\dot{m}_{q\alpha} + \sum_{q\alpha} i\langle\psi_0|\frac{\partial^2|\psi_0\rangle}{\partial m_{q\alpha}m_{r\mu}}\dot{m}_{q\alpha} + \sum_{\alpha} S_r\frac{\partial A_{r\mu}}{\partial m_{r\alpha}}\dot{m}_{r\alpha}\end{aligned}$$

are evaluated, the lucid dependence of the ground state on the impurity spins is omitted for the sake of clarity. We recombine these derivatives to the Euler Lagrange equations and explicitly use $\langle\psi_0|\psi_0\rangle = 1$, $S_r = 1$ as well as $\boldsymbol{\nabla}_r \times \boldsymbol{A}_r = -\boldsymbol{m}_r$ so $\frac{\partial A_{r\alpha}}{\partial m_{r\mu}} - \frac{\partial A_{r\mu}}{\partial m_{r\alpha}} = \sum_\nu m_{r\nu}\,\varepsilon_{\alpha\mu\nu}$.

$$\begin{aligned}0 =& i\sum_{q\alpha}\left(\frac{\partial\langle\psi_0|}{\partial m_{r\mu}}\frac{\partial|\psi_0\rangle}{\partial m_{q\alpha}} - \frac{\partial\langle\psi_0|}{\partial m_{q\alpha}}\frac{\partial|\psi_0\rangle}{\partial m_{r\mu}}\right)\dot{m}_{q\alpha} + \sum_{\alpha}\left(\frac{\partial A_{r\alpha}}{\partial m_{r\mu}} - \frac{\partial A_{r\mu}}{\partial m_{r\alpha}}\right)\dot{m}_{r\alpha} \\ & - \langle\psi_0|\frac{\partial\hat{H}}{\partial m_{r\mu}}|\psi_0\rangle - E_0\frac{\partial}{\partial m_{r\mu}}\langle\psi_0|\psi_0\rangle - 2\lambda_r m_{r\mu} \\ =& \sum_{q\alpha}\Omega_{r\mu,q\alpha}\dot{m}_{q\alpha} + \sum_{\alpha\nu} m_{r\nu}\dot{m}_{r\alpha}\,\varepsilon_{\alpha\mu\nu} - \langle\psi_0|\frac{\partial\hat{H}}{\partial m_{r\mu}}|\psi_0\rangle - 2\lambda_r m_{r\mu}\end{aligned}$$

Furthermore the spin Berry curvature, defined by

$$\Omega_{r\mu,q\alpha} := i\frac{\partial\langle\psi_0|}{\partial m_{r\mu}}\frac{\partial|\psi_0\rangle}{\partial m_{q\alpha}} - i\frac{\partial\langle\psi_0|}{\partial m_{q\alpha}}\frac{\partial|\psi_0\rangle}{\partial m_{r\mu}},$$

is substituted in the last step. Next the projection collinear and perpendicular to $\boldsymbol{m}_r$ are taken. The former yields the condition that determines the Lagrange parameter λ_r while the latter leads to the quantum classical adiabatic equation of motion.

$$\lambda_r = \sum_{\mu}\frac{m_{r\mu}}{2}\left(\sum_{q\alpha}\Omega_{r\mu,q\alpha}\dot{m}_{q\alpha} - \langle\psi_0|\frac{\partial\hat{H}}{\partial m_{r\mu}}|\psi_0\rangle\right)$$

$$\begin{aligned}0 =& \sum_{\mu\lambda}\varepsilon_{\mu\lambda\kappa}m_{r\lambda}\left(\sum_{q\alpha}\Omega_{r\mu,q\alpha}\dot{m}_{q\alpha} + \sum_{\alpha\nu} m_{r\nu}\dot{m}_{r\alpha}\,\varepsilon_{\alpha\mu\nu} - \langle\psi_0|\frac{\partial\hat{H}}{\partial m_{r\mu}}|\psi_0\rangle - 2\lambda_r m_{r\mu}\right) \\ =& \sum_{q\alpha\mu\lambda}\Omega_{r\mu,q\alpha}m_{r\lambda}\dot{m}_{q\alpha}\varepsilon_{\mu\lambda\kappa} + \dot{m}_{r\kappa} - \sum_{\mu\lambda}\langle\psi_0|\frac{\partial\hat{H}}{\partial m_{r\mu}}|\psi_0\rangle m_{r\lambda}\varepsilon_{\mu\lambda\kappa}\end{aligned}$$

Finally the implicit adiabatic equation of motion can be noted in a more convenient form, using $\frac{\partial\langle\hat{H}\rangle_0}{\partial m_{r\mu}} = \frac{\partial}{\partial m_{r\mu}}\langle\psi_0|\hat{H}|\psi_0\rangle = \langle\psi_0|\frac{\partial\hat{H}}{\partial m_{r\mu}}|\psi_0\rangle$.

$$\dot{\boldsymbol{m}}_r = \frac{\partial\langle\hat{H}\rangle_0}{\partial\boldsymbol{m}_r} \times \boldsymbol{m}_r - \sum_{q\alpha\mu\lambda\kappa} \Omega_{r\mu,q\alpha} m_{r\lambda}\dot{m}_{q\alpha}\varepsilon_{\mu\lambda\kappa}\boldsymbol{e}_\kappa$$

A.2.2.1 Rewriting Eigenstate-Derivatives in Terms of Derivatives of the Hamiltonian

The classical spins act as parameters for the quantum-system in our hybrid theory. One might therefore interpret the Hamiltonian $\hat{H}(\boldsymbol{S})$ as well as it's eigenstates $|n(\boldsymbol{S})\rangle$ as parametrically dependent on the impurities $\boldsymbol{S}$, however that explicit dependency is omitted in the notation below. The eigenstates $|n\rangle$ form a full set of orthonormal basis ($\langle m|n\rangle = \delta_{mn}$) of the Hamiltonian $\hat{H}$ with eigenvalues E_n ($\hat{H}|n\rangle = E_n|n\rangle$). The ground state is denoted by $|0\rangle$. For $m \neq n$ the derivative of the matrix element $\langle m|\hat{H}|n\rangle$ with respect so some parameter can be evaluated in terms of

$$\nabla\langle m|\hat{H}|n\rangle = E_n\nabla\langle m|n\rangle = 0$$

on the one hand. On the other hand, using $0 = \nabla\langle m|n\rangle = \langle\nabla m|n\rangle + \langle m|\nabla n\rangle \ \forall m \neq n$, one can reckon it as

$$\begin{aligned}\nabla\langle m|\hat{H}|n\rangle =& \langle\nabla m|\hat{H}|n\rangle + \langle m|\nabla\hat{H}|n\rangle + \langle m|\hat{H}|\nabla n\rangle \\ =& E_n \underbrace{\langle\nabla m|n\rangle}_{=-\langle m|\nabla n\rangle} + \langle m|\nabla\hat{H}|n\rangle + E_m\langle m|\nabla n\rangle\end{aligned}$$

Combining these two results in

$$\begin{aligned}0 &= (E_m - E_n)\langle m|\nabla n\rangle + \langle m|\nabla\hat{H}|n\rangle \\ \Rightarrow \langle m|\nabla n\rangle &= \frac{\langle m|\nabla\hat{H}|n\rangle}{E_m - E_n} \quad \forall m \neq n.\end{aligned}$$

The previously obtained relation can be used to formulate the spin Berry curvature in terms of derivatives of the Hamiltonian. To this end we first consider

$$\begin{aligned}|\nabla_{q\alpha}0\rangle =& \sum_n |n\rangle\langle n|\nabla_{q\alpha}\rangle = \sum_{n\neq 0} |n\rangle\langle n|\nabla_{q\alpha}\rangle + |0\rangle \underbrace{\langle 0|\nabla_{q\alpha}\rangle}_{=0,\ \langle 0|0\rangle=1} \\ =& \sum_{n\neq 0} |n\rangle\frac{\langle n|\nabla_{q\alpha}\hat{H}|0\rangle}{E_n - E_0}\end{aligned}$$

where derivatives with respect to $S_{q\alpha}$ are denoted by $\nabla_{q\alpha}$. Now the matrix elements $\langle\nabla_{q\alpha}0|\nabla_{r\beta}0\rangle$ of the spin Berry curvature (eq. 4.16) can be re-formulated to

$$\begin{aligned}\langle\nabla_{q\alpha}0|\nabla_{r\beta}0\rangle &= \sum_{n\neq 0}\sum_{m\neq 0}\frac{\langle 0|\nabla_{q\alpha}\hat{H}|m\rangle}{E_m - E_0}\langle m|n\rangle\frac{\langle n|\nabla_{r\beta}\hat{H}|0\rangle}{E_n - E_0} \\ &= \sum_{n\neq 0}\frac{\langle 0|\nabla_{q\alpha}\hat{H}|n\rangle\langle n|\nabla_{r\beta}\hat{H}|0\rangle}{(E_n - E_0)^2}.\end{aligned}$$

A.2.2.2 Spin-diagonal Blocks in $\mathbf{\Omega}^{(0)}$ for Spin-Rotation Invariant Hosts

In section 4.1.3.1 we argued that eigenstates of a spin-rotation invariant host can simultaneously be chosen as eigenstates of the unitary operator $\hat{U}(\boldsymbol{n},\varphi)$ that causes spin-rotations in Fock-space. In the limit of weak coupling between impurities and the quantum host, these common eigenstates lead to $[\mathbf{\Omega}^{(0)}_{ij}, \boldsymbol{R}] = 0$, where $\mathbf{\Omega}^{(0)}_{ij}$ is the i,j-impurity block of the weak coupling spin Berry curvature and R the defining matrix representation of SO(3).

Rotation matrices $\boldsymbol{R}(\boldsymbol{n},\varphi) = e^{\boldsymbol{\mathcal{R}n}\varphi}$ can be written in terms of the generators $\boldsymbol{\mathcal{R}}$, the axis $\boldsymbol{n}$ and an angle φ of the rotation. The idea is that any rotation can be constructed as a consecutive application of infinitesimal rotations by $d\varphi$ and $\boldsymbol{\mathcal{R}_n} = \boldsymbol{\mathcal{R}n} = n_x\boldsymbol{\mathcal{R}}_x + n_y\boldsymbol{\mathcal{R}}_y + n_z\boldsymbol{\mathcal{R}}_z$ generate these infinitesimal rotations in $\mathbb{R}^3$ around an axis $\boldsymbol{n} = (n_x, n_y, n_z)^T$. We expand $\boldsymbol{R}(\boldsymbol{n}, d\varphi) = \sum_k \frac{(\boldsymbol{\mathcal{R}_n}d\varphi)^k}{k!} \approx \boldsymbol{\mathcal{R}_n}d\varphi$ and terminate the expansion after the first order (linear in $d\varphi$) because higher orders would contribute by higher powers of the infinitesimal $(d\varphi)^k$ with $k \geq 2$ only. The commutator of $\Omega^{(0)}_{ij}$ and $\boldsymbol{R}$, however, has to vanish independent of the axis of rotation and as commuting is a linear operation, scalars can be extracted.

$$[\mathbf{\Omega}^{(0)}_{ij}, \boldsymbol{\mathcal{R}}_\alpha] = 0,\ \forall\alpha \in \{x,y,z\} \tag{A.14}$$

$$\boldsymbol{\mathcal{R}}_x = \begin{pmatrix}0&0&0\\0&0&-1\\0&1&0\end{pmatrix},\quad \boldsymbol{\mathcal{R}}_y = \begin{pmatrix}0&0&1\\0&0&0\\-1&0&0\end{pmatrix},\quad \boldsymbol{\mathcal{R}}_z = \begin{pmatrix}0&-1&0\\1&0&0\\0&0&0\end{pmatrix} \tag{A.15}$$

Exemplary the commutator

$$0 = [\mathbf{\Omega}^{(0)}_{ij}, \boldsymbol{\mathcal{R}}_x] = \begin{pmatrix}0 & \Omega^{(0)}_{ix,jz} & -\Omega^{(0)}_{ix,jy}\\ \Omega^{(0)}_{iz,jx} & \Omega^{(0)}_{iy,jz} + \Omega^{(0)}_{iz,jy} & -\Omega^{(0)}_{iy,jy} + \Omega^{(0)}_{iz,jz}\\ -\Omega^{(0)}_{iy,jz} & -\Omega^{(0)}_{iy,jy} + \Omega^{(0)}_{iz,jz} & -\Omega^{(0)}_{iy,jz} - \Omega^{(0)}_{iz,jy}\end{pmatrix}$$

is evaluated explicitly. From the matrix equation $[\mathbf{\Omega}^{(0)}_{ij}, \boldsymbol{\mathcal{R}}_x] = 0$ we easily read off that the elements $\{\Omega^{(0)}_{ix,jz}, \Omega^{(0)}_{ix,jy}, \Omega^{(0)}_{iy,jx}, \Omega^{(0)}_{iz,jx}\}$ have to vanish as well as $\Omega^{(0)}_{iy,jy} = \Omega^{(0)}_{iz,jz}$. Combined with $[\mathbf{\Omega}^{(0)}_{ij}, \boldsymbol{\mathcal{R}}_y] = 0$ and $[\mathbf{\Omega}^{(0)}_{ij}, \boldsymbol{\mathcal{R}}_z] = 0$ we derive that all diagonal elements

of $\mathbf{\Omega}_{ij}^{(0)}$ equal each and all the off-diagonal elements have to be zero, thus, $\mathbf{\Omega}_{ij}^{(0)} = \Omega \mathbf{1}_3$ where $\mathbf{1}_3$ is the identity matrix in three dimensions.

A.2.2.3 Conserved Quantities of the Two Impurity Dynamics

For cases where two classical impurity spins are weakly coupled to a host system that is symmetric under spin rotations in Fock space the adiabatic equations of motion take the form of eq. 4.47. Those can be rewritten in terms of

$$\begin{aligned}
\dot{\boldsymbol{m}}_1 =& \frac{J^{RKKY}}{1-\Omega^2 \boldsymbol{m}_1 \boldsymbol{m}_2} \big[\boldsymbol{m}_2 - \Omega \boldsymbol{m}_1 \times \boldsymbol{m}_2\big] \times \boldsymbol{m}_1 \\
=& \frac{J^{RKKY} \boldsymbol{\Sigma} \times \boldsymbol{m}_1}{1-\Omega^2 \boldsymbol{m}_1 \boldsymbol{m}_2} \\
\dot{\boldsymbol{m}}_2 =& \frac{J^{RKKY}}{1-\Omega^2 \boldsymbol{m}_1 \boldsymbol{m}_2} \big[\boldsymbol{m}_1 - \Omega \boldsymbol{m}_1 \times \boldsymbol{m}_2\big] \times \boldsymbol{m}_2 \\
=& \frac{J^{RKKY} \boldsymbol{\Sigma} \times \boldsymbol{m}_2}{1-\Omega^2 \boldsymbol{m}_1 \boldsymbol{m}_2}
\end{aligned}$$

with

$$\boldsymbol{\Sigma} = \boldsymbol{m}_1 + \boldsymbol{m}_2 - \Omega \boldsymbol{m}_1 \times \boldsymbol{m}_2.$$

Subsequent gathering of brief auxiliary calculations shows the preservation of various quantities, which we claim to be conserved in section 4.1.3.3.
Firstly the magnitude of $\boldsymbol{m}_q$ where $q \in \{1, 2\}$ is conserved by eq. 4.47, since $\dot{\boldsymbol{m}}_q$ is perpendicular to $\boldsymbol{m}_q$, thus $\frac{d}{dt}\boldsymbol{m}_q^2 = 2\boldsymbol{m}_q \dot{\boldsymbol{m}}_q = 0$. Secondly, as the adiabatic equations of motion are written in the from of eq. A.2.2.3, we can define some vector $\boldsymbol{\Sigma}$ (eq. 4.48). Its conservation is straight forwardly demonstrated by

$$\begin{aligned}
\dot{\boldsymbol{\Sigma}} =& \quad \dot{\boldsymbol{m}}_1 + \dot{\boldsymbol{m}}_1 - \Omega \dot{\boldsymbol{m}}_1 \times \boldsymbol{m}_2 - \Omega \boldsymbol{m}_1 \times \dot{\boldsymbol{m}}_2 \\
=& \quad \frac{J^{RKKY}}{1-\Omega^2 \boldsymbol{m}_1 \boldsymbol{m}_2} \big[\boldsymbol{m}_2 \times \boldsymbol{m}_1 - \Omega(\boldsymbol{m}_1 \times \boldsymbol{m}_2) \times \boldsymbol{m}_1\big] \\
&+ \frac{J^{RKKY}}{1-\Omega^2 \boldsymbol{m}_1 \boldsymbol{m}_2} \big[\boldsymbol{m}_1 \times \boldsymbol{m}_2 - \Omega(\boldsymbol{m}_1 \times \boldsymbol{m}_2) \times \boldsymbol{m}_2\big] \\
&- \frac{\Omega J^{RKKY}}{1-\Omega^2 \boldsymbol{m}_1 \boldsymbol{m}_2} \big[\boldsymbol{m}_2 \times \boldsymbol{m}_1 - \Omega(\boldsymbol{m}_1 \times \boldsymbol{m}_2) \times \boldsymbol{m}_1\big] \times \boldsymbol{m}_2 \\
&+ \frac{\Omega J^{RKKY}}{1-\Omega^2 \boldsymbol{m}_1 \boldsymbol{m}_2} \big[\boldsymbol{m}_1 \times \boldsymbol{m}_2 - \Omega(\boldsymbol{m}_1 \times \boldsymbol{m}_2) \times \boldsymbol{m}_2\big] \times \boldsymbol{m}_1 \\
=& \quad \frac{\Omega^2 J^{RKKY}}{1-\Omega^2 \boldsymbol{m}_1 \boldsymbol{m}_2} \big[\boldsymbol{m}_1(\boldsymbol{m}_1 \boldsymbol{m}_2) - \boldsymbol{m}_2 \boldsymbol{m}_1^2\big] \times \boldsymbol{m}_2 \\
&- \frac{\Omega^2 J^{RKKY}}{1-\Omega^2 \boldsymbol{m}_1 \boldsymbol{m}_2} \big[\boldsymbol{m}_1 \boldsymbol{m}_2^2 - \boldsymbol{m}_2(\boldsymbol{m}_1 \boldsymbol{m}_2)\big] \times \boldsymbol{m}_1 \\
=& \quad 0.
\end{aligned}$$

Next we show the conservation of the scalar product $\boldsymbol{m}_1\boldsymbol{m}_2$ which implies the conservation of the relative angle φ between the impurities.

$$\begin{aligned}\frac{d}{dt}(\boldsymbol{m}_1\boldsymbol{m}_2) =&\dot{\boldsymbol{m}}_1\boldsymbol{m}_2 + \boldsymbol{m}_1\dot{\boldsymbol{m}}_2\\ =&(\boldsymbol{\Sigma}\times\boldsymbol{m}_1)\boldsymbol{m}_2 + \boldsymbol{m}_1(\boldsymbol{\Sigma}\times\boldsymbol{m}_2)\\ =&(\boldsymbol{\Sigma}\times\boldsymbol{m}_1)\boldsymbol{m}_2 - \boldsymbol{m}_1(\boldsymbol{m}_2\times\boldsymbol{\Sigma})\\ =&(\boldsymbol{\Sigma}\times\boldsymbol{m}_1)\boldsymbol{m}_2 - \boldsymbol{m}_2(\boldsymbol{\Sigma}\times\boldsymbol{m}_2) = 0\end{aligned}$$

Here we used the invariance of the triple product under cyclic permutations in the last step. Furthermore, since $\boldsymbol{\Sigma}$ in conserved, the precession of $\boldsymbol{m}_1$, $\boldsymbol{m}_2$ and $\boldsymbol{m}_T = \boldsymbol{m}_1 + \boldsymbol{m}_2$ takes place with a constant frequency of

$$\begin{aligned}\omega_{prec} =&\sqrt{\boldsymbol{\Sigma}^2} = \sqrt{2+\Omega^2(\boldsymbol{m}_1\times\boldsymbol{m}_2)^2 + 2\boldsymbol{m}_1\boldsymbol{m}_2 - 2\Omega\boldsymbol{m}_1(\boldsymbol{m}_1\times\boldsymbol{m}_2) - 2\Omega\boldsymbol{m}_2(\boldsymbol{m}_1\times\boldsymbol{m}_2)}\\ =&\sqrt{2+\Omega^2\sin^2(\varphi)+2\cos(\varphi)} = \sqrt{4\cos^2(\varphi/2)+\Omega^2\sin^2(\varphi)}.\end{aligned}$$

A.2.3 – Expansion of the Haldane Model at $\boldsymbol{K}$ and $\boldsymbol{K}'$

In the band theory of topological insulators a topological phase transition requires a gap closure in the band structure. Concerning the Haldane model that gap closure occurs in form of a Dirac cone, where the bulk valence and conduction bands touch at exactly one point in the first Brillouin zone. Due to the C_3 symmetry of the bulk Hamiltonian of the Haldane model (eq. 4.75) that band closure takes place at the $\boldsymbol{K}$ or the $\boldsymbol{K}'$ point. The bulk band gap vanishes exactly at the topological phase transition, thus analyzing the band closure condition is an indicator for the topological phase transition. Various topological phases are in general characterized by a change in a topological index, in case of the Haldane model the bulk band Chern number (eq. 4.79), resulting from the integral of the Berry Connection over the first Brillouin zone. Evaluation of the Chern number for an exemplary parameter set between gap closures results in the topological phase diagram.
First we expand the translational invariant Haldane Hamiltonian at $\boldsymbol{K}'+\boldsymbol{\kappa} = \frac{2\pi}{3}(\frac{2}{\sqrt{3}},0)^T + (\kappa_x,\kappa_y)^T$ with $|\boldsymbol{\kappa}| << 1$.

$$\mathcal{H}(\boldsymbol{K}'+\boldsymbol{\kappa}) = 3\tau_2\cos(\xi)\mathbf{1} + \left(M - 3\sqrt{(}3)\tau_2\sin(\xi)\right)\boldsymbol{\sigma}^z + \frac{3}{2}\tau_1\left(\kappa_x\boldsymbol{\sigma}^x - \kappa_y\boldsymbol{\sigma}^y\right) \qquad \text{(A.16)}$$

In proximity of $\boldsymbol{K}'$ the eigenenergies of the Haldane model are thus given by

$$\epsilon_\pm(\boldsymbol{K}'+\boldsymbol{\kappa}) = 3\tau_2\cos(\xi) \pm \sqrt{\left(M - 3\sqrt{3}\tau_2\sin(\xi)\right)^2 + \frac{9}{4}\tau_1^2\boldsymbol{\kappa}^2}. \qquad \text{(A.17)}$$

The bulk gap closes as the root becomes zero at $\kappa = 0$ which yields the condition

$M = 3\sqrt{3}\tau_2 \sin(\xi)$ for a gap closure at $\boldsymbol{K}'$.

Second, a gap closure can also take place at $\boldsymbol{K} = \frac{2\pi}{3}(\frac{1}{\sqrt{3}}, 1)^T$, thus expanding equation 4.75 at $\boldsymbol{K} + \boldsymbol{\kappa}$ hints towards another criterion for a topological phase transition. The Hamiltonian expanded around $\boldsymbol{K}$ is given by

$$\mathcal{H}(\boldsymbol{K}+\boldsymbol{\kappa}) = 3\tau_2\cos(\xi)\mathbf{1} + (M + 3\sqrt{(}3)\tau_2\sin(\xi))\boldsymbol{\sigma}_z + \frac{3}{4}\tau_1\big((\kappa_x + \sqrt{3}\kappa_y)\boldsymbol{\sigma}_x - (\sqrt{3}\kappa_x - \kappa_y)\boldsymbol{\sigma}_y\big), \tag{A.18}$$

which yields the two bands

$$\epsilon_\pm(\boldsymbol{K}+\boldsymbol{\kappa}) = 3\tau_2\cos(\xi) \pm \sqrt{\big(M + 3\sqrt{3}\tau_2\sin(\xi)\big)^2 + \frac{9}{4}\tau_1\boldsymbol{\kappa}^2}, \tag{A.19}$$

so the bulk gap vanishes at $\boldsymbol{k} = \boldsymbol{K}$ as $M = -3\sqrt{3}\tau_2\sin(\xi)$.

A.2.4 – Integrating I_{bulk}

The following integral arises from considerations on whether the spin Berry curvature in the weak coupling limit diverges at the topological phase transition of the Haldane model as discussed in 4.3.1.5. Ω is continuous at the topological phase transition if the limit $m \to 0$ of I_{bulk} exists or rather is finite. We consider

$$I_{bulk} \sim \int_A d^2\kappa \int_A d^2\kappa' \frac{1}{(\sqrt{m+\boldsymbol{\kappa}^2} + \sqrt{m+\boldsymbol{\kappa}'^2})^2}, \tag{A.20}$$

and parameterize the two dimensional $\boldsymbol{\kappa}$ in polar coordinates (κ, ϕ) to express the integral $\int d^2\kappa$ as $\int d\phi \int d\kappa\kappa$. The κ-independent part is of the form $e^{i\phi}$ and therefore cannot lead to divergences (analog for κ'), so we are left with

$$I_{bulk} = \int_0^\Lambda d\kappa \int_0^\Lambda d\kappa' \frac{\kappa\kappa'}{(\sqrt{m+\kappa^2} + \sqrt{m+\kappa'^2})^2} \tag{A.21}$$

which is straight forwardly calculated analytically. We approach the analytical integration by substitution $u = k + k'$ and $v = k - k'$ in a first step. Furthermore we set $m = 0$ so we are parametrically right at the topological phase transition. Initially k and k' are independent but u and v are not, so one has to be cautious when it comes to the limits of the defined integral. In fact, when the outer u-integration runs from $0 < u \leq \Lambda$ the inner v-integral runs form $-u < v \leq u$, while in the remaining interval of $\Lambda < u \leq 2\Lambda$ the inner v-integration is limited to $u - 2\Lambda < v \leq 2\Lambda - u$. Jacobi

determinant of the applied substitution is $\left|\frac{\partial(k,k')}{\partial(u,v)}\right| = -\frac{1}{2}$.

$$\begin{aligned} I_{bulk} &= \int_0^\Lambda d\kappa \int_0^\Lambda d\kappa' \frac{\kappa\kappa'}{(\kappa+\kappa')^2} \\ &= \int_0^\Lambda du \int_{-u}^{u} dv \left|\frac{\partial(k,k')}{\partial(u,v)}\right| \left(1-\frac{v^2}{u^2}\right) + \int_\Lambda^{2\Lambda} du \int_{u-2\Lambda}^{2\Lambda-u} dv \left|\frac{\partial(k,k')}{\partial(u,v)}\right| \left(1-\frac{v^2}{u^2}\right) \\ &= \frac{1-\ln(4)}{2}\Lambda^2 \end{aligned} \tag{A.22}$$

A.2.5 – Finite Size Effects of Ω

Finite system sizes and small overall energy gaps, here causes by weak next nearest neighbor hopping $\tau_2 \ll \tau_1$, can result in large spin Berry curvatures $\mathbf{\Omega}$. In the limit of weakly coupling the impurities to a spin rotation invariant host, such as the spinful Haldane model, the spin Berry curvature is determined by a single real number $\Omega \sim J^2$ (eq. 4.37). The gap if the topological insulating phase (left) and the topologically

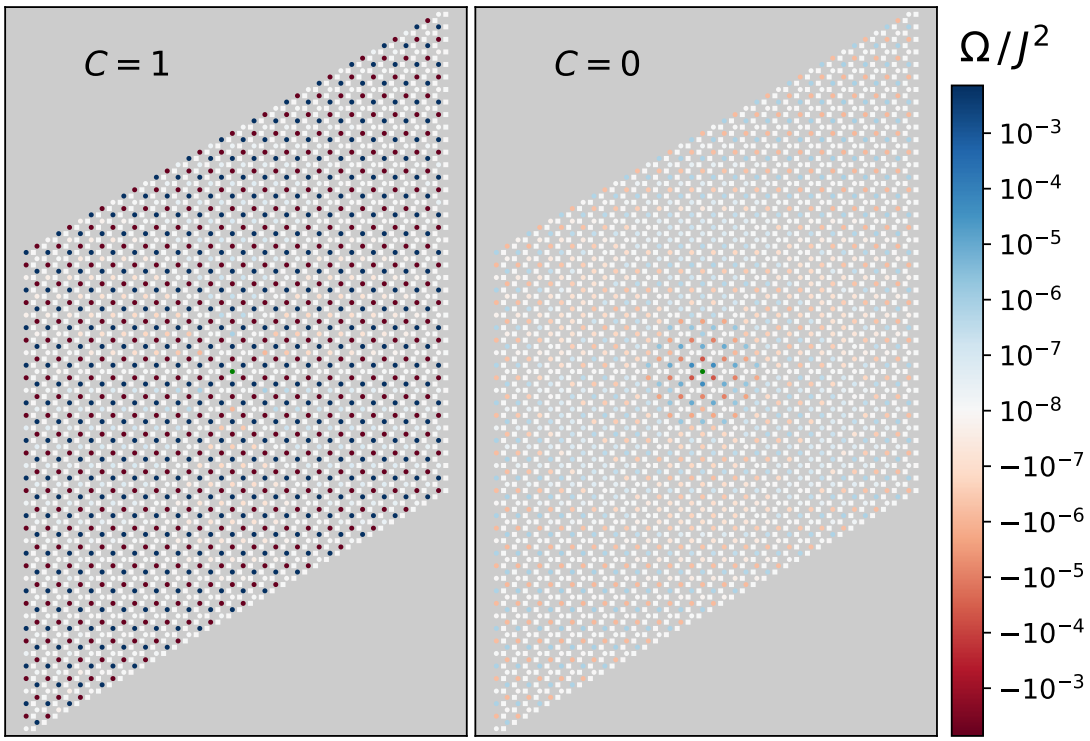

Figure A.4: Same setup as in figure 4.5, but with a smaller $\tau_2 = 0.001\tau_1$. In the phase of nontrivial bulk band topology ($C = 1$) the on-site potential is $M = 0.8M_{crit}$ and in the trivial phase ($C = 0$) $M = 1.2M_{crit}$. Accordingly, ΔE is the same in both panels with constant $\xi = \pi/4$.

trivial insulator (right) equal each other, but orders of magnitude smaller than in fig. 4.5 with $\tau_2 = 0.1$. In contrast results presented in section 4.3.1.1, the close range region reaches over the whole lattice when the host is in a topologically nontrivial

state (left panel), no significant decay with distance in that case. Super lattice of sites where Ω is large and alters sign on super-lattice-A to super-lattice-B sites. in the trivial phase (right), the close rage region spreads over a few unit cells only and Ω decreases significantly with increasing distance on the scale of this finite lattice. It is not unexpected, that effects related to the finite extension of this model become more pronounced with smaller gaps [48].

A.2.6 – Parametric Dependencies of Ω for Various Distances

In the weak coupling limit, the bulk band gap closes at the topological phase boundaries of the Haldane model, which is illustated in figure A.5.

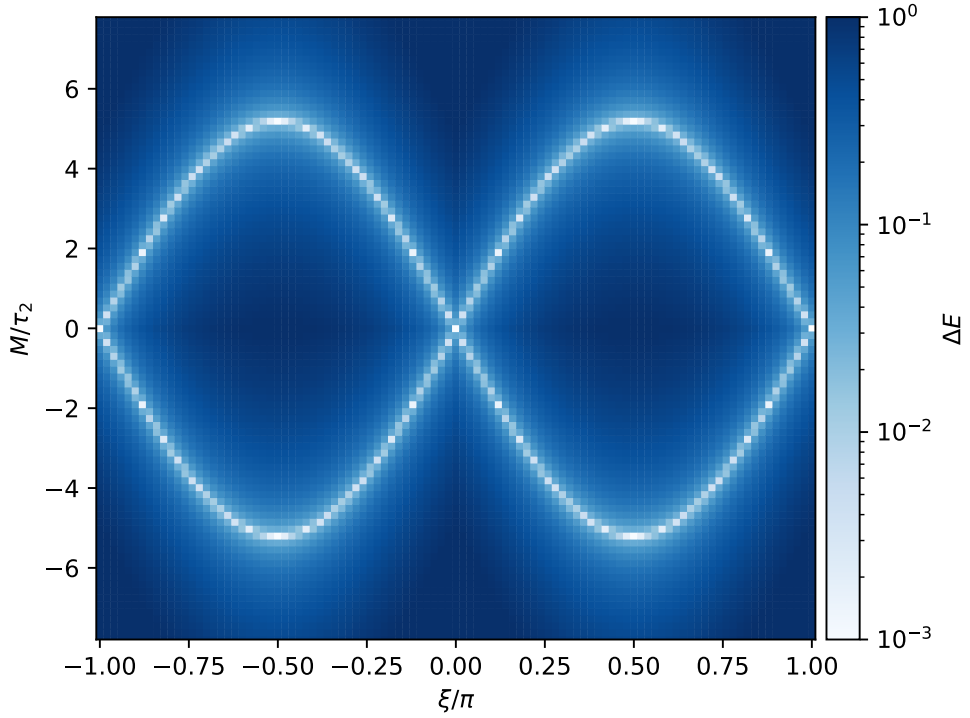

Figure A.5: Energy gap ΔE between the highest occupied and the lowest unoccupied single-particle eigenenergy ϵ_k in the weak coupling limit with two impurities coupled to the host at $d = \sqrt{3}$. The host-impurity exchange coupling is $J = 0.01$ and $\tau_2 = 0.1$.

The following examples illustrate the intricate structure of the weak coupling spin-Berry curvature in the M/τ_2-ξ plane. For all plots of Ω/J^2, we maintain consistent coloring, indicated by the same norm of the color bar. Impurity distances d range from the close to far regime.

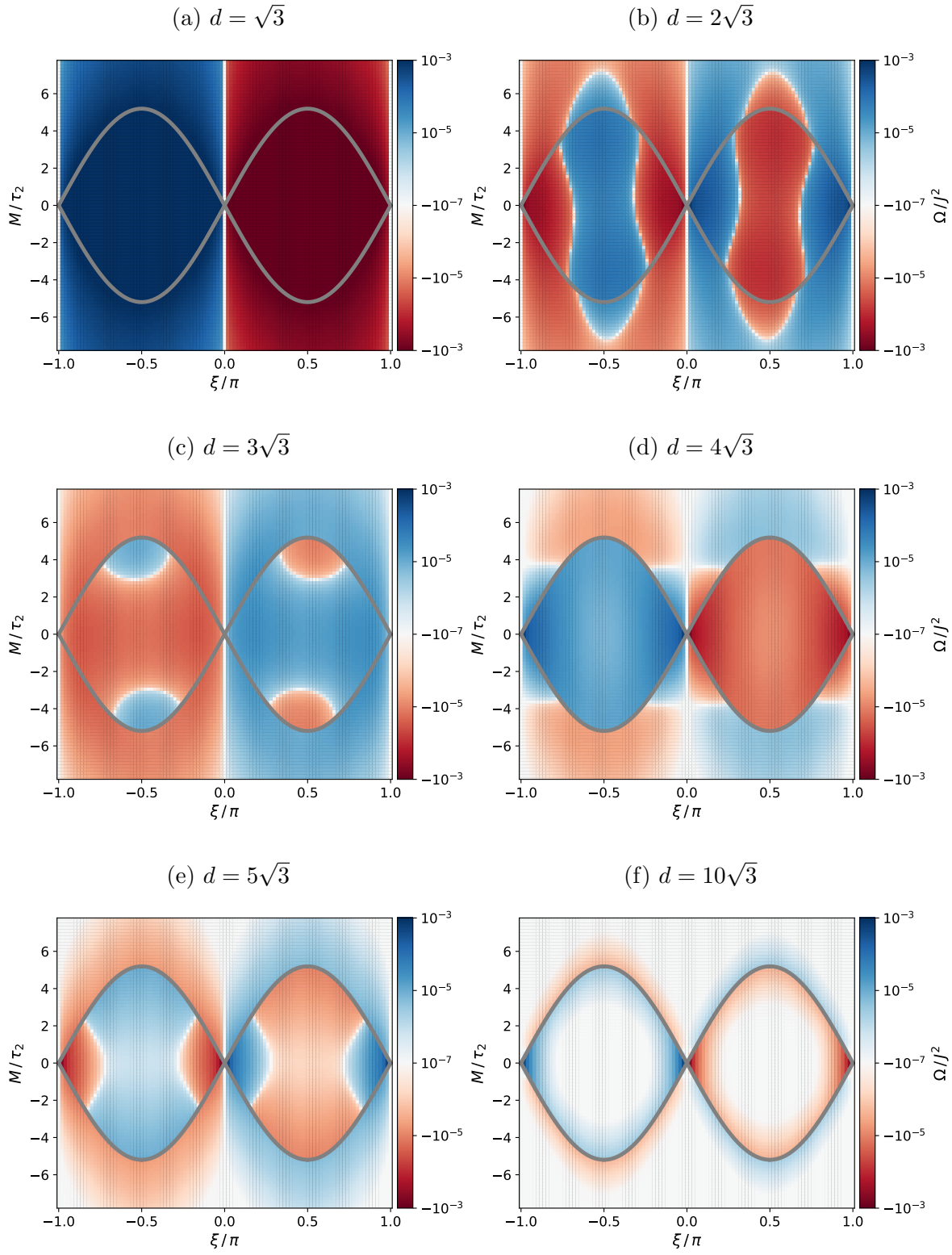

Figure A.6: Dependence of Ω/J^2 on ξ and M/τ_2 in the Haldane phase diagram for various distances between the impurities. Gray lines mark the topological phase boundaries (see fig. 4.3). The underlying lattice with periodic boundary conditions extends 27×27 unit cells , $\tau_2 = 0.1$ and distances are taken in the $\boldsymbol{v}_1$ direction.

A.2.7 – Chemical Potential in Insulators at Zero Temperature

The chemical potential determines the the energy up to which energy levels of a model are occupied at zero temperature. In non-interacting fermionic systems (ideal Fermi gas) the Fermi-Dirac statistic [170, 171]

$$f = \frac{1}{1 + e^{\beta(\epsilon(\omega)-\mu)}} \tag{A.23}$$

describes the probability of energy levels $\epsilon(\omega) = \hbar\omega$ being occupied at finite temperature T, thus finite $\beta = 1/(k_B T)$. We set $\hbar = 1$ and $k_B = 1$ as absolute values of ϵ and β are of minor relevance for now. The following argument validates, that the chemical potential μ of an insulator is in the center of the band gap at zero temperature. This statement holds even when the density of states $\rho_v(\omega)$ at the valence band differs from the density of states $\rho_c(\omega)$ at the conduction band, which shifts the chemical potential out of the center at non-zero temperature. For the sake of simplicity we imagine a band structure as depicted in figure A.7 with a gap Δ, the valence band has constant density of states ρ_v in its entire bandwidth of $1/\rho_v$ and the conduction band is constructed in an analogue fashion but with $\rho_c \neq \rho_v$. The expectation value of the number of particles in this description is determined by integrating the density of states weighted by the Fermi-Dirac distribution as a partition function over the entire energy spectrum.

$$\begin{aligned}
\langle N \rangle =& \int_{-\infty}^{\infty} d\omega \frac{\rho(\omega)}{1 + e^{\beta(\omega-\mu)}} \\
=& \rho_v \int_{-\Delta/2-1/\rho_v}^{\Delta/2} \frac{d\omega}{1 + e^{\beta(\omega-\mu)}} + \rho_c \int_{\Delta/2}^{\Delta/2+1/\rho_c} \frac{d\omega}{1 + e^{\beta(\omega-\mu)}} \\
=& \rho_v \Big[\frac{-1}{\beta} \ln(1 + e^{-\beta(\omega-\mu)}) \Big]_{-\Delta/2-1/\rho_v}^{\Delta/2} + \rho_c \Big[\frac{-1}{\beta} \ln(1 + e^{-\beta(\omega-\mu)}) \Big]_{\Delta/2}^{\Delta/2+1/\rho_c}
\end{aligned} \tag{A.24}$$

Per design, $\langle N \rangle = 1$ is required to fully occupy the valence band. To find the chemical potential that meets this requirement best, we vary μ in equation A.24 and evaluate numerically when the $\langle N \rangle$ is closes to unity.

From figure A.8 we read off, that as β increases the chemical potential approaches zero. Consequently lowering the temperature to zero results in a chemical potential at zero which is right in the center of the band gap for the model under investigation here. Even thought we designed a case where $\int_{-\infty}^{0} d\omega \frac{\rho_v}{1+e^{\beta(\omega-\mu)}} = \int_{0}^{\infty} d\omega \frac{\rho_c}{1+e^{\beta(\omega-\mu)}}$, the full partition of the valence band does not have to match the full partition of the conduction band and the gap Δ does not have to be symmetric around zero for the previous statement to remain valid. The point we make is that although the the density of states below the gap differs from the one above it, the chemical potential approaches the center of the gap at zero temperature. Accordingly, we define the Fermi energy the be midway through the band gap. At finite temperatures, however, different densities of states in

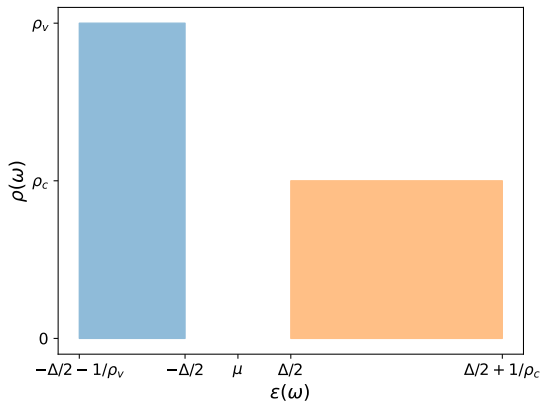

Figure A.7: Exemplary model with unequal densities of states in the valence and conduction band and gap Δ.

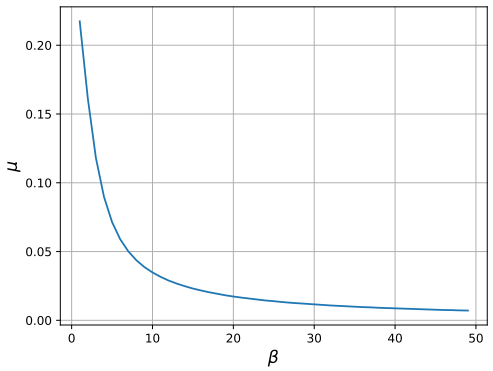

Figure A.8: Convergence of the chemical potential μ in the limit of zero temperature respectively $\beta = 1/T \to \infty$.

the valence and the conduction band generically lead to a less symmetric situations and naturally μ is not longer midway through the gap.

A.2.8 – Local Onsite Potential Analogue to Spin Chern Transition

Similar to the local magnetic impurities $\boldsymbol{S}_q$, one can add a local potential $\hat{H}_{loc} = M_{loc} \sum_{q,\sigma} \hat{c}^{\dagger}_{i_q\sigma} \hat{c}_{i_q\sigma}$ to the the Haldane model (eq. 4.73) to generate non-magnetic local bound states around impurity sites. Characteristics of in-gap states when varying M_{loc} (base manifold is $\mathcal{S}^1$ as compactification of $\mathbb{R}$) local to an island of radius R (fig. A.9 displays $R = 1$) can be explained by a virtual topological phase transition in analogy to the J-spectral flow (fig. 5.1) of single-electron eigenvalues which leas to a transition of the spin Chern number $C_1^{(S)}$.

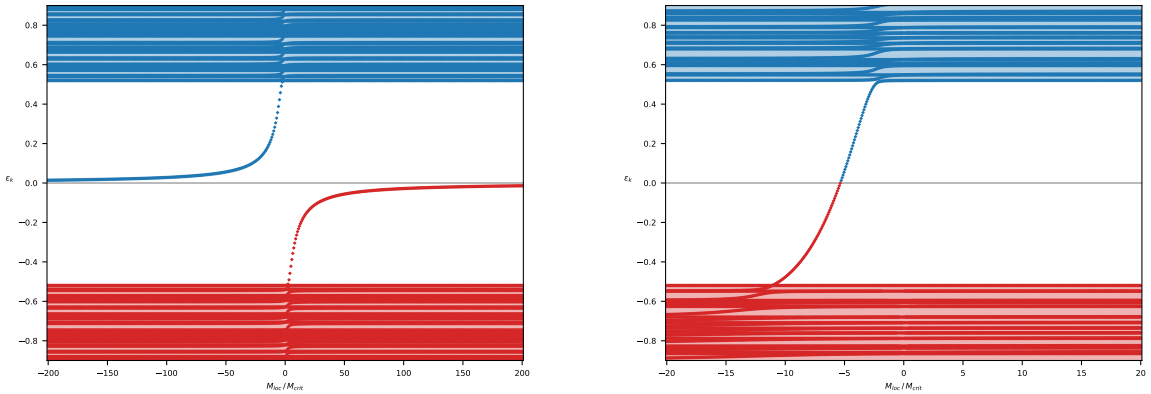

(a) Topologically nontrivial bulk with global $M = 0$.

(b) Topologically trivial bulk with global $M = 2M_{crit}$.

Figure A.9: One impurities site with an additional on-site potential M_{loc} at an A-site in the bulk of the host. The gray line indicates the chemical potential at $\mu = 0$. Further model parameters are $\tau_2 = 0.1$ and $\xi = \pi/2$, hence the bulk band structure is particle hole symmetric. $M = 0$ and $M = 2M_{crit}$ with $M_{crit} \approx 0.52$ feature the same bulk band gap, i.e. ΔE is identical in both panels. The bulk is modeled by a lattice of 39×39 unit cells with periodic boundary conditions.

Bibliography

[1] P. W. Andersen. More is different. *Science*, 177(4047):393–396, 1972.

[2] Robert T. Sullivan. Insect Swarming and Mating. *The Florida Entomologist*, 64(1):44, 1981.

[3] Roland Bouffanais. Design and Control of Swarm Dynamics. *SpringerBriefs in Complexity*, 2016.

[4] Leo Gao, John Schulman, and Jacob Hilton. Scaling Laws for Reward Model Overoptimization. 2022.

[5] Jason Wei, Yi Tay, Rishi Bommasani, Colin Raffel, Barret Zoph, Sebastian Borgeaud, Dani Yogatama, Maarten Bosma, Denny Zhou, Donald Metzler, Ed H Chi, Tatsunori Hashimoto, Oriol Vinyals, Percy Liang, Jeff Dean, and William Fedus. Emergent Abilities of Large Language Models. *Transactions on Machine Learning Research*, 2022.

[6] Jean Kaddour, Joshua Harris, Maximilian Mozes, Herbie Bradley, Roberta Raileanu, and Robert Mchardy. Challenges and Applications of Large Language Models. 2023.

[7] Robert B. Laughlin. *A different universe : reinventing physics from the bottom down*. Basic Books, 2005.

[8] J. R. Schrieffer. *Theory of super conductivity*, volume 108. American Physical Society, 2018.

[9] Pierre Curie. Sur la symétrie dans les phénomènes physiques, symétrie d'un champ électrique et d'un champ magnétique. *J. Phys. Theor. Appl.*, 3(1):393–415, 1894.

[10] Charles 1916-2019 Kittel and Siegfried 1939 Hunklinger. *Einführung in die Festkörperphysik*. Oldenbourg, München [u.a.], 2006.

[11] T. H.R. Skyrme. A non-linear field theory. *Proceedings of the Royal Society of London. Series A. Mathematical and Physical Sciences*, 260(1300):127–138, 1961.

[12] T. H.R. Skyrme. A unified field theory of mesons and baryons. *Nuclear Physics*, 31(C):556–569, 1962.

[13] U. K. Rößler, A. N. Bogdanov, and C. Pfleiderer. Spontaneous skyrmion ground states in magnetic metals. *Nature*, 442(7104):797–801, 2006.

[14] Y Y Dai, H Wang, P Tao, T Yang, W J Ren, and Z D Zhang. Skyrmion ground state and gyration of skyrmions in magnetic nanodisks without the Dzyaloshinsky-Moriya interaction. *Physical Review B*, 88(5):54403, 2013.

[15] P A M Dirac. Quantised Singularities in the Electromagnetic Field. pages 1–13, 1931.

[16] P. A.M. Dirac. The theory of magnetic poles. *Physical Review*, 74(7):817–830, 1948.

[17] C. Castelnovo, R. Moessner, and S. L. Sondhi. Magnetic monopoles in spin ice. *Nature*, 451(7174):42–45, 2008.

[18] Xiao Liang Qi, Rundong Li, Jiadong Zang, and Shou Cheng Zhang. Inducing a magnetic monopole with topological surface states. *Science*, 323(5918):1184–1187, 2009.

[19] B. Andrei Bernevig and Taylor L. Hughes. *Topological insulators and topological superconductors*. Princeton University Press, 2013.

[20] Ching Kai Chiu, Jeffrey C.Y. Teo, Andreas P. Schnyder, and Shinsei Ryu. Classification of topological quantum matter with symmetries. *Reviews of Modern Physics*, 88(3):1–70, 2016.

[21] W P Su, J R Schrieffer, and A J Heeger. Solitons in polyacetylene. *Physical Review Letters*, 42(25):1698–1701, 1979.

[22] The rise of quantum materials, 2016.

[23] Chetan Nayak, Steven H Simon, Ady Stern, Michael Freedman, and Sankar Das Sarma. Non-Abelian anyons and topological quantum computation. *Reviews of Modern Physics*, 80(3):1083–1159, 2008.

[24] Ville Lahtinen and Jiannis K. Pachos. A Short Introduction to Topological Quantum Computation. *SciPost Physics*, 3(3), 2017.

[25] Hengxin Tan, Yongkang Li, Yizhou Liu, Daniel Kaplan, Ziqiang Wang, and Binghai Yan. Emergent topological quantum orbits in the charge density wave phase of kagome metal CsV3Sb5. *npj Quantum Materials*, 8(1):1–9, 2023.

[26] Charles Kittel. Introduction to Solid State Physics. 2005.

[27] L. D. Landau. On the theory of phase transitions. *Zh. Eksp. Teor. Fiz.*, 7:19–32, 1937.

[28] F. D.M. Haldane. Model for a quantum hall effect without landau levels: Condensed-matter realization of the "parity anomaly". *Physical Review Letters*, 61(18):2015–2018, 1988.

[29] J. M. Kosterlitz and D. J. Thouless. Ordering, metastability and phase transitions in two-dimensional systems. *Journal of Physics C: Solid State Physics*, 6(7):1181, 1973.

[30] Nobel Committee. NobelPrize.org, 2016.

[31] Alexander Altland and Martin R Zirnbauer. Nonstandard symmetry classes in mesoscopic normal-superconducting hybrid structures. *Physical Review B*, 55(2):1142–1161, 1997.

[32] Jeffrey C.Y. Teo and C L Kane. Topological defects and gapless modes in insulators and superconductors. *Physical Review B*, 82(11), 2010.

[33] M. V. Berry. Quantal phase factors accompanying adiabatic changes. *Proceedings of the Royal Society of London. A. Mathematical and Physical Sciences*, 392(1802):45–57, 1984.

[34] P. Ehrenfest. Adiabatische Invarianten und Quantentheorie. *Annalen der Physik*, 356(19):327–352, 1916.

[35] M. Born and V. Fock. Beweis des Adiabatensatzes. *Zeitschrift für Physik*, 51(3-4):165–180, 1928.

[36] Tosio Kato. On the Adiabatic Theorem of Quantum Mechanics. *Journal of the Physical Society of Japan*, 5(6):435–439, 1950.

[37] Albert Messiah. *Quantenmechanik Band 2*. Berlin, 1979.

[38] Barry Simon. Holonomy, the Quantum Adiabatic Theorem, and Berry's Phase. *Physical Review Letters*, 51(24):2167, 1983.

[39] Mikio Nakahara. *Geometry, Topology and Physics*. CRC Press, 2 edition, 2003.

[40] C Alden Mead. The geometric phase in molecular systems. *Reviews of Modern Physics*, 64(1):51–85, 1992.

[41] Raffaele Resta. Manifestations of Berry's phase in molecules and condensed matter, 2000.

[42] Elliott H. Lieb. The classical limit of quantum spin systems. *Communications in Mathematical Physics*, 31(4):327–340, 1973.

[43] Hiroshi Kuratsuji and Shinji Iida. Effective Action for Adiabatic Process: Dynamical Meaning of Berry and Simon's Phase. *Progress of Theoretical Physics*, 74(3):439–445, 1985.

[44] John Moody, A Shapere, and Frank Wilczek. Realizations of magnetic-monopole gauge fields: Diatoms and spin precession. *Physical Review Letters*, 56(9):893–896, 1986.

[45] Bernard Zygelman. Appearance of gauge potentials in atomic collision physics. *Physics Letters A*, 125(9):476–481, 1987.

[46] M. V. Berry and J. M. Robbins. Chaotic classical and half-classical adiabatic reactions: geometric magnetism and deterministic friction. *Proceedings of The Royal Society A: Mathematical, Physical and Engineering Sciences*, 442(1916):659–672, 1993.

[47] Christopher Stahl and Michael Potthoff. Anomalous Spin Precession under a Geometrical Torque. *Physical Review Letters*, 119(22), 2017.

[48] Simon Michel and Michael Potthoff. Spin Berry curvature of the Haldane model. *Physical Review B*, 106(23):235423, 2022.

[49] M Z Hasan and C L Kane. Colloquium: Topological insulators. *Reviews of Modern Physics*, 82(4):3045–3067, 2010.

[50] Xiao Liang Qi and Shou Cheng Zhang. Topological insulators and superconductors. *Reviews of Modern Physics*, 83(4), 2011.

[51] Shiing-Shen Chern. Characteristic Classes of Hermitian Manifolds. *Source: Annals of Mathematics*, 47(1):85–121, 1946.

[52] M. F. Atiyah and I. M. Singer. The Index of Elliptic Operators on Compact Manifolds. *Bulletin of the American Mathematical Society*, 69(3):422–433, 1963.

[53] Michael Potthoff. Dynamical Mean-Field Theory for Correlated Topological Phases. pages 1–34, Forschungszentrum Jülich, 2022.

[54] Robin Quade. Private Correspondence, 2023.

[55] V.I. Arnold. *Mathematical Methods Of Classical Mechanics*. Springer, New York, 1978.

[56] Phillip A. Griffiths. On a theorem of chern. *Illinois Journal of Mathematics*, 6(3):468–479, 1962.

[57] H. Blaine. Lawson and Marie-Louise Michelsohn. *Spin geometry*. Princeton University Press, 1989.

[58] Hassler Whitney. On the Topology of Differentiable Manifolds. In *Hassler Whitney Collected Papers*, pages 175–215. 1992.

[59] Georges de Rham. Sur l'analysis situs des variétés à n dimensions. *Journal de Mathématiques Pures et Appliquées*, 10:115–200, 1931.

[60] E. Stiefel. Richtungsfelder und Fernparallelismus in n-dimensionalen Mannigfaltigkeiten. *Commentarii Mathematici Helvetici*, 8(1):305–353, 1935.

[61] Hassler Whitney. Differentiable Manifolds. *Source: Annals of Mathematics*, 37(3):645–680, 1936.

[62] Samuel Eilenberg. Cohomology and Continuous Mappings. *The Annals of Mathematics*, 41(1):231, 1940.

[63] W. Hurewicz and N. E. Steenrod. Homotopy Relations in Fibre Spaces. *Proceedings of the National Academy of Sciences of the United States of America*, 27(1):60–64, 1941.

[64] Shiing-Shen Chern. A Simple Intrinsic Proof of the Gauss-Bonnet Formula for Closed Riemannian Manifolds. *Second Series*, 45(4):747–752, 1944.

[65] Shiing-shen Chern. Integral Formulas for the Characteristic Classes of Sphere Bundles. *Proceedings of the National Academy of Sciences of the United States of America*, 30(9):269–273, 1944.

[66] B. Andrei Bernevig and Shou Cheng Zhang. Quantum spin hall effect. *Physical Review Letters*, 96(10), 2006.

[67] C. L. Kane and E. J. Mele. Quantum Spin hall effect in graphene. *Physical Review Letters*, 95(22):0–3, 2005.

[68] C. L. Kane and E. J. Mele. Z2 topological order and the quantum spin hall effect. *Physical Review Letters*, 95(14):3–6, 2005.

[69] Nicolas Lenzing, Alexander I Lichtenstein, and Michael Potthoff. Emergent non-Abelian gauge theory in coupled spin-electron dynamics. *Physical Review B*, 106(9):94433, 2022.

[70] Daniel C. Mattis. The Theory of Magnetism I. 17, 1981.

[71] Assa Auerbach. Interacting Electrons and Quantum Magnetism. 1994.

[72] Wolfgang Nolting and Anupuru Ramakanth. Quantum theory of magnetism. *Quantum Theory of Magnetism*, pages 1–752, 2009.

[73] M A Ruderman and C Kittel. Indirect exchange coupling of nuclear magnetic moments by conduction electrons. *Physical Review*, 96(1):99–102, 1954.

[74] Tadao Kasuya. A Theory of Metallic Ferro- and Antiferromagnetism on Zener's Model. *Progress of Theoretical Physics*, 16(1):45–57, 1956.

[75] Kei Yosida. Magnetic Proyerties of Cu-Mn Alloys. 106(5), 1957.

[76] P W Anderson. Antiferromagnetism. Theory of Suyerexchange Interaction. 1950.

[77] Clarence Zener. Interaction between the d-shells in the transition metals. II. Ferromagnetic compounds of manganese with Perovskite structure. *Physical Review*, 82(3):403–405, 1951.

[78] Malgorzata Grazyna Makowska, Markus Strobl, Erik Mejdal Lauridsen, Al , Prince Babbar, Philip Niehoff, Falko Schappacher, Yuki Orikasa, Yuma Gogyo, B Skubic, J Hellsvik, L Nordström, and O Eriksson. A method for atomistic spin dynamics simulations: implementation and examples You may also like Phase Transition Mapping by Means of Neutron Imaging in SOFC Anode Supports during Reduction under Applied Stress Studying the Effects of Carbon Coatings on th. *Journal of Physics: Condensed Matter J. Phys.: Condens. Matter*, 20:12, 2008.

[79] Alexander Cyril Hewson. *The Kondo Problem to Heavy Fermions*. Cambridge University Press, 1993.

[80] S. Doniach. The Kondo lattice and weak antiferromagnetism. *Physica B+C*, 91(C):231–234, 1977.

[81] C Jayaprakash, H R Krishna-Murthy, and J W Wilkins. Two-Impurity Kondo Problem. *Physical Review Letters*, 47(10):737–740, 1981.

[82] Andrej Schwabe, Daniel Gütersloh, and Michael Potthoff. Competition between kondo screening and indirect magnetic exchange in a quantum box, 2012.

[83] Andrej Schwabe, Mirek Hänsel, Michael Potthoff, and Andrew K Mitchell. Screening mechanisms in magnetic nanostructures. *Physical Review B*, 92(15):155104, 2015.

[84] Akimasa Sakuma. First-principles study on the gilbert damping constants of transition metal alloys, Fe-Ni and Fe-Pt systems. *Journal of the Physical Society of Japan*, 81(8), 2012.

[85] Satadeep Bhattacharjee, Lars Nordström, and Jonas Fransson. Atomistic spin dynamic method with both damping and moment of inertia effects included from first principles. *Physical Review Letters*, 108(5), 2012.

[86] Mohammad Sayad and Michael Potthoff. Spin dynamics and relaxation in the classical-spin Kondo-impurity model beyond the Landau–Lifschitz–Gilbert equation. *New Journal of Physics*, 17(11):113058, 2015.

[87] Michael Elbracht, Simon Michel, and Michael Potthoff. Topological Spin Torque Emerging in Classical Spin Systems with Different Timescales. *Physical Review Letters*, 124(19), 2020.

[88] Simon Michel and Michael Potthoff. Non-Hamiltonian dynamics of indirectly coupled classical impurity spins. *Physical Review B*, 103(2), 2021.

[89] Wolfgang Nolting. *Analytische Mechanik*. Springer-Lehrbuch. Springer Berlin Heidelberg, Berlin, Heidelberg, 2014.

[90] L. D. Landau and E. M. Lifschitz. *Mechanik*. De Gruyter, 1962.

[91] L. LANDAU and E. LIFSHITZ. On the theory of the dispersion of magnetic permeability in ferromagnetic bodies. *Physikalische Zeitschrift der Sowjetunion*, 8:153–169, 1935.

[92] Thomas L. Gilbert. A phenomenological theory of damping in ferromagnetic materials. *IEEE Transactions on Magnetics*, 40(6):3443–3449, 2004.

[93] Kuo Ho Yang and Joseph O Hirschfelder. Generalizations of classical Poisson brackets to include spin. *Physical Review A*, 22(5):1814–1816, 1980.

[94] Brian Hall. *Lie Groups, Lie Algebras, and Representations*. Springer, 2015.

[95] Richard P. Feynman, Robert B. Leighton, and Matthew Sands. *Elektromagnetismus*. 2015.

[96] Larry Bates and Jedrzej Śniatycki. An extension of the Dirac theory of constraints. *Journal of Fixed Point Theory and Applications*, 14(2):527–554, 2013.

[97] Luca Lusanna. Dirac-Bergmann constraints in physics: Singular Lagrangians, Hamiltonian constraints and the second Noether theorem, 2018.

[98] P. A. M. Dirac. Generalized Hamiltonian Dynamics. *Canadian Journal of Mathematics*, 2:129–148, 1950.

[99] James L Anderson and Peter G Bergmann. Constraints in covariant field theories. *Physical Review*, 83(5):1018–1025, 1951.

[100] Peter G Bergmann, Irwin Goldberg, Allen Janis, and Ezra Newman. Canonical transformations and commutators in the Lagrangian formalism. *Physical Review*, 103(3):807–813, 1956.

[101] Jun Kondo. Resistance Minimum in Dilute Magnetic Alloys. *Progress of Theoretical Physics*, 32(1), 1964.

[102] Jerzy Dajka. Disentanglement of Qubits in Classical Limit of Interaction. *International Journal of Theoretical Physics*, 53(3):870–880, 2014.

[103] L Fratino, A Lampo, and H. T. Elze. Entanglement dynamics in a quantum-classical hybrid of two q-bits and one oscillator. *Physica Scripta*, 2014(T163), 2014.

[104] K. W. Kim, L. O'Brien, P A Crowell, C Leighton, and M D Stiles. Theory of Kondo suppression of spin polarization in nonlocal spin valves. *Physical Review B*, 95(10), 2017.

[105] Matthias Peschke, Lena Marie Woelk, and Michael Potthoff. Phase diagram of the Kondo model on the zigzag ladder. *Physical Review B*, 99(8), 2019.

[106] Michael Elbracht and Michael Potthoff. Long-time relaxation dynamics of a spin coupled to a Chern insulator. *Physical Review B*, 103(2):24301, 2021.

[107] D B Karki and Mikhail N Kiselev. Overscreened Kondo problem with large spin and large number of orbital channels: Two distinct semiclassical limits in quantum transport observables. *Physical Review B*, 103(20):201402, 2021.

[108] Robin Quade and Michael Potthoff. Controlling the real-time dynamics of a spin coupled to the helical edge states of the Kane-Mele model. *Physical Review B*, 105(3), 2021.

[109] Hans Thomas Elze. Linear dynamics of quantum-classical hybrids. *Physical Review A - Atomic, Molecular, and Optical Physics*, 85(5):52109, 2012.

[110] L. Andrew Wray, Su Yang Xu, Yuqi Xia, David Hsieh, Alexei V. Fedorov, Yew San Hor, Robert J. Cava, Arun Bansil, Hsin Lin, and M. Zahid Hasan. A topological insulator surface under strong Coulomb, magnetic and disorder perturbations. *Nature Physics*, 7(1):32–37, 2011.

[111] J. Honolka, A. A. Khajetoorians, V. Sessi, T. O. Wehling, S. Stepanow, J. L. Mi, B. B. Iversen, T. Schlenk, J. Wiebe, N. B. Brookes, A. I. Lichtenstein, Ph Hofmann, K. Kern, and R. Wiesendanger. In-plane magnetic anisotropy of Fe atoms on Bi2Se 3(111). *Physical Review Letters*, 108(25):256811, 2012.

[112] T. Valla, Z. H. Pan, D. Gardner, Y. S. Lee, and S. Chu. Photoemission spectroscopy of magnetic and nonmagnetic impurities on the surface of the Bi 2Se 3 topological insulator. *Physical Review Letters*, 108(11):117601, 2012.

[113] Florian Goth, David J Luitz, and Fakher F Assaad. Magnetic impurities in the Kane-Mele model. *Physical Review B*, 88(7):75110, 2013.

[114] T Eelbo, M. Waśniowska, M Sikora, M. Dobrzański, A Kozłowski, A Pulkin, G Autès, I Miotkowski, O V Yazyev, and R Wiesendanger. Strong out-of-plane magnetic anisotropy of Fe adatoms on Bi2Te3. *Physical Review B*, 89(10):104424, 2014.

[115] Yuanchang Li, Xiaolong Zou, Jia Li, and Gang Zhou. Ferromagnetism and topological surface states of manganese doped Bi2Te3: Insights from density-functional calculations. *Journal of Chemical Physics*, 140(12):124704, 2014.

[116] Andreas Pieper and Holger Fehske. Topological insulators in random potentials. *Physical Review B*, 93(3):35123, 2016.

[117] V. D Kurilovich, P D Kurilovich, and I S Burmistrov. Indirect exchange interaction between magnetic impurities near the helical edge. *Physical Review B*, 95(11):115430, 2017.

[118] Philipp Rüßmann, Sanjoy K Mahatha, Paolo Sessi, Miguel A Valbuena, Thomas Bathon, Kai Fauth, Sylvie Godey, Aitor Mugarza, Konstantin A Kokh, Oleg E Tereshchenko, Pierluigi Gargiani, Manuel Valvidares, Erika Jiménez, Nicholas B Brookes, Matthias Bode, Gustav Bihlmayer, Stefan Blügel, Phivos Mavropoulos, Carlo Carbone, and Alessandro Barla. Towards microscopic control of the magnetic exchange coupling at the surface of a topological insulator. *JPhys Materials*, 1(1):15002, 2018.

[119] Oleg M Yevtushenko and Vladimir I Yudson. Kondo Impurities Coupled to a Helical Luttinger Liquid: RKKY-Kondo Physics Revisited. *Physical Review Letters*, 120(14):147201, 2018.

[120] K Sumida, M Kakoki, J Reimann, M Nurmamat, S Goto, Y Takeda, Y Saitoh, K A Kokh, O E Tereshchenko, J Güdde, U Höfer, and A Kimura. Magnetic-impurity-induced modifications to ultrafast carrier dynamics in the ferromagnetic topological insulators Sb 2-x V x Te 3. *New Journal of Physics*, 21(9):093006, 2019.

[121] Mir Vahid Hosseini, Zahra Karimi, and Jamal Davoodi. Indirect exchange interaction between magnetic impurities in one-dimensional gapped helical states. *Journal of Physics Condensed Matter*, 33(8), 2020.

[122] M. Born and V. Fock. Beweis des Adiabatensatzes. *Zeitschrift für Physik*, 51(3-4):165–180, 1928.

[123] Sabine Jansen, Mary Beth Ruskai, and Ruedi Seiler. Bounds for the adiabatic approximation with applications to quantum computation. *Journal of Mathematical Physics*, 48(10):102111, 2007.

[124] Wolfgang Nolting. *Quantenmechanik - Methoden und Anwendungen*. Springer-Lehrbuch. Springer Berlin Heidelberg, Berlin, Heidelberg, 2013.

[125] Hans Thomas Elze. Linear dynamics of quantum-classical hybrids. *Physical Review A*, 85(5):52109, 2012.

[126] M Lakshmanan and M Daniel. Comment on the classical models of electrons and nuclei and the generalizations of classical Poisson brackets to include spin. *The Journal of Chemical Physics*, 78(12):7505–7506, 1982.

[127] André Heslot. Quantum mechanics as a classical theory. *Physical Review D*, 31(6):1341–1348, 1985.

[128] Michael J.W. Hall. Consistent classical and quantum mixed dynamics. *Physical Review A*, 78(4), 2008.

[129] Hans Hellmann. *Einführung in die Quantenchemie*. Springer Berlin Heidelberg, 2015.

[130] R. P. Feynman. Forces in molecules. *Physical Review*, 56(4):340–343, 1939.

[131] Issai Schur. *Neue Begründung der Theorie der Gruppencharaktere*. Preussische Akademie der Wissenschaften, Berlin, 1905.

[132] János K. Asbóth, László Oroszlány, and András Pályi. A Short Course on Topological Insulators: Band-structure topology and edge states in one and two dimensions. 2015.

[133] I. Dzyaloshinsky. A thermodynamic theory of "weak" ferromagnetism of antiferromagnetics. *Journal of Physics and Chemistry of Solids*, 4(4):241–255, 1958.

[134] Tôru Moriya. Anisotropic superexchange interaction and weak ferromagnetism. *Physical Review*, 120(1):91–98, 1960.

[135] G. C. Wick. The evaluation of the collision matrix. *Physical Review*, 80(2):268–272, 1950.

[136] Wolfgang Nolting. Grundkurs Theoretische Physik 7. 2015.

[137] D J Thouless, M Kohmoto, M P Nightingale, and M. Den Nijs. Quantized hall conductance in a two-Dimensional periodic potential. *Physical Review Letters*, 49(6):405–408, 1982.

[138] Martin R. Zirnbauer. Riemannian symmetric superspaces and their origin in random-matrix theory. *Journal of Mathematical Physics*, 37(10):4986–5018, 1996.

[139] Roger S.K. Mong and Vasudha Shivamoggi. Edge states and the bulk-boundary correspondence in Dirac Hamiltonians. *Physical Review B*, 83(12):125109, 2011.

[140] N. Bloembergen and T. J. Rowland. Nuclear spin exchange in solids: Tl203 and Tl205 magnetic resonance in thallium and thallic oxide. *Physical Review*, 97(6):1679–1698, 1955.

[141] Qin Liu, Chao Xing Liu, Cenke Xu, Xiao Liang Qi, and Shou Cheng Zhang. Magnetic impurities on the surface of a topological insulator. *Physical Review Letters*, 102(15), 2009.

[142] Jinhua Gao, Weiqiang Chen, X C Xie, and Fu Chun Zhang. In-plane noncollinear exchange coupling mediated by helical edge states in quantum spin Hall systems. *Physical Review B*, 80(24), 2009.

[143] Mir Vahid Hosseini, Zahra Karimi, and Jamal Davoodi. Indirect exchange interaction between magnetic impurities in one-dimensional gapped helical states. *Journal of Physics Condensed Matter*, 33(8):9, 2020.

[144] Wen Yu Shan, Jie Lu, Hai Zhou Lu, and Shun Qing Shen. Vacancy-induced bound states in topological insulators. *Physical Review B*, 84(3):35307, 2011.

[145] Jie Lu, Wen Yu Shan, Hai Zhou Lu, and Shun Qing Shen. Non-magnetic impurities and in-gap bound states in topological insulators. *New Journal of Physics*, 13, oct 2011.

[146] J W González and J Fernández-Rossier. Impurity states in the quantum spin Hall phase in graphene. *Physical Review B*, 86(11):115327, 2012.

[147] Annica M Black-Schaffer and Alexander V Balatsky. Subsurface impurities and vacancies in a three-dimensional topological insulator. *Physical Review B*, 86(11):115433, 2012.

[148] Cheung Chan and Tai Kai Ng. Impurity scattering in the bulk of topological insulators. *Physical Review B*, 85(11):115207, 2012.

[149] Robert Jan Slager, Louk Rademaker, Jan Zaanen, and Leon Balents. Impurity-bound states and Green's function zeros as local signatures of topology. *Physical Review B*, 92(8):85126, 2015.

[150] Lukas Kimme and Timo Hyart. Existence of zero-energy impurity states in different classes of topological insulators and superconductors and their relation to topological phase transitions. *Physical Review B*, 93(3):35134, 2016.

[151] Vibhuti Bhushan Jha, Garima Rani, and R Ganesh. Impurity-induced current in a Chern insulator. *Physical Review B*, 95(11):115434, 2017.

[152] Yanxia Liu and Shu Chen. Diagnosis of bulk phase diagram of nonreciprocal topological lattices by impurity modes. *Physical Review B*, 102(7):75404, 2020.

[153] Seydou-Samba Diop, Lars Fritz, Matthias Vojta, and Stephan Rachel. Impurity bound states as detectors of topological band structures revisited. *Physical Review B*, 101:245132, 2020.

[154] Xiaojuan Ni, Huaqing Huang, and Feng Liu. Robustness of topological insulating phase against vacancy, vacancy cluster, and grain boundary bulk defects. *Physical Review B*, 101(12):125114, 2020.

[155] Simon Michel, Axel Fünfhaus, Robin Quade, Roser Valentí, and Michael Potthoff. Bound states and local topological phase diagram of classical impurity spins coupled to a Chern insulator. *Physical Review B*, 109(15):155116, 2024.

[156] Nicolas Lenzing, David Krüger, and Michael Potthoff. Geometrical torque on magnetic moments coupled to a correlated antiferromagnet. *Physical Review Research*, 5(3), 2023.

[157] Kangkai Liang, Liya Bi, Qingyi Zhu, Hao Zhou, and Shaowei Li. Ultrafast Dynamics Revealed with Time-Resolved Scanning Tunneling Microscopy: A Review. *ACS Applied Optical Materials*, 1(5):924–938, 2023.

[158] Mohammad Sayad, Roman Rausch, and Michael Potthoff. Relaxation of a Classical Spin Coupled to a Strongly Correlated Electron System. *Physical Review Letters*, 117(12), 2016.

[159] Frank Schindler, Ashley M Cook, Maia G Vergniory, Zhijun Wang, Stuart S.P. Parkin, B. Andrei Bernevig, and Titus Neupert. Higher-order topological insulators. *Science Advances*, 4(6), 2018.

[160] Qin Liu and Tianxing Ma. Classical spins in topological insulators. *Physical Review B*, 80(11), 2009.

[161] Roland Wiesendanger. Spin mapping at the nanoscale and atomic scale. *Reviews of Modern Physics*, 81(4):1495–1550, 2009.

[162] D. M. Eigler and E. K. Schweizer. Positioning single atoms with a scanning tunnelling microscope. *Nature*, 344(6266):524–526, 1990.

[163] Roland Wiesendanger. Single-atom magnetometry, 2011.

[164] Friedrich Reinert and Stefan Hüfner. Photoemission spectroscopy - From early days to recent applications, 2005.

[165] Rok Žitko. Quantum impurity on the surface of a topological insulator. *Physical Review B*, 81(24), 2010.

[166] Hai Feng Lü, Hai Zhou Lu, Shun Qing Shen, and Tai Kai Ng. Quantum impurity in the bulk of a topological insulator. *Physical Review B*, 87(19):195122, 2013.

[167] Shi Han Zheng, Ming Xun Deng, Jian Ming Qiu, Qing Hu Zhong, Mou Yang, and Rui Qiang Wang. Interplay of quantum impurities and topological surface modes. *Physics Letters, Section A: General, Atomic and Solid State Physics*, 379(43-44):2890–2896, 2015.

[168] Felipe Crasto De Lima and Adalberto Fazzio. At the Verge of Topology: Vacancy-Driven Quantum Spin Hall in Trivial Insulators. *Nano Letters*, 21(22):9398–9402, 2021.

[169] Oliver Breunig and Yoichi Ando. Opportunities in topological insulator devices. *Nature Reviews Physics 2021 4:3*, 4(3):184–193, 2021.

[170] E. Fermi. Zur Quantelung des idealen einatomigen Gases. *Zeitschrift für Physik*, 36(11-12):902–912, 1926.

[171] P. A. M. Dirac. On the theory of quantum mechanics. *Proceedings of the Royal Society of London. Series A, Containing Papers of a Mathematical and Physical Character*, 112(762):661–677, 1926.

List of Publications

All figures in this work were created by the author, and the results presented were obtained as part of the author's research. Major results of this thesis have been published in the following peer reviewed articles:

Simon Michel, Axel Fünfhaus, Robin Quade, Roser Valentí, and Michael Potthoff. Bound states and local topological phase diagram of classical impurity spins coupled to a Chern insulator. *Physical Review B*, 109(15), apr 2024.

Simon Michel and Michael Potthoff. Spin Berry curvature of the Haldane model. *Physical Review B*, 106(23), dec 2022.

Simon Michel and Michael Potthoff. Non-Hamiltonian dynamics of indirectly coupled classical impurity spins. *Physical Review B*, 103(2), sep 2021.

Michael Elbracht, Simon Michel, and Michael Potthoff. Topological Spin Torque Emerging in Classical Spin Systems with Different Timescales. *Physical Review Letters*, 124(19), feb 2020.

Eidestattliche Versicherung / Declaration on Oath

Hiermit versichere ich an Eides statt, die vorliegende Dissertationsschrift selbst verfasst und keine anderen als die angegebenen Hilfsmittel und Quellen benutzt zu haben.

I hereby declare, on oath, that I have written the present dissertation by my own and have not used other than the acknowledged resources and aids.

Hamburg, November 27, 2023

Simon Michel